



HAL
open science

Additive manufacturing of the high-performance thermoplastic : experimental study and numerical simulation of the Fused Filament Fabrication

Shahriar Bakrani Balani

► **To cite this version:**

Shahriar Bakrani Balani. Additive manufacturing of the high-performance thermoplastic : experimental study and numerical simulation of the Fused Filament Fabrication. Materials. Institut National Polytechnique de Toulouse - INPT, 2019. English. NNT : 2019INPT0055 . tel-04167151v2

HAL Id: tel-04167151

<https://theses.hal.science/tel-04167151v2>

Submitted on 20 Jul 2023

HAL is a multi-disciplinary open access archive for the deposit and dissemination of scientific research documents, whether they are published or not. The documents may come from teaching and research institutions in France or abroad, or from public or private research centers.

L'archive ouverte pluridisciplinaire **HAL**, est destinée au dépôt et à la diffusion de documents scientifiques de niveau recherche, publiés ou non, émanant des établissements d'enseignement et de recherche français ou étrangers, des laboratoires publics ou privés.



Université
de Toulouse

THÈSE

En vue de l'obtention du

DOCTORAT DE L'UNIVERSITÉ DE TOULOUSE

Délivré par :

Institut National Polytechnique de Toulouse (Toulouse INP)

Discipline ou spécialité :

Science et Génie des Matériaux

Présentée et soutenue par :

M. SHAHRIAR BAKRANI BALANI

le vendredi 7 juin 2019

Titre :

Additive manufacturing of the high-performance thermoplastic:
Experimental study and numerical simulation of the Fused Filament
Fabrication

Ecole doctorale :

Sciences de la Matière (SDM)

Unité de recherche :

Laboratoire de Génie de Productions de l'ENIT (E.N.I.T-L.G.P.)

Directeur(s) de Thèse :

MME VALERIE NASSIET

M. ARTHUR CANTAREL

Rapporteurs :

M. GILLES AUSIAS, UNIVERSITE DE BRETAGNE SUD

M. VINCENT SOBOTKA, UNIVERSITE DE NANTES

Membre(s) du jury :

M. FABRICE SCHMIDT, ECOLE NLE SUP DES MINES ALBI CARMAUX, Président

M. ARTHUR CANTAREL, UNIVERSITE TOULOUSE 3, Membre

M. MATTHIEU ZINET, UNIVERSITE LYON 1, Membre

Mme FRANCE CHABERT, ECOLE NATIONALE D'INGENIEUR DE TARBES, Membre

Mme VALERIE NASSIET, ECOLE NATIONALE D'INGENIEUR DE TARBES, Membre

M. ORLANDO SANTANA, UNIV POLITECNICA DE CATALUNYA BARCELONA, Membre



THÈSE

En vue de l'obtention du
DOCTORAT DE L'UNIVERSITÉ DE TOULOUSE

Délivré par l'Institut National Polytechnique de Toulouse

Présentée et soutenue par

Shahriar BAKRANI BALANI

Le 7 juin 2019

**Additive manufacturing of the high-performance
thermoplastics: Experimental study and numerical
simulation of the Fused Filament Fabrication**

Ecole doctorale : **SDM - SCIENCES DE LA MATIERE – Toulouse**

Spécialité : **Sciences et Génie des Matériaux**

Unité de recherche :
LGP - Laboratoire Génie de Production

Thèse dirigée par
Valérie NASSIET

Jury

M. Vincent Sobotka, Rapporteur
M. Gilles Ausias, Rapporteur
M. Fabrice Schmidt, Examineur
M. Matthieu Zinet, Examineur
M. Orlando Santana, Examineur
Mme Valérie Nassiet, Directrice de thèse
Mme France Chabert, Co-encadrante de thèse
M. Arthur Cantarel, Co-directeur de thèse

Dedication:

I am dedicating this thesis to four beloved people who have meant and continue to mean so much to me: my father, my mother and my siblings.

Acknowledgement

This Ph.D. thesis has been carried out in the period of octobre 2015 to mars 2019 in the Laboratoire Génie de Production (EA1905) at Ecole Nationale d'Ingénieurs de Tarbes (ENIT) in the Interfaces and Functional Materials team, and Institut Clément Ader (UMR-CNRS 5312) at IUT Tarbes. I am so grateful to the APR Occitanie Region/Université Fédérale de Toulouse scholarship for making it possible for me to do my research here.

First of all, I would like to express my deepest gratitude to my supervisors: Prof. Valerie Nassiet, Dr. France Chabert and, Dr. Arthur Cantarel for their support, instruction, supervision and patience throughout my doctoral studies. Besides their scientific supervision, I highly appreciate their great personality.

I would like to thanks my defence jury, Dr. Gilles Ausias from Université Bretagne-sud, Prof. Vincent Sobotka from Université de Nantes, Prof. Orlando Santana from Polytechnic University of Catalonia, Prof. Fabrice Schmidt from Ecole Mines d'Albi and Dr. Matthieu Zinet from Université de Lyon for their time and effort they put to provide the feedback to improve the quality of the manuscript.

I am also grateful to the following university staffs: Eliane Casta, Marie Cecile De Barros, Marie Teixeira, Amandine Abadie and, Guillaume Morel, Arthur Visse and Friends: François Grizet, Amevi Tongne, Linda Elmhahbi, Rudy Nahed, Chen Li for their support during my research at Enit.

Finally, my deepest gratitude go to my family: my parents (Zahra and Gholamreza) and to my brother and sister (Alireza and Tahmine) for their unconditional and limitless love and care from miles and miles away. I would like to thanks my uncle (Asghar) and my aunt (Zohre) for supporting me spiritually throughout my studies and my life in general. I highly appreciate Renée and Djafar for their emotional supports during my stay in France. And my special thanks to Hossein my close friend for his great personality and his spiritual support.

And last but by no means least, also to everyone at ENIT and IUT... it was great sharing the laboratory with all of you during these past four years.

Thanks for all your encouragement!

24 March 2019

Shahriar Bakrani Balani

French Abstract

Chapitre 1 : Introduction

La fabrication additive (AM) fait référence à une grande variété de processus de fabrication pour le prototypage rapide et la production de produits finis et semi-finis. La classification des différentes techniques de fabrication additive est définie selon différents critères. Ces critères sont : la source d'énergie (faisceau d'électron, laser, résistance chauffante, ...), la famille de matériaux (polymères, métaux, céramiques, ...), le conditionnement des matières premières (filament, poudre, résine, ...). Les procédés de fabrication additive des polymères regroupent principalement les technologies de dépôt de filament, frittage de poudres et stéréolithographie. Malgré un intérêt croissant des industries et un public nombreux ces cinq dernières années, ces procédés de fabrication ne sont toujours pas bien maîtrisés, en particulier pour les polymères non fabriqués en série. En effet, lorsque les matériaux polymères présentent des propriétés spécifiques, le contrôle de leur traitement est plus délicat. Des efforts supplémentaires sont nécessaires pour élargir les connaissances sur le phénomène physique impliqué au cours de ces processus.

L'industrie a besoin de polymères à hautes performances, c'est-à-dire de matériaux résistants exposés à un environnement hostile : atmosphère thermo-oxydante, résistance aux solvants chimiques et hautes résistances mécaniques telles que le frottement ou la compression. L'émergence de thermoplastiques hautement stables depuis les années 1980, tels que le PAEK (polyaryléthercétone), ouvre la voie à une utilisation généralisée. Ainsi, les thermoplastiques hautes performances sont des candidats potentiels pour la fabrication de pièces structurales destinées aux industries de l'aérospatiale, de l'automobile et du médical. Cependant, contrairement aux polymères conventionnels, le traitement des thermoplastiques hautes performances reste un défi en raison de leurs propriétés spécifiques. Le procédé FFF (Fused Filament Fabrication) est basé sur la fusion d'un fil ou d'un filament polymère dans une extrudeuse ; ce dernier est ensuite déposé couche par couche pour fabriquer les pièces finales. Ces défis sont plus difficiles à relever en cas de dépôt couche par couche où la liaison des couches déposées détermine les propriétés mécaniques des pièces imprimées. Le dépôt de polymère fondu couche par couche conduit à l'échauffement des couches empilées.

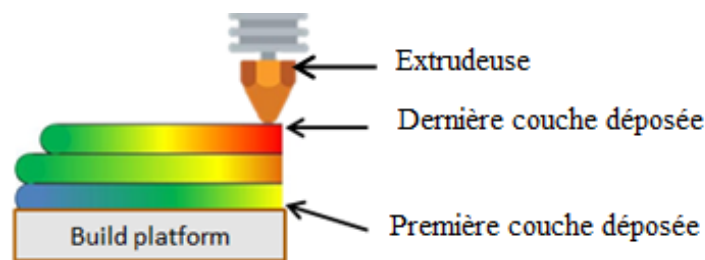


Figure 1: schématique représentation du procédé dépôts de filament couche par couche

Les pièces 3D souffrent de faibles propriétés mécaniques et d'une faible qualité de surface par rapport aux pièces fabriquées selon les techniques de traitement conventionnelles. Les propriétés mécaniques et la rugosité de surface des pièces 3D fabriquées par FFF sont contrôlées par l'adhérence des filaments et le taux de porosité. Les deux proviennent principalement de la capacité d'écoulement et de la tension superficielle du polymère. De plus, l'adhérence des filaments dépend de l'interdiffusion des chaînes polymères. Les propriétés du polymère telles que le comportement rhéologique, les propriétés thermiques, la tension superficielle et la cristallisation jouent un rôle crucial dans la compréhension de

l'effet des conditions d'impression sur la qualité des pièces finales. À notre connaissance, aucune étude du procédé FFF appliqué aux polymères semi-cristallins hautes performances n'était disponible lorsque ces travaux ont commencé en 2015. Depuis, des travaux de recherche similaires ont été lancés dans le monde entier.

Nos études visent à optimiser la qualité des pièces imprimées en comprenant le lien entre les paramètres d'impression, les propriétés du polymère et les propriétés mécaniques des pièces finales 3D. Notre étude porte principalement sur le PEEK (polyétheréthercétone). Les relations entre les paramètres d'impression et les propriétés du matériau (viscosité élongationnelle, viscoélasticité, coefficient de dilatation thermique, capacité thermique, conductivité thermique, cinétique de cristallisation ...) sur le flux de polymère et l'adhésion des filaments ont été clarifiées. Parallèlement, l'objectif était de mettre en place une simulation numérique des phénomènes impliqués dans ce processus. Le flux visqueux du polymère lors de son dépôt à l'état fondu a été modélisé et simulé en prenant en compte le transfert de chaleur et la cristallisation. Dans notre procédure, nous combinons des approches expérimentales, analytiques et numériques.

La première étape exposée au chapitre 2 afin d'étudier l'impression 3D du PEEK a consisté à caractériser le PEEK. Pour mieux comprendre les propriétés du PEEK et les difficultés de son impression 3D, nous avons comparé les propriétés rhéologiques, la cinétique de cristallisation et les propriétés thermiques du PEEK à celles du PLA.

Dans ce même chapitre, la coalescence du PEEK a été étudiée par étude expérimentale, par modèle analytique et par simulation numérique. Cette étude met en évidence le rôle central de la viscosité aux faibles déformations et de la tension superficielle sur la cinétique de coalescence.

Dans le troisième et dernier chapitre, l'influence des paramètres d'impression sur les propriétés rhéologiques tel que le taux de cisaillement, la viscosité de cisaillement et élongationnelle ainsi que le gonflement et la stabilité de l'extrudat a été quantifiée. Ce chapitre est clôturé par une étude numérique sur l'évolution de la température et du taux de cristallinité au cours du dépôt de matière sur la plateforme d'impression en fonction des températures environnementales et de la plateforme d'impression.

Chapitre 2 : Caractérisation polymère et étude de la coalescence

Dans le procédé FFF, la vitesse de refroidissement dépend fortement des conditions d'impression telles que la température d'impression, la température ambiante et la vitesse de dépôt matière. Par ailleurs, la vitesse de refroidissement influence directement la cinétique de cristallisation, la coalescence et le taux de porosité du produit final. Au cours du procédé FFF, le polymère fondu de la première couche est refroidi plus rapidement à la température du substrat par rapport aux couches supérieures pour lesquelles la vitesse de refroidissement du polymère diminue en raison de l'accumulation de couches dans la direction Z.

Par conséquent, la détermination des températures de transition du PEEK et l'influence de la vitesse de refroidissement sur la cinétique de cristallisation est très importante. Dans ce chapitre et le chapitre suivant, on va déterminer la transition vitreuse, la température de fusion et la cristallisation isotherme et non-isotherme du PEEK. Les essais DSC (Figure 2) non-isothermes ont été effectués sur le grade PEEK 450G.

Afin d'éliminer l'historique thermique, les échantillons ont été chauffés à $10\text{ }^{\circ}\text{C}\cdot\text{min}^{-1}$ jusqu'à la température de fusion. Ensuite, ils ont subi le deuxième cycle de chauffage de $2\text{ }^{\circ}\text{C}\cdot\text{min}^{-1}$ et le cycle de refroidissement de $2\text{ }^{\circ}\text{C}\cdot\text{min}^{-1}$.

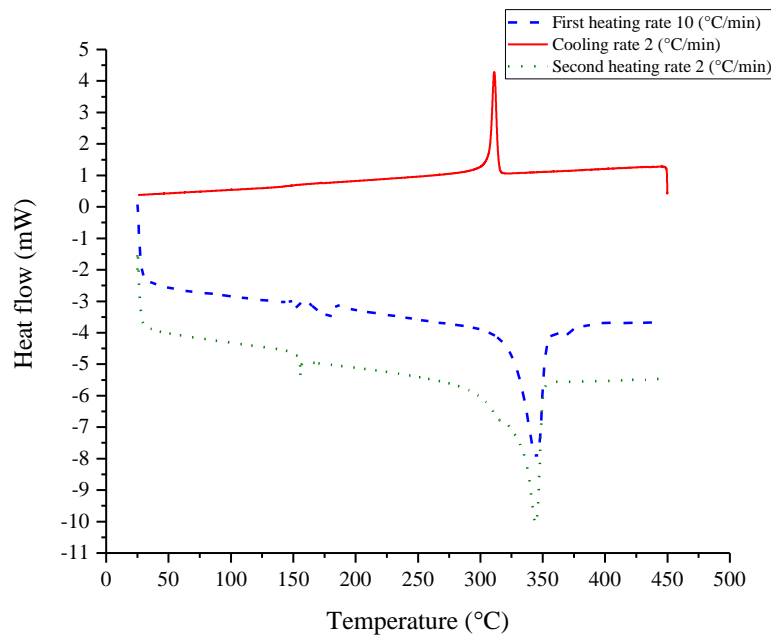


Figure 2: Courbe DSC du PEEK 450G, avec vitesse d'échauffement $2\text{ }^{\circ}\text{C}\cdot\text{min}^{-1}$ au cours du deuxième cycle de chauffage et vitesse de refroidissement de $2\text{ }^{\circ}\text{C}\cdot\text{min}^{-1}$

Au cours de la rampe de refroidissement représentée à la Figure 2, la transition vitreuse est mesurée à $149 \pm 1\text{ }^{\circ}\text{C}$. Durant la rampe de chauffe, la transition vitreuse observée à la même température est suivie d'un pic de fusion commençant à $300\text{ }^{\circ}\text{C}$ et se terminant à $360\text{ }^{\circ}\text{C}$, centrée à $344 \pm 3\text{ }^{\circ}\text{C}$ sans apparition de cristallisation à froid, comme prévu. Dans la première étape, à partir de l'enthalpie de fusion de $37 \pm 0,5\text{ J}\cdot\text{g}^{-1}$, le rapport de cristallinité a été déterminé à 40%. La cinétique de cristallisation du PEEK a été déterminée sous plusieurs vitesses de refroidissement. Avec une vitesse de refroidissement à $25\text{ }^{\circ}\text{C}\cdot\text{min}^{-1}$, la cristallisation a lieu de $295 \pm 2\text{ }^{\circ}\text{C}$ à $250 \pm 5\text{ }^{\circ}\text{C}$ et le début aux alentours de $289 \pm 1\text{ }^{\circ}\text{C}$.

L'enthalpie de cristallisation est de $41 \pm 1 \text{ J.g}^{-1}$, conduisant à un rapport de cristallinité de 31%. Par conséquent, le polymère atteint son rapport maximal de cristallinité à $2 \text{ }^\circ\text{C.min}^{-1}$.

Les propriétés rhéologiques influencent fortement la qualité des pièces fabriquées par FFF. La coalescence entre les couches et les segments déposés, la déformation des segments, le gonflement de l'extrudat en sortie de la buse sont directement liés aux propriétés rhéologiques.

Pour déterminer la viscosité de PEEK nous avons utilisé un rhéomètre en configuration plan-plan pour les basses fréquences et la filière élongationnelle pour les hautes fréquences.

Les tests de balayage en fréquence à différentes températures ont été réalisés en configuration plan-plan, sur la plage de fréquences $[0,05 \text{ à } 100 \text{ rad.s}^{-1}]$ sous 1% de déformation, pour quatre isothermes: $350 \text{ }^\circ\text{C}$, $366 \text{ }^\circ\text{C}$, $383 \text{ }^\circ\text{C}$ et $400 \text{ }^\circ\text{C}$.

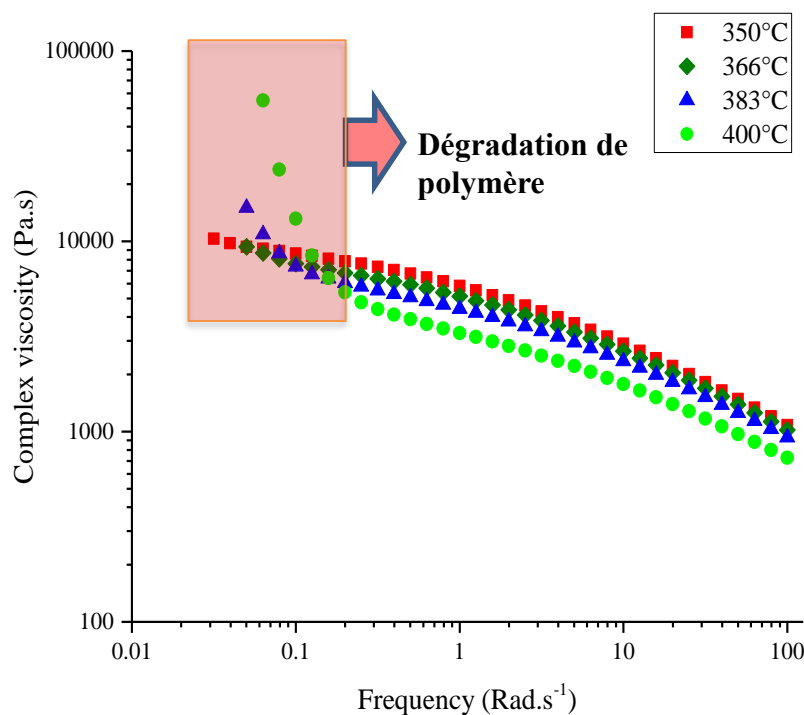


Figure 3: Viscosité complexe du PEEK (η^*) déterminée par la Rhéomètre

Le PEEK présente logiquement un comportement Rhéo-fluidifiant avec un plateau newtonien aux fréquences les plus basses. La viscosité complexe à 1 rad.s^{-1} est de 5841 Pa.s à $350 \text{ }^\circ\text{C}$, 5144 Pa.s à $366 \text{ }^\circ\text{C}$, 4413 Pa.s à $383 \text{ }^\circ\text{C}$ et finalement 3292 Pa.s à $400 \text{ }^\circ\text{C}$. Les résultats pour différentes températures montrent que l'augmentation de la température conduit à une diminution de la viscosité. En augmentant la fréquence, la viscosité de la PEEK diminue. Pour les températures élevées et les basses fréquences, la viscosité du PEEK augmente considérablement. Pour les températures les plus élevées, les chaînes moléculaires de la PEEK subissent par dégradation, une recombinaison des liaisons moléculaires et des ramifications sur le squelette principal de la chaîne.

La coalescence de deux filaments en contact est le principal processus influençant les propriétés mécaniques des pièces fabriquées par FFF. En effet, une bonne coalescence entre les filaments déposés réduit le taux de porosité dans les pièces fabriquées et augmente la liaison de deux filaments déposés, puis la cohésion structurelle des pièces.

La cinétique de coalescence entre deux filaments déposés a été déterminée expérimentalement, selon le modèle analytique modifié de Frankel et par simulation numérique. Les résultats obtenues avec les trois méthodes sont représentées en Figure 4.

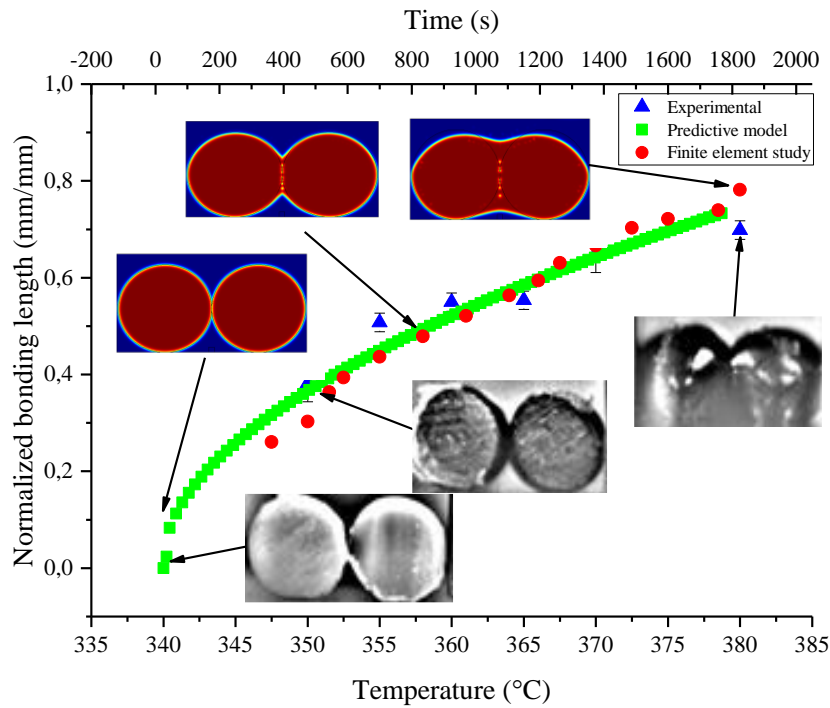


Figure 4: Evolution de la coalescence des filaments en fonction de la température

La Figure 4 montre la coalescence du PEEK. Le temps de coalescence est relativement long dû à la haute viscosité et la faible tension de surface du PEEK aux environs de 350 °C d’après la formule de Parachor.

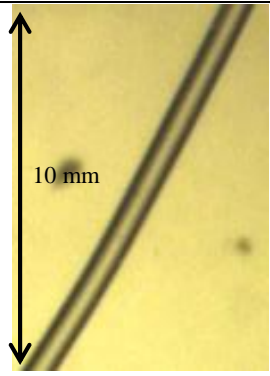
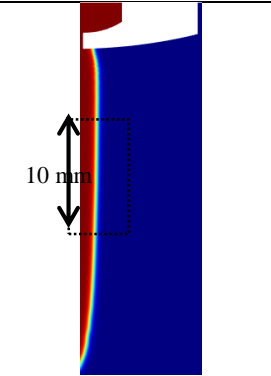
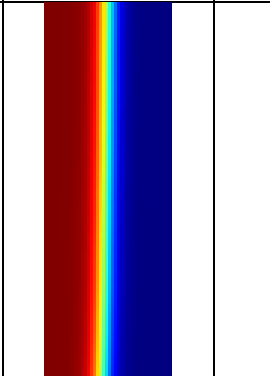
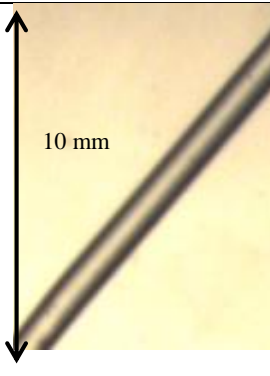
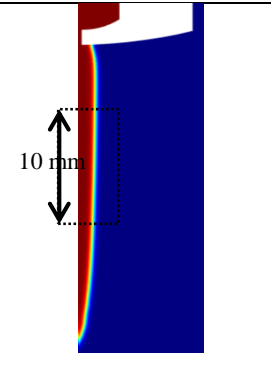
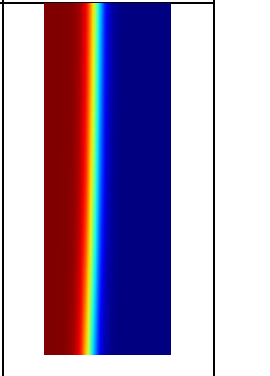
La comparaison de l’étude expérimentale avec le modèle prédictif montre que les résultats sont proches malgré quelques écarts attribués principalement à la cristallinité du PEEK et la présence des forces de gravité non représentées dans le modèle analytique et la simulation numérique.

Chapitre 3 : Simulation numérique de dépôt de matière et cristallisation

L'influence du taux de cisaillement sur la forme des extrudés a été déterminée entre 1200 s^{-1} et plus de 5000 s^{-1} . Les observations optiques ont révélé que, pour les taux de cisaillement les plus bas, la forme de l'extrudat reste cylindrique avec une surface lisse, alors qu'à des vitesses de cisaillement et des vitesses d'entrée plus élevées, des déformations étaient observées à la surface. La limite semblait être d'environ

4000 s^{-1} . En dessous de cette valeur, la forme de l'extrudat reste régulière, alors que lorsque le cisaillement dépassait 4000 s^{-1} , le forme de l'extrudat présentait des défauts. À 4100 s^{-1} , une instabilité macroscopique a été observée sur l'extrudat.

Les résultats des simulations numériques du TPF (Two-Phase Flow) ont révélé qu'à des vitesses d'entrée et des taux de cisaillement plus élevés, une certaine instabilité du flux de polymère était observée. Ce résultat est cohérent avec les observations expérimentales. Lorsque la vitesse d'entrée était inférieure à 145 mm.s^{-1} , le flux de polymère était stable et aucune déformation de l'extrudat n'était observée.

Vitesse d'entrée ($\text{mm}\cdot\text{s}^{-1}$)	Taux de cisaillement (s^{-1})	Etude Expérimentale	Simulation numérique (Fraction volumique)	Vue magnifiée	Légende
88	1561				
99	1753				

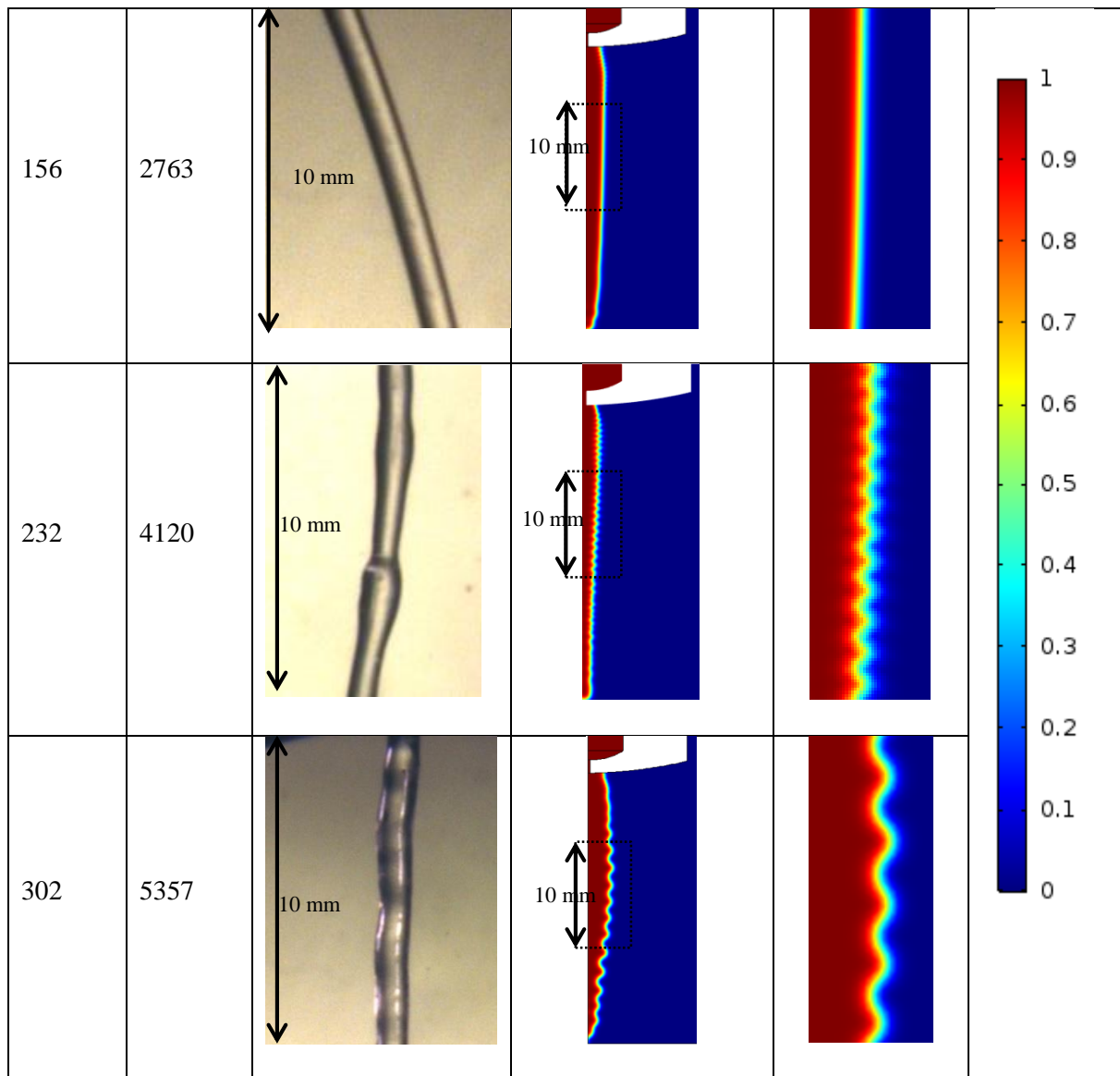


Figure 5: Influence de la vitesse d'entrée et taux de cisaillement sur la forme de l'extrudat sortant de la buse avec un diamètre de 0.5 mm

La détermination le taux de gonflement dans le procédé d'extrusion (et le procédé de FFF) peut améliorer la qualité des pièces fabriquées. Pour déterminer le taux de gonflement il est nécessaire de connaître le spectre des temps de relaxation et la viscosité élongation en sortie de filière. Des mesures rhéologiques en configuration plan-plan ont permis la mesure de la viscosité dynamique aux basse fréquences de $0,01 \text{ s}^{-1}$ à 100 s^{-1} dans le domaine viscoélastique linéaire. Pour les taux de cisaillement les plus élevés, compris entre 100 s^{-1} et $10\,000 \text{ s}^{-1}$ ainsi que pour la viscosité élongationnelle, une filière jonc a été positionnée en sortie d'extrudeuse.

La Figure 6 illustre les résultats de viscosité déterminée par les deux méthodes expérimentales à 383 °C . La viscosité complexe est représentée par les points bleus et la viscosité au cisaillement déterminée par la filière en extension est représentée par les points roses. De plus, la viscosité en extension déterminée par la filière est représentée en points rouges.

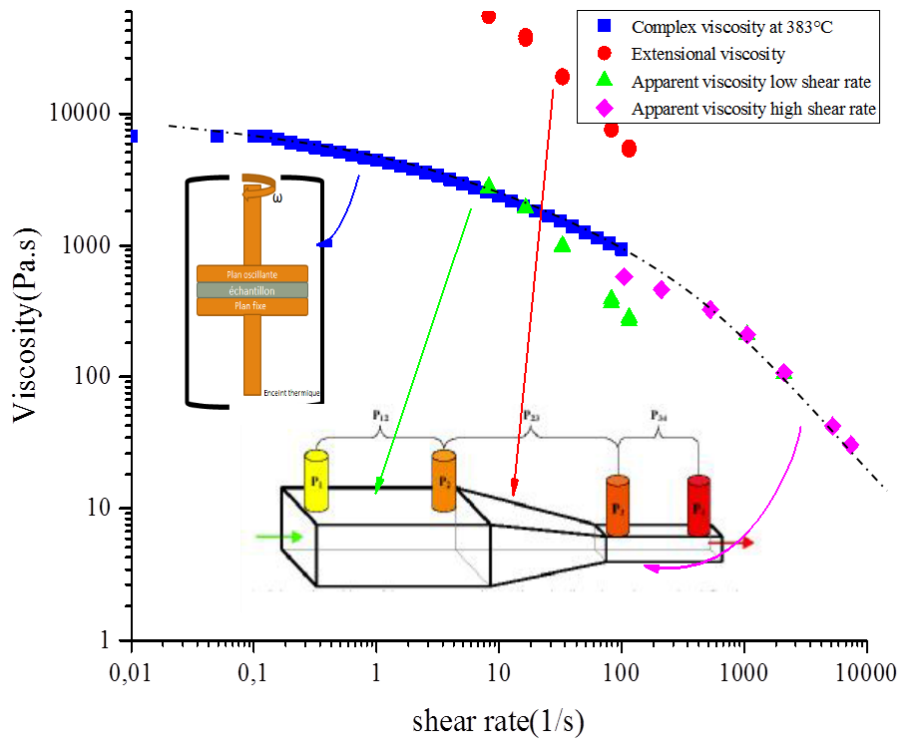


Figure 6: Viscosité de PEEK à 383 °C déterminée par Rhéomètre et la filière élongationnelle

Les termes du modèle de Carreau ont été déterminés avec interpolation de la courbe de viscosité sur les résultats obtenus avec le rhéomètre et la filière élongationnelle. Le tableau 1 présente les valeurs des termes du modèle de Carreau déterminées par interpolation des points.

Dans la simulation numérique du TPF, la viscosité est insérée dans le modèle de Carreau, ce qui pourrait permettre de déterminer la viscosité en fonction du taux de cisaillement et de la température.

Les données de viscosité en fonction du taux de déformation suivent une loi de Carreau implémentée dans le modèle numérique. Le Tableau 1 présente les valeurs des termes du modèle de Carreau déterminées par interpolation des points.

Tableau 1: Les termes de la modèle Carreau à 383 °C

Polymère	PEEK
Température	655 K
η_0	7071 \pm 153
η_{inf}	0
λ	1.45 \pm 0.6
a	0.78 \pm 0.12
n	0.59 \pm 0.06

La Figure 7 représente le temps de relaxation à 350 °C, 366 °C, 383 °C et 400 °C déterminé à partir des données de viscosité et de complaisance. Comme prévu, les temps de relaxation sont plus courts pour les températures les plus élevées et répondent à une loi d'Arrhénius.

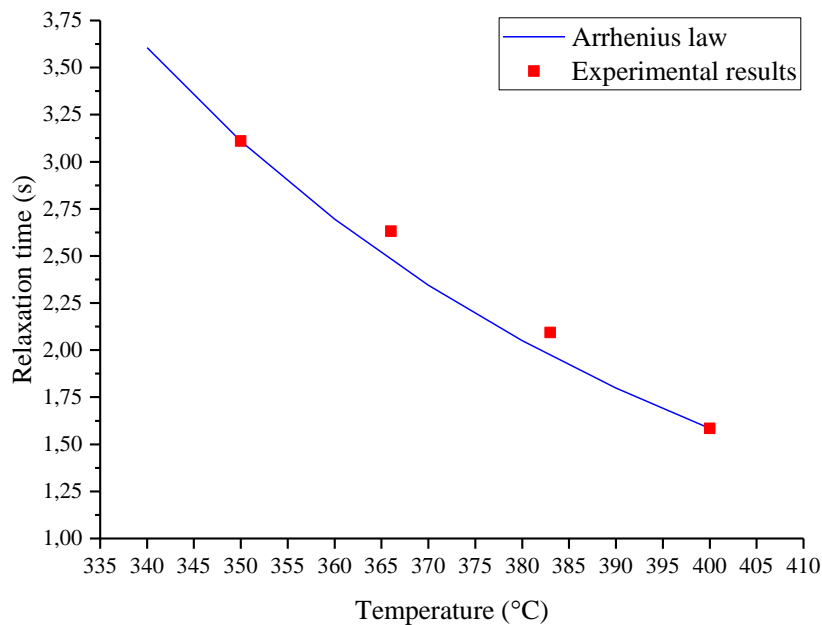


Figure 7: Le temps de relaxation en fonction de la température détermine étude expérimentale et loi d'Arrhenius

Le taux de gonflement de l'extrudat en sortie de la buse a été déterminé selon l'hypothèse :

- Le Capillaire est court

Notre mesure sur le taux du gonflement montre que lorsque la température augmente, le taux de gonflement du PEEK diminue légèrement. Ceci est dû à la réduction du temps de relaxation. En FFF, le taux maximum de gonflement du PEEK sera d'environ 3,5 dans ces conditions.

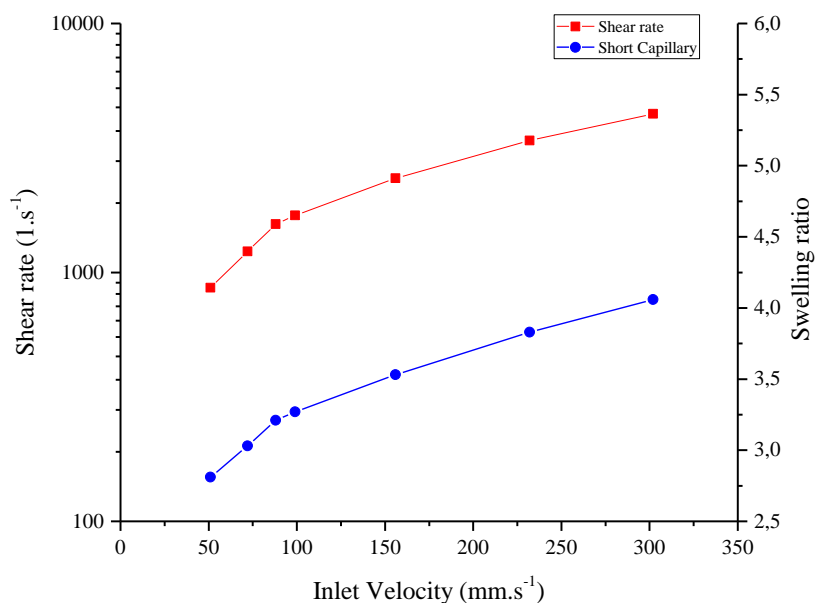


Figure 8: Influence de la vitesse d'entrée sur le taux de cisaillement et le gonflement de l'extrudate en PEEK à 383 °C

Comme prévu, l'augmentation de la vitesse d'entrée entraîne une augmentation du taux de gonflement du PEEK. Pour les paramètres d'impression du procédé FFF, le taux de cisaillement est inférieur à 1000 s^{-1} et le taux de gonflement maximal du PEEK sera inférieur à 2,5 dans ces conditions.

La Figure 9 montre le coefficient de cinétique d'Avrami déterminé par l'approche d'Avrami et le modèle prédictif. Le coefficient de cinétique d'Avrami montre l'évolution des phases amorphes et des phases cristallines. Les résultats expérimentaux ont été interpolés par l'équation de Hoffman-Lauritzen afin de déterminer la cristallisation à mi-temps à différentes températures allant de la température de fusion à la transition vitreuse. Le modèle prédictif est en accord avec les résultats expérimentaux. Pour des températures proches de la température de fusion, l'exposant d'Avrami tend vers 4 alors que pour les basses températures, il tend vers 3. Ce résultat est cohérent avec nos observations sur l'existence de deux structures cristallines pendant la fusion du PEEK représentée dans Figure 2 par un épaulement du pic de fusion. Selon les résultats de DSC de la Figure 2, la température de transition de la première structure cristalline à la deuxième structure cristalline a lieu à environ 315 °C .

La Figure 9 montre que la cinétique de cristallisation du PEEK 450G est à sa valeur maximale autour de 243 °C . Cependant, au voisinage de la température de fusion et de la transition vitreuse, la cinétique de cristallisation est plus lente.

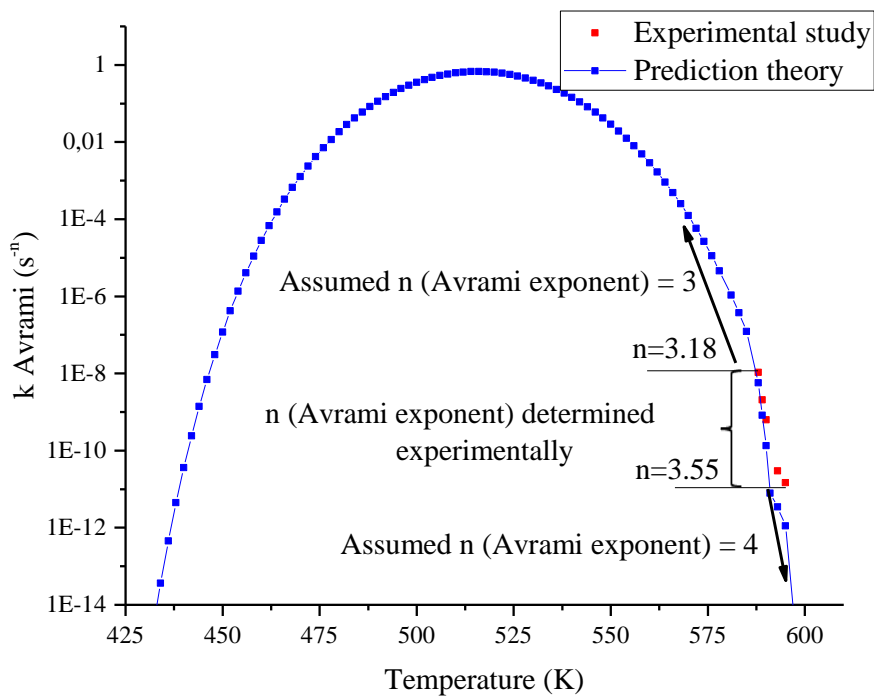


Figure 9: Détermination de la cinétique d'Avrami de la transition vitreuse jusqu'à la température de fusion

La simulation numérique du dépôt de polymère sur le substrat a été réalisée par COMSOL Multiphysics. L'écoulement du polymère, la distribution de la température et le taux de cristallinité lors du procédé FFF ont été déterminés par simulation numérique. En ajoutant un terme de convection à la cristallisation non isotherme de Nakamura, nous sommes en mesure de déterminer l'évolution du champ de cristallisation lors du refroidissement de polymères semi-cristallins en tenant compte de l'écoulement du fluide.

Sur la Figure 10, la légende représente la fraction volumique du fluide dans le système : le bleu (ce qui équivaut à 0 dans la légende de la couleur) représente l'air dans le système et le rouge (1 dans la légende de la couleur) représente le polymère.

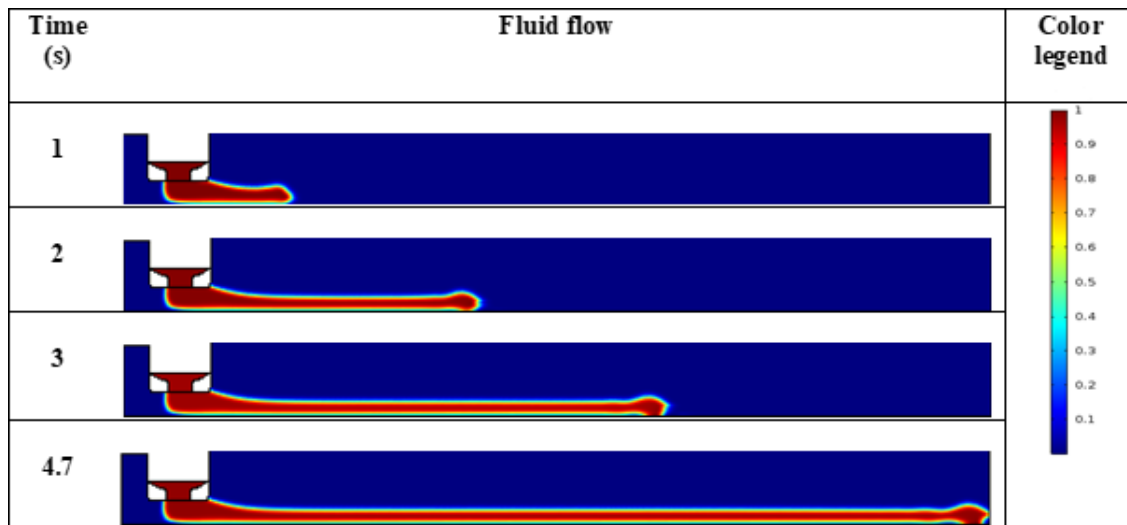


Figure 10: Simulation numérique de première couche sur platine mobile

La Figure 11 illustre la répartition cristalline à différents moments pour la température environnementale $T_{Env.} = 160\text{ °C}$ et la température du substrat $T_{Sub.} = 160\text{ °C}$. Le taux de cristallinité au centre de l'extrudat lorsque la température est encore élevée est très faible, tandis qu'en début d'extrudat où la vitesse de refroidissement est élevée, la cristallinité atteint 23 %. D'autre part, près de la surface lorsque la surface de l'extrudat est soumise à un transfert de chaleur avec l'air, la cinétique de cristallisation est plus lente qu'au centre du cordon. Par conséquent, près de la surface, la cristallisation n'a pas pu atteindre sa valeur maximale.

Par conséquent, la température de l'environnement proposée pour favoriser l'interdiffusion est comprise entre 285 °C et 300 °C . Le choix des températures dépend également de la vitesse d'impression. À une vitesse d'impression plus élevée, lorsque le dépôt du second cordon sur le premier cordon est relativement rapide, nous pourrions utiliser une température encore plus basse. Contrairement à l'impression rapide, lorsque la vitesse d'impression est lente, la température d'environnement doit être augmentée.

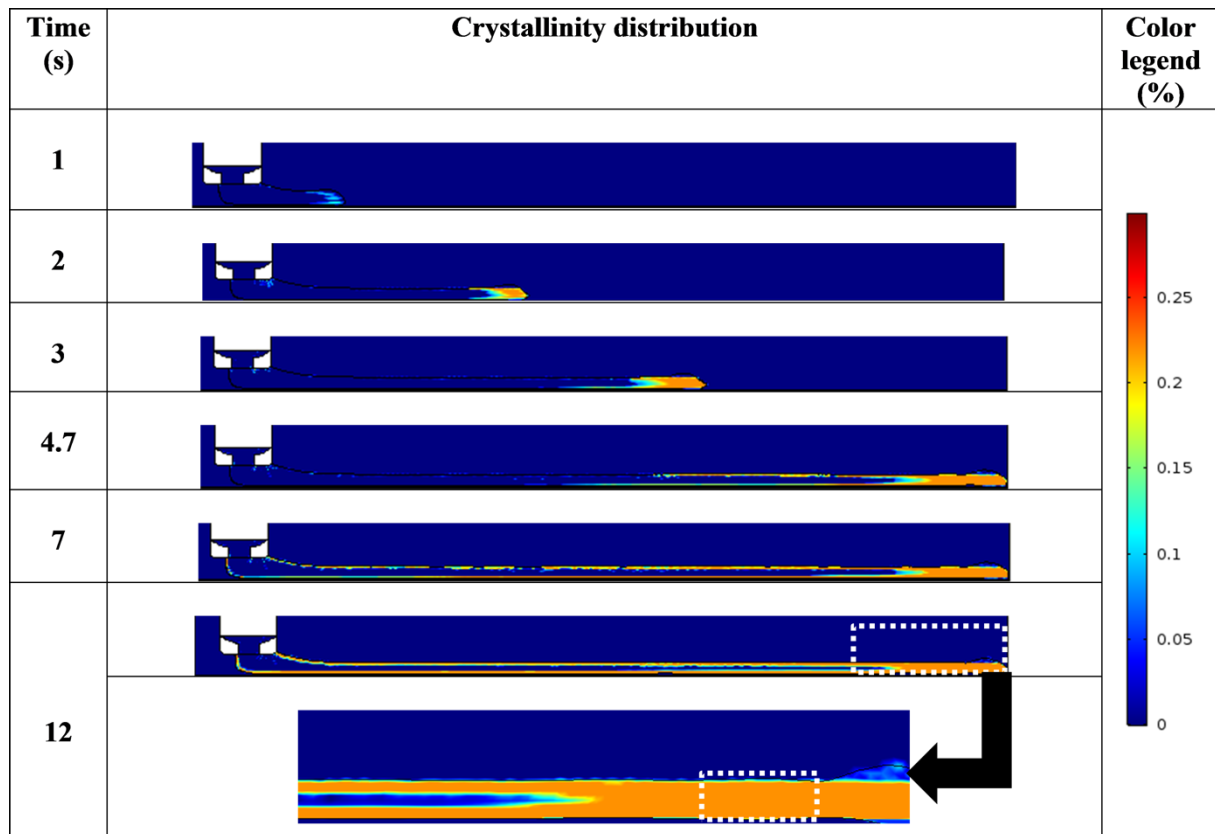


Figure 11: Distribution de la cristallinité de PEEK pour $T_{\text{substrat}} = 160^{\circ}\text{C}$ and $T_{\text{env.}} = 160^{\circ}\text{C}$

Conclusion

Nos études ont visé à optimiser la qualité des pièces imprimées en comprenant le lien entre les paramètres d'impression, les propriétés du polymère et les propriétés mécaniques des pièces finales 3D. Notre étude porte principalement sur le PEEK (polyétheréthercétone). Les relations entre les paramètres d'impression et les propriétés du matériau (viscosité élongationnelle, viscoélasticité, coefficient de dilatation thermique, capacité thermique, conductivité thermique, cinétique de cristallisation ...) sur le flux de polymère et l'adhésion des filaments ont été clarifiées. Parallèlement, l'objectif était de mettre en place une simulation numérique des phénomènes impliqués dans ce processus. Le flux visqueux du polymère lors de son dépôt à l'état fondu a été modélisé et simulé en prenant en compte le transfert de chaleur et la cristallisation. Dans notre procédure, nous combinons des approches expérimentales, analytiques et numériques.

Sur la base de la revue de la littérature, les paramètres d'impression les plus influents ont été identifiés : la température du filament, la température de l'environnement, la vitesse de dépôt et l'orientation du raster. Les études existantes soulignent le manque de connaissances sur le lien entre les paramètres d'impression et les propriétés des polymères dans le procédé FFF. Dans la plupart des études sur le procédé FFF, les auteurs font varier les paramètres d'impression pour imprimer des spécimens, ces derniers étant caractérisés par des tests mécaniques. Cependant, les propriétés du matériau ne sont pas prises en compte. Parmi ces propriétés, le comportement viscoélastique, la tension superficielle, le taux de cristallisation (pour les polymères semi-cristallins) et les propriétés thermiques sont les propriétés déterminantes qui influent sur la qualité des pièces fabriquées. De plus, les phénomènes physiques tels

que la coalescence, la coulée du matériau, le transfert de chaleur et la cristallisation sont les éléments les plus importants pour optimiser le processus FFF.

Après avoir identifié les propriétés du polymère impliquées dans ce processus, le polymère PEEK a été caractérisé au chapitre 2. Le PLA est utilisé comme polymère comparatif pour comprendre le phénomène physique, avec un point de fusion inférieur. Pour les deux, leurs transitions thermiques, leur cinétique de cristallisation et leur sensibilité à la dégradation ont été clarifiées. Contrairement à la PEEK, la cinétique de cristallisation du PLA est lente. Dans le cas du PLA, la cristallisation pourrait être évitée dans le procédé FFF en appliquant une vitesse de refroidissement élevée, tandis que dans le cas du PEEK, le polymère cristallisait quelle que soit la vitesse de refroidissement étudiée. En pratique, la vitesse de refroidissement dépend de la température du polymère fondu sortant de la buse, de la température de la plate-forme (substrat) et de la température ambiante.

Les propriétés thermiques telles que la conductivité thermique, la diffusivité et le coefficient de dilatation ont été déterminées. Contrairement à la conductivité thermique, la diffusivité thermique diminue lorsque la température augmente. Les propriétés rhéologiques ont été déterminées pour des vitesses de cisaillement inférieures à 100 s^{-1} en mode oscillatoire. La comparaison du PEEK avec le PLA montre que la viscosité du PEEK est beaucoup plus élevée que celle du PLA. De plus, les deux polymères sont sensibles à la dégradation thermique. En conséquence, la plage de température de traitement est limitée pour empêcher leur dégradation. Le PLA et le PEEK subissent un mécanisme de dégradation différent, ce qui entraîne une diminution de la viscosité du PLA en raison du mécanisme de scission de la chaîne. Au contraire, le mécanisme de dégradation de la PEEK se produit par recombinaison moléculaire, conduisant à une augmentation de la viscosité. La tension superficielle du PEEK et du PLA à l'état solide a été déterminée par un appareil de mesure de l'angle de contact. En outre, la tension superficielle du PLA à l'état liquide à 200 °C a été déterminée par une étude expérimentale. Comme la mesure n'était pas possible pour le PEEK à l'état fondu, la tension superficielle du PEEK en fonction de la variation de température a été calculée à l'aide de l'équation de Parachor. Toutes ces propriétés sont utilisées ultérieurement dans la modélisation analytique et numérique. Dans la deuxième partie de ce chapitre, la coalescence de deux gouttelettes de glycérol et de deux filaments polymères adjacents a été étudiée, par approche expérimentale, équation analytique et simulation numérique.

La simulation numérique en 2D de la coalescence du fluide dans l'air a été réalisée à l'aide des équations CFD et TPF-LS. Nos résultats numériques sur la coalescence du glycérol montrent une grande concordance avec ceux expérimentaux. L'étude expérimentale du phénomène de coalescence appliquée au PEEK confirme que la viscosité influence fortement le collage des polymères. Cette liaison aurait un impact sur les propriétés mécaniques des pièces imprimées : si l'interdiffusion et la liaison n'étaient pas terminées, l'adhérence entre les couches serait faible, ce qui entraînerait une faible résistance à la rupture des pièces. La longueur de liaison entre deux filaments de PEEK adjacents a été enregistrée avec le temps et la température. Ces résultats ont été comparés à un modèle prédictif : les résultats démontrent un bon accord de la température de fusion. En effet, la coalescence commence lorsque le polymère est complètement à l'état fondu. Cela signifie que la phase cristalline empêche la mobilité des chaînes polymères, ce qui signifie que la coalescence des polymères adjacents n'est pas possible avant la température de fusion. Par conséquent, il existe un écart entre les résultats expérimentaux et le modèle prédictif avant la température de fusion.

Notre approche de la simulation numérique donne une très bonne compréhension de la simulation TPF-LS. Les investigations montrent que les maillages locaux influencent la convergence de la simulation.

γ , le paramètre de ré-initialisation et le ε_{LS} paramètre contrôlant l'interface dans la série LS sont les paramètres numériques majeurs qui influencent les résultats de la coalescence. Ces paramètres modulent la précision de la simulation numérique et la convergence des résultats obtenus. ε_{LS} doit être petit pour avoir une meilleure interface entre les phases. De la même manière, la sélection du paramètre de ré-initialisation est très délicate. Le paramètre de réinitialisation doit être proche de la vitesse maximale du système. Le pas de temps doit être minimisé afin de rapprocher la simulation numérique de l'étude expérimentale.

Au chapitre 3, nous nous sommes concentrés sur la simulation numérique du dépôt de polymère sur le substrat. La simulation est divisée en plusieurs étapes afin de modéliser le dépôt du matériau sur un substrat, le dépôt sur un substrat en mouvement, la détermination du transfert de chaleur et la variation de la viscosité dans le système. Enfin, le dépôt d'une couche de polymère sur une couche précédemment déposée a été effectué. Le comportement de l'extrudat après la sortie de la buse a été étudié, ainsi que le matériau s'écoulant de la buse, la stabilité à l'écoulement, le transfert de chaleur et la cristallisation non isotherme.

Afin de déterminer le transfert de chaleur lors du dépôt du matériau, nous avons intégré l'équation de transfert de chaleur sous la forme d'une PDE dans le logiciel COMSOL afin de conjuguer le TPF-LS au transfert de chaleur. Au cours de l'extrusion de forme libre, la fraction volumique, la distribution de température et la variation de la viscosité ont été déterminées. L'influence de la viscosité sur le flux de polymère et les effets sur le comportement de l'extrudat ont été déterminés. Notre modèle initial montre que l'interface des deux phases (air et polymère) est large (environ 2 mm). Dans cette bande, la viscosité du polymère varie en fonction de la viscosité de l'air en fonction de la fraction de phase (loi des additifs). Afin d'améliorer la précision de notre modèle numérique, la largeur de cette zone de transition a été réduite.

L'influence de la viscosité du polymère sur le comportement de l'extrudat a été étudiée par simulation numérique. Nos études montrent que, pour les viscosités élevées, la forme de l'extrudat ne change pas tellement, tandis que pour les viscosités faibles, la forme est totalement différente. La même variation est observée lorsque l'influence de la température est prise en compte.

Afin de valider notre modèle à la première étape, le processus FFF appliqué au PLA a été étudié via des expériences, des équations analytiques et une simulation numérique. Les effets des paramètres d'impression (diamètre de la buse, vitesse d'alimentation et hauteur de couche) et des propriétés physiques du polymère (transitions thermiques et comportement rhéologique) sur la vitesse d'entrée, la vitesse de cisaillement et la viscosité dans le liquéfacteur ont été déterminés. La vitesse maximale d'entrée du filament dans le liquéfacteur a été déterminée en fonction de paramètres d'impression, tels que le diamètre de la buse, le débit d'alimentation et les dimensions du segment déposé. Ensuite, le comportement rhéologique du PLA, tel que le champ de vitesse, le taux de cisaillement et la distribution de la viscosité dans la buse, a été étudié via un modèle analytique et une simulation numérique. Augmenter la vitesse d'entrée ou diminuer le diamètre de la buse augmente le taux de cisaillement et diminue la viscosité du PLA. Pendant ce temps, la réduction de la viscosité a amélioré l'adhésion entre les billes et les couches déposées et une viscosité trop basse a pour résultat une précision faible. De plus, à des vitesses de cisaillement supérieures à 4000 s^{-1} , les extrudats de PLA ont subi une déformation importante due à l'effet « peau de requin ». La déformation de l'extrudat influence la forme des billes déposées et réduit par conséquent le contrôle de la rugosité et de la fiabilité de la pièce fabriquée.

La cristallisation isotherme et non isotherme du PEEK a été déterminée par des expériences de DSC. De plus, le dépôt de matière au cours du processus FFF appliqué au PEEK a été modélisé par simulation

numérique. À partir de la simulation numérique, nous avons déterminé les propriétés d'écoulement du polymère fondu, le transfert de chaleur, ainsi que les variations de viscosité et de cristallinité au cours de l'étape de dépôt.

La cristallisation à mi-temps du PEEK a été déterminée expérimentalement entre 310 °C et 322 °C. Les résultats expérimentaux ont été interpolés par l'équation de Hoffman-Lauritzen afin de déterminer la cristallisation à mi-temps à différentes températures allant de la température de fusion à la transition vitreuse. La vitesse de cristallisation est maximale à 512 K (240 °C) pour le PEEK. En ajoutant un terme de convection à la cristallisation non isotherme de Nakamura, nous sommes en mesure de déterminer l'évolution du champ de cristallisation lors du refroidissement de polymères semi-cristallins en tenant compte de l'écoulement du fluide. Une simulation numérique TPF a été réalisée pour modéliser le dépôt de matériau et le flux de fluide, avec les équations de Navier-Stokes, de continuité et de niveau. Le transfert de chaleur a été déterminé en implémentant une équation différentielle partielle dans le modèle. En utilisant l'approche de simulation TPF, nous avons déterminé le flux de matériau, le transfert de chaleur et la cristallisation dans le processus FFF. Les résultats montrent le gradient de vitesse de cristallisation le long du filament au cours du dépôt. Le taux de cristallinité du PEEK atteint sa valeur maximale (environ 22%) au cours du dépôt. En outre, la cristallisation libère de la chaleur dans le système, ce qui augmente progressivement la température de la perle déposée jusqu'à 20 K. Alors que la température du substrat influence fortement la cinétique de cristallisation du centre des billes, la température ambiante n'influence que la cristallisation de la surface. Afin de favoriser l'interdiffusion de la chaîne moléculaire des couches et des billes déposées (et d'augmenter les propriétés mécaniques), la température de l'environnement et de la plate-forme de dépôt doit être comprise entre 285 °C et 300 °C. Notre proposition de température de fusion et de construction de la température de la plateforme est conforme à la proposition de la température de la plateforme et du liquéfacteur déterminée expérimentalement par d'autres auteurs. Bien que de nombreuses simulations numériques de processus de fabrication additive soient basées sur l'approche par activation de maillage en tant que dépôt pas à pas, nous avons proposé ici un nouveau modèle d'approche du dépôt de matériau réel dans un système à deux phases pour simuler le processus FFF. Notre approche pour déterminer la cristallisation non isotherme en tenant compte de l'écoulement du fluide pourrait être appliquée à d'autres procédés de fabrication de polymères. À ce jour, cette approche semble n'avoir jamais été utilisée.

Ensuite, nous avons déterminé les temps de relaxation pour le PEEK à partir des mesures rhéométriques de 350 à 400 °C. Les temps de relaxation du PEEK sont relativement élevés: à 350 °C, il faut 3,1 s et à 400 °C, il est réduit à 1,6 s. Quelle que soit la température dans cette plage, les temps de relaxation sont suffisamment bas pour assurer une interdiffusion et des enchevêtrements de chaînes polymères avant la cristallisation.

Enfin, le gonflement des matrices se produisant dans le processus FFF a été prédit. Le taux de gonflement de la matrice dépend fortement de la géométrie du liquéfacteur et des paramètres d'impression. Le taux de gonflement des matrices pour PEEK dans le processus FFF dépend des paramètres d'impression: il passe de 1 (pas de gonflement) à 2,5. Afin de réduire le gonflement de la matrice, il est conseillé d'augmenter la température, de diminuer la vitesse d'entrée ou d'adapter la géométrie de la buse (diamètre du capillaire, longueur du capillaire, angle de convergence et diamètre du réservoir).

Ces résultats sont essentiels pour optimiser la résistance mécanique des pièces imprimées et ne peuvent pas être facilement déterminés par des mesures expérimentales. C'est la première fois que la simulation numérique est appliquée de cette manière au processus FFF afin de prédire le taux cristallin de pièces

fabriquées par le processus FFF. Cependant, des études complémentaires sont nécessaires dans l'axe suivant :

Nous avons précédemment expliqué l'importance de mesurer la tension superficielle des polymères en fonction de la température et spécialement à l'état de fusion. La détermination de la tension superficielle à haute température et spécialement pour les polymères à haute viscosité et sensibles à la dégradation thermique nécessite davantage d'études et d'innovations. Une nouvelle méthode mériterait d'être développée.

Dans ce travail, nous avons étudié en détail le dépôt d'une seule perle sur la plate-forme d'impression. Le dépôt de plus de deux couches alourdit considérablement la simulation numérique et prend plus de temps. Par conséquent, pour modéliser le dépôt de plusieurs couches, de nombreux serveurs de calcul puissants sont nécessaires. Cependant, la modélisation de plusieurs couches de dépôt répondra à d'autres points obscurs pour comprendre les propriétés des pièces imprimées. De plus, en ajoutant le comportement mécanique au modèle de dépôt, nous pourrions modéliser la contrainte résiduelle et l'influence de différents paramètres d'impression sur la déformation sous refroidissement.

L'étape suivante consiste à imprimer des échantillons PEEK dans un environnement contrôlé à différentes températures et paramètres d'impression et à comparer les propriétés mécaniques des pièces imprimées en 3D dans différentes conditions. En outre, la détermination de la température et du champ thermique à l'aide de la thermographie infrarouge serait nécessaire pour valider le transfert de chaleur prévu par notre modèle numérique.

Nous avons étudié le mécanisme d'interdiffusion des chaînes macromoléculaires et la relaxation à une température supérieure à la température de fusion. Cependant, l'interdiffusion commence au-dessous de la température de fusion à une vitesse lente. Déterminer les temps de relaxation à une température plus basse pourrait donc aider à optimiser la vitesse d'impression. En outre, l'influence des conditions d'impression sur la résistance au soudage (liaison) de quelques filaments est un pas en avant vers l'amélioration de la résistance. Pour cela, un test mécanique spécifique serait développé pour quantifier l'adhérence entre filaments.

Enfin, lorsque l'utilisation du procédé FFF sera maîtrisée pour les thermoplastiques hautes performances, des composites à base de polymères pourraient également être utilisés. Les composites biosourcés, les composites à longues fibres de carbone et de carbone et les mélanges de métaux / polymères pourraient être utilisés comme matières premières pour atteindre de nouvelles propriétés. Pour tous ces matériaux, le procédé FFF nécessite un contrôle minutieux des propriétés du matériau pendant le dépôt afin d'assurer la meilleure qualité des pièces imprimées en 3D.

Contents

French Abstract	i
Chapitre 1 : Introduction	i
Chapitre 2 : Caractérisation de polymère et de l'étude de coalescence.....	iii
Chapitre 3 : Simulation numérique de dépôt de matière et cristallisation.....	vi
Conclusion.....	xii
Table of figures	xx
Table of Tables.....	xxiii
General introduction.....	1
<i>Chapter 1: Literature review</i>	4
Introduction	5
1.1 What is additive manufacturing?.....	5
1.2 FFF: Fused Filament Fabrication	7
1.2.1 Evolution of the machines	7
1.2.2 Characteristics of the current machines.....	8
1.2.3 Materials used in FFF.....	9
1.2.4 Adhesion of the part to the platform.....	9
1.2.5 Principle of RepRap	10
1.3 Parameters and physical phenomenon influencing the quality of the manufactured parts.....	12
1.3.1 Raster orientation and deposition strategy	12
1.3.2 Experimental studies and modeling of the coalescence phenomenon.....	13
1.3.3 Fluid flow and heat transfer during material deposition.....	17
1.3.4 Surface roughness and accuracy.....	18
1.4 Polymer properties influencing the quality of printed PEEK parts	19
1.4.1. Polymer definition and conformation.....	19
1.4.2. Amorphous and semi-crystalline state.....	21
1.4.3. Printing of PEEK by FFF process	22
1.4.4 Crystallization of PEEK and its effect on mechanical properties.....	23
1.4.5 Definition of the viscoelastic behavior of melted polymers.....	25
1.4.6 Definition and determination of the surface tension	27
1.5 Conclusion.....	28

<i>Chapter 2: Characterization of the polymers and coalescence study</i>	30
2.1 Characterization of PEEK and PLA.....	31
2.1.1 Introduction	31
2.1.2 Presentation of PEEK and PLA.....	31
2.1.3 Thermal transitions and preparation of the samples	32
2.1.4 Other characterizations of PEEK.....	39
2.2 Coalescence study	48
2.2.1 Analytical study of coalescence	48
2.2.2 Numerical simulation of the coalescence phenomenon	50
2.2.3 Experimental study of the kinetics of coalescence	54
2.2.4 Modifications on the numerical simulation model	61
2.3 Conclusion.....	65
 <i>Chapter 3: Numerical simulation of material deposition and crystallization</i>	 68
3.1 Introduction	69
3.2 From material deposition to crystallization in the FFF process	71
3.2.1 Free-form material extrusion.....	71
3.2.2 Heat transfer of free-form material extrusion.....	73
3.2.3 Deposition of the filaments	76
3.2.4 Determination of the heat transfer during deposition of two layers	78
3.2.5 Crystallization study.....	79
3.3 Influence of printing parameters on the stability of deposited beads in fused filament fabrication of poly (lactic) acid.....	80
3.3.1 Importance of determining the shear rate and viscosity in the FFF process	80
3.3.2 Experimental set up	81
3.3.3 Rheological investigation of the polymer flow in the liquefier via analytical study.....	81
3.3.4 Inlet velocity in the liquefier	83
3.3.5 Shear rate and viscosity of the polymer in the liquefier	84
3.3.6 Influence of shear rate on extrudate shapes.....	86
3.4 Determination of the die swelling for PEEK.....	89
3.4.1 Theoretical basis of the die swelling	89
3.4.2 Elongational viscosity	91
3.4.3 Determination of the pressure drop in the extruder's nozzle.....	93
3.4.4 Determination of the relaxation time for PEEK	94
3.4.5 Die swelling for PEEK	99
3.5 Crystallization kinetics of PEEK in the FFF process	103

3.5.1 Isothermal crystallization	104
3.5.2 Non-isothermal crystallization	107
3.5.3 Numerical simulation	107
3.5.4 Results of crystallization	109
3.5.5 Numerical study of polymer deposition in FFF process.....	114
3.5.6 Determination of the optimal environment temperature in order to promote the interdiffusion of the beads and layers.....	119
3.6 Conclusion.....	120
<i>General conclusion</i>	123
References	128
<i>Annexes</i>	139

Table of figures

Figure 1: Three different additive manufacturing groups according to Hernandez et al. [14]	6
Figure 2: Illustration of the layer by layer deposition during FFF	10
Figure 3: Picture of a basic RepRap printer [23].....	10
Figure 4: Used extruder in RepRap FFF machine.....	11
Figure 5: Coalescence of 2 droplets or 2 particles to form a single one [47].....	14
Figure 6: Levels of analysis for FFF prototypes [49].....	14
Figure 7: Neck growth evolution for ABS P400 at constant temperature [54]	15
Figure 8: Two possible conformation of a polymer chains composed of 10 monomers [91]	19
Figure 9 :Scheme of the end-to-end distance of a polymeric chain	20
Figure 10 : Scheme of the volume occupied by polymer coil	20
Figure 11: Structure of the thermoplastics (a) Amorphous state (b) Semi-crystalline state [92]	21
Figure 12: The spherulites in PEEK [105]	24
Figure 13: Chemical structure of PEEK.....	32
Figure 14: Chemical structure of PLA	32
Figure 15: DSC curves of PEEK 450G, sample undergoes 25°C.min ⁻¹ during the second heating cycle and 25°C.min ⁻¹ cooling rate.....	33
Figure 16: DSC curve of the PEEK 450G, sample undergoes 2 °C.min ⁻¹ during the second heating cycle and 2 °C.min ⁻¹ cooling rate	34
Figure 17: Cooling curve determined by DSC according to different cooling rates	35
Figure 18: DSC curve of PLA at 30 °C.min ⁻¹ cooling rate.....	36
Figure 19: DSC curve of PLA at 3 °C.min ⁻¹ cooling rate.....	36
Figure 20: Schematic illustration of the hot compression press used to manufacture the polymeric plates.....	38
Figure 21: Processing conditions used to manufacture the plates by hot compression molding.....	38
Figure 22: DSC curve of PLA sample manufactured by hot compression molding	39
Figure 23: Thermal expansion of PEEK 450G versus temperature during heating and cooling at different rates.....	40
Figure 24: Thermal diffusivity determined by experimental study and comparison with existing works [131]	41
Figure 25: Thermal conductivity determined by Hot disc apparatus and flash method.....	42
Figure 26: Schematic representation of the parallel plate configuration.....	44
Figure 27: Stress-strain curve in linear domain for PEEK at 383°C determined by strain sweep test..	45
Figure 28: Complex viscosity (η^*) of the PEEK determined by the parallel-plate configuration	46
Figure 29: Complex viscosity of PLA at different temperatures.....	47
Figure 30: Schematic representation of the coalescence of two particles a) Initial state before coalescence b) Filaments undergoing bonding by coalescence [47]	49
Figure 31: presentation of different phases in two-phase flow simulation by LS	53
Figure 32: High-speed camera and the syringe used for the deposition of glycerol	55
Figure 33: Schematic representation of the experimental set up for the coalescence study.....	55
Figure 34: Schematic representation of the experimental set up for the coalescence study of PEEK in heating furnace	55
Figure 35: (a) Meshed model used in the numerical simulation, (b) initial conditions and dimensions of the numerical model	56
Figure 36: Obtained results by (a) experimental study, (b) numerical simulation	58

Figure 37: (a) Meshed model used in the numerical simulation, (b) initial conditions and dimensions of the numerical model	58
Figure 38: Evolution of the coalescence by experimental and numerical simulation for PEEK	59
Figure 39: Evolution of the coalescence of the filaments according to temperature for PEEK	61
Figure 40: Different types of the meshes used for the simulation (a) Default meshes with pre-defined normal size (b) Default meshes with pre-defined extra fine size (c) Locally modified meshes on different regions (d) Modified meshes with finer mesh on the interface	62
Figure 41: Used model for the axisymmetric numerical simulation (a) Meshed model (b) Initial conditions of the model	62
Figure 42: Results of numerical simulation (a) Axisymmetric simulation (b) Axisymmetric simulation with symmetry on the contact region	63
Figure 43: Influence of ϵ_{ls} , the parameter controlling the interface on the clearance of the interface between two phases	64
Figure 44: Influence of the surface tension on the kinetics of coalescence	65
Figure 45: Representation of the followed steps in the Chapter 3.....	70
Figure 46: The schematic representation of the boundary condition for TPF numerical of free-form extrusion.....	72
Figure 47: Influence of the viscosity on the behavior of the extruding polymer (a) Constant viscosity = 1 Pa.s (b) Shear rate-dependent viscosity (c) Constant temperature = 7000 Pa.s, (d) Constant viscosity = 11000 Pa.s	72
Figure 48: Boundary conditions used for modeling the heat transfer during free-form extruder	73
Figure 49: The free-form extruder for relatively low viscosity fluid (a) volume fraction (b) temperature field.....	74
Figure 50: Determination of the temperature-dependent viscosity (a) Volume fraction, (b) Temperature field, (c) viscosity field.....	75
Figure 51: The values of volume fraction, temperature and viscosity during the free-form extruder...	76
Figure 52: Deposition of two consecutive layers	77
Figure 53: Deposition, at 5s, of the two layers for different viscosities.....	77
Figure 54: Detail view of two layer deposition	77
Figure 55: Heat transfer according to the different definitions of thermal diffusivity (a) additively law defined thermal diffusivity, (b) thermal diffusivity introduced as a combination of additively law and step function, (c) thermal diffusivity introduced as a step function.	78
Figure 56: Diagram of the printing parameter effects and physical properties of the polymer on the mechanical properties of printed parts	80
Figure 57: (a) Extruder system used for the experimental study. (b) Scheme of the 0.5-mm diameter nozzle	81
Figure 58: Cross section of a deposited bead	83
Figure 59: Influence of nozzle diameter on inlet velocity, shear rate and viscosity of the PLA at T = 195 °C.....	84
Figure 60: Distribution of velocity field, shear rate and viscosity in the liquefier determined via numerical simulation and analytical study	85
Figure 61: Distribution of the viscosity along the radius in the liquefier at various temperatures.....	86
Figure 62: Influence of inlet velocity and shear rate on the shape of the extrudate exiting from the nozzle with a diameter of 0.5 mm	88
Figure 63: Representation of the convergence angle in the extrusion.....	90
Figure 64: Viscosity of the PEEK at 656 K (383°C).....	92
Figure 65: Illustration of different pressure drop region in an extruder's nozzle	93
Figure 66: A macromolecular chain in a network of fixed obstacles.....	94

Figure 67: Representation of the interdiffusion of the macromolecular chains (a) Initial state of the two layers before interdiffusion (b) after diffusion of the macromolecular chains	95
Figure 68: Cole-Cole representation for the determination of η_0 from frequency sweeps	97
Figure 69: Relaxation time versus temperature for PEEK determined from loss (G'') and storage (G') moduli and, curve of Arrhenius law for relaxation times	99
Figure 70: Influence of the temperature on the die swelling for PEEK	100
Figure 71: Influence of the inlet velocity on the shear rate and die swelling for PEEK at 383 °C	101
Figure 72: Influence of the nozzle diameter on the shear rate and die swelling for PEEK at 383 °C.	102
Figure 73: Influence of the convergence angle on the die swelling for the short capillary die determined for PEEK at 383 °C for 0.5 mm diameter nozzle	102
Figure 74: Sequence of the works done in this study in order to determine the crystallization kinetics in the FFF process	104
Figure 75: Schematic presentation of the crystallization curve and its enthalpy at different temperatures	105
Figure 76: Crystallization of PEEK 450G with 30 K.min ⁻¹ cooling rates. Crystallization starts at T = 583 K.....	106
Figure 77: Illustration of the model and the geometry model used for the numerical simulation.....	108
Figure 78: Isothermal study of PEEK 450G at T=588K	110
Figure 79: Isothermal study of PEEK 450G at the different temperature from 595K to 581K	110
Figure 80: Half-time crystallization determination and fitted Hoffman-Lauritzen on the experimental points	111
Figure 81: Plotting $\ln - \ln(1 - \alpha t)$ versus $\ln t$ to determine Avrami kinetics and exponent	112
Figure 82: Determination of the Avrami kinetics along processing range near glass transition up to melting temperature.....	113
Figure 83: Nakamura Kinetics of crystallization for PEEK 450G in blue and PEEK 150G in red. PEEK 150G data are from [103]	114
Figure 84: Numerical simulation of first layer deposition on the moving substrate at the different moments	115
Figure 85: Temperature distribution for the Case 3 (T substrate =433K and Tenv. =433K)	116
Figure 86 : Temperature distribution at different moments for the case 3 for the center line of the extrudate	116
Figure 87: Distribution of the crystallinity for Case 3 (T substrate =433 K and Tenv. =433 K)	117
Figure 88: Non-isothermal crystallization of PEEK t=12s for different case studies	117
Figure 89: Influence of the Substrate and environment temperature on the crystallinity percentage of the deposited bead	118
Figure 90: Temperature distribution and crystallinity ratio in the center of the deposited extrudate for the three cases.....	119
Figure 91: Crystallization of PEEK at 563K and 573K	119

Table of Tables

Table 1: List of professional 3D printers trademark for printing PEEK and high-performance thermoplastics in 2019 [19].....	8
Table 2: Mechanical properties of the printed parts with PEEK 150P from Victrex [101]:	23
Table 3: Fundamental properties, techniques and specimen shape for the tests	31
Table 4: Value of crystallization for different cooling rates	35
Table 5: Coefficient of thermal expansion	40
Table 6: Obtained values for the surface tension of PLA and PEEK by using the Parachor equation .	44
Table 7: Properties of air and glycerol used in the numerical model	56
Table 8: Boundary conditions used in the numerical model	56
Table 9: Properties of the fluids used for numerical simulation.....	58
Table 10: Values of terms of Carreau–Yasuda model for the viscosity curve fitting	83
Table 11: Values of the printing parameters	83
Table 12: Terms of Carreau model for PEEK at 656 K	93
Table 13: The value of the constants in the Hoffman-Lauritzen equation	106
Table 14: Thermal properties of air and PEEK for determining the thermal diffusivity (from [123] [115]).....	108
Table 15: Boundary conditions used for TPF simulation and PDE heat transfer simulation.....	109
Table 16: Influence of different isothermal study on the enthalpy and half-time crystallization of PEEK 450G	111
Table 17: Values of the parameters of Hoffman-Lauritzen equation determined for PEEK	111
Table 18: The values of Avrami isothermal kinetics and exponent for different isothermal temperature	112
Table 19: Case studies for the numerical simulation of temperature distribution and Crystallization rate	115

General introduction

Additive Manufacturing (AM) applied to polymers, commonly known as 3D printing, includes mainly filament deposition, powder sintering and stereolithography technologies. These technologies rely on the accumulation of material by stacking successive layers until the generation of a 3D part. These manufacturing machines (printers) are computer-controlled, with a file from a computer-aided design (CAD) software. Additive manufacturing allows both the creation of unique pieces at a lower cost and access to complex shapes.

Launched in the 1980s, the craze for 3D printing is palpable for both the general public and industry, as shown by numerous articles and studies published by the media in the five last years. In France, the Midi-Pyrénées region was a pioneer, with the first FabLab open to the public in Toulouse in 2009. FabLabs are associative digital fabrication workshops, where everyone can design and build custom objects. The interest in AM was perceived very early by companies for manufacturing of prototypes or small series. The company VOLUM-e was in 1993, the first French company which invested in the acquisition of production capacity in additive manufacturing for rapid prototyping [1]. Not too long ago, the printing speed and limited output of 3D printers made them suitable only for rapid prototyping. Since, many companies gamble on additive manufacturing to be at the heart of full-scale production capabilities from aerospace to automotive to healthcare [2] [3].

Though, the "industrial revolution" as presented by some media is still far away. Indeed, the improvement of processes, rates and suitable materials would open prospects for innovation in the industry. Among the technologies applied to polymeric materials, FFF (Fused Filament Fabrication), also named FDM (Filament Deposition Modeling) seems the most promising, because of its simplicity of use and storage of the raw material. Similar to other types of AM processes, FFF enables free-form fabrication and optimized structures by using polymeric filaments or pellets as raw material. Another point to consider is the absence of powders or liquid resins that can release VOC (volatile organic compound) and require special safety equipment.

The type of materials suitable today for AM constitutes another obstacle to overcome: they are mainly mass-produced polymers, i.e. with low mechanical properties and durability, such as polylactic acid (PLA), acrylonitrile butadiene styrene (ABS) or polyesters. The industry requires high-performance polymers, that is to say, thermal resistance greater than 200 °C in continuous use, some GPa moduli and low sensitivity to thermo-oxidative aging. The behavior of these polymers, which have been on the market since the 1990s, is still little known. The study of their durability has shown that PAEK (polyaryletherketone) polymers family are the most durable, they keep longer their mechanical properties during exposure to a temperature close to their glass transition [4]. Generally, processing these PAEK materials while controlling their final properties are difficult, as proved by many research works in the last five years [5] [6] [7]. Identically for AM, these processes are still not well mastered for high-performance polymers. More efforts are needed to enlarge the knowledge about the physical phenomenon involved during these processes.

Indeed, 3D parts suffer from low mechanical properties and low surface quality, compared to injection molded parts. The mechanical properties and the surface roughness of 3D parts manufactured by FFF are controlled by the adhesion of filaments and the porosity rate. The both mainly stem from the flowing ability and surface tension of the polymer. Moreover, the adhesion of filaments depends on the interdiffusion of polymeric chains. The interdiffusion of macromolecular chains at the interfaces has

been studied for amorphous thermoplastics: from the reptation theory [8], models make it possible to predict the kinetics of diffusion of entangled chains. The interdiffusion is less mastered for semi-crystalline polymers, for which the crystalline phase slows down the motion of the macromolecules of the amorphous phase.

To our knowledge, no study of the FFF process applied to high-performance semi-crystalline polymer was available in 2015. Since, some similar research works have started worldwide.

The aim of this Ph.D. thesis consists in clarifying the relations between the printing parameters such as filament temperature, temperature of the previous layer, deposition rate and the properties of the material (elongational viscosity, viscoelasticity, coefficient of thermal expansion, thermal capacity, thermal conductivity, kinetics of crystallization ...) on the polymer flow and the adhesion of filaments. Our study focuses mainly on PEEK (polyetheretherketone), but the results could be transferred to any other polymer. At the same time, the objective is to set up a numerical simulation of the phenomena involved in this process. The viscous flow of the polymer during its deposition in the molten state is modeled and simulated while considering heat transfer and crystallization. The material properties are temperature-dependent; that is why our simulation considers the evolution of the physical properties with temperature until the solidification of the material during cooling.

This project, named 3D-TPHP, standing for : « Impression 3D des ThermoPlastiques Hautes Performances : Etude expérimentale et modélisation numérique du procédé par dépôt de filament » received a funding from APR Occitanie Region/Université Fédérale de Toulouse. The work was carried out in collaboration with two research laboratories: Laboratoire Génie de Production (EA1905) at Ecole Nationale d'Ingénieurs de Tarbes (ENIT) in the team Interfaces and Functional Materials, and Institut Clément Ader (UMR-CNRS 5312) at IUT Tarbes, in the research group Materials and Composite Structures.

This manuscript is divided into three chapters. The first chapter is a literature review on the FFF process: After defining the FFF process; the process parameters affecting the properties of 3D printed parts are presented as well as the properties of the polymeric materials playing a crucial role in the properties of the final parts.

The second chapter is concentrated on two topics: the first one is the characterization of the PEEK properties, the second one is the study of the coalescence of filaments. We have focused on the determination of the material properties which influence the properties of the parts manufactured by the FFF process. The studied properties are the thermal transitions and the crystallization kinetics, the thermal properties including thermal diffusivity, thermal conductivity and coefficient of thermal expansion, the surface tension and dynamic thermomechanical properties. These properties are the basic ones to study the FFF process properly. They are required to study the coalescence in the following part, in which, the coalescence of two adjacent filaments have been carried out by experimental study, analytical study and numerical simulation.

Chapter 3 is mainly based on the numerical simulation of the filament flowing and deposition, and the polymer crystallization. In the first part, we have studied the rheological properties such as velocity field, shear rate and viscosity of the melted polymer flowing in the liquefier. Also, the flowing instability after exiting from the nozzle is explained, from experiments and numerical simulation with the aim to define the onset (limit of shear stress, as a result of shear rate and temperature) from which the extrudate undergoes instabilities and surface defects. Then, in the following part of chapter three, we have modeled the material deposition on the substrate during the FFF process, considering heat transfer and non-isothermal crystallization. In this part, we aim to determine the optimal environment temperature and

substrate temperature to enhance the coalescence and the interdiffusion of deposited beads by keeping them longer in the amorphous state after deposition. Before including the crystallization kinetics in our model, we have determined the isothermal crystallization of PEEK at temperatures ranging from glass transition up to melting temperature. The isothermal crystallization data have been transferred to non-isothermal crystallization kinetics by using Nakamura non-isothermal crystallization equation. Then, Nakamura non-isothermal crystallization has been conjugated with heat transfer and polymer flow to model the crystallization kinetics after the material deposition.

Lastly, from the results presented, several points may be highlighted in conclusion. Some perspectives are drawn for the direction in which this work should be extended.

Chapter 1: Literature review

Introduction

Additive manufacturing (AM) refers to a wide variety of manufacturing processes for rapid prototyping and production of final and semi-final products. Despite a growing interest from industries and a large audience in the last five years, these manufacturing processes are still not well mastered, especially for not mass-produced polymers. Indeed, when the polymeric materials display specific properties, controlling their processing is trickier. More efforts are needed to enlarge the knowledge about the physical phenomenon involved during these processes. In this chapter, the literature review is presented in three parts, as the background to introduce the work presented in this thesis. The first paragraph defines the FFF process; the second one focuses on the process parameters affecting the properties of the printed parts. In the last one, the properties of the polymeric materials playing a crucial role in the properties of the final parts are highlighted.

1.1 What is additive manufacturing?

In opposite to conventional or subtractive processes, in additive manufacturing, the material is gradually added layer by layer to form the parts. Indeed, in these processes, a material is assembled or solidified under computer control to create a three-dimensional object. AM enables the fabrication of complex parts which were impossible or not cost-effective to manufacture until now with the traditional and subtractive processes. Starting from about 2000 [9], technical development and research studies have enabled the growth of additive manufacturing as a feasible alternative to subtractive and formative techniques [10]. Indeed, additive manufacturing processes reduce the lead time and processing costs for parts in small series and prototypes. Moreover, the parts are worthy of being re-design doing a topological optimization. The topological optimization is a mathematical method that optimizes the material layout within a given design space, for a given set of loads, boundary conditions and constraints with the goal of maximizing the performance of the system, such as the mechanical resistance and weight reduction of the structures.

Early additive manufacturing processes were developed in the 1980s. In 1981, Hideo Kodama invented the additive manufacturing process of 3D models. The invented method is based on the hardening of a liquid resin under ultra-violet exposure. In 1984, Chuck Hull of 3D System Corporation[®] developed a prototype system based on a process known as stereolithography, in which the layers are added by curing photopolymers with ultraviolet light lasers. Chuck Hull defined the process as a “system for generating three-dimensional objects by creating a cross-sectional pattern of the object to be formed.” Kodama has already introduced this processing concept, however, the contribution of Chuck Hull in additive manufacturing is mainly because of creating the STL (STereoLithography) format which is widely used by 3D printing software as well as the digital slicing and infill strategies common to many processes today [11].

The first commercially available machine in the world was the “SLA-1” in 1987, the precursor of the once popular SLA 250 machine, with SLA standing for Stereo-Lithography Apparatus. The Viper SLA machine from 3D Systems replaced the SLA 250 many years ago [9].

In 1988, at the University of Texas, Carl Deckard brought a patent for the SLS technology, another 3D printing technique in which powder grains are melted together locally by a laser.

In 1991, three other technologies were commercialized, different than stereolithography, including Fused Deposition Modeling (FDM) from Stratasys [12], solid ground curing (SGC) from Cubital, and

laminated object manufacturing (LOM) from Helisys. FDM extrudes thermoplastic materials in filament form to produce parts layer by layer. SGC used a UV-sensitive liquid polymer, solidifying full layers in one pass by flooding ultraviolet light through masks created with electrostatic toner on a glass plate. LOM bonded and cut sheet material using a digitally guided laser.

Selective laser sintering (SLS) from DTM (part of 3D Systems) and the Soliform stereolithography system from Teijin Seiki became available in 1992. Using heat from a laser, in SLS, the material in powder is melted to stick the grains together. The Soliform technology was initially developed by DuPont under the name Somos and was subsequently licensed to Teijin Seiki for exclusive distribution rights in parts of East Asia. Also in 1992, Allied Signal introduced vinyl ether Exactomer resin products for SL [9].

Additive manufacturing processes are sub-divided into several processing technologies according to different criteria: Power source (electron beam, laser, heating resistance, etc.), materials (polymers, metals, ceramics or their composites) and raw materials shape (liquid resins, powders, wires) [13].

Among various classifications, these processes are divided into three different sub-processes, according to Hernandez et al. [14], as illustrated in Figure 1:

- Liquid based processes
- Solid based processes
- Powder based processes

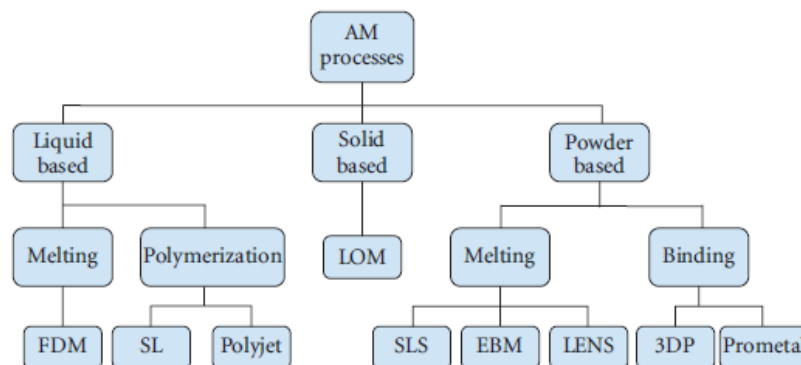


Figure 1: Three different additive manufacturing groups according to Hernandez et al. [14]

Besides, another example of classification is proposed by Jasiuk et al. [15]. For him, all the additive manufacturing processes using polymers as raw materials are a sub-division of one of the following categories:

- Binder jetting
- Directed energy deposition
- Material extrusion (fused deposition modeling of fused filament fabrication, 3D bioprinting)
- Material jetting (inkjet printing)
- Powder bed fusion (selective laser sintering, selective laser melting, electron beam melting)
- Sheet lamination (laminated object manufacturing, ultrasonic additive manufacturing)
- Vat photopolymerization (stereolithography, digital light processing, two-photon polymerization)

Advantages and drawbacks of these polymeric based processes are summarized in Annex I for each of the above mentioned [15].

The work presented in this Ph.D. thesis focuses on the “Fused Filament Fabrication” (FFF) also called “Fused Deposition Modeling” (FDM). FDM was developed by S. Scott Crump, co-founder of Stratasys, in 1988. With the 2009 expiration of the patent on this technology, people could use this type of printing without paying Stratasys for the rights to do so, opening up commercial open-source (RepRap) 3D printer applications. This has led to a two-orders-of-magnitude price drop since this technology's creation. Stratasys still owns the trademark on the term "Fused deposition modeling" [12].

In the whole manuscript, the term FFF is preferably used to name the additive manufacturing by layer by layer deposition of a polymeric filament. FFF is the most used process to form polymeric parts from thermoplastic polymers in filaments. The principle and applications are described below.

1.2 FFF: Fused Filament Fabrication

FFF is based on the melting of a polymeric wire or filament in an extruder; the latter is then deposited layer by layer to manufacture the final parts [16] [17].

1.2.1 Evolution of the machines

In 1996, Stratasys introduced the Genisys machine, which used an extrusion process similar to FDM but based on a technology developed at IBM's Watson Research Center. After eight years of selling stereolithography systems, 3D Systems sold its first 3D printer (Actua 2100) in 1996, using a technology that deposits wax material layer by layer using an inkjet printing mechanism. In July 2000, Stratasys introduced Prodigy, a machine that produces parts in ABS (acrylonitrile butadiene styrene) plastic using the company's FDM technology. In September 2001, Stratasys began the commercial shipment of its FDM Titan, a machine capable of producing parts in polycarbonate (PC), ABS, polyphenylsulfone, and PC+ABS blend. In early 2002, Stratasys introduced its Dimension product for \$29,900. The Dimension machine, which deposits ABS plastic, is based on the former Prodigy product. In March 2004, Stratasys introduced the “Triplets,” which consisted of three variations of the FDM Vantage machine. Prices ranged from \$99,000 to \$195,000. These machines are capable of processing both ABS and PC materials. In March 2005, Stratasys dropped the price of the Dimension SST from \$34,900 to \$29,900. The machine offers a soluble support removal system that automates the process. Stratasys unveiled a biocompatible FDM material, ABS-M30i, in March 2008.

Then, Stratasys announced that it would offer ULTEM 9085 (polyetherimide from Sabic Innovative Plastics) for its FDM 900mc and 400mc machines. This material is widely used in aircraft interiors for its flame retardancy and low smoke emissions. Also in December 2008, Stratasys introduced a vapor-honing product called Fortus Finishing Stations for finishing FDM parts made in ABS.

When a key FDM patent expired, inexpensive equipment in the form of kits and fully assembled machines based on the RepRap open-source project became available. Since their introduction, these low-cost “personal” systems have experienced substantial growth. Also, Bits from Bytes of England released the RapMan 3D printer kit (\$1100) based on the RepRap open-source system launched at Bath University of England.

In April 2009, MakerBot Industries introduced its Cupcake CNC product based on the RepRap open-source system in April 2009. Stratasys announced the compatibility of its large-frame Fortus 900mc machine with ULTEM 9085, PC-ABS, PC-ISO, and ABS-M30i in August.

In 2011, BotMill (Boca Raton, Florida) released the Axis 2.1 kit for \$1,065 and a preassembled, extrusion-based machine Glider 3.0 for \$1,395. The both are single extruder head machines based on

the RepRap open-source work. Buildatron Systems (New York, New York) announced the availability of its RepRap-based Buildatron 1 3D printer in September 2011. The single material and machine is sold as a kit for \$1,200 and as an assembled system for \$2,000. In May 2012, Stratasys acquired Solidscape, a company that offers high-resolution 3D printers for creating wax patterns for investment casting, particularly for the jewelry and dental markets. Solidoodle (Brooklyn, New York) introduced its RepRap-based Solidoodle 3D printer for \$699 [9].

When this Ph.D. thesis started in 2015, none of the machines was suitable to print high-performance thermoplastics such as PEEK (polyetheretherketone). Indeed, PEEK is a high-performance semi-crystalline thermoplastic with a melting temperature above 340 °C and a higher viscosity compared to other conventional polymers which are typically used in FDM (FFF) process. A high viscosity combined with a high melting temperature increases the difficulties to process this kind of material. Because of these properties, the use of PEEK as raw material for 3D printing is limited. However, in June 2015, INDMATEC launched the PEEK 3D Printer as the first FDM 3D Printer for high-temperature polymers. This new 3D printer, which features a build volume of 155 x 155 x 155 mm, is equipped with a hotend that reaches up to 420 °C. It can 3D print objects out of PEEK [18].

The evolution of the FFF (FDM) printers from 1990 until now shows that their ability to print a broader range of polymers with higher precision increases while their price is reduced.

1.2.2 Characteristics of the current machines

The FFF machines differ from various criteria. Their differences are mainly:

- The printing volume (the maximum size of the printable part),
- The accuracy,
- The range of materials (from the simplest mass-produced and low-cost materials like ABS and PLA (polylactic acid) to high-performance polymers such as PEI and PEEK)
- The possibility of printing complex parts (3-axis and more axis)
- The possibility of controlling the printing environment (temperature, vacuum and nitrogen chamber).

In 2019, more companies propose 3D printers with the characteristics mentioned above. In Table 1, some of the companies selling 3D printers for high-performance thermoplastics are presented [19]. As we could conclude, these printers vary from different characteristics such as build volume, maximum extruder temperature, maximum printing bed temperature, maximum environment temperature, and price. Furthermore, the geographic distribution of the manufacturers all around the world shows the strategic importance for the industry, specially for high-performance thermoplastic. The number of manufacturers of 3D printers has significantly increased in 2019 compared to 2015, when the first printer for PEEK was introduced. This corroborates the emergence of this technology.

Table 1: List of professional 3D printers trademark for printing PEEK and high-performance thermoplastics in 2019 [19]

PEEK 3D printer	Price (€)	Build volume (in mm)	Max. extruder tem. (°C)	Max. print bed tem. (°C)	Max. build chamber tem. (°C)	Country
3D PrinterWorks HT-5800	15.950	457 x 457 x 457	420	160	-	US
3DGence Industry F340	20K-25K	260 x 300 x 340	500	160	85	Poland

AON 3D AON-M2	47,000	454 x 454 x 640	470	170	120	Canada
Apium P220	30K-40K	205 x 155 x 150	540	160	180	Germany
Hyrel 3D Hydra 16A	13,000	600 x 400 x 500	450	200	55	US
IEMAI Magic-HT-PRO	22,000	310 x 310 x 480	450	170	120	China
INTAMSYS FUNMAT PRO 410	23,000	305 x 305 x 406	450	160	90	China
Machina Corp X30 HT	8,000	300 x 300 x 280	500	150	90	Canada
miniFactory Ultra	49,000	330 x 180 x 180	480	250	250	Finland
Roboze One+400 Xtreme	70,000	300 x 200 x 200	500	180	-	Italy
SpiderBot 4.0 HT	7,495	200 x 200 x 180	470	240	350	France
Tractus3D T850P	11,900	300 x 300 x 380	450	175	65	Netherlands
VeraShape VSHAPER MED	11K-55K	450 x 450 x 450	450	150	70	Poland

1.2.3 Materials used in FFF

The FFF process is applied to most of the materials including metals and thermoplastic polymers. In a glance, the thermoplastics used in FFF are divided into two categories:

The initial version of the FDM printer was intended to print wax. By improvement in FFF technologies, new materials such as ABS and PC were used as raw materials. Furthermore, ABS loses its popularity because of the emission of toxic gas (styrene derivatives) during printing. Then, by the introduction of the RepRap project in 2008, PLA has replaced ABS and PC as a low-cost and easy to use polymer. Also, PLA has a lower environmental impact because it is a biosourced, biodegradable and compostable material. The blends of different polymers such as PC+ABS are also used in FFF.

Later, thermoplastics for printing higher performances parts appeared. These polymers are relatively expensive materials with performances suitable for high added value products. For this category, we could mention polyetherimide (PEI) known as the brand ULTEM from Sabic Innovative Plastics, PAEK (polyaryletherketone) polymers such as PEEK and PEKK.

1.2.4 Adhesion of the part to the platform

FFF is based on the melting of a polymeric wire or filament in an extruder; the latter is then deposited layer by layer to manufacture the final parts. The layer thickness is generally less than 0.4 mm. The principle of the FFF process is shown in Figure 2. As it is represented, the first layer is deposited on a building platform, in most cases made of toughened glass.

The deposition of the first layer on the substrate is the most critical step to print the parts without any defaults. Because of the temperature of the platform, the cooling rate of the first layer is faster compared to the following layers deposited on the previous layers. When the cooling rate of the first bead is too fast, it causes deformation of the printed part. If the part is not correctly attached to the deposition platform, the part will be taken off. For this reason, a toughened glass surface is principally used as the building platform to maintain the adhesion of the part to the substrate during printing. Also, the glass facilitates the removing of the part at the end of the manufacturing. Furthermore, empirical tests made

by users of FFF and RepRap suggest that using polyvinylpyrrolidone (a component of hairspray) could improve the adhesion of the part to the platform.

1.2.5 Principle of RepRap

As mentioned previously, when this thesis started in 2015, no commercial machine in the world was suitable to print PEEK. However, to begin the study of the physical phenomenon occurring during printing of semi-crystalline polymers, we choose to work with a RepRap machine available at ENIT with PLA (Polylactic acid).

The RepRap project started in England in 2005 at the University of Bath as an initiative to develop a low-cost 3D printer that could print most of its own components. The project is now made up of hundreds of collaborators worldwide. RepRap is the abbreviation of “replicating rapid prototype” [20]. Among available machines on the market, RepRap is an open source project to use the FFF process at low-cost fabrication to “home manufacturing,” Fablabs as well as towards education [21] [22]. Because of the simplicity of use and cost-effectiveness of the process, FFF is one of the most popular additive manufacturing processes.

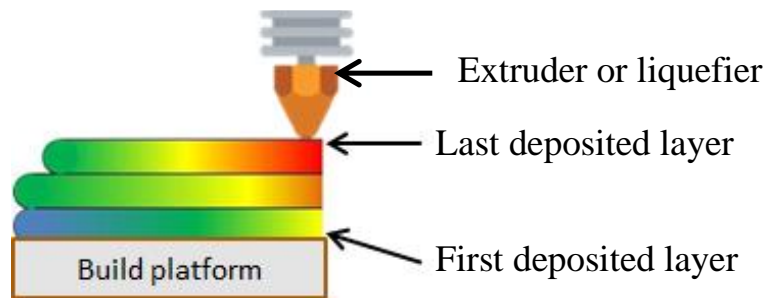


Figure 2: Illustration of the layer by layer deposition during FFF

Furthermore, to remain cheap and easy to achieve, these machines are simply made of a frame as shown in Figure 3, a liquefier and open-source developed software.



Figure 3: Picture of a basic RepRap printer [23]

The liquefier is composed of several parts such as a heating block, a nozzle, and a cooling sink. The Figure 4 shows a scheme of the liquefier assembly typically used in RepRap printers.

The liquefier is the most important part of the RepRap printers. The polymeric filament is melted through the liquefier before deposition. The liquefier is composed of three parts:

- **Nozzle:** The polymeric filament passes through the nozzle and changes from the solid state to the melted state. The melted polymer exits through the nozzle to be deposited. The diameter of the nozzle is from 0.25 mm to 0.6 mm. The diameter of the nozzle influences the accuracy of the manufactured part.
- **Heating block:** This part of the liquefier is mainly a heating resistance. The heating block provides the energy required to melt the polymer. This block is equipped with a thermocouple in order to control the temperature.
- **Cooling sink:** The cooling sink is made of aluminium to cool the upper part of the liquefier. In the liquefier, the polymeric filament is pushed into the liquefier by the gears or the drivers. If the filament is not rigid enough, in case the temperature is above the glass transition the polymer, the drive could not push the filament into the liquefier.

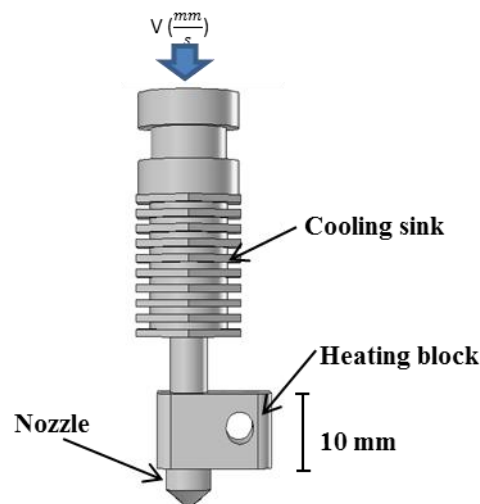


Figure 4: Used extruder in RepRap FFF machine

Although these open-source printers provide robustness and low-cost manufacturing, however, the parts manufactured with these printers still suffer from different problems. Stress concentration resulting in distortion [15], high porosity rate and lack of adhesion between the layers, the both decreases the mechanical properties of the parts [24], surface roughness and lack of dimensions' accuracy are the main drawbacks of the parts manufactured by FFF process.

The origin of these problems mainly comes from the lack of mastering the properties of materials and the influence of the printing parameters on the material properties. Indeed, the plentiful users all around the world bring “rule of thumb” experimental practice. As an example, selecting high temperature and high printing speed leads to harsh deformation and discontinuity of the printed layers while low temperature leads to uncompleted melting of the filament and lack of adhesion between deposited filaments. Consequently, understanding the flow properties of the used polymers for printing and also the influence of the printing parameters on the flow properties is crucial to improve the quality of the printed parts.

1.3 Parameters and physical phenomena influencing the quality of the manufactured parts

1.3.1 Raster orientation and deposition strategy

In parallel to the experience gained by household users, the first scientific studies which aim to improve the quality of the parts manufactured by the FFF process were done by Yardimici et al. in 1999 [25]. They have studied the FFF process from different points of view: their studies cover the structure design of the machines and the deposition raster orientation. Also, they provided an extensive study of thermal and flow analysis of the process. According to the equations of viscosity for non-Newtonian fluids, they proposed a relationship to determine the pressure drop in the liquefier [26]. The same authors have suggested the thermal equations to determine the temperature distribution in the liquefier and the extruder [25] [26].

Most of the studies on FFF focus on the deposition orientation and the influence of different deposition strategy and raster orientation on the mechanical properties of the parts printed by FFF such as tensile strength [27] [28] [29] [30], compression [31], and flexural properties [27] [32] [33]. The numbers of studies on the deposition strategy show the importance of the printing parameters for controlling the properties of the parts manufactured by FFF. However, many studies combine several parameters at the same time, so that the results do not lead to an incontestable conclusion about the effect of parameters.

Fatimatuzahraa et al. [27] studied the influence of the raster orientation $90^\circ/0^\circ$ and $45^\circ/-45^\circ$ on the flexural strength, tensile strength and impact strength. According to them, the raster orientation does not highly influence the mechanical properties, however, for the $45^\circ/-45^\circ$ orientation, the flexural and impact strength is slightly higher than for $90^\circ/0^\circ$. De Ciurana et al. [28] have studied the influence of the raster orientation, the thickness of the deposited beads and the distance between each deposited bead on the Young's modulus of the printed parts. Their results show that the specimens with $45^\circ/-45^\circ$ have a higher Young's modulus than other raster strategies. On the other hand, they have shown that a higher bead thickness leads to higher Young's modulus. Most of the studies on the printing parameters propose the raster orientation of $45^\circ/-45^\circ$ to get the best mechanical properties.

Furthermore, from our practical experience and literature, the layer thickness must not exceed 0.4 mm and not below 0.2 mm. A higher nozzle diameter (higher than 0.4 mm) highly decreases the accuracy and surface roughness of the printed parts. On the other hand, a small nozzle diameter (less than 0.2 mm) although increases the accuracy and surface roughness of the printed parts, however it reduces the mechanical properties of the printed part.

Gomez et al.[34] studied the influence of the printing strategy on the fatigue properties of the printed parts. The influence of four factors: layer height, fill density, nozzle diameter and velocity reveal that the fill density is the most influential parameter on the fatigue life, followed by the layer height. A higher fill density improves the mechanical properties of the printed parts by reducing their porosity.

However, many contradictions are revealed in the above-mentioned studies to select the optimum raster strategy. One of our hypothesis to explain these contradictions could be the lack of knowledge of the properties of polymers. Indeed, some authors attribute the variability of results in terms of diversity of colors [35] or supply companies. Bell et al.[36] studied the influence of the specimen size on the mechanical properties of printed parts with acrylic polymer. Their study shows that the mechanical properties of the printed parts are size dependent. Another hypothesis is that the authors use different types of printers with different design structures such as diameter of the nozzle, heat transfer and so on. Also, the stability of the printer structure from vibrational point of view could be different for each study

and so it could influence the quality of the parts. Furthermore, the geometry of the nozzle is different in all these studies, that could be another source of deviation of the results when comparing different studies.

Concerning printing of high-performance polymers, only a few studies worth to be cited. In the first one, the influence of the printing strategy and orientation and the processing temperature of PEEK on mechanical properties have been carried out by Rahman et al. [37]. They have determined the influence of raster orientation on the tensile strength, flexural strength, and impact strength. They have studied three different raster orientations (0° , 90° , and $0^\circ/90^\circ$). Among them, 0° shows the best impact resistance, tensile and compression strength and flexural strength. Arif et al. also studied the influence of raster orientation on mechanical properties [38]. Their results on a biocompatible grade of PEEK agree with those obtained by Letcher: In both studies, the raster orientation must be selected as 0° to have the best mechanical properties. Then, Xiaoyong [39] studied the influence of the printing conditions such as the printing speed, temperature, layer thickness and filling ratio and environment's temperature on the tensile strength of PEEK parts. Their studies indicate that the optimal combination of tensile strength is the printing speed of 60 mm.s^{-1} , the layer thickness of 0.25 mm, the printing temperature of 370°C and the filling rate of 60 %. However, the influence of each parameter has not been studied separately.

Worth to be mentioned, the parts manufactured by FFF could be used directly as a final product with or without post-processing treatments. Moreover, many studies have been conducted to measure and decrease the surface roughness of the parts manufactured by FFF [40]. Indeed, most of the parts need a surface treatment to minimize their roughness. Ahn et al. [40] have developed a theoretical model to express the surface roughness distribution according to changes in the surface angle of the printed parts. They concluded that the most important parameter influencing the surface quality of the printed parts is the cross-section of the deposited beads. The cross-section of the beads mainly depends on the diameter of the nozzle and the height of the deposited beads. The comparison of their model with experiments shows a good agreement. The influence of the process variables such as layer thickness, road width and deposition speed on the surface quality of parts manufactured by FFF [41] [42] have been investigated. The studies on the process variables reveal that the layer thickness is the most important parameter influencing the surface quality. The road width and speed look to have less impact on the quality of the surface of the printed parts.

1.3.2 Experimental studies and modeling of the coalescence phenomenon

When the filaments are deposited one next to the other, they bond together to form the layers: this physical phenomenon is called coalescence. Controlling the coalescence is crucial in many processes [43] such as foaming [44], sintering and rotomolding [45]. The coalescence is usually described as the mechanism when two fluid droplets or two particles meet and bond together to form a single droplet or particle as represented in Figure 5. Modeling the coalescence is a step towards the optimization of processes to control the void growth in the plastic parts [46]. Indeed, this phenomenon has been extensively studied for thermoplastic powders in case of rotomolding process.

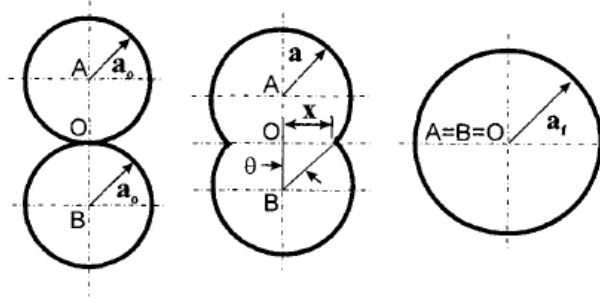


Figure 5: Coalescence of 2 droplets or 2 particles to form a single one [47]

For FFF, the improvement of the coalescence of filaments is a step forwards to print parts with optimized resistance [48]. The filaments coalesce and bond together in order to form the layers and the parts. The mechanical properties of the printed parts highly depend on the coalescence and bonding. Nevertheless, because of poor coalescence between the layers and deposited beads, the mechanical properties of the parts manufactured by FFF do not meet the requirements for functional parts. Indeed, the low mechanical strength comes mostly from the lack of coalescence between the filaments. The lack of coalescence generates weak filaments bonding and high porosity rate.

The coalescence phenomenon has been specifically applied to the FFF process by Bellehumeur et al. [49] as shown in Figure 6. The coalescence is mainly governed by the viscosity and the surface tension of polymers. Understanding the influence of the temperature on the rheological properties of the polymer is necessary to control and improve the coalescence of the deposited beads. Abbot et al. [50] studied the influence of the process parameters on the bonding conditions of ABS parts. They studied the effect of the extruder temperature, printing speed, and layer height. Their observations show that the printing speed has a large impact on the tensile strength, the latter depends on the coalescence of filaments. Printing at high speed generally yields lower mechanical strength.

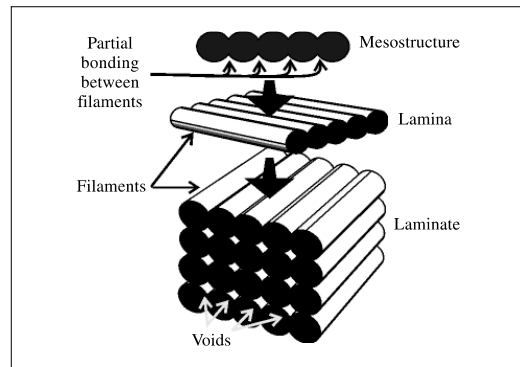


Figure 6: Levels of analysis for FFF prototypes [49]

Several analytical models have been developed to describe the kinetics of coalescence. Frankel [51] derived the first analytical model, which was subsequently corrected by Eshelby [52]. Frankel's model is based on the balance of the work of the surface tension and the viscous dissipation. The modified Frankel's model by Eshelby is represented in eq. 1.

$$\frac{x}{a} = \left(\frac{t\gamma}{\mu a_0} \right)^{\frac{1}{2}} \quad \text{eq. 1}$$

Where a is the particle radius changing with time, a_0 is the initial particle radius, t is the time, x is the sintering neck radius, γ is the surface tension and η is viscosity. Frankel's model has been used by many authors to describe the kinetics of sintering of Newtonian fluids. Despite its simplicity, it gives insight on the effect of material properties on the coalescence rate. The validity of Frankel's model is limited to Newtonian flow for the description of early stage sintering when the particle diameters remains relatively constant. Hopper [53] proposed an exact analytical solution of the Navier-Stokes equations for two-dimensional viscous flow driven by capillary forces acting on the free-surface. Hopper's theory is limited to two-dimensional and Newtonian flow problems.

Pokluda et al. [47] developed a sintering model using an approach similar as Frankel's one: in their model, they take into account the variation of the particle radius. The Frankel's modified model developed by Pokluda is represented in eq. 2.

$$\theta' = \frac{\gamma}{\mu a_0} \frac{2^{-\frac{5}{3}} \sin \theta \cos \theta (2 - \cos \theta)^{\frac{1}{3}}}{(1 - \cos \theta)(1 + \cos \theta)^{\frac{1}{3}}} \quad \text{eq. 2}$$

In which θ' is the rate of angle evolution with time and θ is the angle between intersecting lines from the center to the neck of the coalescence. The initial value for the angle between the two spheres (θ) is zero.

For the experimental studies of the coalescence of spheres and filaments, the protocol is always the same. They are mainly based on the optical observation of the neck growth evolution by camera or under a microscope. As it is represented in Figure 7, for two filaments in ABS (0.74 mm diameter and 0.3 mm length) at 200 °C, in the primary step ($t = 0$) two filaments meet together. With time, the length of the neck between the two filaments increases and finally at $t = 840$ s, the length of the neck is close to the initial diameter of the filaments [54].

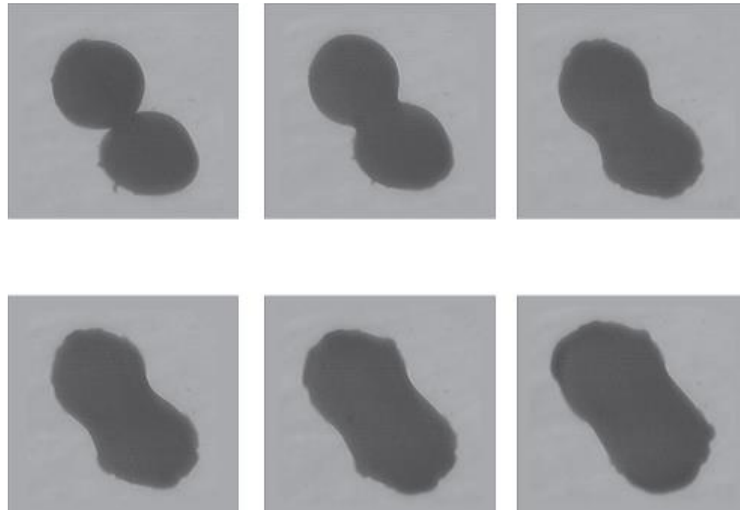


Figure 7: Neck growth evolution for ABS P400 at constant temperature [54]

Most of the studies reported in the literature are carried out at isothermal temperature. Nevertheless, in most polymer processes including FFF, the temperature is not constant. For instance, the coalescence of two thermotropic polymers in the air was investigated by Scribber et al. [55]. They have used the same methodology in order to integrate the viscoelastic behavior to the model. The viscous neck growth model

using the upper convected Maxwell constitutive equation (UCM) was extended to the transient stress case in order to incorporate the slow growth of viscosity at the startup of flow.

In the same manner, Bellehumeur et al. [56] showed the importance of the viscoelastic behavior of the polymers in the coalescence phenomenon. Based on Frankel's approach [57], Eshelby [52] and the model proposed by Pokluda [47], Bellehumeur with the integration of the UCM, introduced the effect of the viscoelastic behavior for the sintering.

The majority of the studies on the coalescence combine experimental study and numerical modeling. As, it is explained in the following parts, the numerical simulations are limited to low viscosity fluids such as water and gas.

Chen et al. [58] studied the coalescence and breakup of gas bubbles with an axisymmetric numerical simulation of two-phases (gas/liquid) transient flow. Their numerical simulation approach is based on multiphasic flow algorithm and finite-volume method. Verdier [59] studied the coalescence of polymeric particles. He proposed a new method to study the collision of droplets of various viscosities under a microscope. They have shown that under the action of van der Waals forces only, two spherical droplets get closer and eventually meet. Another experimental study has been carried out by using a polarized light optical microscope (POM) combined with a hot stage by Aid et al. [60]. They have investigated the influence of the temperature and particle size on the coalescence. They also proposed a predictive modeling for the coalescence of polymeric particles including PVDF (Polyvinylidene fluoride) and PMMA (Polymethylmethacrylate) [60]. In this research, a numerical model based on Bellehumeur's approach is suggested to predict the coalescence phenomenon between two particles of different polymers. This model aims to generalize the Bellehumeur's relation commonly used to describe the coalescence between identical grains in the case of different polymers. High-speed particle image velocimeter has been used by Betton et al. [61], who observed the impact and coalescence of droplets on a solid surface.

The same authors [61] modeled the coalescence of low viscosity fluids: glycerol and water. Their experimental studies have been compared with analytical simulation by lattice Boltzmann method. The simulations slightly overpredict the coalescence kinetics. The numerical simulation of the coalescence of inviscid drops (fluids with zero or near zero viscosity) on a solid surface was modeled by boundary element method in which the free surface of the drop is represented by a moving grid [62]. In the same idea, Laurent et al. [63] modeled the coalescence of liquid spray coalescence and evaporation. They used the direct quadrature method of moments (DQMOM) to model the coalescence of spray. Mohammadi et al. [64] modeled the coalescence of water droplets in oil by using Computational Fluid Dynamics (CFD) techniques. Their numerical simulation was carried out by finite volume numerical method and by solving the Navier–Stokes equations in conjunction with the Volume of Fluid (VOF) approach for interface tracking.

B. Sirkarwar et al. [65] used COMSOL Multiphysics software and Level-set equation for modeling the coalescence of water droplets. These studies are based on a comparison of the numerical simulation and experimental study: the kinetics by numerical simulation are five times slower than the experimental results. In opposite, J. Zheng et al. [66] using COMSOL Multiphysics found a good agreement between experimental results and numerical modeling for the coalescence of glycerol. Their experimental apparatus is based on two sessile droplets resting on an organic glass substrate. Furthermore, M. Sellier et al. [67] made the numerical simulation of a sessile droplet by COMSOL Multiphysics. Their numerical simulation for low viscosity sessile droplet agrees with their experimental study.

The influence of electric field on the coalescence of two water droplets has been investigated by Q. Li [68]. With experimental study and numerical simulation, they have shown that the electric field could boost the coalescence rate.

Some other studies were carried out with commercial softwares for modeling the coalescence of droplets. However, only a few studies relate to polymers, most of them are for droplets of low viscosity fluids at isothermal temperature.

Among studies on polymeric droplets, W. Du et al. [69], used the volume of fluid (VOF) equations and Fluent software for modeling the coalescence of PVDF grains. In their study, they have considered that the viscosity of PVDF is 4000-4500 Pa.s. Their observation shows that the kinetics of coalescence determined by the numerical simulation is faster than the one determined experimentally. M. Asgarpour [70] by using VOF and Fluent software worked on the sintering of polymeric particles. He determined the porosity of the parts manufactured by rotomolding by stationary simulation.

Subsequently, our literature review shows that there is no adequate study on the coalescence phenomenon for high viscosity polymers. Moreover, only a few experimental works report the coalescence of filaments applied to FFF. From our knowledge, none of these works deals with the numerical simulation of the coalescence of filaments taking place during the FFF process. Existing studies are mainly based on isothermal coalescence while in FFF process, the coalescence takes place in non-isothermal conditions.

1.3.3 Fluid flow and heat transfer during material deposition

Modeling the fluid flow and heat transfer is the primary concern in the study of polymer processing and especially in the FFF process [71]. The heat transfer and the temperature of the deposited beads is one of the most crucial issues which influence the quality of parts manufactured by FFF. Indeed, heat transfer is the factor governing the coalescence of the filaments as well as the crystallization of the polymer on cooling after deposition. However, measuring the heat fields during the FFF process is tough, as it requires non-destructive techniques such as infrared thermography. To our knowledge, this kind of in-situ monitoring has been published only once until now for FFF. Seppala et al. in 2016, studied the heat transfer of the FFF process using infrared (IR) imaging [72]. Their study shows that the cooling rate of the deposited filament is relatively fast during the process. Depending on the printing speed and the number of layers, the cooling rate changes from 60 to 180 °C.s⁻¹: For the third layer and a printing speed of 10 mm.s⁻¹ the cooling rate is 60 °C.s⁻¹, while for the same layer and a printing speed of 90 mm.s⁻¹ the cooling rate is 180 °C.s⁻¹. The cooling rate for the eighth layer at the same speeds are respectively 50 °C.s⁻¹ and 10°C.s⁻¹ [72].

This lack of measurements of heat fields could be explained by the cost of this equipment and also by the issues to access the view of the filaments during deposition through the frame of the machine. For these reasons, the numerical simulation would be useful to access the heat transfers that are not experimentally accessible. In this case, the numerical simulation is cost-effective to achieve reliability and to improve the quality of printed products.

Similarly to the extrusion process, during the FFF process, the filament goes through a liquefier before the deposition. Despite many works on the experimental point of view, only a few works dealing with the numerical simulation of the flow when the polymer exits the liquefier are reported. However, the existing approaches are generally based on the Finite Element Methods (FEM) study of the one phase flow and they are applied to extrusion and injection molding [73].

Concerning specifically our case (numerical simulation of material deposition) only a few works worth to be cited: Lirvani [74] using numerical simulation and Navier-Stokes equations modeled the extrusion process of a fluid with a viscosity of about 20 Pa.s. Kopplmayr [75] used OpenFOAM software and Volume Of Fluid (VOF) equations for modeling the extrusion of polyethylene, polypropylene and polyethylene terephthalate. The comparison of their numerical modeling with experimental studies shows a good agreement. Comminal [76] by VOF equations modeled the free-form extrusion of the polymer by taking into account its viscoelastic behavior. He noticed the deformation and instability of the extrudate from a value of shear rate. Bot [77] studied the impact and solidification of a metal droplet on a substrate using VOF and TVD (Total Variation Diminishing) method. Nevertheless, his study consists of a segregated droplet and the impact of this isolated droplet on the substrate and not a continuous deposition of a filament on a substrate. Amico et al. [78] using adaptable finite element analysis determined the heat transfer in the FFF process. In the case of this model, the material flow was not directly simulated and instead, the material deposition was approached as a uniform change in height across the part. They have taken an insight into the influence of feed rate on the cooling rate of the deposited bead. Additionally, the thermal behavior of a RepRap 3D printer liquefier was studied by Jerez-Mesa et al. [79]. They have modeled the fluid flow and the temperature in the liquefier by continuity equations. The closest work to our study is done by Comminal in 2015 [80] in which he modeled the behavior of the extrudate of a viscoelastic material. He also considered streamlines due to the elastic instabilities in the die. It is known that a sharkskin phenomenon is related to elastic instability in the die. His numerical approach takes into account the viscoelasticity to model the flow behavior. For that, he used VOF and log-conformation tensors. In 2018, the same authors [81] modeled the material deposition on the substrate while taking into account the fluid flow. They have shown the influence of the geometry and inlet velocity on the shape of the cross-section of the deposited bead, using CFD simulation.

Still in 2018, Peng et al. [82] studied the material flow in the FFF process by an experimental study. Using pigments distribution, they have revealed the velocity distribution in the liquefier. Osswald et al. in 2018 [83] developed an analytical model for the polymer melting during FFF process. The model presented in this paper solves a coupled mass, momentum and energy balance to predict the flow into the nozzle, as well as the melting rate in a polymer extrusion in the FFF process. The model includes the effects of initial temperature of the filament, heater temperature, applied force, nozzle tip angle, capillary diameter and length as well as rheological and thermal properties of the polymer. Their predictive model shows a relatively good agreement with experimental studies. The model predicts quite well the melting rates at forces up to 40 N. However, at higher forces, the melting rate is over-predicted [83].

According to our bibliography study, there is a lack of studies on numerical modeling of the material deposition during FFF. To our knowledge, when I started my Ph.D., no study existed, most of them have been published last year.

1.3.4 Surface roughness and accuracy

The main flaw in FFF is the high surface roughness of the printed parts. Indeed, the surface roughness is directly linked to the nozzle diameter. Several post-processing treatments are proposed to decrease the surface roughness of the printed parts. Using chemical post-processing treatment [84] [85] [86], modifying the generated code and slicing [86] [87] [88] and using post-processing machining [89] are the effective approaches to reduce the roughness. Percoco et al. [84] made a surface treatment with a solution of 90 % dimethylketone and 10 % water for ABS parts. Their results show that the quality of the surface has been improved up to 90 %. Also, they noted an improvement in mechanical properties.

Their hypothesis is that the solvent diffuses inside the parts, which results in chemical changes influencing the mechanical behavior. In our opinion, the chemical treatment reduces the number of the micro-cracks onto the part surface. Consequently, there is less possibility to initiate and to propagate the cracks. That is reason why they observed an improvement in mechanical properties.

Moreover, optical observations proved that the curved zones do not have the same accuracy of flat geometries: their roughness and porosity rates are higher than on flat surfaces. An adequate procedure of slicing is required to improve the quality of the curved regions [87] [88] [90].

1.4 Polymer properties influencing the quality of printed PEEK parts

1.4.1. Polymer definition and conformation

The modern concept of polymers as covalently bonded macromolecular structures was proposed in 1920 by H. Staudinger. A polymer is a large molecule composed of repeated units called monomers. The length of a macromolecular chain is quantified by the degree of polymerization, which is the number of monomers into the chain.

In polymer melt or in amorphous phase, the ideal chain can be described as random walk statistics. A random walk denotes a path of successive steps in which the direction of each step is uncorrelated with or independent of the previous steps: Steps forward and backward, left and right, up and down do all have the same probability. Figure 8 describes two possible states of a chain with 10 segments [91].

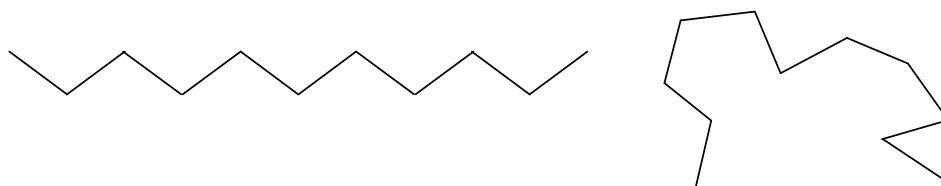


Figure 8: Two possible conformation of a polymer chains composed of 10 monomers [91]

The flexibility of the chain is mainly due to torsion angles: the chain adopts gauche and trans bond conformations along the backbone, it means a single chain can adopt many different conformations.

When describing an ideal chain of $N+1$ atoms, the average end-to-end vector of a random walk of N steps, taken over many possible conformations, is zero because of the equal probability to step in opposite directions:

$$\langle R \rangle = 0 \quad \text{eq. 3}$$

The root-mean-square end-to-end distance is finite, and it characterizes the average spatial dimension traversed. If the length of each step is l , the root-mean-square end-to-end distance is expressed as following:

$$\langle R^2 \rangle^{1/2} = N^{1/2} l \quad \text{eq. 4}$$

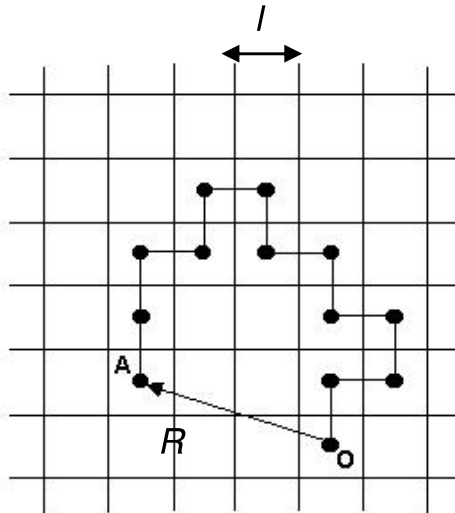


Figure 9 :Scheme of the end-to-end distance of a polymeric chain

This model is valid for freely jointed chains. In most polymers, there are restrictions of motion because of bond angles (typically for double and triple covalent bonds). To describe this limitation of motion, a characteristic ratio C_∞ is introduced. The root-mean-square end-to-end distance R_0 for the polymer chain of N bonds is then:

$$R_0 = \langle R^2 \rangle^{1/2} = N^{1/2} C_\infty^{1/2} l \quad \text{eq. 5}$$

The length of each step l is ~ 0.154 nm for a C-C bond. The characteristic ratio C_∞ depends on each polymer. As an example, a chain of $N = 10,000$ monomers with $2N$ C-C bonds : Its fully extended length would be $2.N.l = 3080$ nm and its root-mean-square end-to-end distance would be $R_0 \approx 72$ nm in the melt or glassy state.

A polymer chain has a characteristic size, which scales with N the number of monomers in the chain to the one-half power:

$$R_0 \sim N^{1/2} \quad \text{eq. 6}$$

Nevertheless, the average volume occupied by the coil is much greater than the volume of the chain itself, as seen in Figure 10.

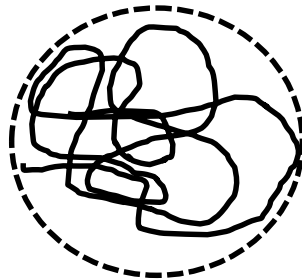


Figure 10 : Scheme of the volume occupied by polymer coil

So that in the melt or in the glassy state, many other chains will be intermingled with a single chain. The volume of the coil is:

$$V_{coil} \approx R_0^3 \sim N^{3/2} \quad \text{eq. 7}$$

The volume of a chain is:

$$V_{chain} = N \cdot v_{monomer} \sim N \quad \text{eq. 8}$$

So that the volume available for the other chains to enter the volume of a single chain and to create entanglements is:

$$V_{coil}/V_{chain} \sim N^{1/2} \quad \text{eq. 9}$$

The entanglement increases with N, the higher the molecular weight, the higher is the polymer melt viscosity. This volume $N^{1/2}$ available to create entanglements leads to the unique rheological and mechanical properties exhibited by polymers. In the section 1.4.5, we describe the viscoelastic behavior of polymers resulting from this free volume.

1.4.2. Amorphous and semi-crystalline state

When the polymers are cooled from the melting state or it is concentrated from a dilute solution, the chains attract to each other in order to form a solid structure. During cooling, two arrangements are possible:

- The molecular chains randomly coil and entangle together without ordered structure. This solid and glassy (transparent) structure is called amorphous structure or amorphous phase.
- The second structure is when the molecular chains create an organized structure. In this case, the molecular chains fold and pack themselves in a regular manner. These organized structures are called crystalline structures.

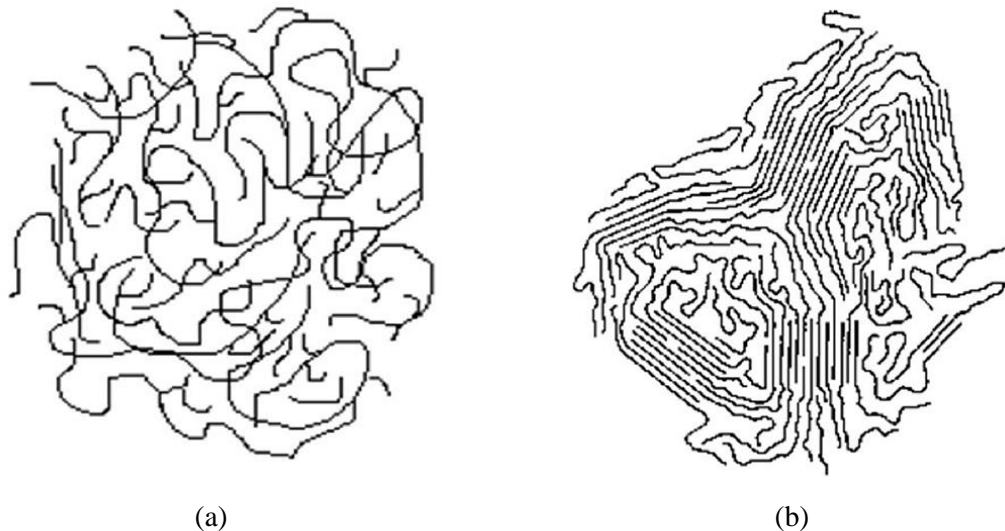


Figure 11: Structure of the thermoplastics (a) Amorphous state (b) Semi-crystalline state [92]

As defined in the previous part, polymers are constituted of long molecular chains. Because of polymolecularity (distribution of macromolecular length), defects and irregularities in the repetition of the chemical structure, some chains cannot fold themselves into crystals. Consequently, the polymeric structures are not fully crystalline. For this reason, the non-amorphous polymers are called semi-

crystalline polymers. The crystalline rate is defined by the ratio of the mass (or volume) of the crystalline phase over the total mass (or volume).

The liquid-solid phase transition is called crystallization. The crystallization is an exothermic transition. During crystallization, the polymeric material releases energy to return into an equilibrium state. The energy released by the crystallization increases the temperature inside the polymer. The existing models to describe the crystallization rate and crystallization enthalpy are presented in Chapter 3.

1.4.3. Printing of PEEK by FFF process

Among high performance thermoplastics, polymers of PAEK (Polyaryletherketone) family is one of the most resistant in severe conditions. The various PAEK differ mainly in thermal properties, but not so much in the other characteristics. 250 °C is the maximum temperature of use in continuous operation, without mechanical stress, of the different PAEK without load or reinforcement. This high value, compared to 230 °C obtained by polyamide-imide (PAI) and liquid crystal polymers (LCP), shows the excellent heat resistance of PAEK compared to other competing technical polymers. These polymers are renowned for being the only ones which can be used as a last resort where all the others have turned out to be unsuitable. The development prospects of the PAEK are extremely favorable, as the growth is of around 15 % per year, with a strong presence in the aerospace, automotive, electronics and energy sectors. [91]. PEK (Polyetherketone) was introduced to the world market in 1982 by ICI, which then marketed PEEK (Polyetheretherketone) in 1987. The full description of PEEK is done in Chapter 2.

Only a few articles report the printing of PEEK parts by FFF. They have been published in 2017 and 2018. The first one is from Zhao et al. [93] who printed PEEK parts for medical applications. The nozzle temperature, platform temperature, and the deposited filament diameter were tightly controlled to improve the mechanical strength. Based on mechanical characterization of printed parts, they conclude that the nozzle temperature and the printing platform temperature are the most important parameters influencing the tensile strength. According to them, the environment temperature is relatively insignificant. Considering the difficulty of insulation and regulation of the temperature of the environment, they believe it is better to print PEEK at room temperature.

Still for medical applications, Otero et al. [94], Deng et al. [95] and Rinaldi et al. [96] studied the fracture resistance of printed parts of PEEK. They have studied their mechanical properties with tensile tests, their thermal transition by differential scanning calorimetry (DSC), their microstructure by X-Ray diffraction (XRD) and their morphology by optical microscopy and computed-tomography. The results have been compared with the raw filament of PEEK. No difference was found in terms of thermal transition such as glass transition, melting temperature, and crystalline rate. However, the cold crystallization phenomenon, that is to say, the crystallization occurring from low temperature when the polymer has been quenched, was noticed in the printed samples. This indicates that the cooling rate after the deposition was so fast that the polymer had not enough time to crystallize on cooling. Also, they remarked that the printed samples evidence great differences in mechanical performances depending on the printing orientation and conditions.

Yang et al. [97] studied the influence of the thermal conditions on the crystallization and the mechanical properties of PEEK printed parts. They show that the crystalline rate grows from 17 % to 31 % as the environment temperature increases from 25 °C to 200 °C. In opposite to Zhao et al. [93], these results indicate that the environment temperature has a large influence on the crystalline rate. Furthermore, the crystalline rate highly influences the mechanical properties of PEEK [98].

Alternatively, because of high melting temperature and high viscosity of PEEK, Tseng et al. [99] proposed and designed a screw base liquefier to print with raw material in form of pellets instead of filaments. They have also studied the printability of PEEK with their own designed screw base liquefier. They have printed two series of PEEK parts: one of the batches was submitted to annealing (heat treatment). The second batch is the printed parts without heat treatment. When performing the mechanical tests, they measured identical mechanical properties. Their advice to optimize the mechanical properties is to set the temperatures for the liquefier at 370–390 °C and for the platform up to 280 °C. Furthermore, they have shown that in order to prevent the void formation and residual stress, the liquefier’s temperature must be 390 °C [99].

In most of the works reported in the literature, only the influence of the printing conditions of PEEK on the properties of parts are highlighted. Indeed, the authors do not consider the polymer properties such as viscoelasticity, thermal properties and crystallinity. However, PEEK is a semi-crystalline polymer. A deep understanding of the mechanisms influencing the crystallization in FFF process is necessary to improve the mechanical properties of the manufactured part. Definitely, printing PEEK is trickier than other thermoplastics because of its viscoelastic properties and crystallization kinetics.

1.4.4 Crystallization of PEEK and its effect on mechanical properties

Controlling the crystallization is a key point to optimize the properties of the parts printed with semi-crystalline polymers. Furthermore, controlling the kinetics of crystallization and the parameters influencing the crystallization kinetics is essential to improve the FFF process.

The kinetics of crystallization has an effect on the coalescence of filaments in FFF: the macromolecular interdiffusion, resulting in filament bonding, must occur faster than the crystallization. If the crystallization is faster, the filaments will solidify rapidly and they will not bond together. In opposite, when the crystallization takes place slowly, a cross-interfacial crystallization could appear like it has been shown for the study of the auto-adhesion of PEEK [98], that is to say, some of the macromolecules across two adjacent filaments are linked into a single crystalline structure.

More generally, the crystalline rate influences the mechanical properties of printed parts. As an example, the elastic modulus increases with the crystalline phase [100]. Talbott et al. studied the influence of the crystalline rate on the mechanical properties of the parts manufactured with PEEK 150P [101]. Their observations show that increasing the crystallinity results in improving the tensile modulus and the tensile strength. As expected, a larger amorphous phase increases the toughness of the parts. The sum up of these results are presented in Table 2:

Table 2: Mechanical properties of the printed parts with PEEK 150P from Victrex [101]:

Properties	Crystalline rate = 16%	Crystalline rate = 40%
Tensile Modulus (MPa)	3447	4688
Tensile strength (MPa)	76	97
Shear modulus (MPa)	1172	1448
Shear strength (MPa)	48	70
Compression strength (MPa)	152	193
Mode I fracture toughness (MPa.m^{1/2})	11	2.75

In order to determine the crystalline rate in the printed parts, an identification of the crystallization kinetics of PEEK is necessary. Atkinson et al. [102] show that the maximum crystallinity of PEEK is about 40%. They also showed the effect of crystallization on the glass transition temperature and

enthalpic relaxation in PEEK. Increasing the crystalline rates results in moving the glass transition towards higher temperatures [102]. Tardif et al. studied the crystallization of PEEK 150G over a large temperature range from the glass transition up to the melting temperature by using a nano-calorimeter [103]. The crystallization kinetics of PEEK is the fastest at 235 °C. Wei et al. [104] studied the kinetics of crystallization of PEEK 150P using temperature-modulated DSC (Differential Scanning Calorimeter) and isothermal DSC. The isothermal crystallization kinetics of PEEK was analyzed between 290 and 320°C by Avrami equation. The Avrami equation is commonly used to model the kinetics of isothermal crystallization and also to predict the form of the crystalline phases. It works quite well for all the semi-crystalline polymers. The corresponding Avrami constants n_1 increased from 1.50 to 2.98, and n_2 changed from 0.52 to 1.37. Kumar et al. [105] identified the crystalline morphology of PEEK as spherulitic form. The spherulite crystal of PEEK is represented in Figure 12. They have also explained that the spherulite growth rate is faster at 300 °C than at 320 °C. Besset et al. [106] studied the morphology of PEEK; he shown that PEEK exhibits a double crystallization peak. Additionally, several authors studied this double peak crystallization which represents the first and secondary crystallization of PEEK, each of them is associated to a size of spherulites [107]. Sauer et al. by temperature-modulated DSC (TMDSC) characterized the melting and recrystallization of the polymers exhibiting multiple melting endotherms [108]. Lin et al. [109] studied the morphology of semi-crystalline PEEK; they investigated the morphology by various microscopy, thermal and spectroscopy techniques. By Flash DSC, they shown a “double melting” phenomenon of isothermally crystallized PEEK. Fougnyes et al. [110] studied the cold crystallization of PEEK by X-ray scattering (SAXS). They studied the cold crystallization by heating PEEK from below the glass transition temperature to above the melting point. They have shown that the largest degree of entanglements of the high molecular weight samples impedes the reorganization mechanism with the consequence that the apparent melting temperature decreases with increasing the average molecular weight.

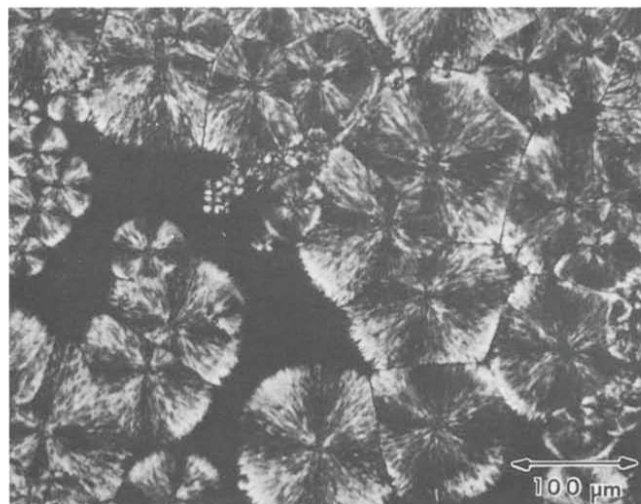


Figure 12: The spherulites in PEEK [105]

Although there are many studies on the crystallization of PEEK in isothermal conditions, there is no study on the non-isothermal crystallization of PEEK. During FFF, the polymeric filament is melted and deposited onto a previous layer. The filament occurs non-isothermal history during cooling from the melted state. For this reason, these studies are not suitable to FFF in order to determine the crystallization kinetics during printing.

1.4.5 Definition of the viscoelastic behavior of melted polymers

The viscoelasticity is the property that represents the elastic and viscous behavior of the materials under an applied strain or stress. Polymers always demonstrate a viscoelastic behavior because they consist out of long molecules entangled with their neighbors, as described in section 1.4.3. Below glass transition, the segment rotation time is very long. When a small stress is applied, the polymer chains can only bend a little. This gives the polymer a stiff behavior (mainly elastic). Above glass transition, the segment rotation time is faster, the macromolecular chains have more mobility and then, the viscous behavior overtakes the elastic one.

A description of the principle of rheometers and the methods for measuring the viscoelastic behavior of the materials is given in Annex II.

The behavior of viscoelastic materials is described by rheological models. A convenient representation is those using the images of a spring and a damper. The solid elasticity is modeled by a spring with E (or G) modulus as its rigidity and the fluid viscosity (η) is modeled as the damper. The elastic part is the capacity of the material for keeping and releasing the energy stored once the material is deformed. The viscous part of a material is the capacity of dispersing (losing) the energy under heat release, due to the friction of macromolecules. All polymers exhibit a viscoelastic behavior, with a various proportion of viscosity over elasticity: the ratio is called the loss factor.

As it is represented in the eq. 10, the viscosity of a fluid is the measurement of its resistance to gradual deformation by shear stress or tensile stress [111].

$$\eta = \frac{\tau}{\dot{\gamma}} \quad \text{eq. 10}$$

With η (Pa.s) is the viscosity, τ (Pa) is the shear stress and $\dot{\gamma}$ (s^{-1}) is the shear rate. The viscous behavior of a fluid either Newtonian or non-Newtonian is influenced by several parameters. The main parameters influencing on the viscosity are classified into two parts as following [112]:

1. The flow conditions:

- Shear rate
- Temperature
- Pressure
- Time and thermomechanical history of the fluid

2. The chemical structure, morphology and composition:

- Chemical nature of the monomer
- Molecular weight distribution
- Presence of long chain branches
- Nature and concentration of additives, fillers, etc.

As the polymer is chosen in this thesis, the chemical structure, morphology and composition could not be changed. That is why we concentrate only on the flow conditions. The parameters are developed below:

Shear rate

Depending on the nature of the fluid, increasing the shear rate may decrease or increase the viscosity. The viscosity of the fluids is explained in the easiest form by the power law equation or with the Carreau-Yasuda model which takes into account the Newtonian plateau at low shear rates. These models

determine the viscosity of a fluid according to the shear rate [112][113]. The power law viscosity equation and Carreau model are represented in eq. 11 and eq. 12 respectively.

$$\eta = K|\dot{\gamma}|^{n-1} \text{ for shear – thinning fluids } (n < 1) \quad \text{eq. 11}$$

$$\eta = \eta_{inf} + (\eta_0 - \eta_{inf})[1 + (\lambda\dot{\gamma})^a]^{\frac{n-1}{a}} \quad \text{eq. 12}$$

Where n is the pseudoplasticity index, K is the consistency coefficient, η_0 is the viscosity of the fluid at zero shear rate, η_{inf} is the viscosity of the fluid at infinite shear rate, λ is the relaxation time index, a is a dimensionless parameter describing the transition between the first Newtonian plateau and the power law zone and, $\dot{\gamma}$ the shear rate. For the shear-thinning fluids $n < 1$, the viscosity decreases by increasing the shear rate. Oppositely, the viscosity of shear-thickening fluids increases by increasing the shear rate, with $n > 1$. For Newtonian fluids, $n = 1$, it means that the shear rate does not influence on the fluid viscosity. All thermoplastics demonstrate a shear-thinning behavior: their viscosity decreases exponentially with the shear rate. A typical example of Newtonian fluid is water.

Temperature

Alongside with the shear rate, the temperature has much influence on the viscosity of the fluids [112]. It has been shown that increasing the temperature leads to decreasing the viscosity. In fact, the influence of the temperature is considered equivalent to increasing the shear rate. This is known as time-temperature equivalence. Consequently, as it is represented in eq. 13, the viscosity of the fluids could be written as a function of shear rate and temperature.

The dependency of the viscosity with the temperature follows an Arrhenius law. From the viscosity at a specified temperature, the viscosity is determined at all the temperature range above the melting temperature.

$$\eta(\dot{\gamma}, T) = a_T \eta(\dot{\gamma} a_T, T_0) \quad \text{eq. 13}$$

In the eq. 13, $a_T(T)$ is the Arrhenius coefficient which is determined by eq. 14.

$$a_T = \exp \left[\frac{E_a}{R} \left(\frac{1}{T} - \frac{1}{T_0} \right) \right] \quad \text{eq. 14}$$

where E_a is the activation energy [114] [115] and R is the gas constant [114]. At $T = T_0$, the Arrhenius coefficient is 1. The viscosity curve at T_0 is known as the master curve. At this temperature $a_T(T) = 1$. For the shear-thinning fluids like thermoplastics, for T higher than T_0 , $a_T(T) > 1$ means the viscosity decreases for these temperatures T .

The time-temperature equivalence is not relevant for long chain branched polymers. Moreover, it cannot be applied close to thermal transitions such as glass temperature, crystallization and melting temperature. Identically, when the chemical structure of the polymer changes due to degradation, evaporation and so on, the equivalence is no longer appropriated.

Pressure

Increasing the pressure increases the viscosity of polymers. It is caused by the compression of the melt which decreases the free volume between macromolecules. The latter being closer, the macromolecules have less mobility to slide over each other. The pressure shift factors can be used to generate master

curves just as temperature shift factors are used in time–temperature equivalence. The Barus equation represented in eq. 15 is often found to describe the pressure dependency of viscosity :

$$\ln\left(\frac{\eta_0(P)}{\eta_0(P_0)}\right) = \beta(P - P_0) \quad \text{eq. 15}$$

Which could be written as eq. 16:

$$\eta(p) = \eta_0 \exp(\beta P) \quad \text{eq. 16}$$

Where β is the compressibility coefficient.

Time or history

In the case of thixotropic materials for which the shear thinning property is time-dependent, the influence of the shear history must be considered [113]. Some gels or complex fluids that are viscous under static conditions will flow (less viscous) over time when shaken, agitated, sheared or otherwise stressed. These materials keep their shear history over a period of time. Consequently, in the case of viscosity measurement, the resting time before the viscosity measurement highly influences on the viscosity. Consequently, in order to measure the viscosity properly, an accurate time interval must be followed during the measurement [116].

1.4.6 Definition and determination of the surface tension

As seen previously, one of the most important properties which conduct the coalescence of two particles or filaments (and consequently increase the bonding and reduce the porosity ratio in the printed parts by FFF) is the surface tension or surface energy. This term is stated by different symbols: γ , Y and σ are normally use to describe the surface energy of the materials.

Atoms and molecules of the materials are under cohesion forces on the interface, the existence of an interface, for example an air/fluid interface needs to compensate this force. The energy necessary to retain this surface is called “surface energy”. The surface energy is also defined as the sum of all intermolecular forces that are on the surface of a material, the degree of attraction or repulsion force of a material surface exerts on another material. The surface energy of the materials depends directly on the chemical composition of solids and liquids; however, the surface energy is independent on the molecular weight.

There are several methods for measuring the surface tension; here is a brief list of methods for measuring the contact angle and energy surface of materials and liquids:

- Capillary rise method
- Stalagmometer method- drop weight method
- Wilhelmy plate or ring method
- Maximum bulk pressure method
- Methods analyzing the shape of hanging or deposited liquid drop or gas bubble
- Dynamic methods

Depending on the measurement, each method has its advantages and flaws as well as its methodology and equations.

Several studies have been carried out in order to determine the surface energy of PEEK at room temperature. All these studies aim to improve the hydrophilicity of PEEK. However, the results obtained for the surface tension from the different studies show a large dispersion.

S. Kluska and his colleagues [117] used helium/nitrogen and nitrous oxide plasma to modify the surface energy of PEEK. They obtained the value of $43.7 \pm 0.8 \text{ mJ.m}^{-2}$ for the total surface energy of unprocessed PEEK. On the other hand, Bhatnagar [118] used low-pressure plasma under radio frequency to modify the surface properties of PEEK, they measured 51.14 mJ.m^{-2} for the surface tension of PEEK at room temperature. The study of Dresier et al. shows the influence of different grades of PEEK and also the crystalline rate on the surface tension of PEEK [119]. They have shown that the surface energy changes according to the grade of polymer and also the crystalline rate. They have obtained: 33.2, 30.4, 40.6 mJ.m^{-2} for different grades of PEEK.

D. Rymuszka [120] also measured the value of the surface energy by the different devices after plasma treatment. The methods used in this study are contact angle hysteresis approach (CAH), Owens and Wendt theory (O-W) and Lifshitz-van der Waals acid-based approach (LWAB). Their measurement shows the value of 40, 42, 42 mJ.m^{-2} respectively for each approach.

To sum up, the studies on the surface tension of PEEK, the value of 40 mJ.m^{-2} is the average of the measurements done with different methods.

It has been shown that the surface energy of a polymer is highly influenced by the temperature and it could change up to 50% from its initial value at room temperature [121]. Because of the difficulties for measuring the temperature dependent surface tension, not many studies were conducted to determine the surface energy of polymers at high temperature.

The other difficulties for determining the surface tension in the melted state is the degradation of the polymers when exposed a long time at high temperature. Moreover, thermoplastics have generally a high viscosity comparing to other fluids. This high viscosity is another issue to solve for the measurement of the surface tension, like it is for PEEK. Consequently, the measurement of the surface tension of PEEK in the melted state is even more difficult than for other thermoplastics.

1.5 Conclusion

This chapter makes an overview of the works carried out until now on the Fused Filament Fabrication (FFF) process, on an experimental and modeling point of view. Our interest focuses on FFF for high performances applications.

In the first part, after presenting the principle of the process and the commercially available machines, we review the effect of process parameters on the quality of printed parts. In most of the studies on the FFF process, the authors vary the process parameters to print specimens, the latter are characterized by mechanical tests. Moreover, these studies are concentrated on the optimization of the strategy of deposition such as raster orientation, layer height and layer width of the deposited layer and feed rate during deposition. However, the properties of the materials are not considered in such studies. Similarly to any polymer processing, the effect of the properties of the material must be taken into account to optimize the processing conditions. Indeed, the material properties such as viscosity, surface tension and crystallinity are among properties influencing on the quality of printed parts by FFF. Understanding the rheological properties such as velocity field, shear rate and viscoelasticity is a step towards the optimization of the process to make FFF a reliable and robust process. The porosity rate and so the mechanical properties of the printed parts stem from the flow and the bonding of filaments in their

melting state, that is why the studies on the coalescence phenomenon have been reviewed. Our literature assessment shows that there is no adequate study on the coalescence phenomenon for high viscosity polymers but only on low viscosity Newtonian fluids. Moreover, only a few experimental works report the coalescence of filaments applied to FFF. From our knowledge, none of these works deals with the numerical simulation of the coalescence taking place during the FFF process. Existing studies are mainly based on isothermal coalescence while in FFF process, the coalescence occurs in non-isothermal conditions.

In the second part, after giving some definitions of polymer conformation and the amorphous and semi-crystalline phases, the review focuses on the use of PEEK (Polyetheretherketone) in Fused Filament Fabrication. Indeed, most of the polymers used in the FFF process are mass-produced thermoplastics such as PLA (polylactic acid), ABS (acrylonitrile butadiene styrene), PC (polycarbonate) and more. Although these polymers are easily printable for home-manufacturing and rapid prototyping, the industry needs materials with higher performances. However, the lack of works carried out on the printing of high-performance thermoplastics demonstrate that this field is emerging. PEEK is a thermoplastic polymer with high mechanical properties and resistance to chemicals and thermo-oxidation aging. For these reasons, the demand in PEEK and PEEK composites is rising for structural parts and severe environment. Nevertheless, only a few studies on rheological properties of PEEK for using in FFF process are relevant. Furthermore, the crystallization of PEEK as a semi-crystalline polymer plays an important role in the processability of PEEK in the FFF process. The studies on the crystallization of PEEK are limited to isothermal crystallization whereas in the FFF process, the polymer undergoes non-isothermal crystallization. However, studying the non-isothermal crystallization of a semi-crystalline polymer during the process is tricky. Most of the studies on the kinetics of crystallization of PEEK has been carried out with a nano-DSC or modulated DSC or by temperature-modulated DSC (TMDSC). Nevertheless, there is no crystallization study suitable to understand the crystallization occurring during the process. Consequently, because of the importance of crystallization on the mechanical properties, a part of this thesis is dedicated to non-isothermal study, as it is a step towards the optimization of the parts printed with semi-crystalline polymers in FFF process.

Instead of experimental analysis, another method is to use numerical simulation to determine the flow behavior, the coalescence and the kinetics of crystallization. To our knowledge, no numerical study for modeling the deposition of the polymer on the substrate exists yet. The flow behavior in the liquefier is influenced by the printing parameters. The determination of the rheological properties such as velocity field, shear rate and viscosity in the FFF process and the influence of the printing parameters on the shape and flow stability of the extrudate when it exits from the nozzle is necessary to optimize the FFF process. The coalescence is highly influenced by the rheological properties and the surface tension of the polymer. The viscoelastic properties have been explained as well as the surface tension and the existing methods to measure it. The surface tension is a temperature dependent parameter. Accordingly, the variation of the surface tension with temperature must be determined. Although many studies give a value of surface tension at room temperature for PEEK at 40 mJ.m^{-2} , however, there is no indication of its variation with temperature in the literature.

The next chapter focuses on measuring the PEEK properties required for modeling its flow behavior, the coalescence and the kinetics of crystallization. Then, the coalescence of two adjacent PEEK filaments will be explored by experimental measurements, analytical analysis and numerical simulation.

**Chapter 2: Characterization of the polymers and
coalescence study**

2.1 Characterization of PEEK and PLA

2.1.1 Introduction

In the previous chapter, the advantages and flaws of the FFF process are displayed. We have also explained the process parameters and the material properties influencing the quality of the printed part. The quality of the parts refers as mechanical properties, surface roughness, warpage and dimension accuracy. These notions are highly influenced by some fundamental material properties. Consequently, understanding these properties of raw polymers is required to enhance the quality of the parts. The transition temperatures, crystallization, viscosity, thermal properties (thermal expansion, thermal conductivity), surface tension are the fundamental material properties which must be quantified and measured in order to predict and improve the quality of manufactured parts.

Table 3 gathers these fundamental properties, the techniques and the shape of the specimens to carry out the characterization of the polymer.

Table 3: Fundamental properties, techniques and specimen shape for the tests

Polymer properties	Testing utility	Specimen shape
Transition temperatures	DSC (Differential Scanning Calorimeter)	Pellets
Crystallization	DSC	Pellets
Thermal conductivity	Hot Disk	Plate
Thermal expansion	TMA (Thermomechanical analyzer)	Plate
Surface tension	Digidrop surface tensiometer	Plate
Thermomechanical properties	Rheometer	Plate

These fundamental properties are necessary for our further studies on the process parameters and on the crystallization kinetics. After presenting the materials, we will study the thermal transitions of our polymers to propose an optimized cycle to manufacture the plate samples.

PLA (polylactic acid) is chosen to study the physical phenomena occurring in FFF when PEEK is not convenient because of high temperatures. Hence, low viscosity and melting temperature about 160 °C/190 °C, make the experimental study of PLA much easier than PEEK. In Chapter 1, we have seen that the use of PLA is common in the FFF process because it is relatively low-cost material and easy printable.

2.1.2 Presentation of PEEK and PLA

PEEK is high-performance thermoplastic of the PAEK (polyaryletherketone) family. PAEK is obtained by electrophilic substitution. Various polymers of this family are proposed according to the ether/ketone ratio groups, such as PEK, PEEK, PEEKK, PEKEKK and so on. The latter influences mainly the thermal transitions: adding ketone groups into the chemical structure increases the glass transition (T_g) and melting temperature (T_m) [122]. These polymers are semi-crystalline, rigid and impact resistant. Because of high resistance in severe environment, PAEK is used in chemical industry, automobile and aerospace [122]. Moreover, different grades reinforced with carbon and glass fibers are commercially available.

PAEK have a longer durability and thermal stability than other high-performance polymers [4]. Additionally, they are stable to UV irradiation. However, the drawbacks of PAEK are the high cost and the difficulty to process them, mainly because of high viscosity and high melting temperature. Then, studying the properties of PEEK will help us to improve the manufacturability of PEEK by selecting the best process parameters according to its properties.

For our studies, PEEK 450G by VICTREX Company is selected. As it is represented in Figure 13, the chemical structure of PEEK consists of alternating aromatic, ether and ketone groups.

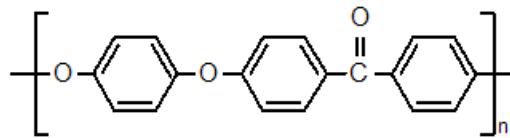


Figure 13: Chemical structure of PEEK

According to the datasheet provided by VICTREX Company, the typical value for the tensile strength of PEEK 450G is 98 MPa which is a high value compared to other polymers and especially conventional polymers using in the FFF process. The datasheet is presented in annex III.

For all the experiments, the samples were dried during 24h at 120 °C in the heating furnace to eliminate all the moisture in the polymer structure [123]. After 24h, the pellets were cooled until the room temperature in the furnace. Then the pellets were kept in the desiccator in order to avoid water absorption.

The density of PEEK 450G is 1.3 g.cm⁻³ [123]. PEEK is a semi-crystalline thermoplastic with a high melting temperature starting at 340 °C. This high temperature makes printing of PEEK very complicated compared to other thermoplastics which could be used for 3D printing and specially for the FFF process. That is why, in order to get better insights into the printability of PEEK, we will also study PLA.

PLA is a biobased and biodegradable semi-crystalline thermoplastic. The chemical structure of PLA is presented in Figure 14 [124].

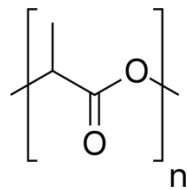


Figure 14: Chemical structure of PLA

PLA (NaturePlast PLI 005) in pellets was dried for 3 h in an oven at T=60 °C to remove moisture before processing. The PLA pellets were cooled until room temperature in a furnace, then they were placed in a desiccator for storage.

2.1.3 Thermal transitions and preparation of the samples

2.1.3.1 Thermal transitions of PEEK by DSC

In the FFF process, the cooling rate highly depends on the printing conditions such as printing temperature, environment temperature and inlet velocity of the polymer filaments. On the other hand, the cooling rate directly influences on the crystallization kinetics, bonding rate and porosity ratio of the final product. During the FFF process, the melted polymer of the first layer is more rapidly cooled to

the temperature of the substrate compared to the upper layers in which the cooling rate of the polymer decreases due to the accumulation of layers in the z-direction.

In this chapter and the next one, we will study the isothermal and non-isothermal crystallization of PEEK. The tests were performed with a Q200 – TA instrument DSC apparatus under isothermal and non-isothermal conditions. The operational conditions of DSC are reported in Annex II.

For each experiment, the glass transition, melting temperature and crystallization kinetics were measured. All experiments were carried out under nitrogen atmosphere in order to prevent oxidation. The crystalline ratio is calculated by eq. 17, the ratio of the crystallization enthalpy ΔH_c to the crystallization enthalpy of the fully crystallized PEEK which is 130 J.g^{-1} [125][103].

$$\%C = 100 * \frac{\Delta H_c}{\Delta H_{100\%C}} \quad \text{eq. 17}$$

The crystallization enthalpy is the area under the peak of crystallization on non-isothermal DSC curves.

Non-isothermal DSC tests were performed on dried PEEK 450G. In order to eliminate the thermo-mechanical history, the samples were heated at $10 \text{ }^\circ\text{C.min}^{-1}$ up to melting temperature. Then, they underwent the second heating cycle at $25 \text{ }^\circ\text{C.min}^{-1}$ and the cooling cycle at $25 \text{ }^\circ\text{C.min}^{-1}$.

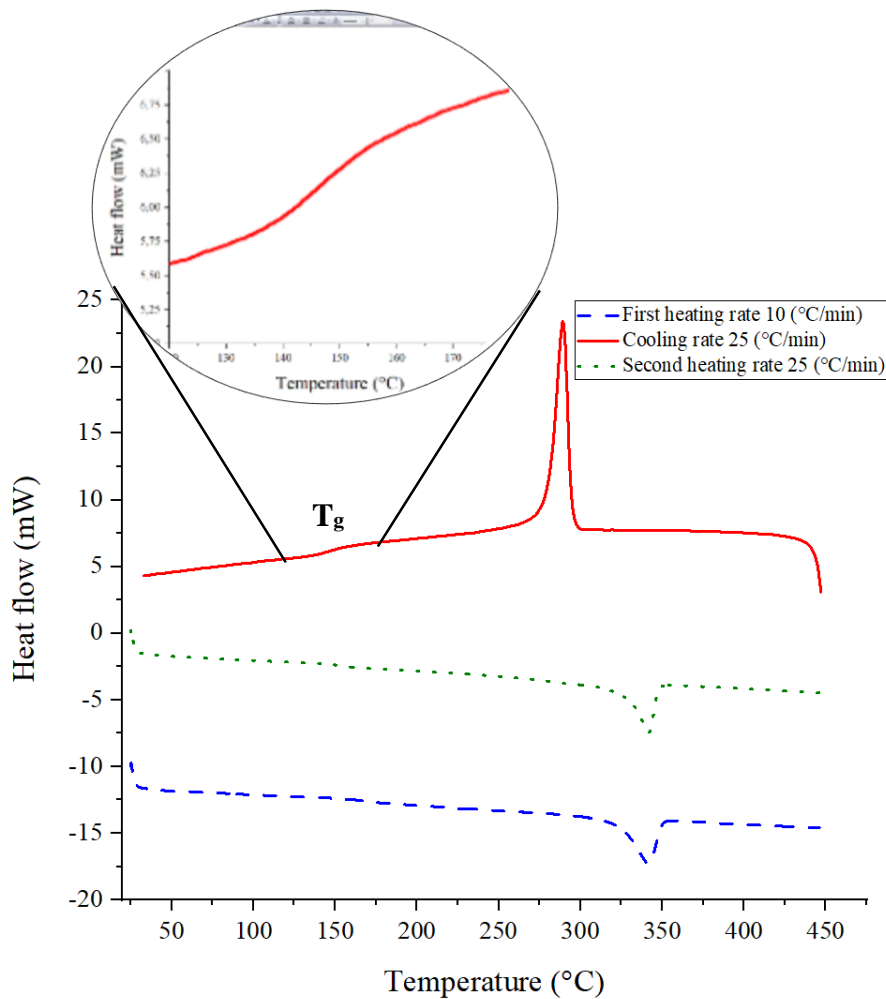


Figure 15: DSC curves of PEEK 450G, sample undergoes $25^\circ\text{C.min}^{-1}$ during the second heating cycle and $25^\circ\text{C.min}^{-1}$ cooling rate

During the cooling ramp displayed in Figure 15, the glass transition is measured at 149 ± 1 °C. At the heating ramp, the glass transition is observed at the same temperature and it is followed by a melting peak starting at 300 °C and finishing at 360 °C, it is centered at 344 ± 3 °C without cold crystallization occurrence, as expected. In the first step, from the melting enthalpy of 37 ± 0.5 J.g⁻¹, the ratio of crystallinity was determined at 40%. The kinetics of crystallization of PEEK have been determined under several cooling rates. With a cooling rate at 25 °C.min⁻¹, the crystallization takes place from 295 ± 2 °C to 250 ± 5 °C and the onset around 289 ± 1 °C. The enthalpy of crystallization is 41 ± 1 J.g⁻¹, leading to a ratio of crystallinity of 31 %. Hence, the polymer reaches its maximal ratio of crystallinity at 2 °C.min⁻¹. During the second heating ramp performed at 25°C.min⁻¹, the glass transition is slightly shifted towards higher temperatures (155 ± 2 °C). For both heating steps, no cold crystallization is measured, showing that the polymer has fully crystallized during the cooling step. Furthermore, the absence of cold crystallization at high cooling rate shows that the manufactured samples are stable and they will not undergo cold crystallization.

The melting temperature for both ramps is measured within the same ranges; however, for the second heating rate (2 °C.min⁻¹) two endothermic peaks are observed. This, lately, indicates the coexistence of two different crystalline structures in the polymer (Figure 16).

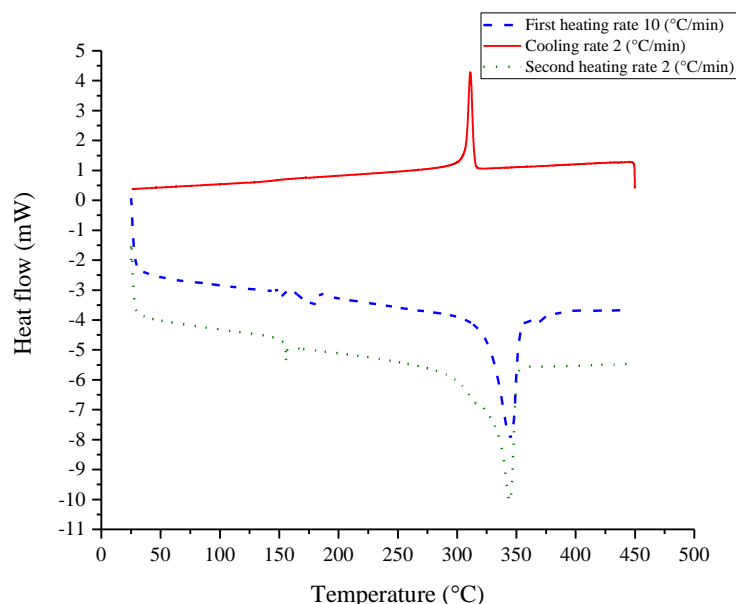


Figure 16: DSC curve of the PEEK 450G, sample undergoes 2 °C.min⁻¹ during the second heating cycle and 2 °C.min⁻¹ cooling rate

To a better quantification of the crystallization kinetics of PEEK, the thermograms for different cooling rates are represented in Figure 17. The enthalpy of crystallization and ratio of crystallinity for each cooling rate are reported in Table 4. By increasing the cooling rate, the peak of crystallization is shifted towards the glass transition. As an example, for the cooling rate of 2 °C.min⁻¹, the crystallization peak is close to 310 °C, while for the 25 °C.min⁻¹ the crystallization peak is at 275 °C. The results highlight the ability of PEEK to crystallize. Even at very high cooling rate, PEEK undergoes crystallization.

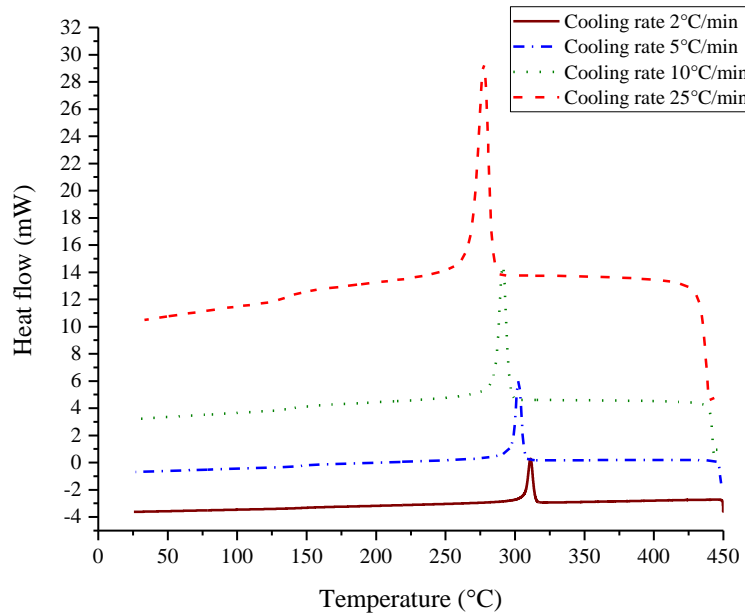


Figure 17: Cooling curve determined by DSC according to different cooling rates

For the cooling rate below $5\text{ }^{\circ}\text{C}\cdot\text{min}^{-1}$, the ratio of crystallinity remains at the maximum attainable value for PEEK, about 37 % close to the 40 % maximum ratio experimentally evidenced by Atkinson [102]. At $10\text{ }^{\circ}\text{C}\cdot\text{min}^{-1}$, it becomes $30\pm 1\%$ and at $25\text{ }^{\circ}\text{C}\cdot\text{min}^{-1}$, it decreases to 23 %. Obviously, to promote the crystallization of manufactured parts in PEEK, the cooling rate must be kept lower than $5\text{ }^{\circ}\text{C}\cdot\text{min}^{-1}$. Moreover, a slow cooling rate will benefit to the interdiffusion process. Before complete cooling of the manufactured parts, the macromolecules must have enough time to interdiffuse to create adhesion at the interface between the successive layers. Hence, the cooling rate of the PEEK during additive manufacturing must be minimized in order to allow motion of polymers, reorganization to entanglements in order to finally get the best adhesion. A thorough discussion of the interdiffusion times, related to the relaxation times are presented in the section 3.4.4.

Table 4: Value of crystallization for different cooling rates

Cooling rate ($^{\circ}\text{C}\cdot\text{min}^{-1}$)	Crystallization enthalpy ($\text{J}\cdot\text{g}^{-1}$)	Crystallization percentage (%)	Fusion enthalpy ($\text{J}\cdot\text{g}^{-1}$)	Fusion crystallization percentage (%)
2 ($^{\circ}\text{C}\cdot\text{min}^{-1}$)	44	34	48	38
5 ($^{\circ}\text{C}\cdot\text{min}^{-1}$)	43	33	44	34
10 ($^{\circ}\text{C}\cdot\text{min}^{-1}$)	41	31	38	30
25 ($^{\circ}\text{C}\cdot\text{min}^{-1}$)	41	31	30	23

2.1.3.2 Thermal transitions of PLA with DSC

In the previous section, we have studied the non-isothermal crystallization of PEEK by means of DSC. Hereby, we will study in the same way the crystallization of PLA.

PLA Natureplast PLI 005 in pellets form has been used for the experimental study. The filaments of PLA for 3D printers are formulated with additives to tune their properties. Nevertheless, we choose to work with a PLA as pure as possible for a better understanding of the phenomena. The density of PLA in its melted state is 1.25 g.cm^{-3} according to the technical datasheet provided by the manufacturer [126] [127]. Figure 18 represents the first step (heating until the melting temperature) and second step (fast cooling until room temperature without crystallization).

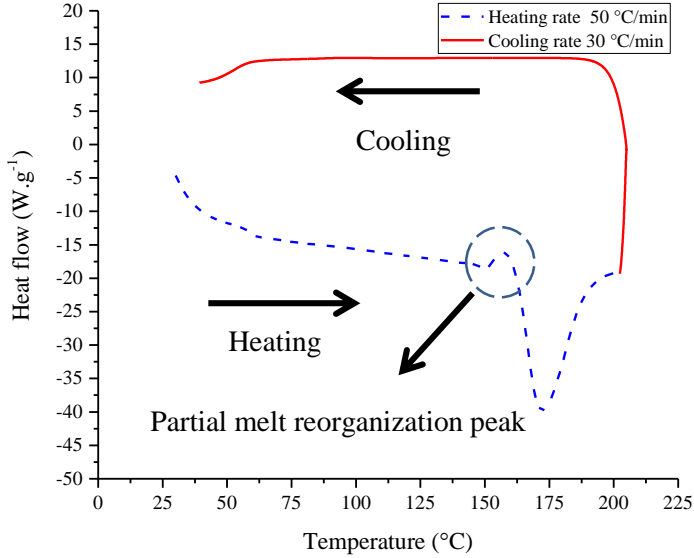


Figure 18: DSC curve of PLA at 30 °C.min^{-1} cooling rate

The results in Figure 18 show the glass transition of PLA at $70 \pm 3 \text{ °C}$. The 100 % melting enthalpy of PLA when it is entirely crystallized is 93 J.g^{-1} [128]. At the first heating step, at $150 \pm 3 \text{ °C}$, a peak corresponding to partial melting reorganization has been observed. The melting peak is observed at $175 \pm 1 \text{ °C}$. The melting enthalpy is $41 \pm 2 \text{ J.g}^{-1}$ which corresponds to 44 % of crystallinity. There is no crystallization during cooling from melting state to room temperature at 30 °C.min^{-1} .

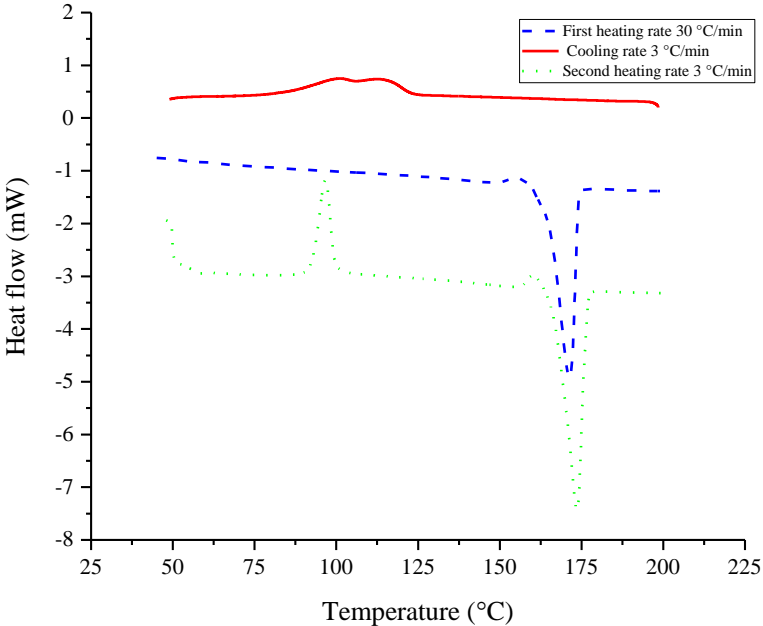


Figure 19: DSC curve of PLA at 3 °C.min^{-1} cooling rate

At low cooling rate of $3\text{ }^{\circ}\text{C}\cdot\text{min}^{-1}$ (Figure 19), PLA undergoes a crystallization broad peak between $107 \pm 3\text{ }^{\circ}\text{C}$ and $95 \pm 3\text{ }^{\circ}\text{C}$. The enthalpy of crystallization is $19 \pm 3\text{ J}\cdot\text{g}^{-1}$ which is about 19% of crystallization ratio. At the second heating rate, PLA presents two cold crystallization peaks. The existence of two cold crystallization peaks during the second heating shows that the crystallization of the PLA was not completed at this cooling rate. The first cold crystallization peak takes place between $93 \pm 2\text{ }^{\circ}\text{C}$ and $97 \pm 3\text{ }^{\circ}\text{C}$ with an enthalpy of $23 \pm 2\text{ J}\cdot\text{g}^{-1}$ corresponding to 25 % of crystallization ratio. The second cold crystallization peak takes place right exactly before the melting peak. The enthalpy of the second cold crystallization is $2 \pm 1\text{ J}\cdot\text{g}^{-1}$, corresponding to 2 % of crystallization ratio. The existence of two cold crystallization peaks for PLA shows that PLA has two different mechanisms of crystallization. The melting of the crystalline phases starts right after the second cold crystallization peak at about $162 \pm 2\text{ }^{\circ}\text{C}$ and ends around $180 \pm 3\text{ }^{\circ}\text{C}$. The melting peak takes place at $174 \pm 2\text{ }^{\circ}\text{C}$. At the second heating, the crystallization peak is shifted towards higher temperatures. The crystallization enthalpy during the second heating rate is $57 \pm 2\text{ J}\cdot\text{g}^{-1}$ which is 55 % of crystallization. The existence of the two crystalline phases in the PLA structure has been reported also in other studies for PLA [129] [130].

The results for PEEK and PLA show a faster crystallization kinetics for PEEK compared to PLA. In the case of PLA, the crystallization could be avoided in the FFF process by applying a high cooling rate while, in the case of PEEK, the polymers crystallize whatever the cooling rate. Practically, the cooling rate depends on the temperature of the melt polymer exiting from the nozzle, the temperature of the platform (substrate) and also the environment temperature. The crystallization kinetics is then depending on the variation of the temperature (ΔT) and also on the printing parameters (specially the feed rate). Decreasing the (ΔT) by increasing the platform temperature and the environment temperature increases the crystallization kinetics and the final crystalline ratio by decreasing the cooling rate. Consequently, in order to control the kinetics of crystallization, we have to control the ΔT .

Consequently, the determination of the crystallization kinetics in the FFF process for PEEK is necessary in order to control the properties of the manufactured parts by FFF. Moreover, the results for kinetics of crystallization of PEEK and PLA show the importance of controlling the cooling rate during the process for the PEEK, while the cooling rate does not highly influence on the crystallinity ratio for PLA. For all the reasons previously exposed, an in-depth study of the kinetics of crystallization of PEEK is necessary to assess the influence of the crystallization kinetics in the FFF process.

2.1.3.2 Fabrication and preparation of the testing samples

As it is mentioned previously, various characterization tests must be carried out on polymeric plate samples. These characterization tests are:

- Thermal properties: thermal conductivity, thermal expansion coefficient
- Surface tension
- Viscoelastic properties in liquid state

Consequently, in order to manufacture plates, an adequate fabrication process according to the polymer properties (crystallization kinetics and melting temperature) must be selected. To manufacture the PEEK plates, a hot compression press has been used. In hot compression press, the temperature and pressure applied on the specimens are controlled, as well as the heating and cooling rate of the sample. The hot compression press is from PEI Company. In order to decrease the surface roughness and protect the samples from any contamination, steel paper sheets were placed between the plateaus and the frame, as represented in Figure 20.

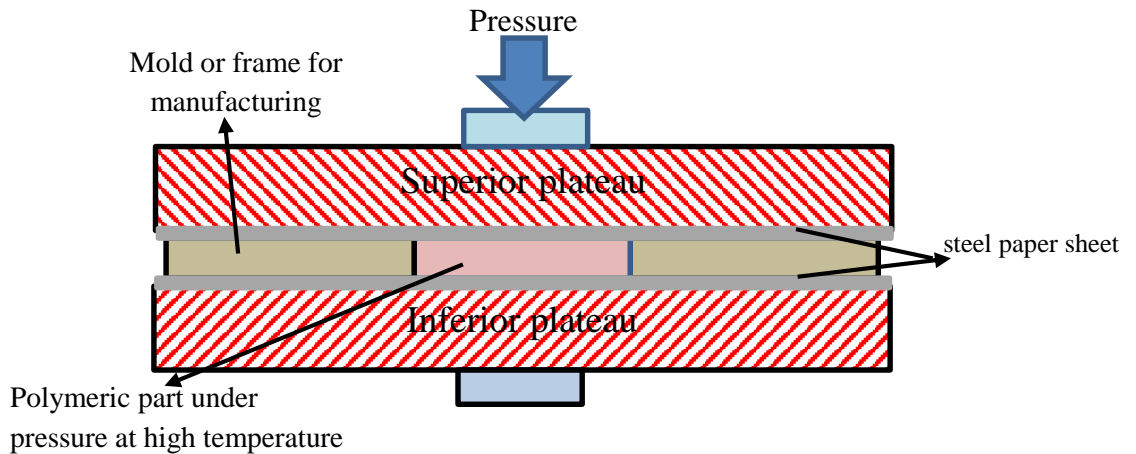


Figure 20: Schematic illustration of the hot compression press used to manufacture the polymeric plates

The process cycle is selected according to the properties of polymers such as melting, glass transition and crystallization temperatures. The process cycle used to manufacture the PEEK plates is represented in Figure 21.

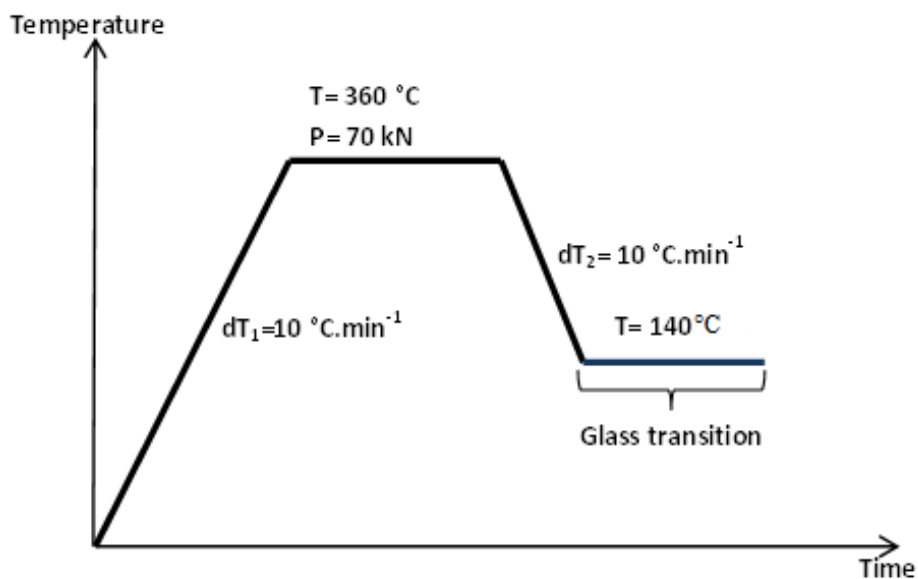


Figure 21: Processing conditions used to manufacture the plates by hot compression molding

The polymer initially in the form of pellets has been used as raw material. The pellets are placed in a $150 \times 75 \times 2 \text{ mm}^3$ mold (a metallic frame) and heated at $10 \text{ °C}\cdot\text{min}^{-1}$ until melting temperature (360 °C). In the second step, the plate is maintained at 360 °C with a pressure of 70 kN for 10 minutes. In the last step, the sample has been cooled down until 140 °C with a cooling rate of $10 \text{ °C}\cdot\text{min}^{-1}$. At 360 °C , the melting of all crystalline phases of the PEEK is completed. The cooling rate of the sample is selected in a manner to maximize the crystallization kinetics during the cooling phase. Finally, the samples are cooled down below glass transition (150 °C). The samples manufactured by the above mentioned procedure are thermally stable, meaning no cold crystallization would occur.

Contrary to PEEK, PLA has a relatively low melting temperature and low viscosity, thus we could manufacture the plate samples in a simple furnace. For that, the same compression principle represented

in Figure 20 was used. The pellets were heated higher than the melting temperature (200 °C) under 55 N ensured by calibrated masses. When the melting process is completed, the samples were taken out from the furnace and quenched to the room temperature. By using this procedure, we obtain fully amorphous PLA samples. The DSC curve of the PLA samples manufactured by hot compression molding is represented in Figure 22.

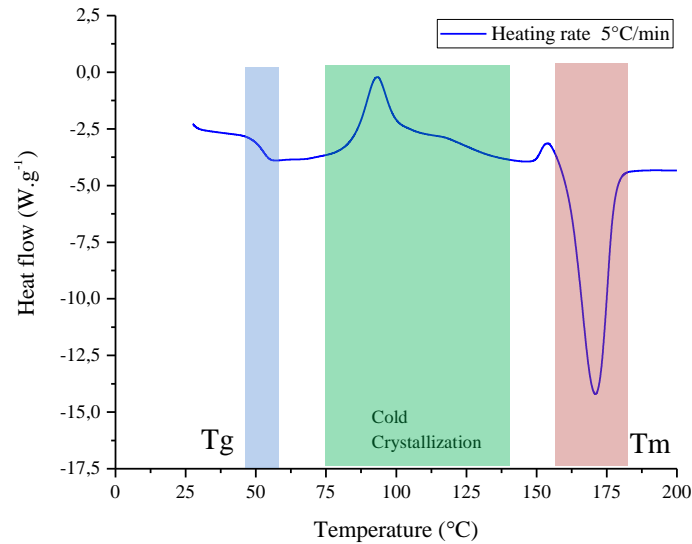


Figure 22: DSC curve of PLA sample manufactured by hot compression molding

The DSC results in the Figure 22 confirm that the PLA samples are quasi- amorphous. Indeed, after the glass transition, the polymer exhibits two cold crystallization peaks with an exothermic enthalpy of 43 J.g⁻¹. The endothermic melting enthalpy is measured 47 J.g⁻¹.

2.1.4 Other characterizations of PEEK

2.1.4.1 Thermal analyses

The thermal properties of PEEK are among the most important properties influencing the quality of the printed part. The cooling rate and the temperature distribution of printed part highly depend on the thermal properties. Furthermore, the temperature distribution and the cooling rate highly influence on the viscosity, the crystallization kinetics and the residual stresses of the printed part.

One of the main conventional problems between all types of additive manufacturing processes is the high thermal gradient along the manufactured parts. Indeed, because of the layer by layer manufacturing, the cooling rate and thermal gradient at different layers and different zones of the sample are different. This non-homogenous temperature distribution causes the internal and residual stresses, warpage and dimensional inaccuracy of the manufactured parts.

The determination of the expansion coefficient is necessary for modeling the dimensional change in the FFF process. The expansion coefficient of PEEK is determined with a TM7 Thermomechanical analyzer by Perkin-Elmer. The operational conditions of TMA analyzer are reported in Annex II.

The test is carried on under helium-controlled atmosphere in order to prevent oxidation of the sample. The sample is heated from 25 °C to 290 °C with a heating rate of 3 °C.min⁻¹ and a cooling rate of 2 °C.min⁻¹ and 7 °C.min⁻¹. The dimensions of the samples are 1.8 x 7.1 x 7.1 mm in height x thickness x width, respectively to ensure that the expansion is mainly effective in all directions. The force applied by the probe on the sample is 20 mN to maintain the contact. The samples were fully crystallized before

the tests in order to reduce the influence of crystallization on the TMA results. Furthermore, this method is suitable for the determination of the thermal expansion below the melting temperature. Consequently, the test were carried out from room temperature up to 290 °C to ensure the samples do not melt.

As it is represented in Figure 23, the thermal expansion is determined for two different cooling rates.

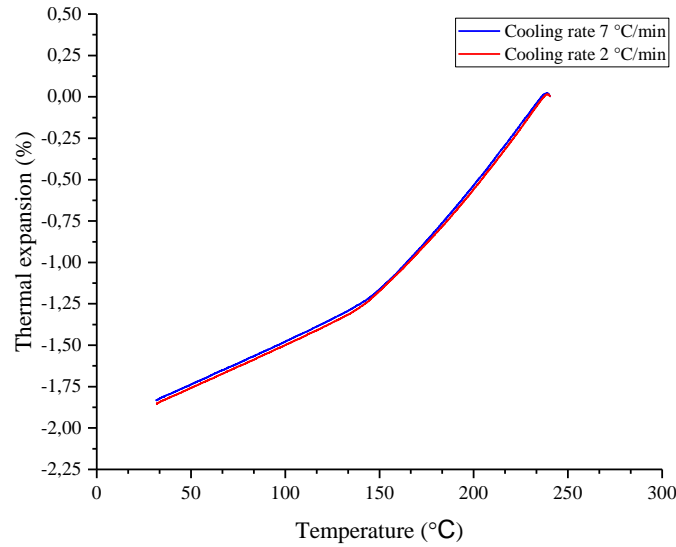


Figure 23: Thermal expansion of PEEK 450G versus temperature during heating and cooling at different rates

The values of the coefficient of thermal expansion are determined by eq. 18 and they are gathered in Table 5.

$$\alpha = \frac{l(T) - l_0}{l_0 * T} = \frac{\epsilon_{Therm}}{T} \quad \text{eq. 18}$$

Where α is the thermal coefficient of expansion, l_0 is the initial length of the sample, $l(T)$ is the length at temperature T and ϵ_{Therm} is the thermal induced strain during the temperature variation.

Table 5: Coefficient of thermal expansion

Cooling rate	CTE - Zone 1 ($\times 1.10^{-6}$) K^{-1}	CTE - Zone 2 ($\times 1.10^{-6}$) K^{-1}
2°C.min⁻¹	59 ± 2	162 ± 1
7°C.min⁻¹	62 ± 2	161 ± 1

The thermal expansion coefficient after the glass transition between 150 °C and 155 °C is about three times greater than its value before the glass transition. Then, during layer by layer manufacturing, the drastic change of the value of the thermal expansion coefficient of PEEK around the glass transition strongly reduces the macromolecular mobility, so causes the internal and residual stresses, warpage at different layers and different zones of the printed parts.

Even if the cooling rate does not seem to influence the thermal expansion (Figure 23), other authors [124] have observed its effect on the residual deformation. At high cooling rate, the majority of the materials and specially the polymers undergo residual stress. Indeed, long chains of the polymer at melted state are in the equilibrium state. The chains in the amorphous state are randomly oriented. While

the solidification occurs, the chains have the tendency to reorganize into crystalline shape. If the polymer solidifies rapidly, the polymer chains could not be reorganized and consequently, flow-induced residual stress occurs. A lower cooling rate results in a lower residual deformation. Consequently, in order to reduce the residual stresses and further deformations, the cooling rate of the deposited beads must be as slow as possible.

Moreover, the deposition of the polymer on the build platform acts as rapid quenching of the polymer during printing. Indeed, the first deposited layers onto the build platform cool rapidly while the following deposited layers are still at high temperature. The temperature gradient causes high residual stresses on the printed parts. Consequently, the manufactured parts undergo warpage and shrinkage because of the thermal gradient.

Then, the thermal conductivity and thermal diffusivity of PEEK must be determined to supplement the analysis of the thermal expansion coefficient. The relation between the thermal diffusivity and the thermal conductivity is represented in eq. 19.

$$\alpha = \left(\frac{k}{\rho C_p} \right) \quad \text{eq. 19}$$

k is the thermal conductivity, ρ is the density and C_p is the heat capacity of PEEK. The thermal conductivity and thermal diffusivity have been determined using a Hot Disk TPS 2500S. The operational conditions of the Hot disk are reported in Annex II.

Lamethe [131] has used the flash method in order to determine the thermal diffusivity of PEEK. In the flash technique, one surface of a sample with slab geometry is illuminated with a pulse of radiant energy, and the subsequent temperature transient is recorded at the opposite surface [132]. Using flash method, we could determine the thermal diffusivity, heat capacity, and thermal conductivity. Our results for the thermal diffusivity and thermal conductivity of the PEEK are represented in Figure 24 and Figure 25 respectively with the comparison to the literature.

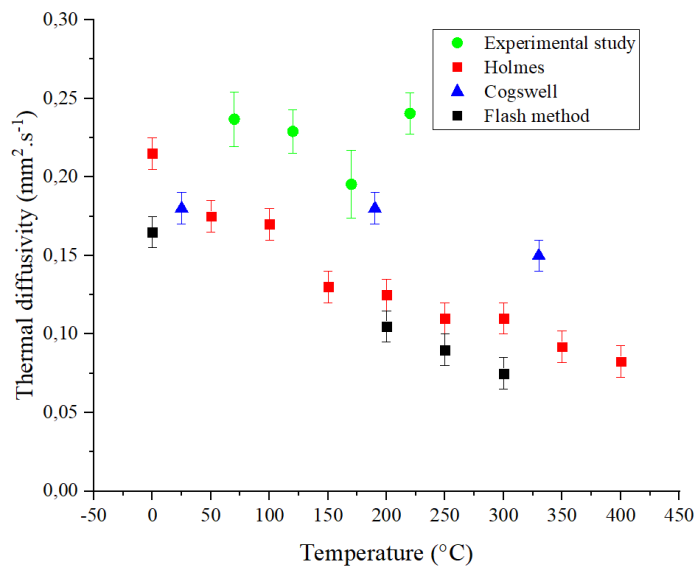


Figure 24: Thermal diffusivity determined by experimental study and comparison with existing works [131]

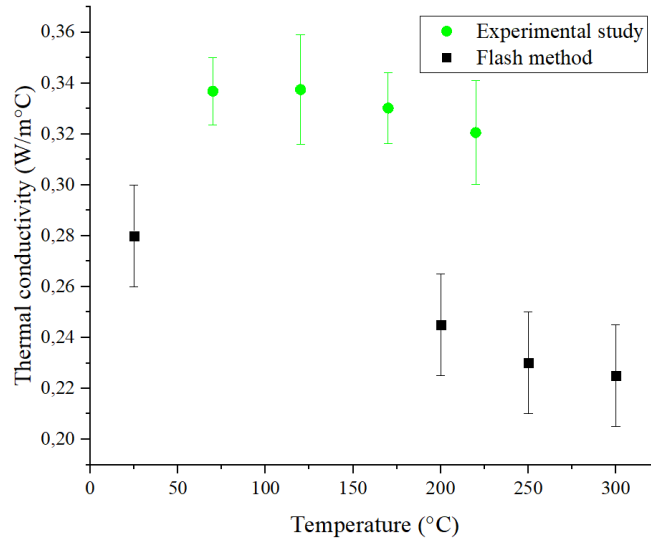


Figure 25: Thermal conductivity determined by Hot disc apparatus and flash method

The thermal diffusivity decreases while the temperature increases. This is in good agreement with the previous studies on the thermal diffusivity of PEEK. However, there is a wide dispersion. The variation of the results for different studies could be due to the different grades of PEEK, different crystallization ratios, different measuring methodologies and surface roughness.

The thermal conductivity is calculated from the thermal diffusivity by using eq. 19. According to Lamethe [131], the thermal conductivity reduces from $0.28 \text{ W} \cdot (\text{m} \cdot \text{K})^{-1}$ at $25 \text{ }^\circ\text{C}$ to 0.22 at $300 \text{ }^\circ\text{C}$. That represents about 20 % reduction from the initial value. Contrary to Lamethe, our measurement by Hot disk method indicate that the variation of the thermal conductivity according to temperature is very small which could be neglected.

Furthermore, Lamethe [131] has determined the specific heat from the melting temperature up to the room temperature by using MDSC (Modular Differential scanning calorimeter) Lamethe and Cogswell shown that the specific heat capacity of PEEK is temperature dependent and it follows a linear fonction represented in eq. 20.

$$C_p \left(\frac{\text{J}}{\text{kg} \cdot ^\circ\text{C}} \right) = 2.5 T(^{\circ}\text{C}) + 1250 \quad \text{eq. 20}$$

Furthermore, eq. 20 shows that increasing the temperature leads to linear increase of the heat capacity and also Figure 23 shows that increasing the temperature decreases the density of PEEK by increasing the thermal expansion. Considering both density and heat capacity are the denominator of the thermal diffusivity (eq. 19), the heat capacity is the most influential parameter on the thermal diffusivity of PEEK.

As a summary, the thermal conductivity of the solid PEEK at room temperature is $0.32 \text{ W} \cdot (\text{m} \cdot \text{K})^{-1}$. The thermal diffusivity of PEEK at room temperature is about $0.24 \text{ mm}^2 \cdot \text{s}^{-1}$. Contrary to the thermal conductivity, the thermal diffusivity decreases while the temperature increases. The thermal diffusivity of semi-crystalline polymers also depends on its crystalline rate. We have shown in the Figure 15 that our samples are fully crystallized: It means that there is no further variation of the crystalline rate in our samples during the test.

2.1.4.2 Surface tension

In order to determine the surface tension of PEEK and PLA in the solid state and at the ambient temperature, a GBX DigiDrop contact angle meter has been used.

For solid PEEK at room temperature, the surface tension is $38.7 \pm 3 \text{ mN.m}^{-1}$ with 35.1 mN.m^{-1} and 3.6 mN.m^{-1} for the dispersing and polar components respectively. The surface tension of PLA at room temperature is $42.1 \pm 3 \text{ mN.m}^{-1}$ with 38.2 mN.m^{-1} for the dispersing component and 3.9 mN.m^{-1} for the polar component. The higher surface tension of PLA shows that PLA would have more tendency to coalesce with the adjacent polymer and beads in FFF process than PEEK.

The sessile drop method is a suitable method for determining the surface tension of the polymers at solid state and ambient temperature. The coalescence in the FFF process takes place when the polymer is at the melted state or at high temperature. However, the majority of the available methods for the determination of the surface tension is suitable for the solid state and room temperature. On the other hand, it is reported that the surface tension of the polymers changes according to the temperature, the chemical and physical state of the polymer, to reach up to 50 % of the initial value of the surface tension at room temperature [121]. Here in our laboratory, we do not have suitable apparatus in order to determine the surface tension at melted state. However, in order to determine the surface tension at the temperature above room temperature and also at melted state for the polymers, we have contacted external colleagues (Benoit Duchemin, research engineer, LOMC UMR CNRS 6294 at Université du Havre) who are able to determine the surface tension in the melted state.

The method used to determine the surface tension at melted state is based on the deposition of the melted polymer on a substrate with known surface tension. The apparatus used in this method is a tensiometer equipped with a syringe and a camera to measure the profile of the droplet or the contact angle of a droplet on a substrate. The operational conditions of the apparatuses used for determination of surface tension are explained in Annex II. In our study we have selected glass slides, stainless steel and Teflon plates as the deposition substrates. The surface tension of PLA at melted state at $200 \text{ }^\circ\text{C}$ has been measured at $27 \pm 3.2 \text{ mN.m}^{-1}$.

However, this method has its limitation: this method is suitable for the polymers with a viscosity less than about 800 Pa.s . Furthermore, we could not use this method for the polymers with higher melting temperature. PEEK has high melting temperature (about $340 \text{ }^\circ\text{C}$) and its viscosity is relatively high comparing to PLA and other polymers. Consequently, we could not use the above-mentioned method for PEEK.

For this reason, we have to find another method to determine or approximate the surface tension of PEEK at melting point. For this purpose, we use the Parachor equation to approximate the surface tension at the melted state. eq. 21 shows the Parachor model which have been used to estimate the surface tension at high temperatures [133].

$$\gamma = \left(\frac{P_s}{V} \right)^4 \quad \text{eq. 21}$$

Where V is the molar volume, P_s is the molecular Parachor, M is molecular weight and ρ is the density.

$$V = \frac{M}{\rho} \quad \text{eq. 22}$$

The molecular Parachor P_s is an additive, constitutive, property of the material [134]. The molecular Parachor is independent from the temperature [133]. Thus, we could determine P_s from the surface tension of the polymer at solid state and room temperature. By the determination of the molecular Parachor at room temperature, and considering that, mass, molecular weight and molecular Parachor are independent from the temperature, we could determine the variation of the surface tension from the variation of the density.

In the first step, we will compare the results obtained by experimental study and the Parachor equation for PLA. The results for surface tension of PLA and PEEK determined by the Parachor equation are presented in Table 6.

Table 6: Obtained values for the surface tension of PLA and PEEK by using the Parachor equation

Polymer	Molecular weight (g.mol ⁻¹)	Density (g.cm ⁻³)	Molar volume (cm ³ .mol)	Molecular Parachor	Surface tension (mN.m ⁻¹)
PLA	72	1.27	57.2	145.7	25±3 (150°C)
PEEK	288.31	1.3	221.77	551.2	18±3 (360 °C)

The comparison of the experimental results and predicted results by the Parachor equation for PLA shows that, the predicted value is close to the experimental value, respectively 25±3 mN.m⁻¹ at 150 °C and 27 ± 3.2 mN.m⁻¹ at 200 °C. Considering that the Parachor equation agrees well with the experimental results, the Parachor equation will be used to approximate the surface tension of PEEK in the melted state.

2.1.4.3 Thermomechanical analyses in dynamic mode

The viscoelastic behavior of the polymer highly influences on the printability and quality of the parts manufactured with PEEK. The coalescence and bonding of the deposited beads are driven by the viscosity and the surface tension. A deep understanding of the viscoelastic behavior of PEEK is a step towards the improvement of the manufacturability of PEEK in the FFF process.

The complex viscosity of PEEK as a function of frequency has been studied by parallel-plate rheometry (Figure 26) in viscoelastic linear regime. The tests have carried out with an A.R.E.S rheometer from Rheometrics under air flow condition in melted state for PLA and PEEK.

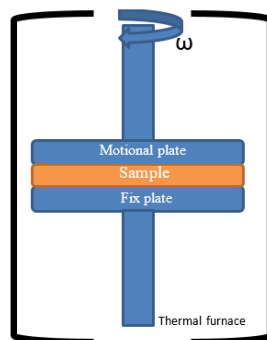


Figure 26: Schematic representation of the parallel plate configuration

The rheometry in dynamic mode is a precious tool to understand the macromolecular dynamics. In the melted state, thermomechanical shear analyses have been carried out. The tests performed at 1 rad.s⁻¹, from 340 °C to 400 °C at 3 °C.min⁻¹ at 0.40 ± 0.01 % applied strain. A 25 mm diameter disk is used for the parallel-plate configuration test. The gap between the two plates is 2 mm.

In dynamic shear mode, the elastic and viscous behavior of the fluid can be separated in the shear elastic/storage modulus G' and the shear viscous/loss modulus G'' (eq. 23). The loss factor is defined as the ratio between G'' and G' (eq. 24). The complex viscosity is calculated from G' and G'' by eq. 25:

$$G^* = G' + iG'' \quad \text{eq. 23}$$

$$\text{Tan}\delta = \frac{G''}{G'} \quad \text{eq. 24}$$

$$\eta^* = \frac{\sqrt{G'^2 + G''^2}}{\omega} \quad \text{eq. 25}$$

2.1.4.4 Frequency sweep tests in oscillatory parallel-plate configuration

The frequency sweep tests at different temperatures were performed by using parallel-plate configuration. The tests were carried out for the frequency range from 0.05 to 100 $\text{rad}\cdot\text{s}^{-1}$ at 1% strain, for four different temperatures: 350 °C, 366 °C, 383 °C, and 400 °C.

As it has been mentioned previously, prior to the frequency test, strain sweeps have been carried out in order to define the linear viscoelastic domain of PEEK at each temperature. As it is represented in Figure 27, at 1 % strain for 383 °C, the loss modulus which is the most suitable parameter in melt state is still within the linear viscoelastic domain. Consequently, for the determination of the complex viscosity at 383 °C, no further correction is needed.

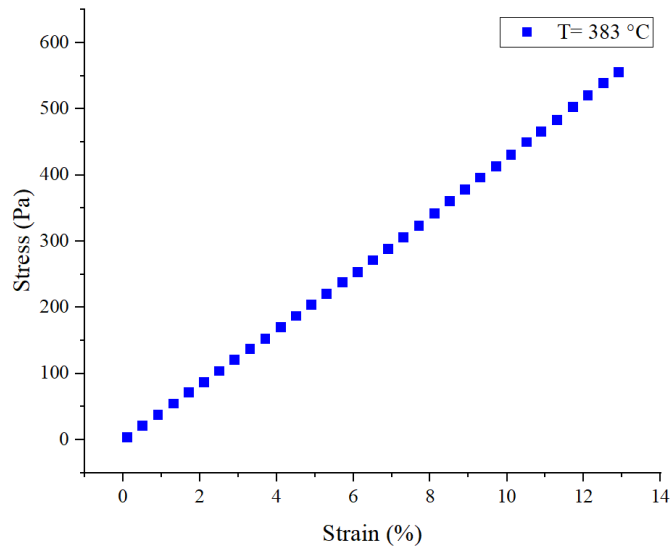


Figure 27: Stress-strain curve in linear domain for PEEK at 383°C determined by strain sweep test

As expected for melted polymers, PEEK demonstrates a shear-thinning behavior with a Newtonian plateau at the lowest frequencies as it is presented in Figure 28. The complex viscosity at 1 $\text{rad}\cdot\text{s}^{-1}$ is 5841 Pa.s at 350 °C, 5144 Pa.s at 366 °C, 4413 Pa.s at 383 °C and finally 3292 Pa.s at 400 °C. The results for different temperatures show that increasing the temperature leads to decrease the viscosity. By increasing the frequency, the viscosity of PEEK decreases. For high temperature and low frequency, the viscosity of PEEK increases drastically. For the highest temperatures, the molecular chains of PEEK undergo recombination of molecular bond degradation and chain branching [135]. This structural modification has consequences on the properties of the polymer when the polymer is exposed at high

temperatures for a long time (hereby for frequencies below 0.1 Hz). Figure 28 shows the results of PEEK for the frequency sweep tests at different temperatures.

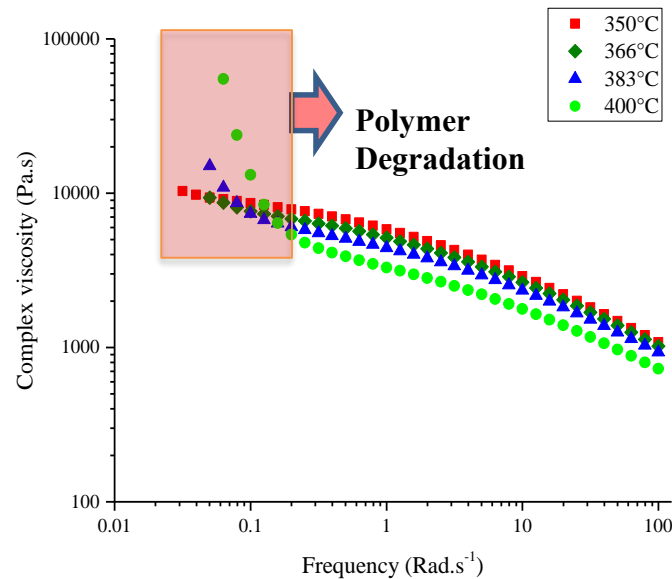


Figure 28: Complex viscosity (η^*) of the PEEK determined by the parallel-plate configuration

In the polymer processing, in order to prevent polymer degradation, the time of exposure at high temperature must be reduced. However, in the case of the FFF process, maintaining the polymer melted above the melting temperature during deposition, promotes the coalescence and bonding of deposited beads. A better coalescence and bonding would increase the mechanical resistance.

In order to increase the bonding and interdiffusion of the deposited layers, it is preferable to select the processing temperature well above the melting temperature where all the crystalline phase is melted. This is mainly because the existing crystalline phase in the polymer act like barriers for interdiffusion of the macromolecular chains in the deposited beads. An insufficient interdiffusion between the layers would cause cracks (or separation between the layers) in the printed parts.

PEEK is a semi-crystalline polymer, in which the melting takes place above 340 °C. In order to make sure that the melting is completed, the printing must be carried out above 350 °C. On the other hand, the polymer degradation appears above 400 °C. Consequently, the printing range must be a compromise between 350°C and slightly above to get the best performances for the printed parts.

When choosing the processing temperature, the printing frequency should be considered. Indeed, as the temperature increases, the polymer becomes more sensitive to the thermal degradation, but at low frequency, the same occurs. As an example, at 400 °C, PEEK undergoes thermal degradation at the frequency below 1.2 Hz, while at 350 °C the polymer degradation starts at frequency below 0.04 Hz. The frequency is equivalent to the shear rate, which is related to the printing velocity in the FFF process. At higher processing temperatures, the degradation frequency shifts towards higher frequencies, thus, we could increase the temperature until the frequency is above the degradation frequency. The printing shear rate for Reprap printers depends on the nozzle diameter of the liquefier. By increasing the nozzle diameter, the printing shear rate decreases. However, the value of the printing shear rate for Reprap printers and conventional nozzle diameters is not less than 30 s⁻¹ [136].

Similarly to PEEK, we have studied the thermomechanical properties of PLA. The study of the rheological properties of PLA could help us to compare PLA and PEEK properly.

The thermomechanical tests on PLA have been carried out at the temperatures above its melting temperature from 175 °C to 220 °C from 0.5 Hz to 100 Hz with 5% applied strain. The results for complex viscosity of PLA at different temperatures are presented in Figure 29.

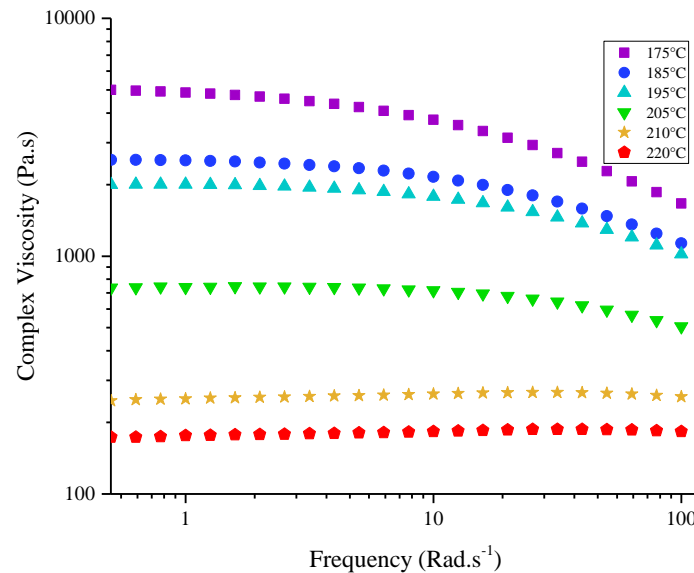


Figure 29: Complex viscosity of PLA at different temperatures

As expected, PLA demonstrates a shear-thinning behavior. Furthermore, at high temperature, for instance at 220 °C, the viscosity becomes linear versus frequency. At high temperature, the influence of the shear rate on the viscosity is negligible. Moreover, at lower frequency, the viscosity decreases. This is mainly because of the degradation of the polymer at high temperature and low frequency. These results show the sensitivity of PLA at these temperatures. At 185 °C, the viscosity at 0.5 Hz is 2500-3000 Pa.s. At higher temperatures, the viscosity at the same frequency is reduced to about 100-200 Pa.s.

The mechanism of polymer degradation for PLA is different than for PEEK: polymeric chain breakage occurs when exposed at high temperature. This mechanism leads to reduce the viscosity at low frequency [137]. In opposite to PLA, for PEEK, the macromolecular chains undergo recombination of molecular bond degradation and chain branching, which causes drastic increase of the viscosity at low frequency [138]. The comparison of the viscosity of PEEK and PLA shows that, PEEK has much higher viscosity than PLA. Furthermore, the shear rate has much influence on the viscosity of PEEK than PLA. For PEEK, the viscosity reduces up to 90 % of the initial value from 0.3 Hz to 100 Hz, while in the case of PLA, the influence of the shear rate on the viscosity is negligible. This lately shows that, controlling the shear rate during 3D printing of PEEK is crucial. The lower viscosity of PLA compared to PEEK shows that the printability of PLA is easier than for PEEK. Furthermore, the interdiffusion and coalescence kinetics of the deposited beads would be faster for PLA than for PEEK.

To sum up, the polymer degradation highlights the importance of controlling the shear rate and temperature during printing in the FFF process.

2.2 Coalescence study

2.2.1 Analytical study of coalescence

Bonding by coalescence of two nearby beads is the main process influencing the mechanical properties of the parts fabricated by FFF. Indeed, a good coalescence between the deposited beads reduces the porosity rate in the manufactured parts and increases the bonding of two deposited beads, then the structural cohesion of the parts.

There are several models to describe the coalescence of particles. Initially, these models were developed for ceramics and metals sintering, such as in SLS processes. As it is represented in Figure 30, the sintering of two particles consists of different stages [56]:

- The particles adhere to each other (a).
- A neck is formed but the particles remain as individuals.
- The neck between the particles keeps growing, as the densification develops, the particles lose their identity (b).

The first bonding model for crystalline structure and sintering of two spheres was proposed by Frankel [139][57]. Frankel assumed the particle radius to be constant. Frankel's model is based on the balance of the work or surface tension and the viscous dissipation. All other forces, including gravity or applied stresses, are neglected. Frankel has explained that sintering and coalescence takes place because of viscous flow under the effect of surface tension. Later, several bonding models were proposed to determine the coalescence of different materials such as ceramics and metals, the majority of these models are not applicable for thermoplastics. Therefore, Frankel's model was modified by Vlachopoulos [56] [140]. This model is based on the surface tension and viscous forces. This model developed for the sintering of thermoplastics looks the most suitable for the FFF process. The main difference between the Frankel's sintering model and modified Frankel's model is the approximation for small angles ($\cos(\theta) = 1 - \frac{\theta^2}{2}$).

The modified Frankel's model has been originally developed for the coalescence of spheres. Nevertheless, it has been applied to predict the coalescence of filaments of amorphous thermoplastics, such as ABS (Acrylonitrile Butadiene Styrene) by Bellehumeur in 2004 [141]. Bellehumeur has applied the sintering model to ABS cylinders of 0.47 mm diameter and 0.3 mm thickness. The modified Frankel's model applied by Bellehumeur is represented by eq. 26.

$$\theta' = \frac{\gamma}{\mu(T)a_0} \frac{2^{-\frac{5}{3}} \sin \theta \cos \theta (2 - \cos \theta)^{\frac{1}{3}}}{(1 - \cos \theta)(1 + \cos \theta)^{\frac{1}{3}}} \quad \text{eq. 26}$$

In which θ' is the rate of angle evolution with time, γ is the surface tension, a_0 is the initial radius of the particle (in our case radius of filament), μ is the viscosity depending on several parameters such as temperature and shear rate (in the case of our coalescence study depends only on temperature), θ is the angle between intersecting lines between the center and neck of the coalescence. The initial value for the angle between the two spheres (θ) is zero.

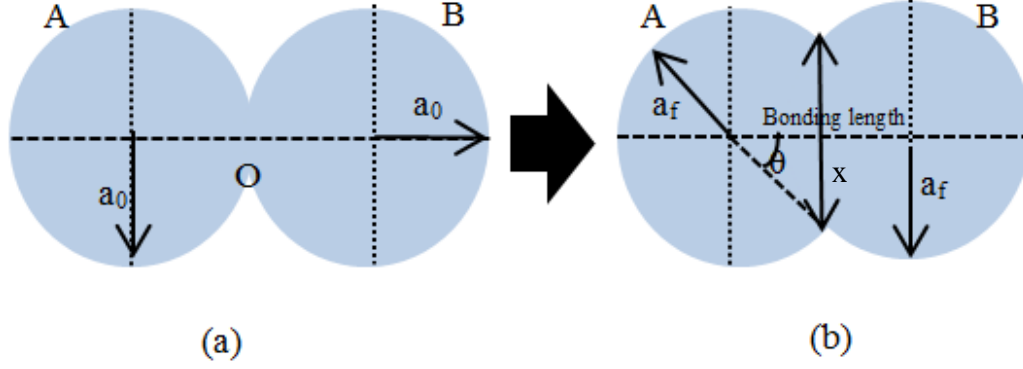


Figure 30: Schematic representation of the coalescence of two particles a) Initial state before coalescence b) Filaments undergoing bonding by coalescence [47]

Solving eq. 26 leads to eq. 27:

$$\theta(t) = \left(\frac{\gamma \cdot t}{\mu \cdot a_0} \right)^{\frac{1}{2}} \quad \text{eq. 27}$$

Where t is the time. The evolution of the sintering neck radius with time is given by eq. 28.

$$\sin(\theta) = \frac{x}{a} \quad \text{eq. 28}$$

eq. 26 must be initiated at a positive and finite value to prevent numerical instability. Because eq. 26 and eq. 27 are ordinary differential equations (ODE), they cannot be solved analytically. For solving eq. 26 and also eq. 27 which are unstable on $\theta = 0$, we will use the 4th order Runge-Kutta method [140]. eq. 29 to eq. 34 show the series of Runge-Kutta which has been used to solve the eq. 26 .

$$\theta_{i+1} = \theta_i + \frac{1}{6} \Delta t (k_1 + 2k_2 + 2k_3 + k_4) \quad \text{eq. 29}$$

$$t_{i+1} = t_i + \Delta t \quad \text{eq. 30}$$

$$k_1 = f(t_i, \theta_i) \quad \text{eq. 31}$$

$$k_2 = f\left(t_i + \frac{1}{2} \Delta t, \theta_i + \frac{1}{2} \Delta t k_1\right) \quad \text{eq. 32}$$

$$k_3 = f\left(t_i + \frac{1}{2} \Delta t, \theta_i + \frac{1}{2} \Delta t k_2\right) \quad \text{eq. 33}$$

$$k_4 = f(t_i + \Delta t, \theta_i + \Delta t k_3) \quad \text{eq. 34}$$

The temperature effect is represented by the viscosity and the surface tension which are temperature dependent terms in eq. 26 and eq. 27.

In our study, because in a real case of the FFF process, heat transfer into a filament must be considered at all stage of the process, the temperature dependency of viscosity and surface tension is applied to the eq. 26 in order to take it into account in the model.

2.2.2 Numerical simulation of the coalescence phenomenon

2.2.2.1 Theoretical basis

The CFD (Computational Fluid Dynamic) is widely used in numerical simulation in order to solve the fluid flow problems. With CFD, we are able to determine the interaction of the fluids by considering the boundary conditions and environment.

However, sometimes one phase flow CFD is not sufficient to solve the complex problems. In the cases where another phase influences on the system and there is more than one phase in the system, simple CFD is unable to solve the problem. As an example, we could mention the coalescence as a real problem which could not be solved simply by the one phase flow CFD problem.

Consequently, an additional equation must be added to the CFD module to solve these complex systems. These additional equations could help to track the interface of several fluids (for example polymer and air in the case of coalescence). Tracking the interface of the fluids could be done with different methods such as:

- Two-phase flow Level set
- Two-phase flow Phase field
- Two-phase flow moving mesh (ALE)
- The volume of fluid (VOF)

By adding these two-phase flow (TPF) equations to CFD, we are able to track the interface of two immiscible fluids and follow the interaction of this fluids. Level-set (LS) and Phase field (PF) are the most used approaches to track the interface of two fluids or three fluids (PF).

While the level set and phase field methods are solved on a fixed mesh, the two-phase flow moving mesh method tracks the interface position with a moving mesh using the arbitrary Lagrangian-Eulerian ALE method.

In our studies, we use the Two-phase flow (TPF), module of COMSOL Multiphysics in order to study the coalescence and the material deposition on the substrate. In the following section, we will explain briefly the Navier-Stokes equations which are used in the CFD simulation and also LS and PF series which are used for tracking the interface of the two phases.

2.2.2.2 Navier-Stockes equations

In the CFD numerical simulation and also TPF simulations for each phase, Navier-Stokes and continuity equations are solved for the conservation of the momentum and conservation of mass [77].

eq. 35 shows the general form of the Navier-Stokes equation.

$$\underbrace{\rho \frac{\partial \mathbf{u}}{\partial t} + \rho(\mathbf{u} \cdot \nabla) \mathbf{u}}_1 = \nabla \cdot \left[\underbrace{-p \mathbf{I}}_2 + \underbrace{\mu(T)(\nabla \mathbf{u} + (\nabla \mathbf{u})^T) - \frac{2}{3} \mu(T)(\nabla \cdot \mathbf{u}) \mathbf{I}}_3 \right] + \underbrace{\rho \mathbf{g} + \mathbf{F}_{st} + \mathbf{F}}_4 \quad \text{eq. 35}$$

Where ρ is the density, u is the fluid velocity, P is the pressure applied to the fluid, μ is the dynamic viscosity of the fluid and g is the gravity field. F_{st} represents the force resulting from the surface tension and F represents all other external forces. The Navier-Stokes equations correspond to the contribution of different forces applied to the fluid: The first part of

eq. 35, (1) refers to inertial forces of the fluid. The influence of the pressure forces by the terms (2) and viscous forces are integrated into the equation by the terms (3). And the last part (4) is the sum of other external forces applied to the fluid. Mass conservation in the study is solved by the continuity equation (eq.10):

$$\frac{\partial \rho}{\partial t} + \nabla \cdot (\rho u) = 0 \quad \text{eq. 36}$$

eq. 37 shows the equation to determine the Reynolds number. The Reynolds number corresponds to the ratio of inertial forces (1) to viscous forces (3). It measures how turbulent the flow is. For a low Reynolds number, the flow is laminar, while for a higher Reynolds number, the flow is turbulent and for a really low Reynolds number, the inertia term, $\rho(u \cdot \nabla)u$, can be neglected and the Navier-Stokes equation become a Stokes equation (eq. 39). In our case, the Reynolds number is below 0.001 and effectively low enough to use the Stokes equation.

$$Re = \frac{\rho UL}{\mu} \quad \text{eq. 37}$$

In the case of coalescence and material deposition, the fluid could be considered as incompressible, thus the continuity equation (eq. 36) yields to eq. 38:

$$\nabla \cdot u = 0 \quad \text{eq. 38}$$

Because of the divergence of the velocity is equal to zero (linked to the incompressibility), consequently we could also omit $-\frac{2}{3}\mu(\nabla \cdot u)I$ term in the Navier-Stokes equation. Finally, the Stokes equation is used in our study as eq. 39:

$$\rho \frac{\partial u}{\partial t} = \nabla \cdot [-pI + \mu(T)(\nabla u + (\nabla u)^T)] + \rho g + F_{st} + F \quad \text{eq. 39}$$

In the eq. 39, the influence of the surface tension on the fluid flow is determined by using eq. 40 :

$$F_{st} = \sigma H \delta n_i \quad \text{eq. 40}$$

Where σ is surface tension, H is mean curvature, δ is Dirac function and n_i is the normal vector. Mean curvature H is described as:

$$H = \frac{1}{2}(k_1 + k_2) \quad \text{eq. 41}$$

Where k_1 and k_2 are the maximum and minimum curvatures of a surface. For the sphere and cylinder, the mean curvature is determined by eq. 42 and eq. 43 respectively:

$$H = \frac{1}{a} \quad \text{eq. 42}$$

$$H = \frac{1}{2a} \quad \text{eq. 43}$$

Where a is the radius.

In two-phase flow simulation (TPF), the density and the viscosity of each mesh are determined using eq. 44 and eq. 45 according to the volume fraction.

$$\rho = \varphi \rho_{polymer} + (1 - \varphi) \rho_{air} \quad \text{eq. 44}$$

$$\mu = \varphi \mu_{polymer} + (1 - \varphi) \mu_{air} \quad \text{eq. 45}$$

Where $\rho_{polymer}$ and ρ_{air} are the densities of polymer and air respectively, $\mu_{polymer}$ and μ_{air} are the viscosities of the polymer and air respectively and φ is the volume fraction of the volume considered. The volume fraction is one of the outputs of TPF simulation which is used for determining the position of the interface of the two phases. The value of the volume fraction for LS equation varies from 0 to 1. The volume fraction in TPF is $\varphi = 0$ for air (or phase 1) and $\varphi = 1$ for polymer (or phase 2). That means when the value of φ is 1 (or the color is red) the mesh or the domain is filled by polymer and when the value of the volume fraction is 0 (or the color is blue) the domain is filled by air.

2.2.2.2 LS, PF and VOF methods

LS and PF methods are two well-known equations to track the interface of two immiscible fluids. LS and PF methods are two transport equations. These equations are added to Stokes equations (eq. 38 and eq. 39) in order to track the interface of two immiscible fluids.

The main difference between the LS method and PF is that LS solves a transport equation in order to track the interface, while PF solves two transport equations. For the LS study, the color function varies between 0 and 1, while for the PF the color function is between -1 and 1. In these functions, the interface of the two fluids could be considered at 0 and 0.5 for PF and LS respectively. Figure 31 shows different notions in the two-phase flow. Normally, in the numerical simulation, solving two transport equations by PF method makes the calculation heavier than LS; however, the PF method is more accurate than the LS method. While the LS method is suitable for up to two-phase simulation, PF method could solve three phase problems. Moreover, the PF method could be used for structure interaction and phase separation simulations and is more recommended for micro-fluidic simulation [142]. Furthermore, in several articles, the comparison of the LS method with other interface tracking methods shows that during the numerical simulation of water collision on the surface by LS equation, there is mass dissipation [143]. This method is not conservative.

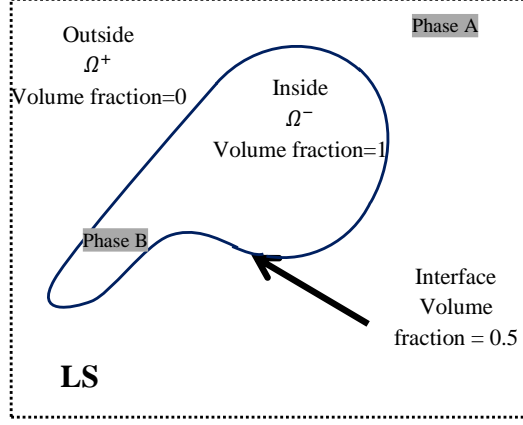


Figure 31: presentation of different phases in two-phase flow simulation by LS

Considering the closed curve as $\alpha(t)$, enclosing Ω in Ω region, moving in two dimensions, the interface of the two phases for LS equation is defined as:

$$\alpha = \{x \in \Omega | \phi(x, t) = 0.5\} \quad \text{eq. 46}$$

The LS equation which is used in TPF simulation is represented in eq. 47.

$$\frac{\partial \phi}{\partial t} + \nabla \cdot (u\phi) = \gamma \nabla \cdot \left(\varepsilon_{ls} \nabla \phi - \phi(1 - \phi) \frac{\nabla \phi}{|\nabla \phi|} \right) \quad \text{eq. 47}$$

Where u is the flow velocity; ϕ is the volume fraction, γ is the re-initialization parameter and ε_{ls} is the parameter controlling the interfacial thickness. The re-initialization parameter (γ) is considered as maximum or close to the maximum velocity of the fluid in the TPF system to ensure the consistency of the results with the whole simulations. Our empirical tests show that reducing the ε_{ls} (interfacial thickness) value, influences the thickness of the interface between two phases, consequently, to get better accuracy between the phases.

With, mass conservation, Stokes and LS equations, we have a system of 3 equations. The equations are eq. 38, eq. 39 and eq. 47. The unknowns are velocity in x and y directions and volume fraction (ϕ) and the known parameters are density, viscosity and inlet velocity (or pressure). The system of equations is solved at each time.

In the PF, the TPF dynamics is governed by a Cahn-Hilliard equation. The equation tracks a diffuse interface separating the immiscible phases. The diffuse interface is defined as the region where the dimensionless phase field variable ϕ varies from -1 until 1. In COMSOL, the Cahn-Hilliard equation is split up into eq. 48 and eq. 49 [143].

$$\frac{\partial \phi}{\partial t} + \nabla \cdot (u\phi) = \nabla \cdot \frac{\gamma \lambda}{\varepsilon_{pf}^2} \Delta \psi \quad \text{eq. 48}$$

$$\psi = -\nabla \cdot \varepsilon_{pf}^2 \nabla \phi + (\phi^2 - 1)\phi + \frac{\varepsilon_{pf}^2}{\lambda} \frac{\partial f}{\partial \phi} \quad \text{eq. 49}$$

Where u is the flow velocity; ϕ is the volume fraction, γ is the mobility parameter ($\text{m}^3 \cdot \text{s} \cdot \text{kg}^{-1}$), λ is the mixing energy density (N), ε_{pf} is the capillary width that scales with the thickness of the interface, x is

the mobility tuning parameter (by default set to 1), which is typically $\frac{h_{max}}{2}$, $\frac{\partial f}{\partial \varphi}$ is the derivate of external free energy and ψ is PF help variable. λ and ε_{pf} are related to the surface tension by eq. 50 .

$$\lambda = \frac{3\varepsilon_{pf}\sigma}{\sqrt{8}} \quad \text{eq. 50}$$

$$\gamma = x\varepsilon_{pf}^2 \quad \text{eq. 51}$$

Too small values for the x leads to numerical instabilities, too large values will not capture the interface movement correctly. A good initial assessment for the mobility tuning parameter is:

$$x = \frac{2u_{max}}{3\sqrt{2}\sigma \frac{h_{max}}{\varepsilon_{pf}}} \quad \text{eq. 52}$$

where u_{max} is the expected maximum velocity magnitude, σ is the surface tension coefficient, h_{max} is the value of the parameter controlling the maximum element size.

In the VOF method, the interface between the phases is followed by solving a continuity equation. The continuity equation for VOF is presented in eq. 53 [144] .

$$\frac{\partial \varphi_n}{\partial t} + \vec{v}\nabla\varphi_n = \frac{S_{a_n}}{\rho_n} \quad \text{eq. 53}$$

Where S_{a_n} is the source term of mass.

2.2.3 Experimental study of the kinetics of coalescence

To validate our models and numerical simulation, several experimental studies have been carried out. Firstly, with a drop of glycerol, which is a classical fluid with well-known properties and after with PEEK filaments.

The coalescence test with glycerol has been carried out with a Digi-drop instrument. A glycerol droplet is deposited with a syringe, on another drop as it is represented in Figure 32. Images were captured by using a Photon Focus high-speed camera with a 35 mm diameter lens, with 1:1.4 magnification scale. The exposure time was selected at 5000 ms. Saving speed of the high-speed camera is 50 images per second.

The coalescence experiment of PEEK is made with two adjacent filaments of 1.65 mm diameter. PEEK filaments were heated in a 200 cm³ oven in order to minimize heat losses. A thermocouple was placed between the two filaments in order to have an accurate measurement of the temperature and heating rate of the filaments. The temperature was recorded using a Graphtec-GL240 data logger. The average 0.019 °C.min⁻¹ slow heating rate was applied to the filaments to set quasi-isothermal conditions and homogenous temperature distribution inside the samples. These experiments were recorded with a high-speed camera. The camera is set on the same axis of the filaments, thus only the cross sections are visible, like it is shown in Figure 33. As it is represented in the Figure 34 the polymeric filaments have been placed between to two metallic blocs in order to maintain the contact between the filaments while applying a slight force by the blocs (as matter of fact, when polymeric filaments pass the glass transition or melting point , they slightly move , probably because of stress relaxation. This movement leads to change the position of the filaments and consequently they get far from each other. The blocs by

applying a very slight force keep the filaments in contact during the test when the temperature pass the transitions of the polymer).

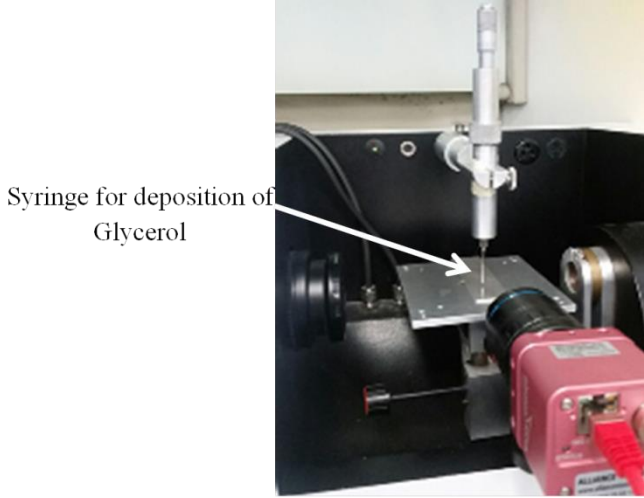


Figure 32: High-speed camera and the syringe used for the deposition of glycerol

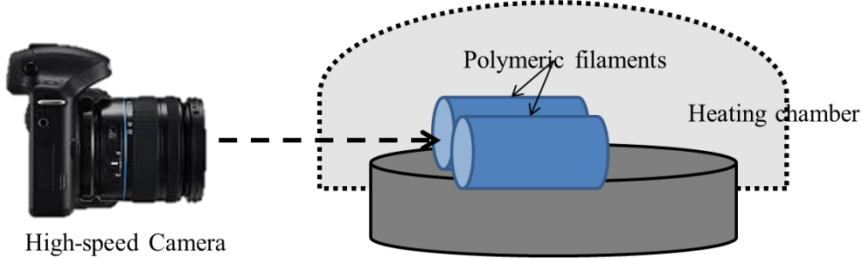


Figure 33: Schematic representation of the experimental set up for the coalescence study

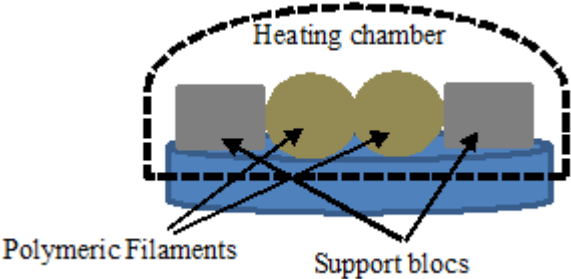


Figure 34: Schematic representation of the experimental set up for the coalescence study of PEEK in heating furnace

2.2.3.1 Coalescence of glycerol

In the first step, we have selected glycerol in order to validate our TPF model with the LS method. The coalescence kinetics of glycerol is relatively slow compared to the coalescence kinetics of water. On the other hand, at room temperature, the viscosity and surface tension of glycerol is constant. According to these properties, glycerol is a good candidate to validate our TPF model.

As we have presented in Figure 32, a Digidrop instrument and its syringe have been used to deposit a glycerol droplet. The numerical simulation of the coalescence was carried out by using TPF and LS equations in COMSOL Multiphysics. The model of the coalescence of glycerol has been implemented

as an axisymmetric model in the software. Figure 35a and b shows the meshed model used for the simulation and the dimensions of the numerical model respectively. Free triangular meshes and predefined finer meshes were used as the size of the meshes.

The properties of air and glycerol such as density, viscosity and surface tension are listed in Table 7.

Table 7: Properties of air and glycerol used in the numerical model

Properties	Value
First phase	Glycerol
Second phase	Air
Air density	1.145 kg.m ⁻³
Glycerol density	1260 kg.m ⁻³
Air viscosity	1.8.10 ⁻⁵ Pa.s
Glycerol viscosity	1.42 Pa.s
Glycerol surface tension	0.062 N.m ⁻¹

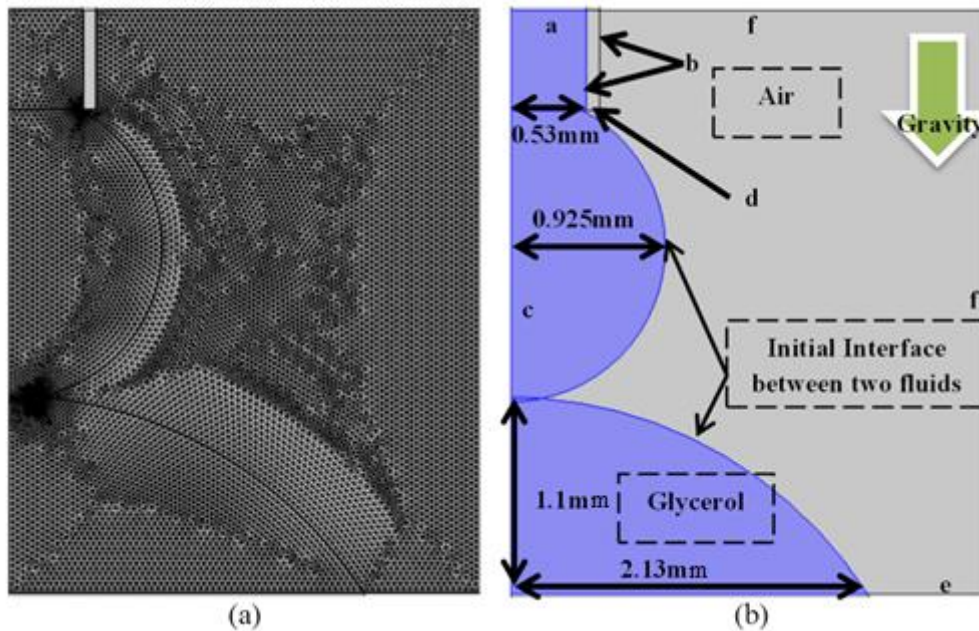


Figure 35: (a) Meshed model used in the numerical simulation, (b) initial conditions and dimensions of the numerical model

The boundary conditions and dimensions of the models are presented in Table 8.

Table 8: Boundary conditions used in the numerical model

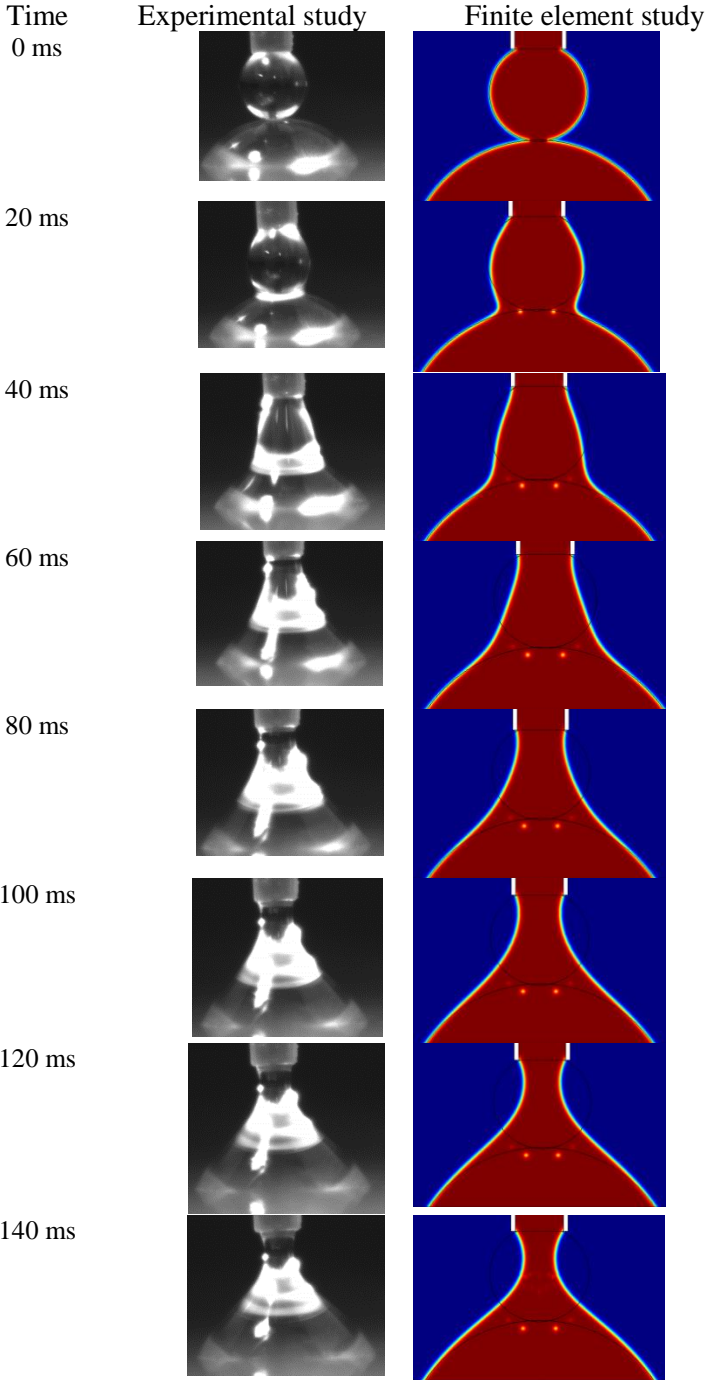
Boundary's name	Initial Condition	
a	Symmetry	
b	No-slip	
c	Axisymmetric	
d	Wetted wall	
e	Wetted wall	
f	Outlet	Pressure : 0

The images of the coalescence of glycerol with time are shown in Figure 36 (a). The glycerol takes 200 ms for making a perfect coalescence (necking, neck growing, and separation from the nozzle). As it is represented in Figure 36, in the early stages of coalescence, two droplets touch each other. Then, in the secondary stage, a neck between two droplets takes place and gradually grows. Finally, at the final

stage of the coalescence, two droplets make a single sphere and the first droplet separate from the syringe.

The results of the numerical simulation approach are represented in Figure 36 (b). The mechanism of coalescence modeled by numerical simulation is similar to the experimental study. The coalescence takes place during 200 ms from the contact of two droplets. At the first stage, two droplets make a contact with each other. The neck between the droplets increases until the separation from the syringe.

The similarities between experimental study and numerical simulation show that we have properly developed our model and numerical simulation for the coalescence of glycerol. Thus, TPF numerical simulation could be used for modeling the coalescence of filaments. After validation of our numerical model, we will apply it for high viscosity fluids such as PEEK.



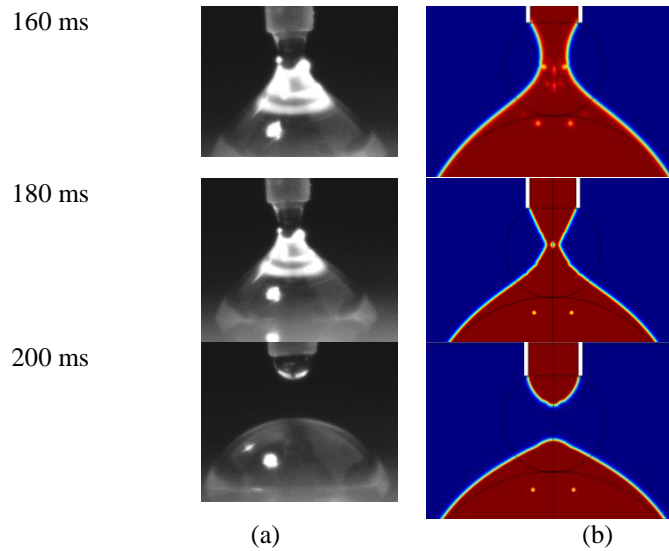


Figure 36: Obtained results by (a) experimental study, (b) numerical simulation

2.2.3.2 Coalescence of PEEK filaments

In the previous section, we have modeled the coalescence of glycerol as low viscosity fluid. In this section, we will study the coalescence of PEEK as a high viscosity fluid. The evolution of the coalescence of filaments when exposed at temperatures above the melting temperature (355 °C for PEEK) were measured experimentally and estimated analytically and by numerical simulation.

Analytical and experimental approaches have been explained previously. In the following section, we will explain the boundary conditions used for the modeling of the coalescence of filaments. Figure 37 (a) shows the meshed model and Figure 37 (b) the boundary conditions used for the coalescence of the polymeric filaments by 2D TPF-LS model.

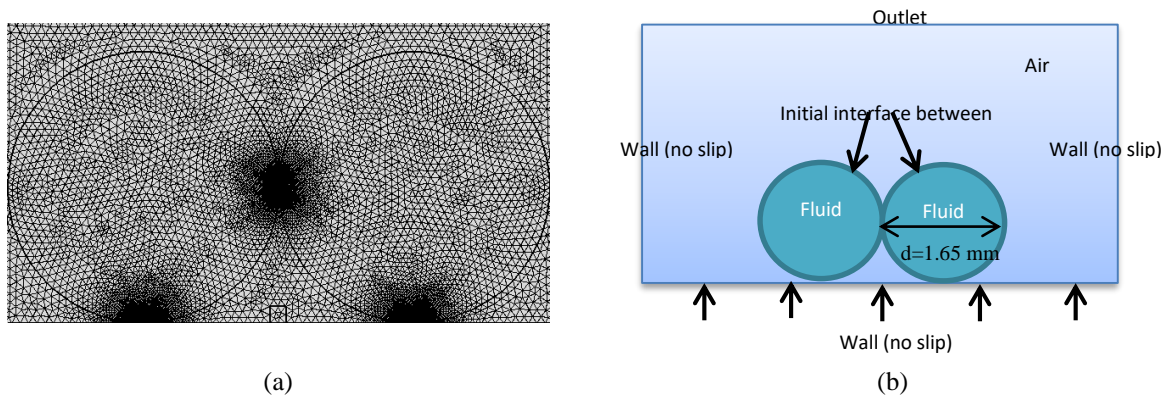


Figure 37: (a) Meshed model used in the numerical simulation, (b) initial conditions and dimensions of the numerical model

The PEEK properties used for the numerical simulation are shown in Table 9. The viscosity of PEEK have been determined previously by rheometry in the previous section (section 2.1) [49].

Table 9: Properties of the fluids used for numerical simulation

Properties	Air	PEEK
Density	1.145 kg.m ⁻³	1320 kg.m ⁻³
Viscosity	1.8 ^e -5 Pa.s	eq. 54
Surface tension	-	0.018-0.015 N.m ⁻¹

The variation of viscosity of PEEK with time has been determined in both analytical and numerical simulation by using eq. 54. Because it is not possible to define the temperature-dependent viscosity in

the TPF-LS numerical simulation, viscosity has been fitted by following equation in order to define as time dependent equation. eq. 54 enable us to define the viscosity according to condition of the experimental study.

$$\mu_{PEEK} = 1.6441E28 * t^{-8.6557} \quad \text{eq. 54}$$

Where t is time in s. The numerical simulation with CFD TPF is not heat transfer conjugated. As a consequence, we could not use directly a temperature-dependent viscosity in our numerical model. On the other hand, the viscosity changes according to the temperature in our model. Therefore, we have inserted a time-dependent viscosity in our model. The time-dependent viscosity is the variation of the viscosity in the experimental model according to time. The time corresponds to temperature changes during the heating rate. The time-dependent viscosity used for the numerical simulation is represented in eq. 54. It has been extracted from the results in Figure 39.

PEEK at the melted state turns into black during degradation, consequently, the processing of images captured by high-speed camera is more complicated. Bonding of PEEK filaments starts at 350°C. Comparing with DSC results (Figure 16), the polymer is fully melted at this temperature. We consider that the influence of the gravity on the shape of the filaments is negligible. At 380°C, the filaments reach their maximum bonding length.

During the experiments, the heat transfer is governed by convection with very low air flow. The air around the filaments act like an insulating media. Furthermore, the interface is between two polymers with low thermal conductivity and the air delays the heating of the interface. This shift the melting of the interface between the two filaments towards higher temperatures. For PEEK, the temperature range for the coalescence is relatively wide, 350°C to 380°C. The coalescence takes relatively a long time, it is due to high viscosity and low surface tension of PEEK.

The evolution of the bonding length according to the different temperatures by experimental study and numerical simulation is represented in Figure 38.

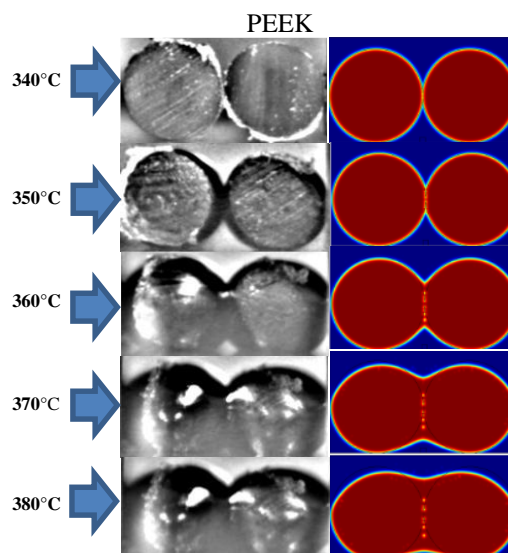
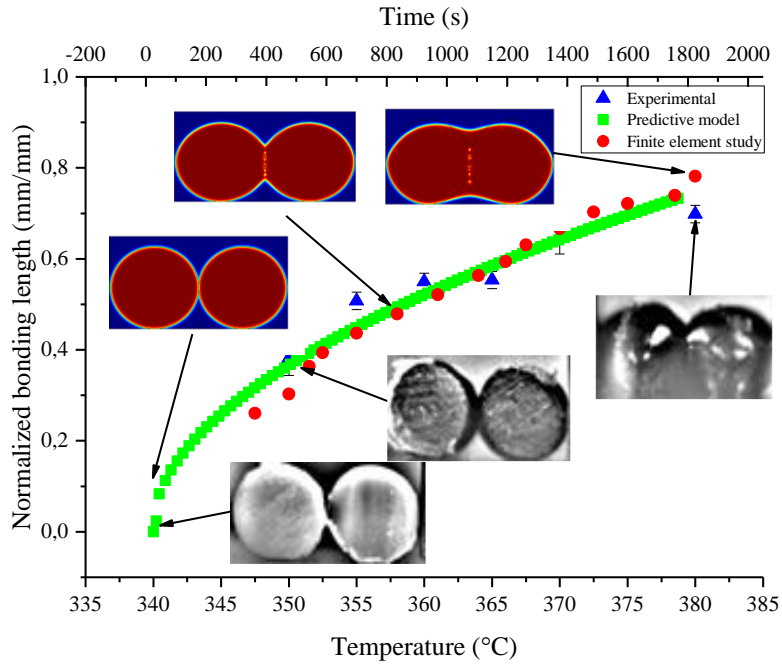


Figure 38: Evolution of the coalescence by experimental and numerical simulation for PEEK

The coalescence takes place after the melting temperature of the polymer when the crystalline phase has turned into amorphous phase.

The experimental results have been compared to the modified Frankel's [140] bonding model and numerical simulation. Figure 39 shows the coalescence of PEEK. The comparison of the experimental study with the predictive model shows that the results are close to each other. However, there is still several differences. According to the experimental study, the coalescence starts at around 350°C which is mainly because there are still crystalline phases in the polymer. The analytical study and numerical simulation do not take into account the presence of crystalline phase and it is based only on surface tension and viscosity. For this reason, there is some deviation between the results below 350°C. Furthermore, we have to mention that in the analytical study, we have neglected the influence of external forces such as gravity and also applied forces from the metallic blocs on the evolution of the coalescence. Depending on the viscosity of the polymer, these external forces highly influence on the shape of the extrudate. Because of high viscosity of PEEK, the influence of these external forces on the variation of the filament (or particle) shape is not noticeable however, for the materials with lower viscosity these external forces must be considered.

For the numerical simulation by TPF-LS equation for polymers, several important parameters must be considered to model properly the coalescence phenomenon. The initial numerical simulations mostly lead to numerical errors and high deviation of obtained results from the experimental studies. Several sources may explain the deviation of experimental study from numerical simulation. One of the main reasons for this deviation is the systematic errors which could occur during all the tests. For the systematic errors, we could mention the difference between the measured temperature and real temperature of the filaments, errors during the determination of the bonding length because of low quality of recorded images and also the influence of the crystallinity on the results. For PEEK, we have tried to reduce as much as possible the systematic errors in order to get better results, as close as possible to experimental study. Furthermore, selecting the parameters of LS specially γ (Re-initialization parameter) influences on the results. γ must be close to the boundary changing velocity (on kinetics of coalescence), however, the kinetics of coalescence is not constant during the test, which may influence on the results obtained numerically. The quality of the air/polymer interface is another important parameter which influences on the numerical simulation. As explained in eq. 44 and eq. 45 for the determination of the viscosity and the density in TPF-LS, we use the additive function of volume fraction. Thus, we have to reduce the interfacial thickness as much as possible. This lately is possible by reducing the size of the meshes and also ϵ_{LS} (interfacial thickness) in the eq. 47.



(b)

Figure 39: Evolution of the coalescence of the filaments according to temperature for PEEK

The normalized bonding length in eq. 55 is the ratio of the bonding neck length to the initial diameter of the filament.

$$\text{Normalized bonding length} = \frac{\text{Bonding neck length}}{\text{Initial diameter}} \quad \text{eq. 55}$$

2.2.4 Modifications on the numerical simulation model

In order to reduce the percentage of deviation of the numerical simulation from the experimental and the analytical study, some modifications on the coalescence model have been made.

These modifications are based on the refinement of the meshes, changing the meshes from tetrahedral to quadratic meshes and also the locally meshed model. Moreover, the influence of different axisymmetry plans has been determined by numerical simulation to optimize the time calculation.

2.2.4.1 Modifications on the meshes

Figure 40 shows the different types of meshes used for the model in order to reduce the deviation of the numerical simulation study from the experimental study. Figure 40 (a) and (b) show the different sizes of the meshes for the model. Figure 40 (c) and (d) shows locally refinement meshed models, in these models, the meshes of the interface between air and polymer have been reduced.

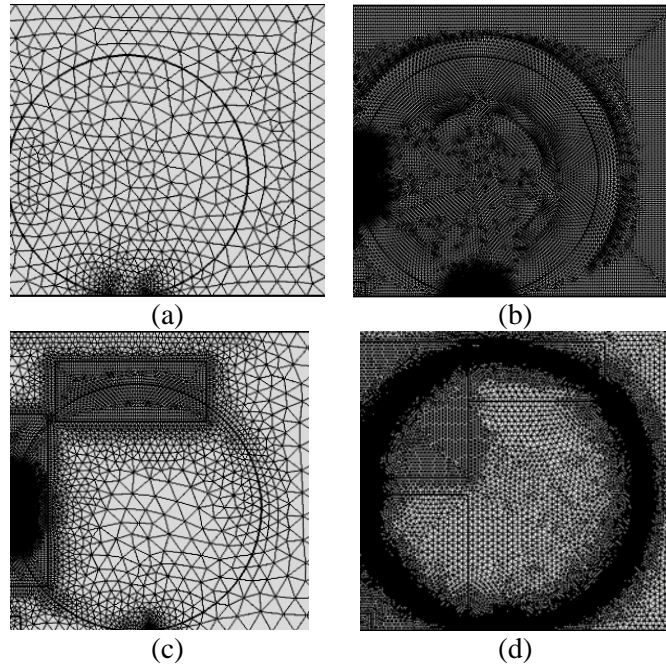


Figure 40: Different types of the meshes used for the simulation (a) Default meshes with pre-defined normal size (b) Default meshes with pre-defined extra fine size (c) Locally modified meshes on different regions (d) Modified meshes with finer mesh on the interface

Our observations show that the size of the meshes highly influences on the thickness of the interface and the time of calculation. The time of the simulation changes from 3 hours to 48 hours according to size of the meshes. However, its influence on the deviation of the obtained results is not obvious. On the other hand, in the case of the locally meshes refinement, the thickness of the interface depends on the biggest mesh in the system. Moreover, using the local meshes makes the model harder to convergence. Consequently, for modeling the coalescence, our suggestion is to use homogenous meshes and not the local meshes. Although selecting the big size of meshes reduce the time of simulation, however, it makes the simulation harder for convergence. In the case of very fine size of meshes, we have the same problem for the convergence. As a consequence, the optimized size of the meshes is homogenous meshes with the medium size.

2.2.4.2 Different symmetry plans

The second approach to reduce the deviation of the numerical simulation from the experimental study was to model the system with different axisymmetric and symmetric plans. Figure 41 shows two different models used for the numerical simulation by taking into account several axisymmetric plans. In the case of using the axisymmetric simulation, we will model the coalescence of two spheres, which is different from our experimental case of two cylinders.

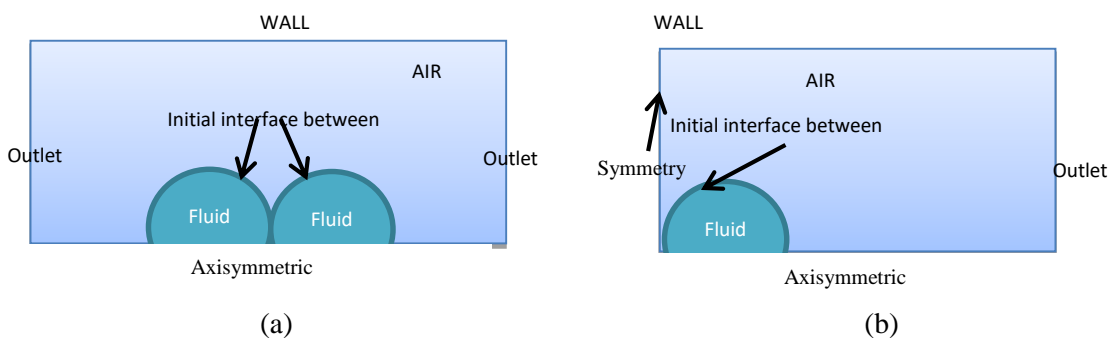


Figure 41: Used model for the axisymmetric numerical simulation (a) Meshed model (b) Initial conditions of the model

The results by axisymmetric simulation represented in Figure 42 (a) also show a high deviation from the experimental study. The results obtained by taking into account the axisymmetric boundary condition and the experiments in Figure 36 are closed together, consequently adding axisymmetric boundary conditions to the model does not highly influenced on the deviation of numerical simulation from the experimental study. However, using symmetries and axisymmetries highly influence on the time of simulation. However, they have no influence on the kinetics of coalescence of the models. Furthermore, as it is represented in Figure 42 (b), symmetry in y-direction has been added to the model. The results of numerical simulation by considering the symmetry and axisymmetric plans are presented in Figure 42.

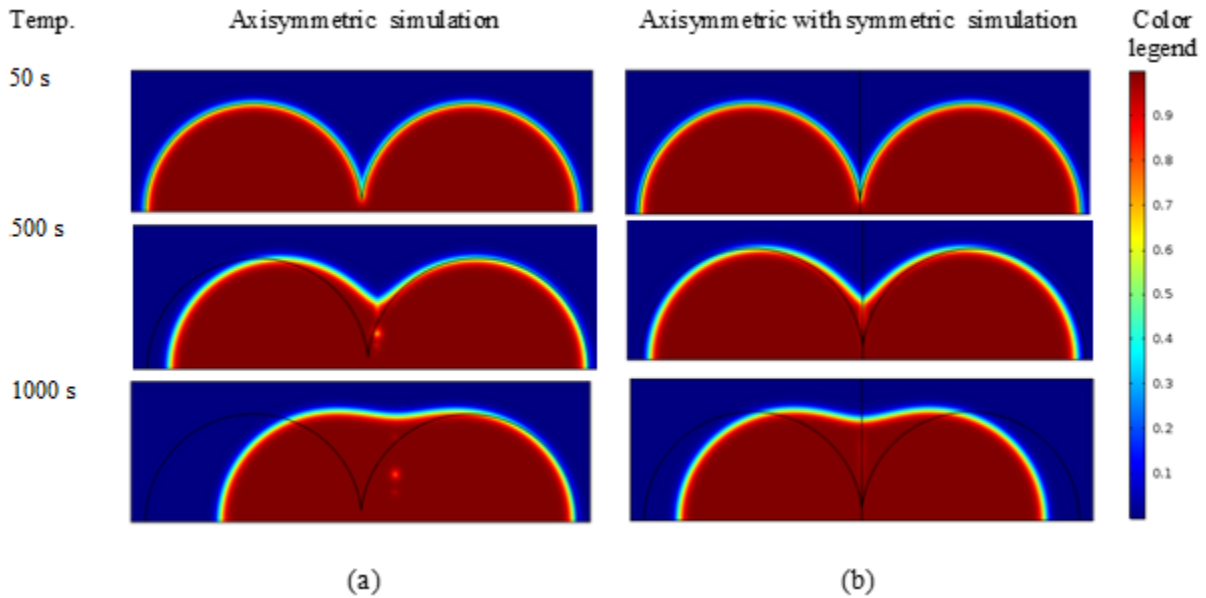


Figure 42: Results of numerical simulation (a) Axisymmetric simulation (b) Axisymmetric simulation with symmetry on the contact region

2.2.4.3 Other parameters influencing the kinetics of coalescence

In this part, we will study the influence of numerical parameters explained in section 2.2.2.2. In the LS equation, γ is the re-initialization parameter and ε_{ls} is the parameter controlling the interfacial thickness. These parameters have the main effect on the kinetics of coalescence and also on the convergence of the results. γ must be close to the kinetics of coalescence to reduce the deviation of numerical results, furthermore, ε_{ls} must be small enough to reduce the size of the interface of air and polymer and make the numerical simulation closer to the real situation. In order to select properly the value of γ we have determined the mean coalescence kinetics by experimental study. The average kinetics of coalescence by experimental study has been selected as re-initialization parameter.

The influence of the ε_{ls} on the interface of two phases is represented in Figure 43. As it could be concluded from Figure 43, a bigger value of ε_{ls} makes the interface between air and polymer wider. While using a smaller value makes the interface narrower and increase the accuracy of the interface between two phases.

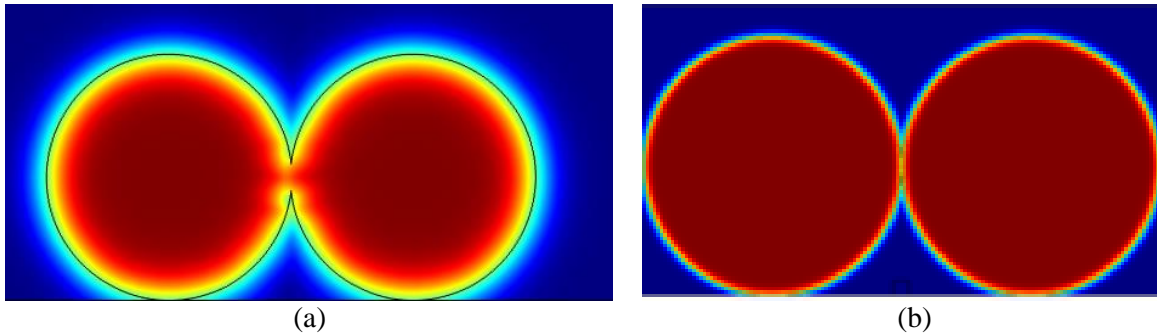


Figure 43: Influence of ϵ_{is} , the parameter controlling the interface on the clearance of the interface between two phases, (a) Size of *mesh*, (b) $\frac{\text{Size of mesh}}{4}$

In the Figure 43 size of the mesh is the is the value of the parameter controlling maximum element size Or the maximum size of the mesh in the model.

Previously we have explained the importance of the surface tension on the kinetics of coalescence. The sensitivity of the kinetics of coalescence to the surface tension is represented in Figure 44. In this figure, the results are presented for four values of surface tension at $t = 500$ s. and $t = 1800$ s. For the lowest surface tension, under the influence of gravity, the particle is spread onto the substrate. However, as the surface tension increases, the polymer particles are more attracted to each other. For the highest surface tension (more than 0.025 N.m^{-1}), the absorption of the particles is relatively high. In this case, the influence of the gravity on the deformation of the polymers is negligible. Furthermore, for the low surface tension, the filaments or spheres have more tendency to spread onto the substrate, while at high surface tension the tendency of the filaments or spheres is more towards unification and making a bigger sphere. As a conclusion, the surface tension highly increases the kinetics of coalescence. Surface tension has been approximated by Parachor model represented in the section 2.1.4.2. Surface tension is considered constant for the temperature above melting temperature in both analytical model and numerical simulation.

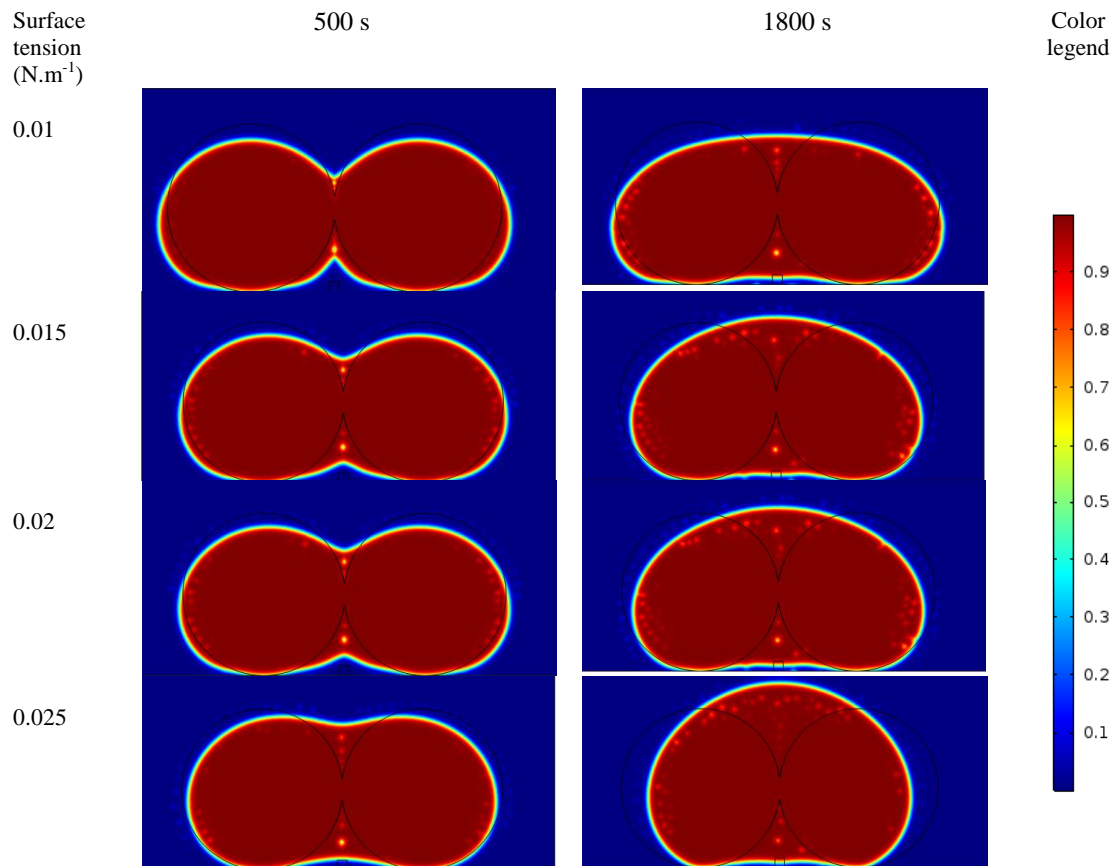


Figure 44: Influence of the surface tension on the kinetics of coalescence

2.3 Conclusion

This Chapter focuses on two parts: the characterization of PEEK and the coalescence study.

The polymer properties having a crucial influence on the quality of the FFF parts have been determined for PEEK and PLA. Their thermal transitions, kinetics of crystallization and sensitivity to degradation have been clarified. The glass transition of PEEK is 150 °C. At higher heating rate, the glass transition is shifted towards higher temperatures. Depending on the heating rate, the melting temperature starts at 300 °C and ends around 355 °C. Same as for the glass transition, at higher heating rates, the melting temperature is shifted to higher temperatures. No cold crystallization has been observed because of fast crystallization of PEEK whatever the studied cooling rates.

PLA has a glass transition at 65 ± 5 °C and a melting temperature at 170 ± 5 °C. Contrary to PEEK, the kinetics of crystallization of PLA is slow. Even at very low cooling rates, the polymer is not fully crystallized. Because of uncompleted crystallization, a cold crystallization peak is observed above the glass transition on heating.

The results for PEEK and PLA show a faster crystallization kinetics for PEEK compared to PLA. In the case of PLA, the crystallization could be avoided in the FFF process by applying a high cooling rate while, in the case of PEEK, the polymer crystallizes whatever the cooling rate. Practically, the cooling rate depends on the temperature of the melt polymer exiting from the nozzle, the temperature of the platform (substrate) and also the environment temperature.

The thermal properties such as thermal conductivity and expansion coefficient have determined. The thermal conductivity of PEEK at room temperature is $0.32 \text{ W} \cdot (\text{m} \cdot \text{K})^{-1}$. The thermal diffusivity of PEEK at room temperature is about $0.24 \text{ mm}^2 \cdot \text{s}^{-1}$. Contrary to the thermal conductivity, the thermal diffusivity decreases while the temperature increases. The coefficient of thermal expansion coefficients have been determined below the glass transition at $59 \cdot 10^{-6} \text{ }^\circ\text{C}^{-1}$ and above the glass transition at $162 \cdot 10^{-6} \text{ }^\circ\text{C}^{-1}$.

The rheological properties have been determined for the shear rates less than 100 s^{-1} in oscillatory mode. The complex viscosity of PEEK at different temperatures at its Newtonian plateau is between $7000 \text{ Pa} \cdot \text{s}$ and $11000 \text{ Pa} \cdot \text{s}$. While at 100 s^{-1} , the viscosity at $383 \text{ }^\circ\text{C}$ reduces up to $1000 \pm 100 \text{ Pa} \cdot \text{s}$. The comparison of PEEK with PLA shows that the viscosity of PEEK is much higher than those of PLA. The viscosity of PLA at its Newtonian plateau at different temperatures is between $700 \text{ Pa} \cdot \text{s}$ and $4000 \text{ Pa} \cdot \text{s}$. Moreover, both polymers are sensitive to thermal degradation. As a consequence, the processing temperature range are limited to prevent their degradation. PLA and PEEK undergo different degradation mechanism, resulting in decreased viscosity for PLA due to chain scission mechanism. On the contrary, the degradation mechanism of PEEK occurs by molecular recombination, leading to viscosity increase.

The surface tension of PEEK and PLA in the solid state has been determined by contact angle meter. $38.7 \text{ mN} \cdot \text{m}^{-1}$ is the surface tension of PEEK and $42.1 \text{ mN} \cdot \text{m}^{-1}$ for PLA at room temperature. Furthermore, the surface tension of PLA at liquid state at $200 \text{ }^\circ\text{C}$ has been determined by experimental study about $27 \pm 3.2 \text{ mN} \cdot \text{m}^{-1}$. As the measurement was not possible for PEEK in its melted state, the surface tension of PEEK according to the temperature variation has been calculated with the Parachor equation.

All these properties will be used further in the analytical and numerical modeling.

In the second part of this chapter, the coalescence of two glycerol droplets and two adjacent polymeric filaments have been studied, by experimental approach, analytical equation and numerical simulation.

The 2D coalescence numerical simulation of the fluid in the air has been carried out by using CFD and TPF-LS equations. The advantage of TPF numerical simulation is that we are able to model the interaction between polymer and air.

Before studying the coalescence of PEEK filaments, we have studied the coalescence of glycerol droplets as a low viscosity fluid by experimental study and numerical simulation. Our numerical results on glycerol show great accordance with the experimental ones. These results validate our coalescence model. Regarding the literature, the studies reported until now deal only with Newtonian fluids of low viscosity. These studies reveal that TPF simulation agree well with the experimental studies; however, for high viscosity fluids and polymers, no studies are reported. To our knowledge, our work is the first one on this topic.

The experimental study of the coalescence phenomenon confirms that the viscosity highly influences the bonding of polymers. This bonding would impact the mechanical properties of the printed parts. Indeed, the mechanical strength of the printed parts stems from the interlayer adhesion. The latter is due to the interdiffusion of polymeric chains in adjacent filaments. This interdiffusion is directly linked to the viscosity of the polymer.

The bonding length between two adjacent PEEK filaments has been registered with time and temperature. These results have been compared to a predictive model: the results demonstrate a good agreement when the melting of the crystalline phases are completed. Indeed, the coalescence starts when the polymer is completely in the melted state. This means that the crystalline phase prevents the mobility of polymeric chains that means, the coalescence of adjacent polymers is not possible before the melting

temperature. From 350 °C until 365 °C obtained results by experimental study is slightly higher than numerical simulation and predicted model. While after 365 °C, obtained results for coalescence by experimental study is slightly less than other methods. This deviation might probably be because of applying force from the metallic bloc to keep the filament in contact together. This external force increase coalescence of two filaments, while after 365 °C, when the filaments are changes state from solid state to fusion, the effect of the forces from metallic bloc is less important. Which leads to decrease of the coalescence kinetics. However, by numerical simulation and predictive model we don't take into account these external forces.

Our numerical simulation approach results in very good understanding of TPF-LS simulation. Our investigations show that local meshes influence on the convergence of the simulation. Consequently, in order to get better convergence, we suggest the homogenous meshes. γ the re-initialization parameter and ε_{ls} the parameter controlling the interfacial in the LS series are the most important parameters influencing the results of coalescence. These parameters, directly influence on the accuracy of the numerical simulation and the convergence of the obtained results. ε_{ls} must be small to have a better interface between the phases. However, a very low ε_{ls} leads to numerical instability, increases the time of calculation and false results. In the same manner, the selection of the re-initialization parameter is very delicate. The re-initialization parameter must be close to the maximum velocity of the system. High velocity and low velocity at the same time leads to instability of simulation and numerical errors. The time-step is also other important parameters during the coalescence study. The time-step must be minimized in order to get the numerical simulation close to the experimental study.

Above mentioned steps must be taken into account in order to increase the accuracy of our numerical simulation and interface between air and polymer. The clearance of the interface is very important specially for assignment of the thermal diffusivity of the phases.

**Chapter 3: Numerical simulation of material
deposition and crystallization**

3.1 Introduction

In Chapter 2, we have introduced the intrinsic properties of the polymers that influence on the quality of the manufactured parts. These material properties are highly dependent on the printing conditions. The properties of the deposited beads, the crystallization kinetics of the polymer, the cooling rate, the initial temperature, the environment temperature or also the thermal conductivity of the polymer are closely imbricated. Because of the dependency of the material properties to the printing conditions and also interdependency of the polymer properties to each other, the study of FFF process must include all of them.

Previously, we have explained that the viscosity of the polymers is shear rate and temperature dependent. Furthermore, in Chapter 2 we have shown that the polymers undergo degradation at high temperature and at a certain shear rate. Consequently, the determination of available range of printing shear rate is necessary in order to avoid degradation during printing. Studying the shear rate in the process needs to take into account the printing conditions such as inlet velocity, the geometry of the deposited beads and the structure of the liquefier. This study allows the optimization of the quality of the manufactured parts by determining the optimum bead geometry and inlet velocity. Understanding the shear rate during the process allows the determination of the evolution of the viscosity but it requires a fine modeling of the fluid flow. Moreover, in order to determine the die swelling of the extrudate after exiting from the nozzle, determining the shear rate is necessary too.

In this chapter we will use the material properties measured in Chapter 2 to make a numerical simulation in order to study the FFF process. The crystallization kinetics of semi-crystalline polymers influences on the mechanical properties and interdiffusion of the deposited beads and layers. The determination of crystallization kinetics and the time of structural evolution from amorphous to crystalline state at different environment conditions is necessary to optimize the mechanical properties of the printed parts. On the other hand, as we have explained in Chapter 2, the crystallization kinetics of PEEK is relatively fast and also the crystallization in FFF process is non-isothermal. As a consequence, firstly an adequate approach to determine the non-isothermal kinetics of crystallization of PEEK is required. And secondly, we have to model the non-isothermal conditions in order to determine the crystallization kinetics of PEEK. By modeling properly, the kinetics of crystallization in FFF process, it would be possible to determine the optimal exposure time and temperature of the deposited beads before crystallization. However, prior to modeling the crystallization kinetics, we have to determine the temperature distribution in the process. The determination of the temperature distribution required the thermal properties measured previously in Chapter 2. Additionally, to model the fluid flow, we have to insert viscosity as a shear rate and temperature dependent parameter. The viscosity determined in Chapter 2 can be written as Carreau-Yasuda law in order to apply in the deposition model.

The FFF process is based on the material deposition on a substrate. Polymer flow undergoes heat transfer and crystallization. Modeling the material deposition is the primary step towards the determination of heat transfer and crystallization. However, in this process, the material is gradually deposited on a substrate. That means, there is an interaction between the substrate, the air and the polymeric filament during this step. Thus, we had to develop a model to take into account these effects. Consequently, our model has to consider the air, the substrate and the polymer at the same time. Our numerical model is based on three different steps. These steps must be conjugated together:

- First step: Deposition of the material on the substrate.

In this first step, we will carry on Two-Phase Flow (TPF) numerical simulation. For numerical simulation of the material deposition, we have used the Two-Phase Flow with LevelSet method to follow the polymer front in the TPF-LS module of COMSOL software. In the previous chapter, we have thoroughly explained the principals and presented the equations of the TPF-LS method. By TPF simulation, we are able to model the interaction of air and polymer flow during FFF process. Hereby, we could determine the velocity field, volume fraction and rheological properties (shear rate and viscosity). This is a crucial step during our numerical simulation. Because in the FFF process, the polymer exits from the nozzle continuously.

In this step, the free-form extruder, deposition of a single bead on the substrate and deposition of the second layer upon the first layer has been investigated.

- Second step: Determination of heat transfers and temperature field in the model.

Heat transfer is the most influential effect during the FFF process because it directly influences the viscosity of the polymer in the liquefier and also the crystallization during cooling. Consequently, it is essential to understand and to optimize heat transfers during the material deposition to be able to determine the variation of the viscosity and also to model the non-isothermal crystallization. We will implement a Partial Differential Equation (PDE) to our TPF-LS model in order to analyze and determine the evolution of heat transfers during deposition.

- Third step: Determination of non-isothermal crystallization.

The final step is to determine and model the kinetics of non-isothermal crystallization. The Nakamura non-isothermal crystallization equation has been implemented into our model as a PDE, after Nakamura’s parameters had been determined. In this step, we could determine the kinetics of crystallization during the FFF process.

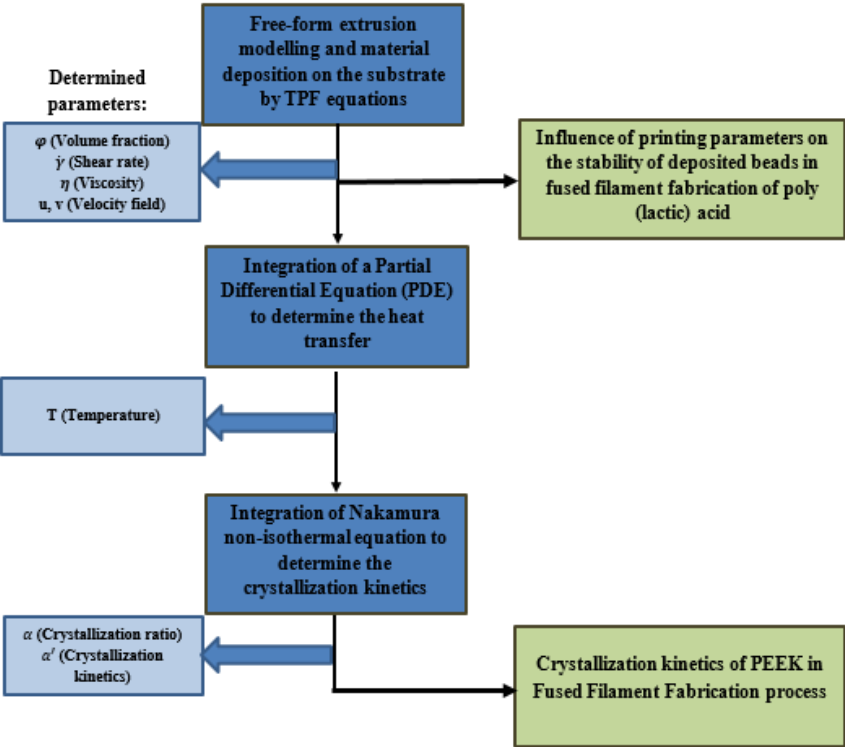


Figure 45: Representation of the followed steps in the Chapter 3

These three steps are presented in Figure 45. At the end of the first step, to validate our model for this step and the numerical simulation, we have studied the shear rate and viscosity of PLA and also the influence of the printing parameters on the stability of the deposited beads. The numerical results are compared to the experimental results.

After the third step, by integration of the heat transfer and non-isothermal crystallization equations in our model, we are able to determine the kinetics of crystallization resulting in solidification in the FFF process.

For the numerical simulation of heat transfer and crystallization study we have used

In the first part of this Chapter we will explain our approaches for modeling the fluid flow and the material deposition. In the second part, we will concentrate on the quality of the extrudate when it exits from the nozzle. In this part, we will determine the shear rate of the polymer flowing from the nozzle, we will also study the influence of the shear rate on the shape of the extrudate according to the printing conditions. And finally, in the last part, we will study the crystallization kinetics and the temperature distribution of PEEK in the FFF process. In the last part of this section, we also aim to find the optimal environment temperature in order to promote the interdiffusion of deposited beads. Lastly, a study of the effect of die swelling applied to the printing conditions is exposed.

3.2 From material deposition to crystallization in the FFF process

The material deposition on the substrate during the FFF process is a complex phenomenon, therefore, the material deposition represents the most important part of our numerical simulations.

TPF numerical simulation is a relatively heavy simulation because of the property gaps of two considered fluids (polymer and air). Consequently, prior to model the material deposition on the substrate, we will model the free-form material extrusion.

3.2.1 Free-form material extrusion

Our initial approach to model the free-form extrusion is to model the material flow from the nozzle under the effect of a given velocity and gravity. The outlet velocity of the polymer from the liquefier in the free-form simulation is a function of the printing parameters such as height of the layer and feed rate. As it is represented in Figure 46, the simulation is based on axisymmetric simulation and the polymer flow exiting from the nozzle. In our model, there are two phases air and polymer melt.

We have used the axisymmetric model for the following reasons:

- Axisymmetric model is more time effective than 3D modeling.
- 2D model does not properly represent the real extrusion process of a droplet.
- 3D model is not suitable for validation part of our model (too heavy, and generate numerical instabilities).

For our numerical model, we have used axisymmetric module of COMSOL for modelling the TPF simulation. Furthermore, to implement the heat transfer and crystallization equations to the model, two PDE (Partial Differential Equation) have been added to the model.

The boundary condition of the TPF simulation is represented in Figure 46.

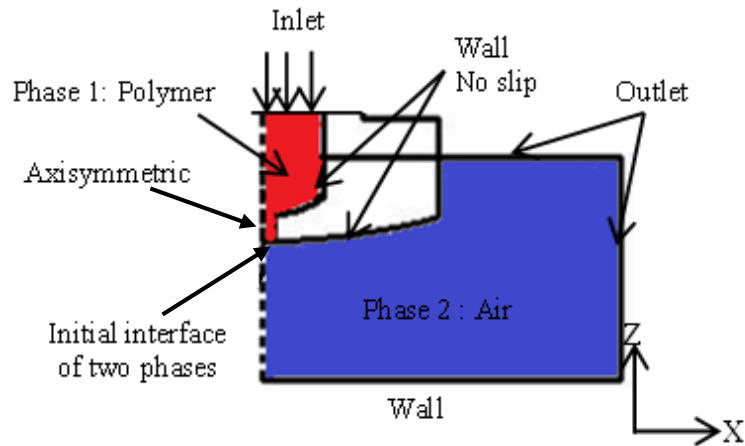


Figure 46: The schematic representation of the boundary condition for TPF numerical of free-form extrusion

In the first approach, the sensibility of free-form extrusion to viscosity has been carried out. 1 Pa.s, 7000 Pa.s, 11000 Pa.s and shear rate-dependent viscosity have been selected. The evolution of volume fraction for different viscosities is represented in Figure 47.

For the shear rate-dependent viscosity, the viscosity has been defined as a Carreau model (eq. 64) for PEEK (Table 12).

Meshing of the model highly influences on the quality of the results. Primarily, the interface of polymer/air highly depends on the size of the meshes. Furthermore, non-uniform meshes with big size of the meshes also influence on the results of the simulation. In the Annex V we have represented some numerical errors generated by not-appropriate meshing.

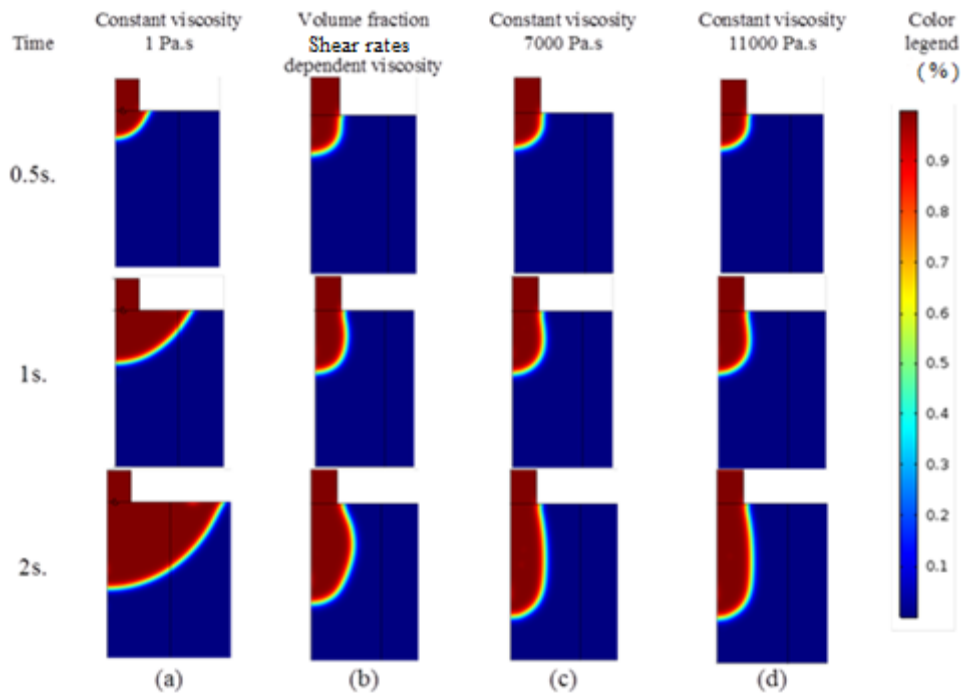


Figure 47: Influence of the viscosity on the behavior of the extruding polymer (a) Constant viscosity = 1 Pa.s (b) Shear rate-dependent viscosity (c) Constant temperature = 7000 Pa.s, (d) Constant viscosity =11000 Pa.s

As it is represented in Figure 47, the viscosity of polymer highly influences on the shape of extrudate exiting from the nozzle. While at the low viscosity, the fluid has the tendency to make a droplet around the nozzle due to surface tension; at higher viscosities, the polymer flows from the nozzle and makes the extrudate. At high viscosities (7000 and 11000 Pa.s), the variation of the shape seems negligible. After modelling the free-form extrusion, we will add the heat transfer equation to the model in order to determine the variation of temperature.

3.2.2 Heat transfer of free-form material extrusion

To determine the heat transfer in the flow simulation, a partial differential equation (PDE) [145] has been added to the model. eq. 56 shows the advection-diffusion equation for determining the variation of the temperature in our model considering the fluid flow in the system:

$$\frac{\partial T_S}{\partial t} + (\vec{u} \cdot \nabla) T_S = \Omega \cdot \nabla^2 T_S \quad \text{eq. 56}$$

$$\Omega = \left(\frac{\lambda}{\rho C_p} \right) \quad \text{eq. 57}$$

Where T is the temperature and \vec{u} is the fluid velocity field. Here, the fluid velocity is the term that links the heat transfer equation to TPF simulation, λ is the thermal conductivity, ρ is the density and C_p is the heat capacity of the fluid. The term Ω represents the thermal diffusivity of the material.

To take into account the metallic parts of the nozzle and the substrate in the model, the velocity term in the eq. 56 is equal to zero.

We have determined the thermal conductivity and thermal diffusivity of PEEK according to temperature in the range 25 °C to 225 °C. The results are presented in Figure 24 in Chapter 2.

The boundary conditions used for modeling the heat transfer in free-form extrusion is represented in Figure 48. In the heat transfer numerical simulation the heat transferred by convection is neglected.

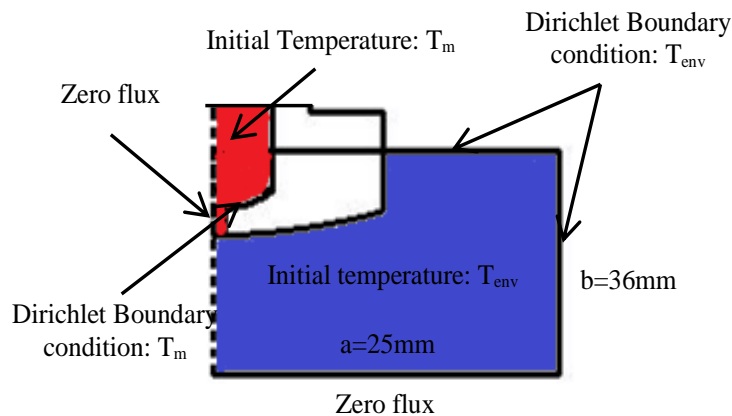


Figure 48: Boundary conditions used for modeling the heat transfer during free-form extruder

In the first approach to determine the heat transfer during free-form extrusion, we had to define a law in order to define the thermal diffusivity for each phase and mixed phases. A volume fraction (φ) dependent equation has been defined to clarify the properties of the interface between air and polymer. At the first time, the method based on the mixing law has been defined for the thermal diffusivity (density, conductivity and specific heat). Mixing law for the thermal diffusivity is described by eq. 58:

$$\Omega = \varphi\Omega_{polymer} + (1 - \varphi)\Omega_{air}$$

eq. 58

Where φ is volume fraction and $\Omega_{polymer}$ and Ω_{air} are the thermal diffusivity of polymer and air respectively.

The results of simulation of heat transfer for the fluid with low viscosity (1 Pa.s) exiting from the nozzle is represented in Figure 49.

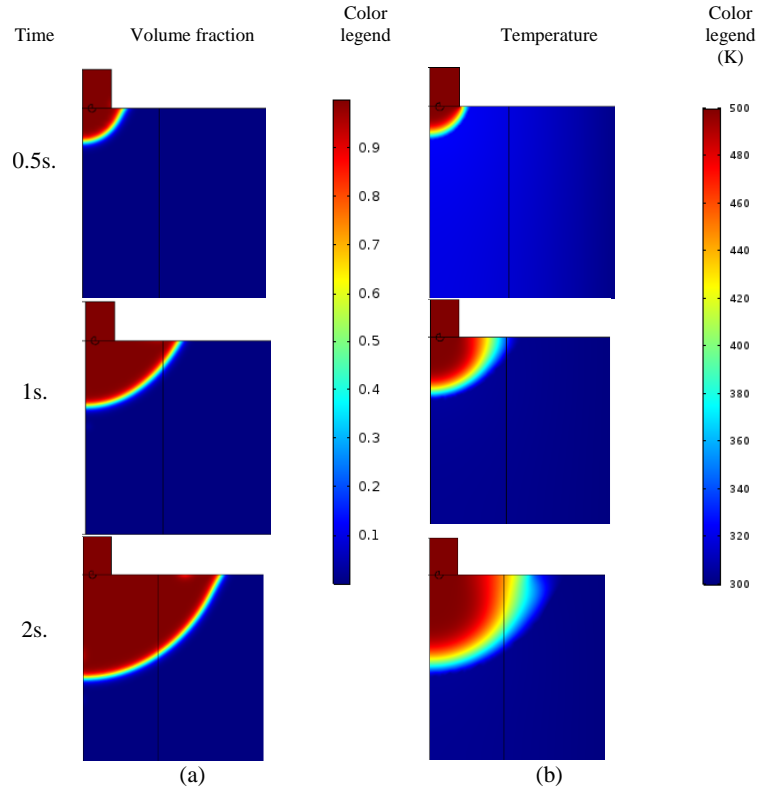


Figure 49: The free-form extruder for relatively low viscosity fluid (a) volume fraction (b) temperature field

The results for the heat transfer show that after 2 seconds, the center of the polymer extrudate is still at the melting temperature, while close to the interface the temperature of the extrudate is reduced.

By adding the heat transfer to the free-form extruder model, we are able to determine the temperature dependent viscosity. Figure 50 shows the results of volume fraction for the temperature-dependent viscosity.

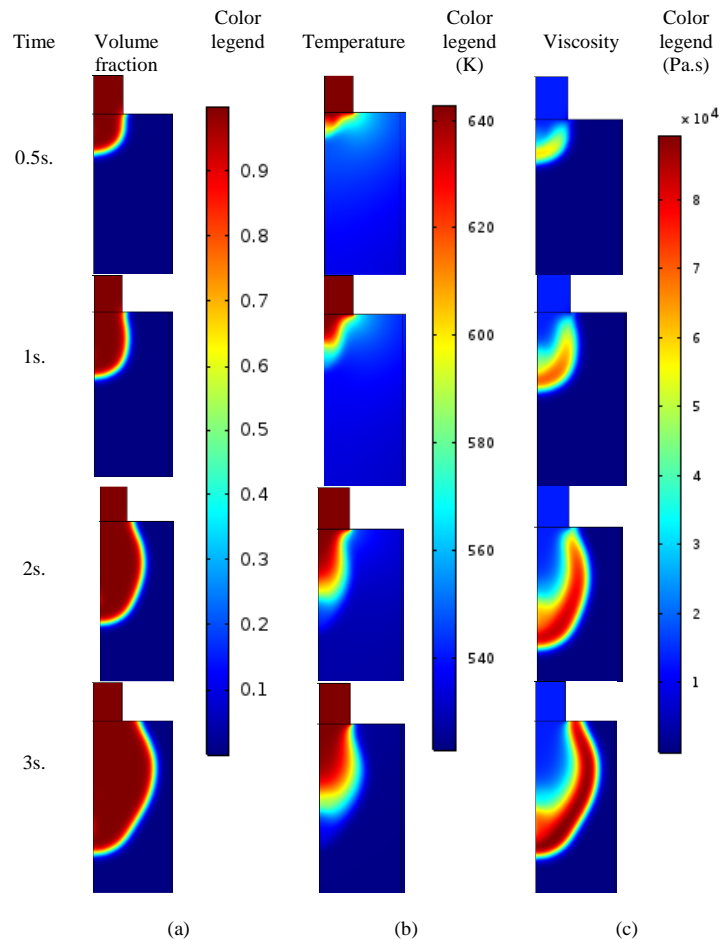


Figure 50: Determination of the temperature-dependent viscosity (a) Volume fraction, (b) Temperature field, (c) viscosity field

Figure 51 shows the variation of volume fraction, temperature and viscosity of the polymer along the cutting line for extruding process at time $t = 3$ s. At the center point of the polymer, the viscosity is the viscosity of the melted polymer (about 10^4 Pa.s) and in the other extremity of the line (about at 5 mm), the viscosity of the system is the viscosity of the air. On the line, the increase of viscosity is visible, the source of this increase of viscosity is due to the cooling of polymer which occurred during the process. On the other hand, as it is represented in this figure, the interface, the polymer/air boundary, seems to be large which is far from the real condition. It has been already mentioned that the boundary of two phases in the LS method is where the volume fraction is 0.5. The theoretical boundary of the two phases is represented by the dash line in the graph and the arrow in the image (Figure 51). Obtained results for the temperature field in Figure 50 by mixing law thermal diffusivity seem that the cooling rate is too fast (the cooling rate is more than $100 \text{ }^\circ\text{C}\cdot\text{s}^{-1}$).

The results in Figure 51 for the volume fraction of free-form extruder shows that the interface of the air and polymer is relatively wide. A wide interface of the phases will influence on the precision of the simulation not only for the volume fraction but also for the heat transfer (mainly because we have defined the thermal diffusivity as an mixing law) and the viscosity estimation. Consequently, to make the simulation more accurate, we have to reduce this interface. For reducing the interface, we can use two options:

- Using finer meshes

- Reducing the value of ϵ_{ls} (the parameter controlling the interfacial thickness) in the LS equation (eq. 47 in chapter 2)

Worth to mention, applying these approaches highly increases the calculation time of the simulation.

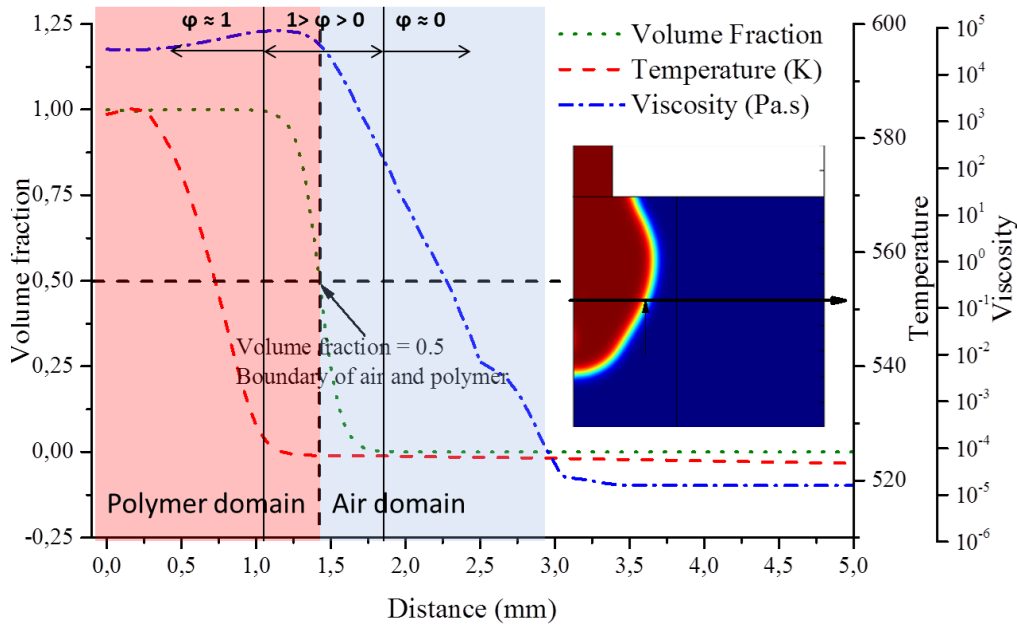


Figure 51: The values of volume fraction, temperature and viscosity during the free-form extruder

3.2.3 Deposition of the filaments

After modeling the free-form extrusion, and determining the heat transfer in the model, we will study the material deposition on the substrate. In section 3.4, we point out the simulation of the material deposition on the substrate. The results for the deposition of the first layer on the substrate are represented in Figure 52, Figure 53 and Figure 87. As it could be concluded from the results, narrower is the interface between the two phases, more accurate are the results of simulation.

In the FFF process, the part is manufactured layer by layer. Thus, being able to model the deposition of a layer material on the another layer just deposited is a step forwards modeling the FFF process.

We have modeled the material deposition in 2D. In 2D simulation, the axis are x and y. In the model, the nozzle is fixed and the substrate is mobile, we impose a constant speed boundary condition. However, we have a problem for the movement in the vertical direction to model the deposition of the second layer. Consequently, we have to find another approach to deposit the second layer. For this reason, it has been decided to add another nozzle to perform the second layer deposition. Figure 52 shows the deposition of the polymer on the substrate at different times. As it is represented in the image, the second nozzle lays down the second layer on the first layer from 2.60 s. This modified configuration enables us to observe the behavior of the first layer when we suppose to add another layer on it.

However, adding another nozzle to model, make the model more complicated and heavier to build.

Figure 53 shows the influence of the viscosity on the shape of the deposited layers. Different viscosities have been selected for this simulation: 100 Pa.s, 500 Pa.s, 1000 Pa.s and 5000 Pa.s. All of the simulations present 5 seconds of deposition.

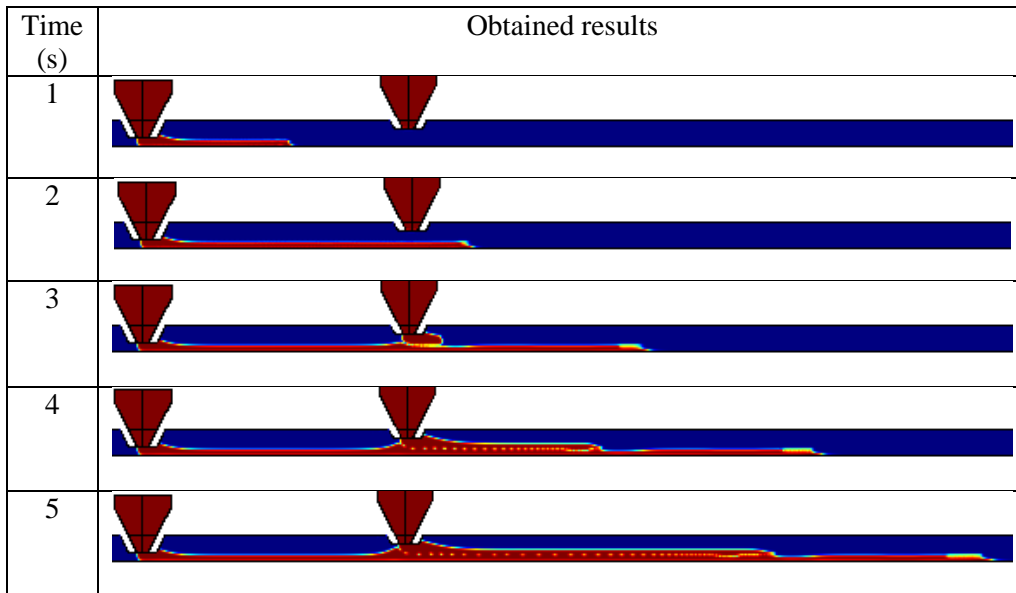


Figure 52: Deposition of two consecutive layers

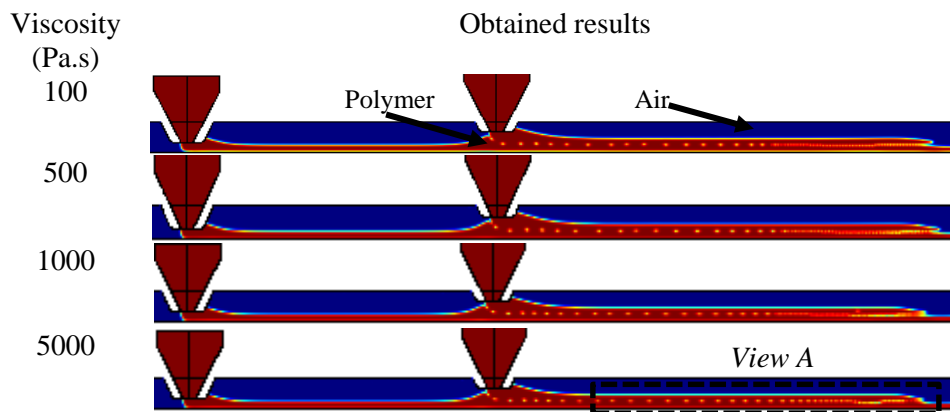


Figure 53: Deposition, at 5s, of the two layers for different viscosities

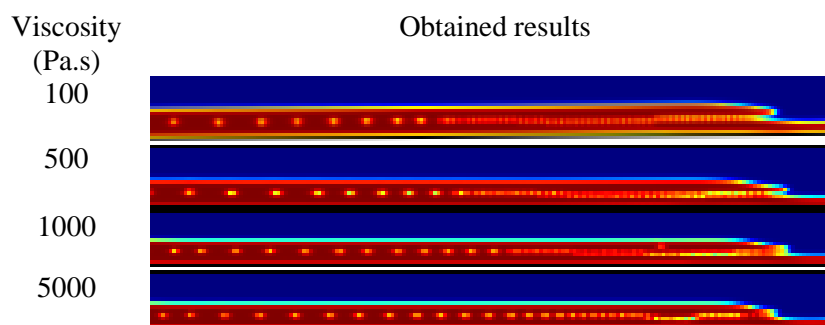


Figure 54: Detail view of two layer deposition

The interface of two layers is represented in Figure 54. The results for the viscosities from 100 Pa.s up to 5000 Pa.s show that, increasing the viscosity increases the gap between the two layers. The interdiffusion of the two layers is more evident for the viscosity of 100 to 1000 Pa.s. As consequence, in order to increase interdiffusion of two layers together we have to reduce the viscosity. In order to

decrease the viscosity, we could increase the temperature or increase the inlet velocity of the filament in the liquefier. In both of the cases, we have to take into account the degradation of the polymer at high temperature and flow instability at higher inlet velocity (high shear rate).

In all cases, the same amount of material is deposited on the layer. We have selected the inlet as inlet velocity (It is also possible to select the inlet as pressure).

3.2.4 Determination of the heat transfer during deposition of two layers

PDE equation has been added to the model in order to determine the heat transfer during the material deposition. Thermal diffusivity of air and polymer must be properly assign to each of them. For that reason, we have tried two other methods for describing the thermal diffusivity for the models. Hereby, we will explain our methodology to properly assign the thermal diffusivity to each phases:

As we have explained in the eq. 58 for the first approach as we have used the mixing law for thermal diffusivity.

Our second approach for the thermal diffusivity is defining a step function (eq. 59).

$$\text{If } \varphi \leq 0.5 \text{ then } \Omega = \Omega_{air} \text{ else } \Omega = \Omega_{polymer} \quad \text{eq. 59}$$

By defining assignment of the thermal diffusivity as a step function, the thermal property sharply changes from on phase to the other phase which could generate numerical errors.

And finally, the thermal diffusivity has been inserted as a combination of both methods. In this approach, the density and specific heat have been introduced as an mixing law and the thermal conductivity has been introduced in the model as the step function. The results for all the three approaches for the heat transfer at t=3s of the material deposition is represented in Figure 55.

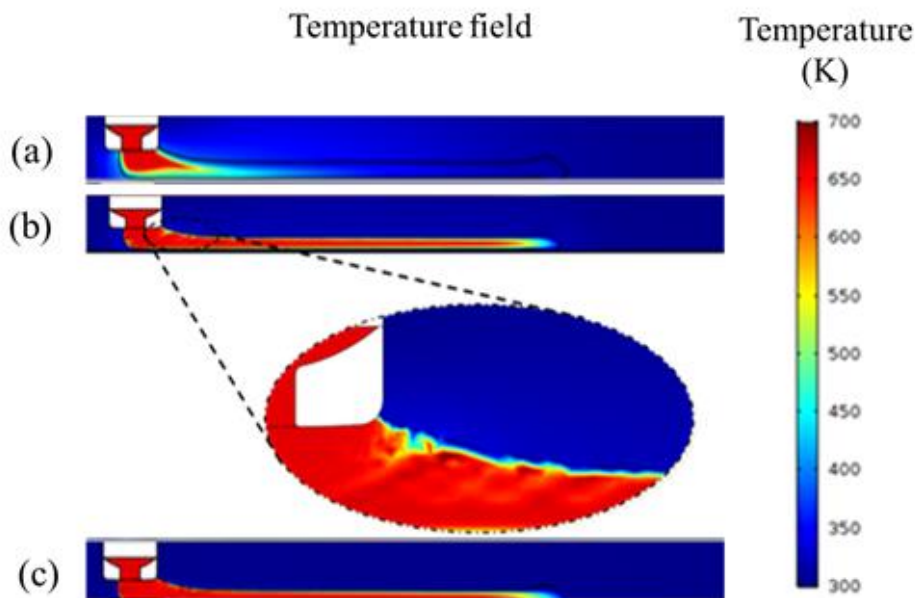


Figure 55: Heat transfer according to the different definitions of thermal diffusivity (a) additively law defined thermal diffusivity, (b) thermal diffusivity introduced as a step function, (c) thermal diffusivity introduced as a combination of additively law and step function.

The results represented in Figure 55 (a) for the additively defined law show that the cooling rate is very fast. For the mixing law defined thermal diffusivity, temperature decreases more than $100\text{ }^{\circ}\text{C}\cdot\text{s}^{-1}$. Indeed, in this case, the thermal diffusivity does not assign properly to the desired phases (the thermal diffusivity of the air is slightly less than real value of the thermal diffusivity of the air and thermal diffusivity of the polymer is higher than real value. This means the thermal diffusivity of the two phases are close together and are not real value of the thermal diffusivity of air and polymer). Consequently, the obtained results do not represent the reality. The results in Figure 55 (b) show that contrary to the additively defined thermal diffusivity, in the case of the step function, the thermal diffusivity has been properly assigned to each phase. However, in this case, the numerical errors occur in the model. In order to reduce the numerical errors and properly define the thermal diffusivity of each phase, we have decided to combine both approaches together. The results obtained for the combined approach in Figure 55 (c) shows that, in this case, we have reduced the numerical errors and in the same time, we have properly assigned the thermal diffusivity to each phase. Furthermore, the obtained results, in this case, are very close to the case when we have defined the thermal diffusivity as the step function. Consequently, a combined method has been used to assign the thermal diffusivity to the phases.

For the following numerical simulations of the material deposition on the substrate we will use the mixed method for the thermal diffusivity. However, we won't apply this method for the previous numerical simulation on free-form extrusion as it takes very long time.

3.2.5 Crystallization study

After integration of the heat transfer equation to our deposition model, we could go to the third step which is the determination of the kinetics of crystallization in the FFF process. This step is crucial in the case of a semi-crystalline polymer because, there is non-isothermal crystallization during deposition. The gradual deposition of the material makes the numerical simulation more complicated.

Our studies on the kinetics of crystallization is based on the non-isothermal crystallization equation of Nakamura [146]. According to Nakamura et al. [146], the percentage of the transformed phase from an amorphous state to the crystalline phase in a semi-crystalline polymer at non-isothermal condition could be obtained using eq. 60:

$$\frac{d\alpha}{dt} = nK(T)(1 - \alpha) \left[\ln \left(\frac{1}{1 - \alpha} \right) \right]^{\frac{n-1}{n}} \quad \text{eq. 60}$$

Where α is the transformed fraction of the polymer into the crystalline state, t is time, n is Avrami exponent, the same as the Avrami exponent in the isothermal study and $K(T)$ is the Nakamura kinetics of crystallization coefficient. $K(T)$ is a temperature dependent term in Nakamura equation.

Levy has applied non-isothermal crystallization equation of Nakamura to COMSOL [147]. Levy applied the Nakamura equation to determine the kinetics of crystallization of solid object in PEEK 150P and he proposed a COMSOL module in order to determine the kinetics of crystallization for the solid object.

However, his module is not directly suitable for the FFF process because it does not consider the velocity of the fluids. In order to apply the model to the fluids, we have added the convection term (presented in eq. 103) to the Nakamura equation to include the velocity of the fluids. We have to clarify that hereby the convective term is the term that take into account the velocity of the fluid in the system (or transport of the crystalline phases during the fluid flow) and must not be confused with the conduction and convection notion in the heat transfer study.

The Nakamura equation presents a singular derivative at the vicinity of $\alpha = 0$ and $\alpha = 1$. Therefore, a modification of the Nakamura function is proposed by extrapolating it below $\alpha_{\min} = 0.01$ and above $\alpha_{\max} = 0.99$ (the influence of these values could be studied). These modifications ensure:

- (i) a robust numerical integration by forcing real values of G when α is not in the interval $[0,1]$, and
- (ii) forces an artificial germination when $\alpha = 0$.

In the section 3.4, we will explain in more detail our approach to study the kinetics of crystallization in the FFF process.

3.3 Influence of printing parameters on the stability of deposited beads in fused filament fabrication of poly (lactic) acid

3.3.1 Importance of determining the shear rate and viscosity in the FFF process

As we have explained previously, the determination of the rheological properties of polymers such as shear rates, viscosity and the density in the FFF process are very important in order to improve the quality of the printed parts.

After achieving our initial studies on modelling the free-form extruder (presented in section 3.2) we will apply our model to the case of FFF in order to study the rheological properties and stability of the extrudate exiting from the nozzle. As explained in the diagram of Figure 56, the printing parameters (i.e. nozzle diameter, feed rate and layer height) affect the inlet velocity in the liquefier and therefore the shear rate. On the basis of the shear rate in the liquefier and the physical properties of the polymer (thermal transitions and rheological behavior), the viscosity field and the extrudate shape are predicted.

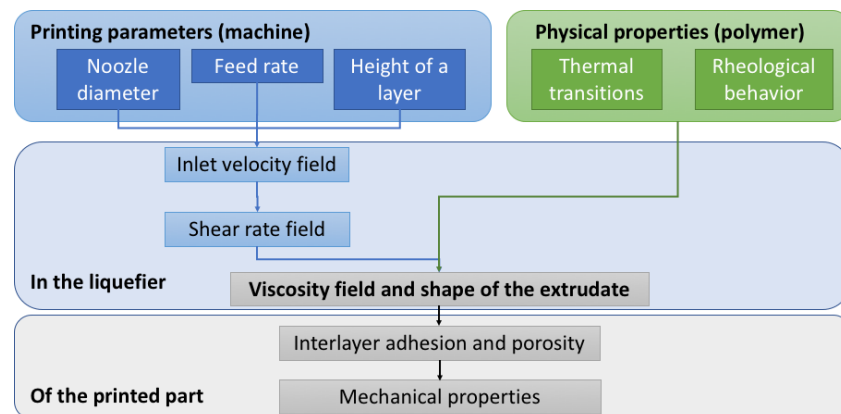


Figure 56: Diagram of the printing parameter effects and physical properties of the polymer on the mechanical properties of printed parts

The temperature of the heater is also used as one of the printing parameters, but it is not mentioned in the diagram because it does not directly affect the inlet velocity field. The present section aims to link the printing parameters and the physical properties of the polymer to the viscosity and the shape of the filament at the exit of the nozzle. The originality of our study is to propose a time-dependent numerical approach that also addresses the changes in the rheological properties with respect to the changes in the shear rate and temperature. In this work, the poly(lactic) acid (PLA) was selected. In the first part, the physical properties (thermal transitions and rheological) of the PLA were determined. In the second part, a relation was proposed to determine the inlet velocity of the polymeric filament in the liquefier according to the printing parameters (i.e. nozzle diameter, feed rate and layer thickness). Then, the

velocity field, shear rate field and viscosity of the PLA for the printing parameters were determined via numerical simulation and analytical study. Finally, the influence of the shear rate on the extrudate shape was investigated via experiments and numerical simulation.

3.3.2 Experimental set up

Measuring the pressure and shear rate are not feasible in commercial 3D and RepRap printers. Therefore, a laboratory extruder was used to study experimentally the fluid flow in a printer as close as feasible. This experimental study was conducted using an extruder system from ThermoFisher Company. As shown in Figure 57(a), the extruder has three units:

- The driver unit is a HAAKE PolyLab OS (not shown in Figure 57).
- The extruder unit is HAAKE Rheomex OS equipped with a single screw with a maximum rotating speed of 150 rpm.
- A gear pump, that is, HAAKE Melt pump OS with a maximum speed of 75 rpm.

At the outlet of the extruder, a 0.5 mm diameter die is used to represent the nozzle; its geometry is shown in Figure 57(b).

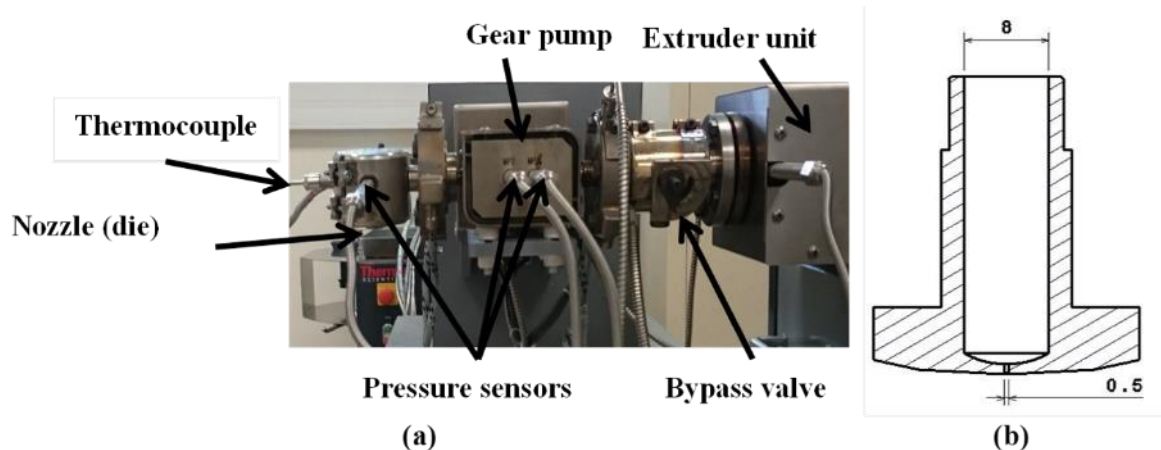


Figure 57: (a) Extruder system used for the experimental study. (b) Scheme of the 0.5-mm diameter nozzle

3.3.3 Rheological investigation of the polymer flow in the liquefier via analytical study

When the printing conditions, such as nozzle diameter and feed rate, vary, the inlet velocity and hence the shear rate change. Consequently, the viscosity of the fluid is also changed. Therefore, determining these properties and the influence of their variations on the quality of the manufactured part is important. The experimental observations have revealed that a higher viscosity results in liquefier clogging and a low viscosity causes inaccurate dimensions, low quality of the deposited filament and liquefier leakage. The filament undergoes temperature variations during the process and the temperature distribution directly influences the viscosity of the polymer.

All melted thermoplastic polymers demonstrate a shear-thinning behavior. The viscosity of shear-thinning fluids changes with temperature and shear rate, and the latter is related to the inlet velocity of the fluid in the liquefier. In the present section, the analytical equations for determining the variation of the viscosity in the liquefier for non-Newtonian fluids are explained.

For non-Newtonian fluids, the viscosity can be expressed in the most convenient form of a power law or by using the Carreau–Yasuda model which considers the Newtonian plateau at low shear rates. The

viscosity according to the shear rate is expressed by eq. 61, following the power law equation [112][113].

$$\eta = K|\dot{\gamma}|^{n-1} \text{ for shear - thinning fluids } (n < 1) \quad \text{eq. 61}$$

Where n is the pseudoplasticity index, K is the consistency coefficient and $\dot{\gamma}$ is the shear rate. By reversing the pseudoplasticity index, the fluidity constant φ is determined using eq. 62 and eq. 63. The parameter n , called ‘the pseudoplasticity index’, is the slope of the viscosity versus the shear rate curve. When the pseudoplasticity is above 1, the fluid exhibits a shear-thickening behavior. When the pseudoplasticity index is below 1, the fluid exhibits a shear-thinning behavior, where K is the viscosity at the shear rate of 1 s^{-1} . The reciprocal of viscosity is generally called ‘‘fluidity’’.

$$n = \frac{1}{m} \quad \text{eq. 62}$$

$$K = \varphi^{-\frac{1}{m}} \quad \text{eq. 63}$$

The fluidity constant φ represents the ability of the fluid to flow. Meanwhile, the viscosity of non-Newtonian fluid can be expressed as the Carreau–Yasuda model, which is presented in eq. 64.

$$\eta = \eta_{inf} + (\eta_0 - \eta_{inf})[1 + (\lambda\dot{\gamma})^a]^{\frac{n-1}{a}}, \quad \text{eq. 64}$$

where η_0 is the viscosity of the fluid at zero shear rate, η_{inf} is the viscosity of the fluid at infinite shear rate, λ is the relaxation time index, n is the power index, a is a dimensionless parameter describing the transition between the first Newtonian plateau and the power law zone and $\dot{\gamma}$ the shear rate. Irrespective of whether the equation is based on the power law or the Carreau–Yasuda model, the viscosity decreases when the shear rate increases. The shear rate dependency varies with the nature of the polymer, the temperature and the velocity field in the geometry. Furthermore, the temperature is regarded as constant with time at a fixed point in the FFF system.

For a shear-thinning fluid, the flow in the extruder is a Hagen–Poiseuille flow. Thus, the flow has a parabolic shape, implying that the velocity attains its maximum value at the center of the nozzle. Meanwhile, the value of the velocity field near the internal wall is zero. For non-Newtonian fluid, the fluid velocity can be determined using eq. 65 [148].

$$u(r) = \frac{3n+1}{n+1} \bar{V} \left[1 - \left(\frac{r}{R} \right)^{\frac{(1+n)}{n}} \right] \quad \text{eq. 65}$$

Where \bar{V} is the average inlet velocity of the fluid in the liquefier, r is the distance from the center of the nozzle, R is the nozzle radius and n is the power index in the Carreau–Yasuda model. The shear rate is determined by determining the velocity based on the radius of the internal nozzle diameter, which can be expressed in eq. 66.

$$\dot{\gamma} = \frac{du}{dr} = \frac{3n+1}{nR} \bar{V} \left[\left(\frac{r}{R} \right)^{\frac{1+n}{n}-1} \right] \quad \text{eq. 66}$$

Finally, the maximum shear rate, located at the internal wall of the nozzle, is obtained using eq. 67.

$$\dot{\gamma}_w = \frac{8(3n+1)Q}{n\pi(2R)^3} = \frac{(3n+1)\bar{V}}{nR}, \quad \text{eq. 67}$$

where Q is the volumetric flow rate and R is the maximum radius of the nozzle.

The viscosity curves of PLA in Figure 29 in Chapter 2 were fitted with the Carreau–Yasuda equation by using Origin software. The terms of the Carreau–Yasuda equation for the investigated temperatures are presented in Table 10. The Carreau–Yasuda model with these terms was implemented in the software to determine the flow properties in the liquefier.

Table 10: Values of terms of Carreau–Yasuda model for the viscosity curve fitting

	175°C	185°C	195°C	205°C
η_0	5169 ± 5	2480 ± 14	1945 ± 16	726 ± 6
η_{inf}	0	0	0	0
λ	0.048 ± 0.02	0.09 ± 0.5	0.08 ± 0.02	0.05 ± 0.01
a	0.82 ± 0.3	1.6 ± 0.8	1.931 ± 0.5	2.60 ± 0.01
n	0.52 ± 0.3	0.7 ± 0.3	0.693 ± 0.2	0.79 ± 0.11

3.3.4 Inlet velocity in the liquefier

Our optical observations and empirical investigations of the shape of the deposited beads revealed that the shape of the section of the filament was changed from the initial circular to an elongated oval shape during printing depending on the printing parameters. Figure 58 shows the final cross section of a deposited bead. The height of a layer, h , is one of the printing parameters.

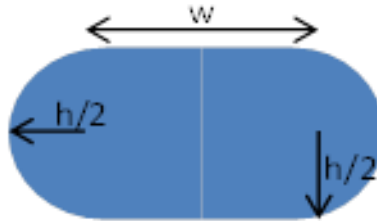


Figure 58: Cross section of a deposited bead

Considering the volume conservative law, the volume of the deposited bead was identical to that of the material exiting from the nozzle. Consequently, the inlet velocity of the polymer in the liquefier can be obtained as a function of the printing parameters, as expressed by equation eq. 68.

$$v = \frac{4f}{\pi D^2} \left(wh + \frac{\pi h^2}{4} \right) \quad \text{eq. 68}$$

where v is the inlet velocity of the polymer in the liquefier, h is the height of the deposited segment, f is the feed rate, D is the nozzle diameter and w is the width of the deposited segment. In most printers, the nozzle diameter is 0.3 mm or 0.5 mm. A nozzle of 0.5 mm diameter was selected for our experimental study. The printing parameters selected for this study are presented in Table 11.

Table 11: Values of the printing parameters

Notations	Printing parameters	Values and units
D	Diameter of the nozzle	0.5 mm

H	Height of the layer	0.7 mm
F	Feed rate	30 mm·s ⁻¹
w	Width of the bead	0.5 mm

3.3.5 Shear rate and viscosity of the polymer in the liquefier

The average inlet velocity (v) was determined using eq. 68 according to the printing parameters presented in Table 11. The inlet velocity field, shear rate field and viscosity of the polymer in the liquefier were determined via numerical simulation and analytical study for $T = 195\text{ }^{\circ}\text{C}$ and a flow rate of $18.5\text{ cm}^3\cdot\text{s}^{-1}$ according to the average inlet velocity.

The experimental study revealed that the PLA flows easily at temperatures higher than $200\text{ }^{\circ}\text{C}$. At lower temperatures (i.e. $175\text{ }^{\circ}\text{C}$), the PLA undergoes partial melting of the polymer pellets in the extruder screw, resulting in the blending of fluid and solid polymers. The DSC curve in Figure 19 in Chapter 2 shows that PLA was completely melted at $180\text{ }^{\circ}\text{C}$. At $185\text{ }^{\circ}\text{C}$, the polymer was melted but the viscosity remains very high. Consequently, a high torque was applied to induce the PLA flowing, which exceeded the limit of the apparatus. Moreover, in the RepRap open-source printers, the printing temperature was commonly $195\text{ }^{\circ}\text{C}$. Hence, the printing temperature of $195\text{ }^{\circ}\text{C}$ was selected for the experiment, as described in the present section.

Figure 59 highlights the influence of the nozzle diameter (one of the printing parameters) on the inlet velocity, shear rate and viscosity in the liquefier at $T = 195\text{ }^{\circ}\text{C}$. The results obtained via numerical simulation and analytical studies were consistent. For example, at a fixed flow rate and temperature, the inlet velocity and shear rate varied from 4 to $484\text{ mm}\cdot\text{s}^{-1}$ and from 27 to 7800 s^{-1} , respectively, when the nozzle diameter was changed from 2 mm to 0.3 mm . Similarly, the nozzle diameter highly influences the viscosity. The maximum value of the viscosity was determined to be $1850\text{ Pa}\cdot\text{s}$ (nozzle diameter of 2 mm), whereas the minimum value of the viscosity was $295\text{ Pa}\cdot\text{s}$ (nozzle diameter of 0.3 mm).

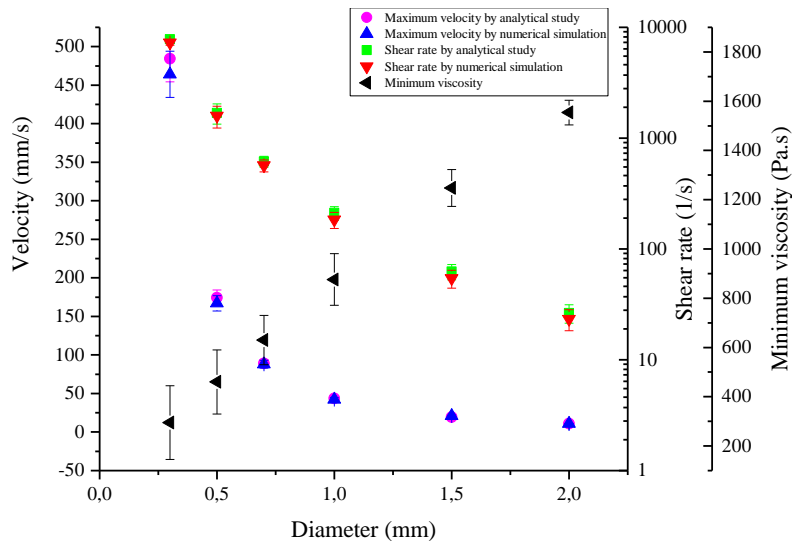


Figure 59: Influence of nozzle diameter on inlet velocity, shear rate and viscosity of the PLA at $T = 195\text{ }^{\circ}\text{C}$

Figure 60 shows the distribution of the inlet velocity, shear rate and viscosity fields for the nozzle diameter of 0.5 mm . The distribution of the velocity in the liquefier (assimilated to a tube) exhibited a large difference between the maximum at the center of the liquefier ($160\text{ mm}\cdot\text{s}^{-1}$) and minimum values near the internal wall (zero). The value zero was expected as it corresponds to the imposed condition of

adhesion at the wall of the tube (no slip condition). The shear rate changes from zero at the center of the liquefier to 1600 s^{-1} near the internal surface of the liquefier. Consequently, near the internal wall, the viscosity reaches its minimum value of approximately $400 \text{ Pa}\cdot\text{s}$, whereas at the center of the tube, the viscosity is at its maximum value, that is, approximately $1900 \text{ Pa}\cdot\text{s}$. Hence, the results obtained via numerical simulation are in good agreement with that obtained via analytical studies.

The viscosity variation from the internal wall up to the center of the liquefier is rapid because the viscosity at the center of the liquefier was at its Newtonian plateau. Moreover, the profile of the shear rate of the material in the liquefier has a parabolic shape. The viscosity near the internal wall of the nozzle is at its minimum value, whereas at the center of the nozzle, the viscosity reaches its maximum value. The parabolic shape of the shear rate profile illustrates the shear-thinning behavior of the PLA according to equation eq. 67.

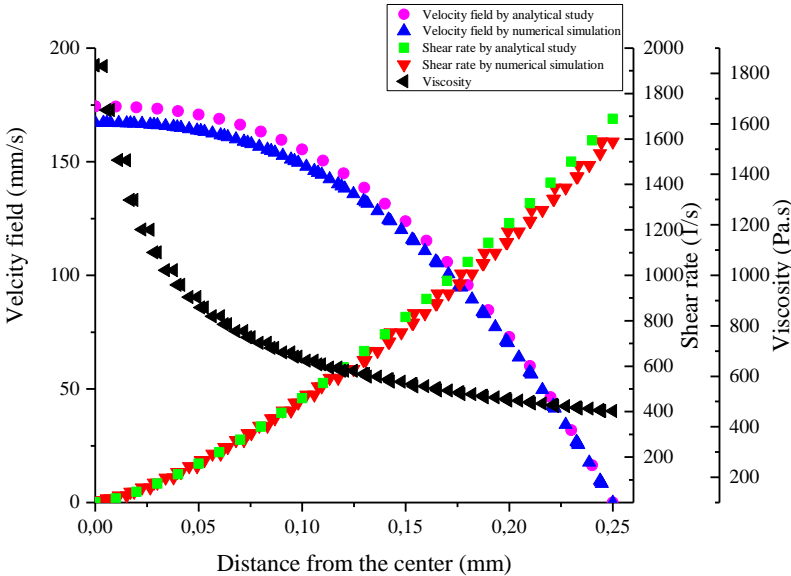


Figure 60: Distribution of velocity field, shear rate and viscosity in the liquefier determined via numerical simulation and analytical study

We now focus on the variation of the viscosity in the liquefier with respect to the distance from the center of the nozzle. The numerical simulation revealed that when the temperature increases, the maximum value of the shear rate value decreases.

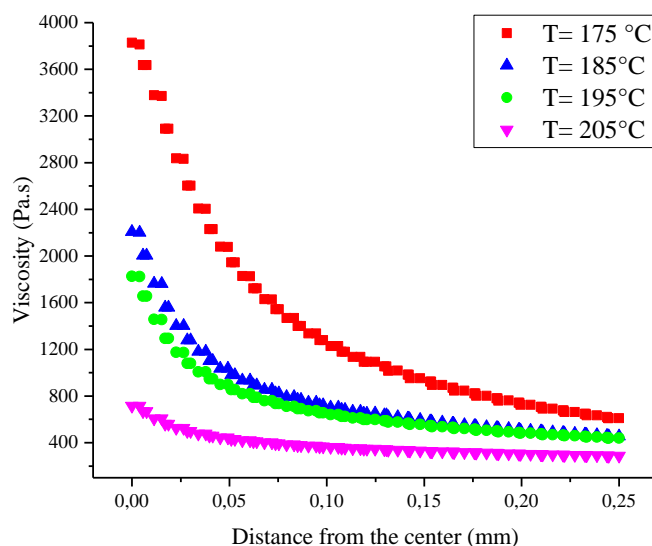


Figure 61: Distribution of the viscosity along the radius in the liquefier at various temperatures

Figure 61 shows the viscosity variation in the liquefier according to the distance from the center of the nozzle at various temperatures for an inlet velocity of $95 \text{ mm}\cdot\text{s}^{-1}$. Irrespective of the temperature, the fluid demonstrates a shear-thinning behavior. A comparison of the viscosity of the polymer at high temperature ($205 \text{ }^\circ\text{C}$) and at low temperature ($175 \text{ }^\circ\text{C}$) for the same inlet velocity and nozzle diameter revealed that when the temperature increases, the difference between the maximum and minimum values of the viscosity decreases. Hence, for $T = 175 \text{ }^\circ\text{C}$, the difference between the maximum and minimum viscosity was approximately $2800 \text{ Pa}\cdot\text{s}$, whereas for $T = 205 \text{ }^\circ\text{C}$, this difference was approximately $400 \text{ Pa}\cdot\text{s}$. Interestingly, for temperatures higher than $200 \text{ }^\circ\text{C}$, the variation of the viscosity according to the shear rate was weak, as shown in Figure 60. For example, at $205 \text{ }^\circ\text{C}$, when the polymer flows easily, the maximum viscosity at its Newtonian plateau was approximately $700 \text{ Pa}\cdot\text{s}$, whereas at very high shear rates (more than 1000 s^{-1}), it was approximately $400 \text{ Pa}\cdot\text{s}$.

High fluidity of the polymer at very low viscosities directly influences the quality of the printed parts. Although at the low viscosity, the coalescence of the beads would be better because the macromolecules exhibit higher mobility required to diffuse and to create entanglements. However, high fluidity results in low accuracy during the deposition of the beads. A deposited bead undergoes creep phenomena under influence of its weight right after exiting from the nozzle at low viscosities, thereby causing low dimensional accuracy of printed parts, especially during creation of the holes and bridges. At high temperature, when the viscosity is excessively low, extra-supports of the parts are necessary to print complex shapes.

3.3.6 Influence of shear rate on extrudate shapes

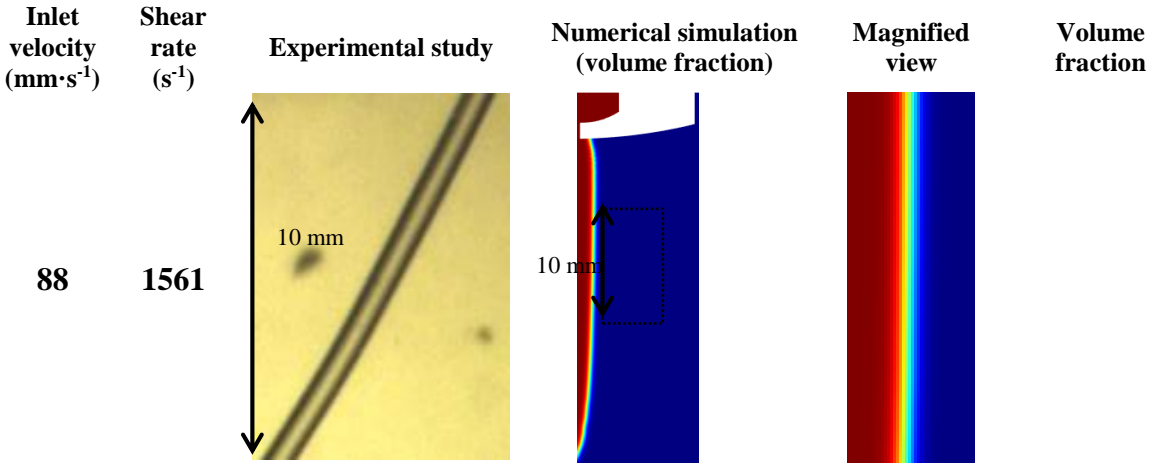
The polymer flow from the nozzle was regulated by controlling the speed of the pump during the experimental tests. Consequently, to precisely determine the shear rate, the weight flow rate was measured by cutting the extrudates at a constant time lapse. Then, the extrudates were weighted. By using the density of the PLA ($1.25 \text{ g}\cdot\text{mm}^{-3}$), the weight flow rate was converted to volumetric flow rate. Finally, the volumetric flow rate was converted to the shear rate and inlet velocity by using eq. 65 and eq. 67.

An identical procedure was applied for various pump speeds. Thereafter, the extrudates were observed under an optical microscope. The images of the extrudates obtained at the different inlet velocities and

shear rates at an isotherm of 195°C are presented in Figure 62. The shape of the extrudates obtained via experimental study and numerical simulation were compared.

The influence of the shear rate on the shape of the extrudates was determined from 1200 s⁻¹ to more than 5000 s⁻¹. The optical observations revealed that for the lowest shear rates, the shape of the extrudate was cylindrical with a smooth surface, whereas at higher shear rates and inlet velocities, deformations were observed on the surface. The limit appeared to be approximately 4000 s⁻¹. Below this value, the shape of the extrudate became regular, whereas when the shear exceeded 4000 s⁻¹, the flow was unstable, and the extrudate displayed defects. At 4100 s⁻¹, some macroscopic instability was observed on the extrudate. At high shear stresses, the contour of the stream changed abruptly from that of a cylinder to an irregular shape. As the shear rate increases beyond the critical rate, at which the change in shape occurred, the degree of irregularity of the emerging stream increases [149].

As shown in Figure 62, the numerical simulation presents the volume fraction field of the fluid in the system. Note that the value of the color function goes from 1 (i.e. red), the polymer, to 0 (i.e. blue), the air. The interface of the two fluids is considered to be 0.5. The results of the TPF numerical simulations revealed that at higher inlet velocities and shear rates, certain instability of the polymer flow was observed. This result is consistent with the experimental observations. When the inlet velocity was below 145 mm.s⁻¹, the polymer flow was stable and no deformation of the extrudate was observed. When the inlet velocity was increased, some instabilities were observed. At the inlet velocity of 232 mm s⁻¹, the maximum shear rate in the system attained 2763 s⁻¹. At this shear rate, instabilities were observed, appearing under wavy flow. Therefore, the numerical simulation reliably recreated the experimentally observed instabilities. By comparing the instability and wavy shape of the extrudate at the maximum shear rate equal to 2763 s⁻¹ with the shape of the extrudate at higher shear rates, these instabilities were apparently thinner than those at higher shear rates. Thus, increasing the inlet velocity and shear rate highly influenced the stability and wavy shape of the extrudates owing to the variation in the shear rate and viscosity of the polymer along the liquefier radius. The difference between the viscosity at the center and near the internal wall of the liquefier was high, thereby causing high extensional stress when the profile exits from the nozzle. This ‘sharkskin’ effect on the extrudate is typically observed for the extrusion of polymers [149] [150][151]. The ‘sharkskin’ is a defect that occurs as deep cracks on the surface of the extrudate. These cracks are forming during stress relaxation, causing a rough surface.



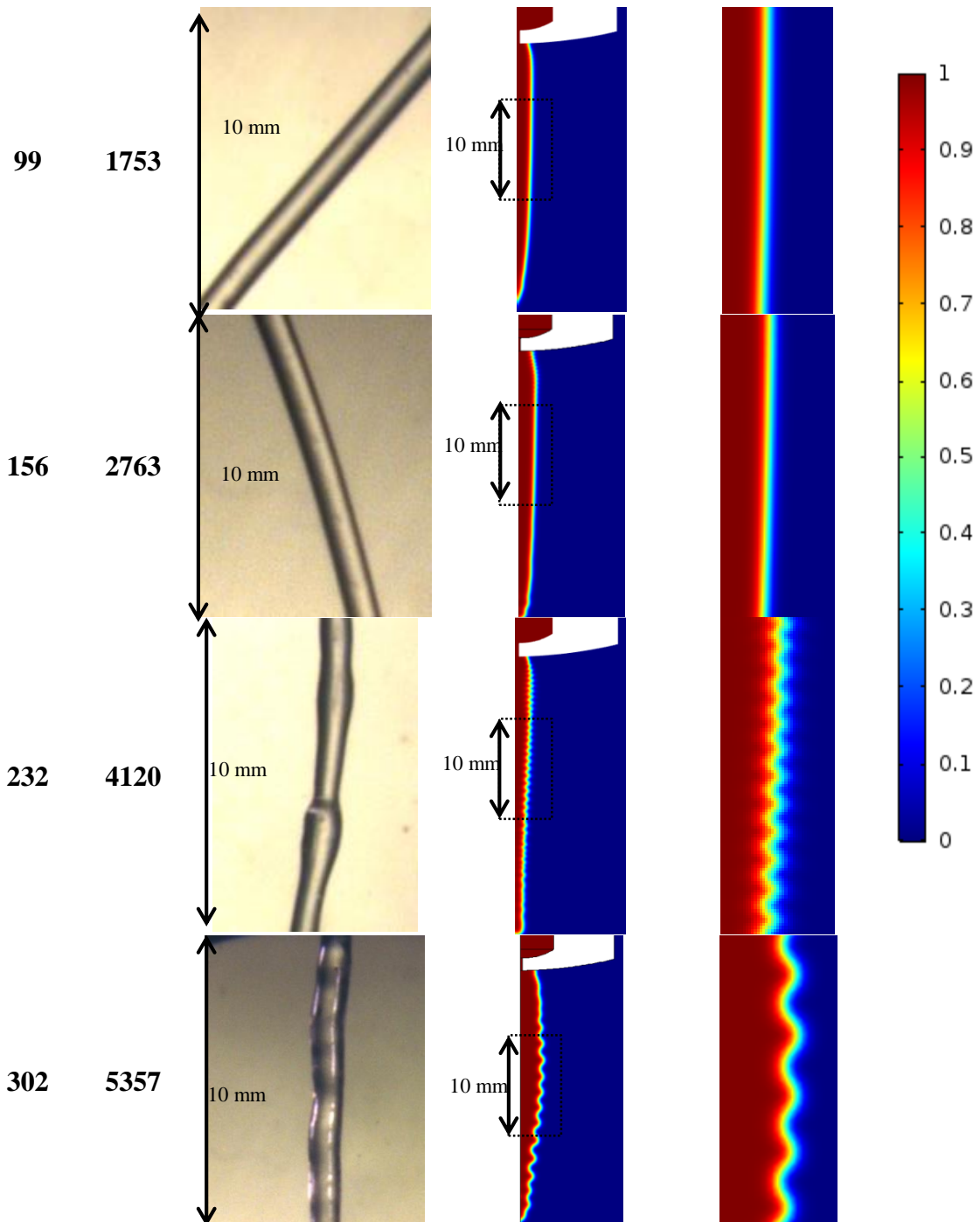


Figure 62: Influence of inlet velocity and shear rate on the shape of the extrudate exiting from the nozzle with a diameter of 0.5 mm

Based on the previous results, the following conditions are recommended for printing PLA:

The printing temperature must be higher than 190 °C to ensure a completely melted filament in the liquefier and prevent the clogging of the liquefier. However, the maximum temperature for printing must not exceed 210 °C. At temperatures higher than 210 °C, the viscosity of the polymer was excessively low, causing severe deformation during printing and degradation of the polymer. Moreover, the variation in the shear rate along the nozzle diameter should be reduced because it results in flow instabilities. We have observed that to achieve this condition, the temperature should be higher than 190 °C. Therefore, the recommended temperature is 200 °C.

To reduce the flow instabilities and surface defects, the shear rate during printing must be below 4000 s⁻¹. The nozzle diameter highly influences the shear rate. That is, increasing the nozzle diameter decreases the shear rate. However, the nozzle diameter influences the roughness (surface quality) and precision of the manufactured parts. Increasing the nozzle diameter reduces the precision of the printed part. Therefore, to reduce the fluid instability and maintain the precision of the printed parts, a nozzle diameter of 0.4 mm or 0.5 mm is recommended.

The volume flow rate was determined on the basis of the feed rate and the geometry of the deposited bead, such as the height of the layer and width of the deposited bead. Therefore, the height of the deposited bead must not exceed 0.4 mm, and the feed rate must be below 30 mm·s⁻¹.

3.4 Determination of the die swelling for PEEK

From experimental tests, the observations show that the diameter of the extrudate increases right after exiting from the nozzle. This phenomenon is commonly known as die swelling phenomenon or Barus effect. The die swelling phenomenon is related to the equilibrium of the velocity profile and the viscoelastic behavior of the polymer.

3.4.1 Theoretical basis of the die swelling

Tanner [152] has proposed an analytical equation in order to determine the die swelling in extrusion in the case of infinite capillary. His model is based on the imposed recoverable strain by normal stress. The swelling ratio according to Tanner for infinite capillary is represented in eq. 69.

$$B = \left[1 + \frac{1}{2} \left(\frac{N_1}{2\tau_w} \right)^2 \right]^{\frac{1}{6}} \quad \text{eq. 69}$$

Where B is the die swelling ratio, N_1 is the normal stress and τ_w is the shear stress near the wall. B and N_1 could be determined using eq. 70 and eq. 71 respectively.

$$B = \frac{d_e}{d} \quad \text{eq. 70}$$

$$N_1 = \frac{2}{3} \tau_w \left[(B)^4 + \frac{2}{(B)^2} \right]^{\frac{1}{2}} \quad \text{eq. 71}$$

Where D is the diameter of the extrudate and d is the nozzle diameter. Determining N_1 by eq. 71 is done by experimental study.

$\frac{N_1}{2\tau_w}$ ratio is the Weissenberg Number. The Weissenberg number (Wi) is a dimensionless number used in the study of viscoelastic flows [153]. The Weissenberg number characterizes the ratio of the elastic stress to viscous stress. The Weissenberg number could be determined using eq. 72 [154]:

$$W_i = \frac{\text{Elastic force}}{\text{Viscous force}} = \frac{\sigma_{xx} - \sigma_{yy}}{\tau_{xy}} = \frac{\eta \lambda \dot{\gamma}^2}{\eta \dot{\gamma}} = \dot{\gamma} t_w \quad \text{eq. 72}$$

Where σ_{xx} and σ_{yy} are the principal stresses, $\dot{\gamma}$ is the shear rate, τ_{xy} is the shear stress, η is viscosity and t_w is the relaxation time of the polymer.

The Tanner equation assumes that the length of the capillary nozzle is infinite (long capillary), which means when the polymer exits from the nozzle, it is fully relaxed. However, his assumptions are not

valid if the capillary is short. In this case, the entry flow is more complicated (the molecular chains are still under effect of diameter changing) and the entry effect is more prominent [155]. Consequently, Liang has described the die swell for the short capillary as eq. 73.

$$B = (1 + \lambda_l S_R)^{\frac{1}{2}} \quad \text{eq. 73}$$

Where S_R is recoverable shear stress exists in the eq. 69 which could determine by Weissenberg Number and λ_l is the elastic strain induced by the stored energy in the capillary reservoir. S_R and λ_l are determined by using eq. 74 and eq. 75.

$$S_R = \left(\frac{N_1}{2\tau_w} \right)^{\frac{1}{2}} \quad \text{eq. 74}$$

$$\lambda_l = 0.5 \tan \alpha_0 \quad \text{eq. 75}$$

α_0 is the half-entry convergence angle. The convergence angle is the angle creates by the fluid flow and the nozzle wall, as shown in the scheme in Figure 63.

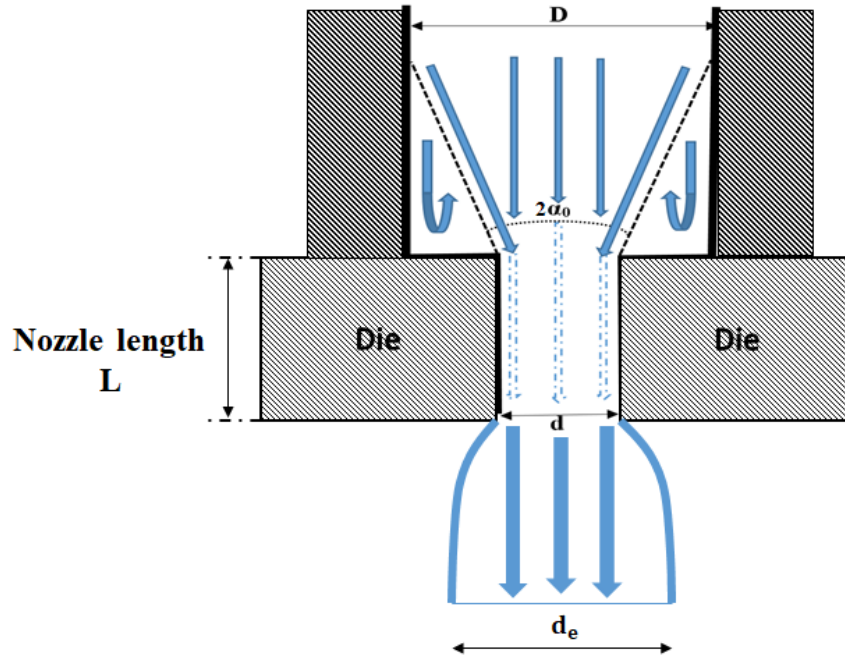


Figure 63: Representation of the die swelling and convergence angle in the extrusion

The half-entry convergence angle is dependent to the pressure loss, the viscoelastic behavior and the geometry of the reservoir. α_0 is determined by eq. 76 and eq. 77.

$$\tan \alpha_0 = \frac{1}{e} \left[\frac{4 \left(1 - \frac{1}{B} \right)^{1.5(n+1)}}{3(n+10)} + \frac{2\xi((B)^{1.5(n+1)} - 1)}{3(1-n)} \right] \quad \text{eq. 76}$$

Where D is the diameter of the reservoir, d is the capillary diameter, n is the pseudoplasticity index, ξ is the pressure loss coefficient and e is the Bagley entrance correction factor. Bagley factor could be determined from the pressure loss during the process.

$$\frac{1}{e} = \frac{\Delta P}{2\tau_w} \quad \text{eq. 77}$$

According to Cogswell [156], the half-entry convergence for a laminar flow is a dependent function of viscosity and extensional viscosity (eq. 78) .

$$\tan \alpha_0 = \sqrt{\frac{2\eta(\dot{\gamma}_{wr})}{\eta_E(\dot{\gamma}_{wr})}} \quad \text{eq. 78}$$

Where η is the viscosity near the wall of the reservoir, η_E is the extensional viscosity and $\dot{\gamma}_{wr}$ Maximum shear rate in reservoir. The term $\frac{\eta}{\eta_E}$ is known as Trouton ratio which is about 3 for the Newtonian fluids and for the polymers at their Newtonian Plateau. At higher shear rate, for the polymers, the Trouton ratio could be obtained using eq. 79 [157].

$$Tr = \frac{\eta(\dot{\gamma}_{wr})}{\eta(\sqrt{3}\dot{\gamma}_{wr})} \quad \text{eq. 79}$$

In the following in order to determine the Trouton ratio we will use eq. 78.

3.4.2 Elongational viscosity

The material flow in the TPF numerical simulation is viscosity dependent. In the TPF numerical simulation, the viscosity could be inserted as a power law or Carreau's model. In our numerical simulation, we have inserted the viscosity as the Carreau model (eq. 64). The terms of the Carreau's model for each temperature is determined by correlation with the viscosity curve obtained experimentally.

The viscosity of the melted PEEK 450G has been determined with two different methods for low shear rates and high shear rates. A parallel-plate configuration was used to determine the viscosity at low shear rates with frequency sweeps test from 0.01 s^{-1} to 100 s^{-1} within the linear viscoelastic domain. The results of complex viscosity at different temperatures for PEEK are gathered in Chapter 2. For the highest shear rates, from 100 s^{-1} to $10\,000 \text{ s}^{-1}$, the extensional die from ThermoFisher Company and extrusion apparatus have been used to measure the extensional viscosity. Figure 64 illustrates the results for the viscosity determined by the two experimental methods at 556 K ($383 \text{ }^\circ\text{C}$). The complex viscosity is represented by the blue points and the shear viscosity determined by extensional die is depicted by the pink points. At very high shear rates, the viscosity of PEEK drastically reduces up to 40 Pa.s . Furthermore, the extensional viscosity determined by the die is represented in red points. The results obtained with the extensional die below 10 s^{-1} show a good correlation with those obtained with the parallel-plate geometry. However, in the case of PEEK at 100 s^{-1} , the viscosity of PEEK is close to 170 Pa.s while at the same shear rate, the extensional viscosity reaches 7000 Pa.s .

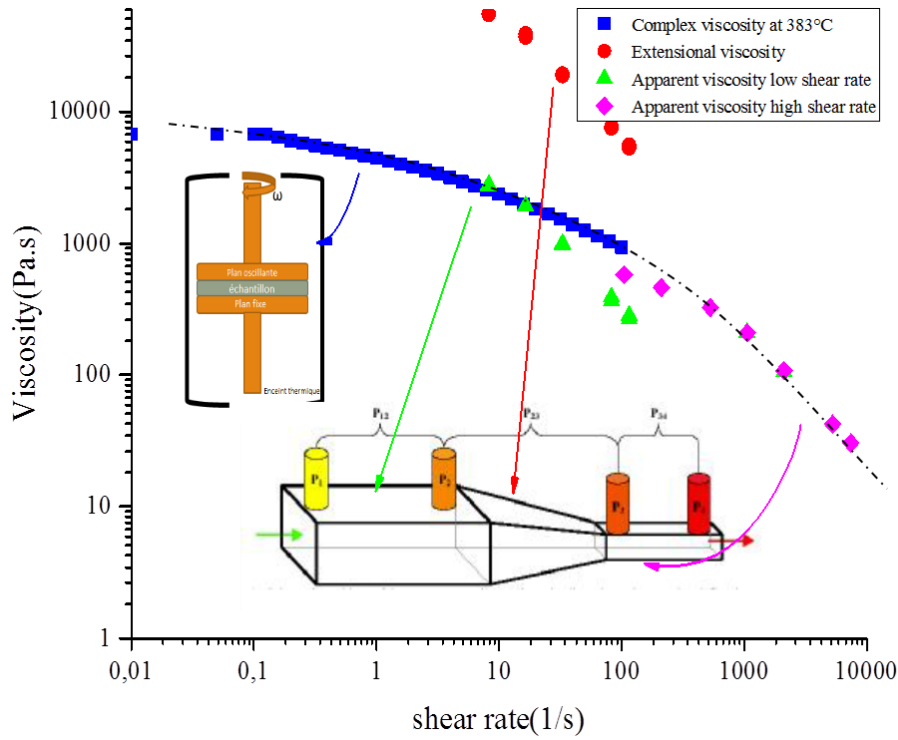


Figure 64: Viscosity of the PEEK at 656 K (383°C)

Linking the dynamic (complex) viscosity to the shear viscosity was done by Cox-Merz relation [158]. As it is represented in eq. 80, Cox et al. noticed that the steady state shear viscosity at a given shear rate is equal to the dynamic viscosity at the same frequency in the linear domain, using empirical studies.

$$\eta(\dot{\gamma} = \omega) = |\eta^*|(\omega) \quad \text{eq. 80}$$

Whereas the shear viscosity is temperature and shear rate dependent as represented in eq. 81, the viscosity of shear-thinning fluids is well described with the Carreau model represented in eq. 99.

$$\eta(\dot{\gamma}, T) = a_T \eta(\dot{\gamma} a_T, T_0) \quad \text{eq. 81}$$

a_T is expressed as the Arrhenius law presented in eq. 82 [153].

$$a_T = \exp \left[\frac{E_a}{R} \left(\frac{1}{T} - \frac{1}{T_0} \right) \right] \quad \text{eq. 82}$$

E_a is the activation energy of PEEK at 82.8 kJ.mol⁻¹, R is the gas constant at 8.314 J.K⁻¹.mol⁻¹, T is the temperature and T_0 is the reference temperature in our case at 556 K (383 °C).

The terms of the Carreau model have been extracted from the fitting of the viscosity curves for both polymers. Table 12 shows the values of the Carreau model terms determined by interpolating the points.

In the TPF simulation, the viscosity is inserted as the Carreau model which could enable the determination of the viscosity according to shear rate and temperature.

Table 12: Terms of Carreau model for PEEK at 656 K

Polymer	PEEK
Temperature	655 K
η_0 (Pa.s)	7071 \mp 153
η_{inf} (Pa.s)	0
λ	1.45 \mp 0.6
a	0.78 \mp 0.12
n	0.59 \mp 0.06

3.4.3 Determination of the pressure drop in the extruder's nozzle

When the polymer melt enters from a reservoir into a small channel, it is subjected to high shear stress. The shear is leading to form an entrance converging flow due to the melt viscoelasticity and the contraction of the channel. In general, entry converging flow consists of elongation flow and shear flow. Consequently, obvious entry pressure losses will be produced. The effect of entrance convergence is an important factor for inducing unsteady flow during extrusion of polymer melts under given conditions. Entry converging flow has been an interesting topic in polymer processing rheology because it influences directly the quality of extruded products and production rate of processing equipment [159] [153].

As it is represented in Figure 65 there are three different regions where the pressure drop occurs. As it is shown in eq. 83 total pressure drop in an extruder's nozzle is the sum of the pressure drop in all regions of the extruder.

$$\Delta P_{Total} = \Delta P_1 + \Delta P_2 + \Delta P_3 + \Delta P_{ex} \quad \text{eq. 83}$$

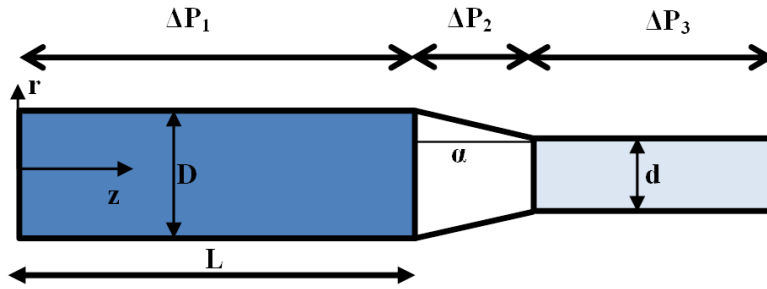


Figure 65: Illustration of different pressure drop region in an extruder's nozzle

The term, ΔP_{ex} refers to the pressure drop at the exit of the die. In the eq. 83 , the term ΔP_{ex} is relatively small; consequently, the influence of the exit pressure drop could be neglected. ΔP_2 is the entry pressure drop in the extruder. As it is depicted in the eq. 84, [153] the pressure drop in the entry of the nozzle is geometry and polymer property dependent.

$$\Delta P_2 = 2K \ln Z \left(2K_1 \dot{\gamma}_w^n + \frac{1}{2} K K_2 \dot{\gamma}_w^m \right) + \frac{K_1 \dot{\gamma}_w^n \left[1 - \left(\frac{1}{Z} \right)^{3n} \right]}{3nK} \quad \text{eq. 84}$$

Where K is a function of the entry angle determined by eq. 87 and Z is the ratio of entry diameter to exit diameter ($Z = \frac{D}{d}$). n and K_1 are the properties for shear flow viscosity; m and K_2 are the properties of

elongational (extensional) viscosity. $\dot{\gamma}_w$ and $\dot{\gamma}_a$ are the shear rates near the wall and the apparent shear rate respectively. The shear rate near the wall and the apparent shear rate are obtained by eq. 85 and eq. 86 respectively.

$$\dot{\gamma}_w = \frac{3n + 1}{4n} \dot{\gamma}_a \quad \text{eq. 85}$$

$$\dot{\gamma}_a = \frac{32Q}{\pi^3 D} \quad \text{eq. 86}$$

$$K = \frac{1}{2} \tan \alpha_0 \quad \text{eq. 87}$$

Furthermore, ΔP_1 and ΔP_3 are determined from the laminar Poiseuille flow pressure loss equation. for the laminar Poiseuille flow in a pipe, the pressure loss is determined by eq. 88.

$$\Delta P_l = \frac{32\eta l V_{avg}}{D^2} \quad \text{eq. 88}$$

Where V_{avg} is the average velocity of the flow and l is the length of the nozzle or capillary [160] .

The die swell ratio is calculated in the part 3.5.4 from the previous equations.

3.4.4 Determination of the relaxation time for PEEK

As it is represented in Figure 66, a macromolecular chain is symbolized in a fixed network of obstacles. The macromolecular chain length is more than the distance L' .

between two close obstacles. Each contact between an obstacle and the chain forms an entanglement. We consider that the distance L between these obstacles is constant. The movement of the chain to release from these obstacles is called reptation, from de De Gennes theory [8].

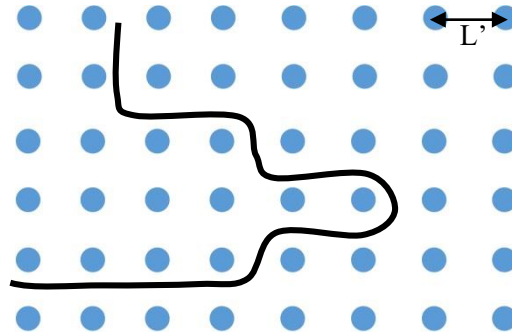


Figure 66: A macromolecular chain in a network of fixed obstacles

The relaxation time is the time associated with large scale motion in the structure of the polymer chain. The relaxation time typically refers to the time required by the chain to return to its equilibrium state.

Self-bonding, also called auto-adhesion, autohesion or welding, is the bonding of two surfaces of an identical polymer. Autohesion takes place at a temperature above the glass transition temperature (T_g) and below or above the melting temperature (T_m), without an adhesive. Voyutskii [161] and Vanenin [162] studied in 1960s the autohesion mechanisms, based on the diffusion of macromolecules above T_g . Then, the theory of reptation exposed by De Gennes [163] and [8] and F.Brochard-Wyart [164]

described the motion of polymeric chains and was successful in predicting the molecular weight dependency of the self-diffusion.

As it is represented in Figure 67 (a), when two surfaces (two layers in the case of the FFF process) are brought together, they form an interface. If the temperature during the process is above the melting temperature of the polymer, the macromolecular chains are in the amorphous state. In the amorphous state, the macromolecular chains are randomly coiled together. Under temperature and pressure, the macromolecular chains release from the obstacles (called entanglements) and pass through the interface to diffuse in the other layer as seen in Figure 67 (b). The time necessary for a chain to release from the obstacles is the relaxation time defined above. Right after diffusion, the macromolecules create new entanglements.

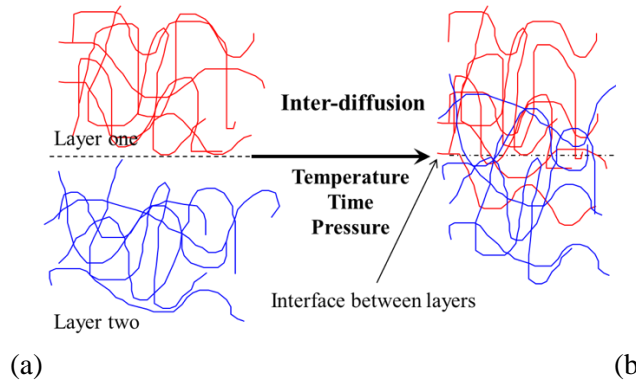


Figure 67: Representation of the interdiffusion of the macromolecular chains (a) Initial state of the two layers before interdiffusion (b) after diffusion of the macromolecular chains

In semi-crystalline polymers, the macromolecular diffusion is reduced because the crystalline phase acts as obstacles on the pathway of the macromolecules. In order to facilitate the interdiffusion of the two layers of semi-crystalline polymers, the processing temperature should be such that the polymer is in its melted state. On cooling from the melting state to room temperature, the time for which the macromolecules are able to interdiffuse must be equal to or higher than the macromolecular relaxation time. For the semi-crystalline polymers, the motion of the macromolecular chains are stopped or strongly reduced when the crystallization occurs. So that time available for interdiffusion is the time available on cooling from the melted state to the crystallization.

The relaxation time can be determined from experimental data of oscillatory tests in the viscoelastic linear regime and the terminal relaxation zone. The average relaxation time is obtained by eq. 89.

$$\frac{1}{t_n} = \frac{1}{\eta_0 G_N^0} \quad \text{eq. 89}$$

Where τ_n is the average relaxation time, η_0 is the zero-shear rate viscosity, and G_N^0 is the plateau modulus. The values of η_0 and G_N^0 are obtained from experiments. t_n can be obtained by experiments, it is the projection of the intersection of the tangent line on loss moduli and the tangent line of storage moduli at rubbery plateau (G_N^0) on the frequency axis. At the terminal regime the slope of the tangent line on the loss moduli and storage moduli must be 1 and 2 respectively.

The weight-average terminal relaxation time (t_w) is determined using eq. 90.

$$\frac{1}{t_w} = \frac{1}{\omega_w} = \frac{1}{\eta_0 J_e^0} \quad \text{eq. 90}$$

Where J_e^0 is the steady-state recoverable shear compliance and ω_w is the projection of the intersection of tangent line of loss moduli and storage moduli at the terminal regime on frequency axis. The shear compliance is also the projection of the intersection point on the moduli axis. The intersection point and the tangent lines is represented in the Figure 70. The breadth of the relaxation time distribution is the obtained using eq. 91.

$$\frac{t_w}{t_n} = G_N^0 J_e^0 \quad \text{eq. 91}$$

For nearly monodisperse polymers, the breadth of the relaxation time distribution is between 2 and 3 [165]. The zero shear rate viscosity and the compliance of elasticity could be also determined using eq. 92 and eq. 93 respectively.

$$\eta_0 = \lim_{\omega \rightarrow 0} \frac{G''(\omega)}{\omega} \quad \text{eq. 92}$$

$$J_e^0 = \frac{1}{\eta_0^2} \lim_{\omega \rightarrow 0} \left[\frac{G'(\omega)}{\omega^2} \right] = \lim_{\omega \rightarrow 0} \left[\frac{G'(\omega)}{G''(\omega)^2} \right] \quad \text{eq. 93}$$

It is convenient to model the linear viscoelastic response of polymers by rheological models. The simplest one is the Maxwell model, which has only one relaxation time. Then, all the relaxation times that can be determined from a frequency sweep response are identical [165].

Previously, we have explained that PEEK undergoes degradation by chain combination when exposed to thermo-oxidative environment for longer than a few minutes. The rheological measurements at low frequency takes a time long enough to induce this degradation. This makes the determination of the viscosity at Newtonian plateau impossible. For that, the Cole-Cole [166] [167] representation is a convenient way to extrapolate the viscosity curve up to Newtonian plateau.

Figure 68 is the Cole-Cole representation of loss (η'') viscosity versus storage (η') viscosity obtained from frequency sweeps at various temperatures. The shape of the Cole-Cole curve is supposed to form a half-circle; the deviation from this circular predicted shape confirms that the polymer undergoes drastic degradation at high temperature and low shear rate. The zero-shear viscosity η_0 is obtained by extrapolating the half-circle up to the x-axis.

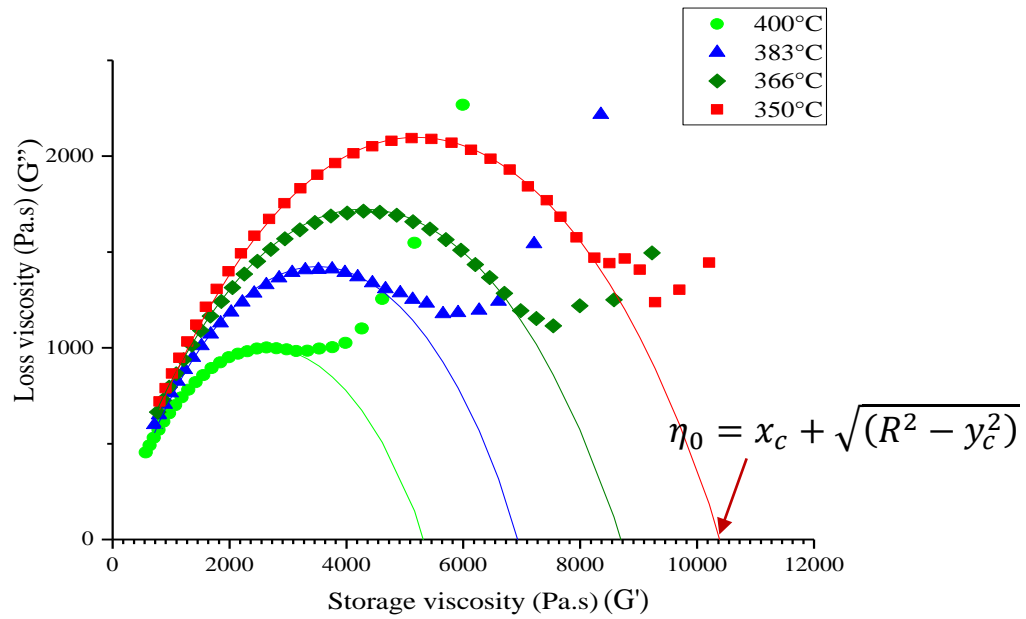


Figure 68: Cole-Cole representation for the determination of η_0 from frequency sweeps

Furthermore, representation of the loss moduli toward storage modul in log graph leads to a straight line could be used in order to determine $\tan \alpha$. Deviation from this straight line represents the degradation of the polymer.

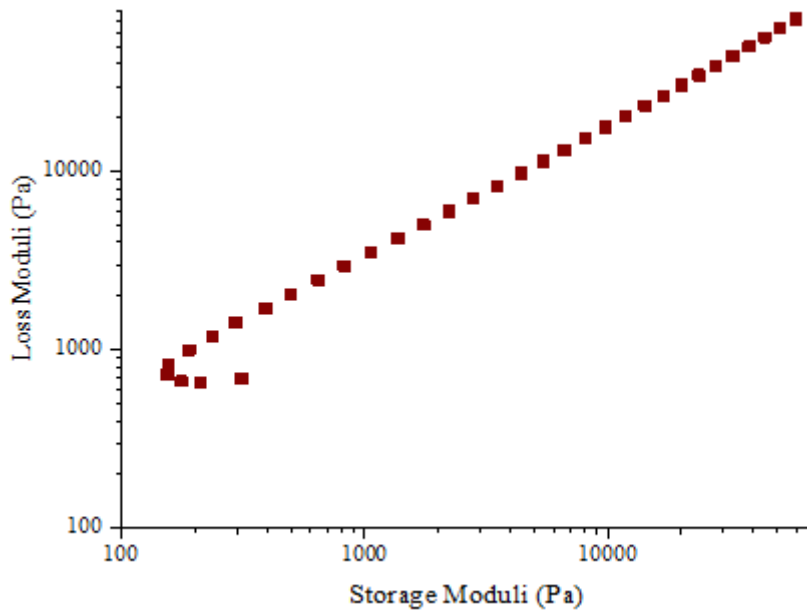


Figure 69: Cole-Cole presentation of the loss moduli versus storage moduli for $T=383 \text{ }^\circ\text{C}$

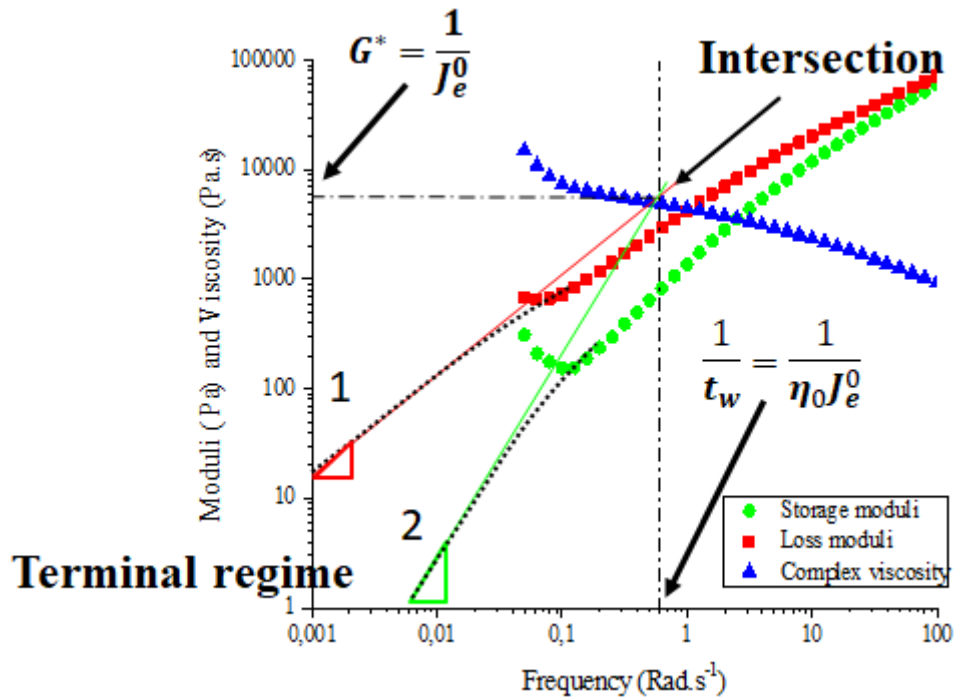


Figure 70: Determination of shear compliance and relaxation time for T=383 °C

Weight-average terminal relaxation time (t_w) has been determined directly from the projection of the intersection point and also multiplication of the zero-shear rate viscosity. Variation of the obtained results by two methodologies show the importance of proper selection of the intersection point. Weight-average terminal relaxation time at T=383 °C is represented in Table 13.

Table 13: Determination of relaxation time according to two methodologies

Method	$\eta_0 J_e^0$	$\frac{1}{\omega_w}$
Relaxation time (t_w) (s.)	$1,75 \pm 0,15$	$2,09 \pm 0,15$

Figure 71 plots the weight-average relaxation time at 350 °C, 366 °C, 383 °C and 400 °C determined from the obtained results. As expected, the relaxation times are shorter for the highest temperatures. The Arrhenius law reminded in eq. 94, shows a good agreement with the relaxation times as it is represented in Figure 71

$$\tau_w = A e^{\frac{-E_a}{RT}} \quad \text{eq. 94}$$

Where, E_a is the activation energy, T the temperature, R is the gas constant and A is the pre-exponential factor.

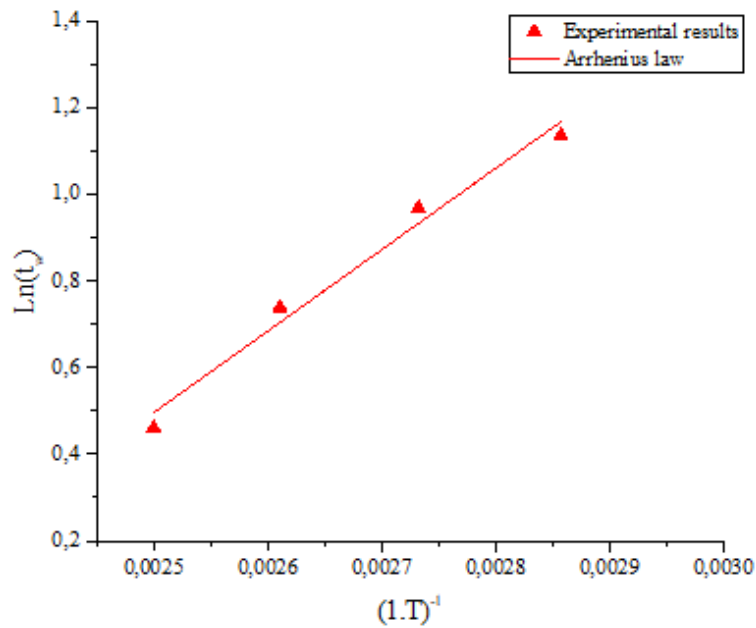


Figure 71: Relaxation time versus temperature for PEEK determined from loss (G'') and storage (G') moduli and, curve of Arrhenius law for relaxation times

The Arrhenius law allows the determination of relaxation times at any temperature when the experimental data are not available. The relaxation times for PEEK are comprised between 1.5 and 3.5 seconds at respectively 400 °C and 340 °C. These relaxation times are longer than those measured for other polymers. Indeed, the viscosity of PEEK is quite high compared to other melted polymers. This is due to the complex chemical structure of PEEK where the double bonds and aromatic cycles reduce the mobility of the chains.

3.4.5 Die swelling for PEEK

Prior to determine the die swelling for PEEK, we have determined the half-angle convergence according to extensional viscosity determined experimentally in section 3.4.2 and the Cogswell equation (eq. 78).

Depending on the shear rate in reservoir the Trouton ratio and consequently the convergence angle change. The variation of the half-convergence angle according to shear rate in the reservoir is represented in Figure 72.

Considering the diameter of the reservoir and the inlet velocity is constant it is considered that the Trouton ratio is constant in our studies. The Trouton ratio has been calculated to be 19, with this Trouton ratio, the half-entry convergence angle is $\alpha_0 = 18^\circ$ (The convergence angle is 36°).

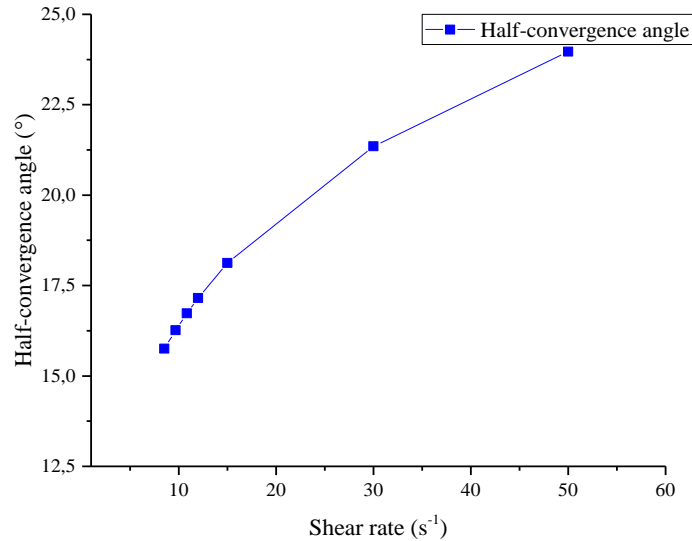


Figure 72: Influence of the shear rate on the half convergence angle

We have previously explained the numerical and analytical approaches in order to determine the shear rate in the FFF process in the section 3.3. In the same section, the shear rate during the process of PLA has been determined by COMSOL Multiphysics. In the following, we determine the shear rate for PEEK and the die swelling ratio is calculated by two different analytical studies developed previously for short capillary and infinite capillary.

Firstly, the influence of the temperature on the die swelling for PEEK is represented in Figure 73. The selected temperatures are the same as those chosen for the determination of the relaxation times. For the calculation, the assumptions are the following ones:

- The convergence angle of the extrudate is 36 °.
- The velocity is constant at 99 mm.s⁻¹.
- The maximum shear rate is constant at 1562 s⁻¹. This value is a consequence of the inlet velocity and the flow properties of the melted polymer.

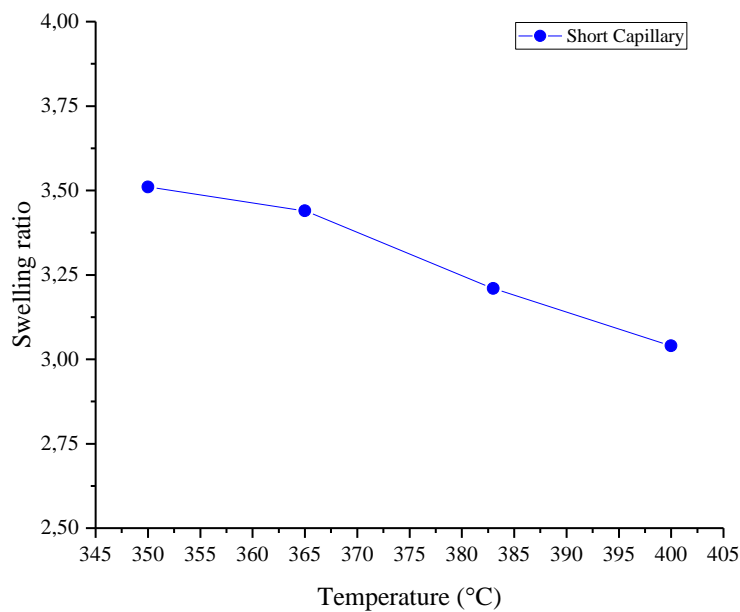


Figure 73: Influence of the temperature on the die swelling for PEEK

When the temperature increases, the die swelling ratio slightly decreases. This is due to a reduction of the relaxation time.

Consequently, in order to reduce the die swelling (and increase the dimensional accuracy) a higher temperature should be selected as printing temperature. This is in line with the proposition made by Tseng et al. [99] concerning the selection of 390 °C as the liquefier temperature to reduce the residual stress.

The influence of the inlet velocity on the die swelling at 383 °C is represented in Figure 74.

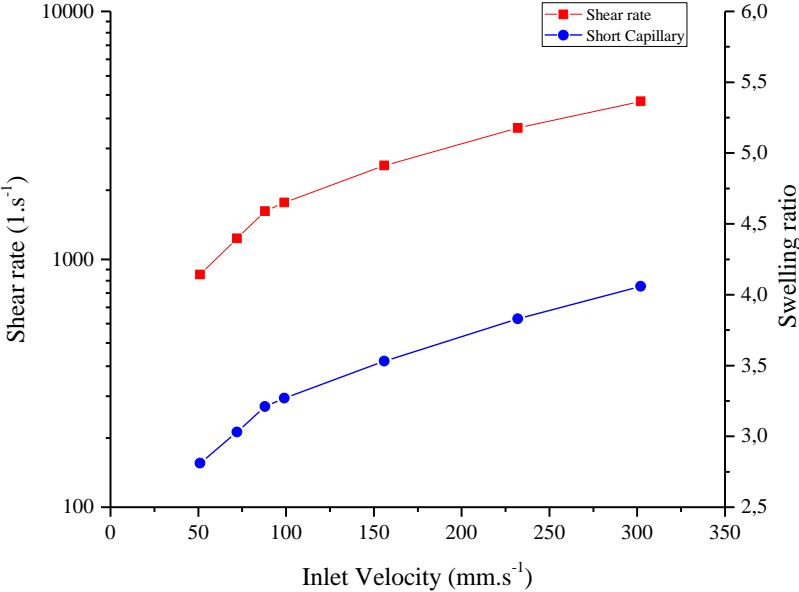


Figure 74: Influence of the inlet velocity on the shear rate and die swelling for PEEK at 383 °C

As expected, increasing the inlet velocity leads to increase the die swelling ratio. For the conventional parameters in the FFF process, the shear rate is below 1000 s⁻¹ and so the maximum die swelling ratio will be less than 2.5 in these conditions.

Moreover, the influence of the nozzle diameter on the die swelling has been determined at 383 °C. In all the cases, the inlet velocity is chosen at 99 mm.s⁻¹.

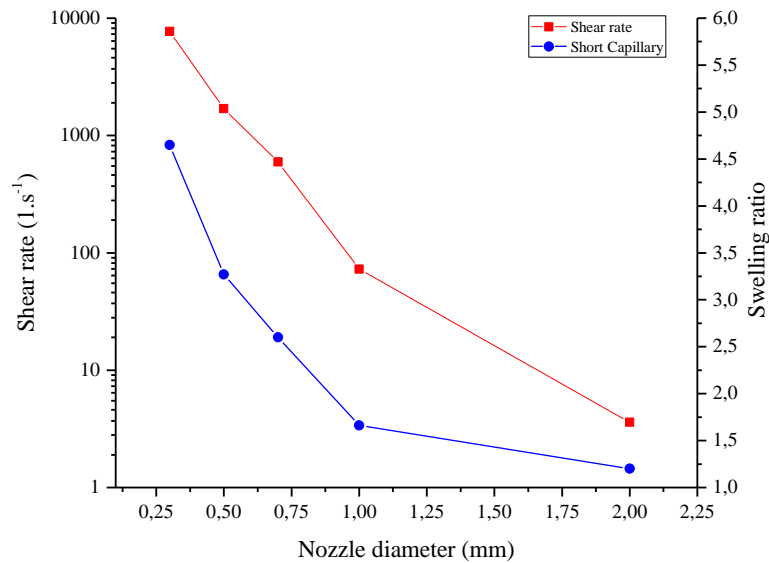


Figure 75: Influence of the nozzle diameter on the shear rate and die swelling for PEEK at 383 °C

The results show that increasing the nozzle diameter highly influences on the die swelling and the shear rate. Both equations for the die swelling give in very close results. For instance, the die swelling ratio is 1.5 for a nozzle diameter of 2 mm. But for a nozzle diameter of 3 mm, which is the common diameter of filaments, the die swelling ratio would be about 1.2.

The temperature is 383 °C and inlet velocity is 99 mm.s⁻¹. The Tanner's equation is independent from the converging angle, while the die swelling at short capillary highly depends on the converging angle. As it is represented in Figure 76, decreasing the convergence angle decreases the die swelling ratio. Consequently, in order to reduce the die swelling, the convergence angle of the nozzle should be decreased.

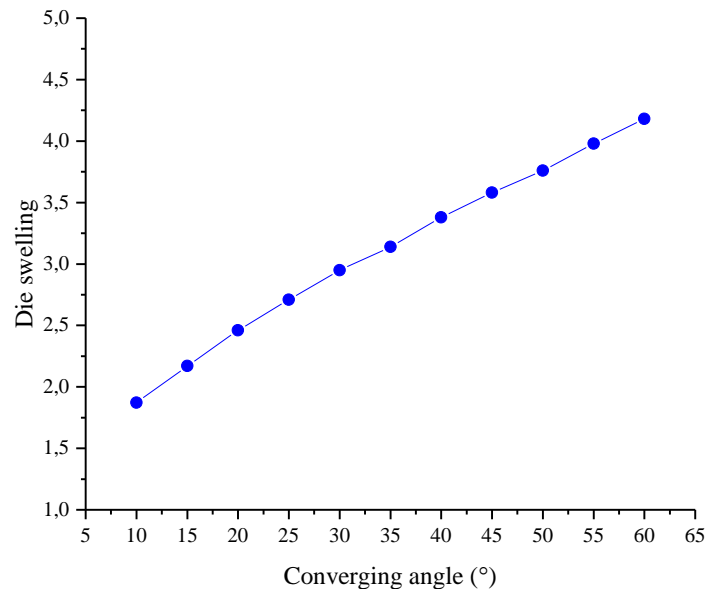


Figure 76: Influence of the convergence angle on the die swelling for the short capillary die determined for PEEK at 383 °C for 0.5 mm diameter nozzle

Lastly, from the results presented, several points may be highlighted, to reduce the die swelling ratio:

- Modifications on the geometry of the capillary: the ratio of the length of the capillary to nozzle diameter (L/d) must be infinite or as big as possible. Higher ratio of the capillary lead to leads to better relaxation of the polymer melt when it is entering from the reservoir to the capillary. Furthermore, the nozzle diameter must be increase (or D/d ratio of the must be smaller possible). In the other word, the diameter of the nozzle and the length of the capillary must be biggest possible and the diameter of the reservoir must be close nozzle diameter.
- The temperature should be high, while preventing degradation when polymers are sensitive to thermo-oxidative aging.
- The inlet velocity should be decreased.
- The pressure loss must be reduced. To reduce the pressure loss, we have to increase the temperature. Also in the case of the production extruder (not the case of FFF liquefier) we have to use the screen packs (or filters) or use screens with larger openings. Moreover, pressure drop occurs because of frictional forces. Reducing the frictional forces could reduce the pressure drop.

In general cases, in the FFF process, the die swelling ratio will be between 1 (no swelling) and 2.5.

3.5 Crystallization kinetics of PEEK in the FFF process

Despite many studies on the crystallization of PEEK, none of them presents the non-isothermal crystallization of PEEK 450G. Additionally, there is no isothermal crystallization study on this grade of PEEK from its glass transition temperature up to the melting temperature. Furthermore, these studies are mainly focused on the morphology and the crystalline phase of PEEK. Consequently, a crystallization study of PEEK is necessary in order to model the crystallization in the FFF process applied to PEEK.

As it is represented in Figure 77, the current section is composed of two steps towards the determination of the crystallinity ratio for PEEK in the FFF process. In the first step, which is represented in orange color, the isothermal and non-isothermal crystallization study of PEEK has been carried out by DSC for the temperature ranging from 595 K (322 °C) to 585 K (312 °C). The results obtained by the experimental study have been extended to the whole crystallization range from glass transition (400 K) up to the melting temperature (623 K) by Hoffman-Lauritzen equation. The non-isothermal crystallization of PEEK was determined using Nakamura equation. The second step represented in green color in Figure 77 consists of numerical simulation of the material deposition in order to determine the temperature and the crystallinity ratio.

Worth to mention, determining the heat transfer in the FFF process experimentally requires special equipment such as infrared camera. Furthermore, the determination of the crystallinity ratio in the FFF process is usually difficult and not cost-effective. Consequently, a simulation approach is necessary and complementary to determine the crystallinity ratio.

According to our bibliography study, it seems that there is no numerical simulation of material flow exiting from the nozzle. Simultaneously, there is no numerical study on heat transfer for an extrudate exposed to air.

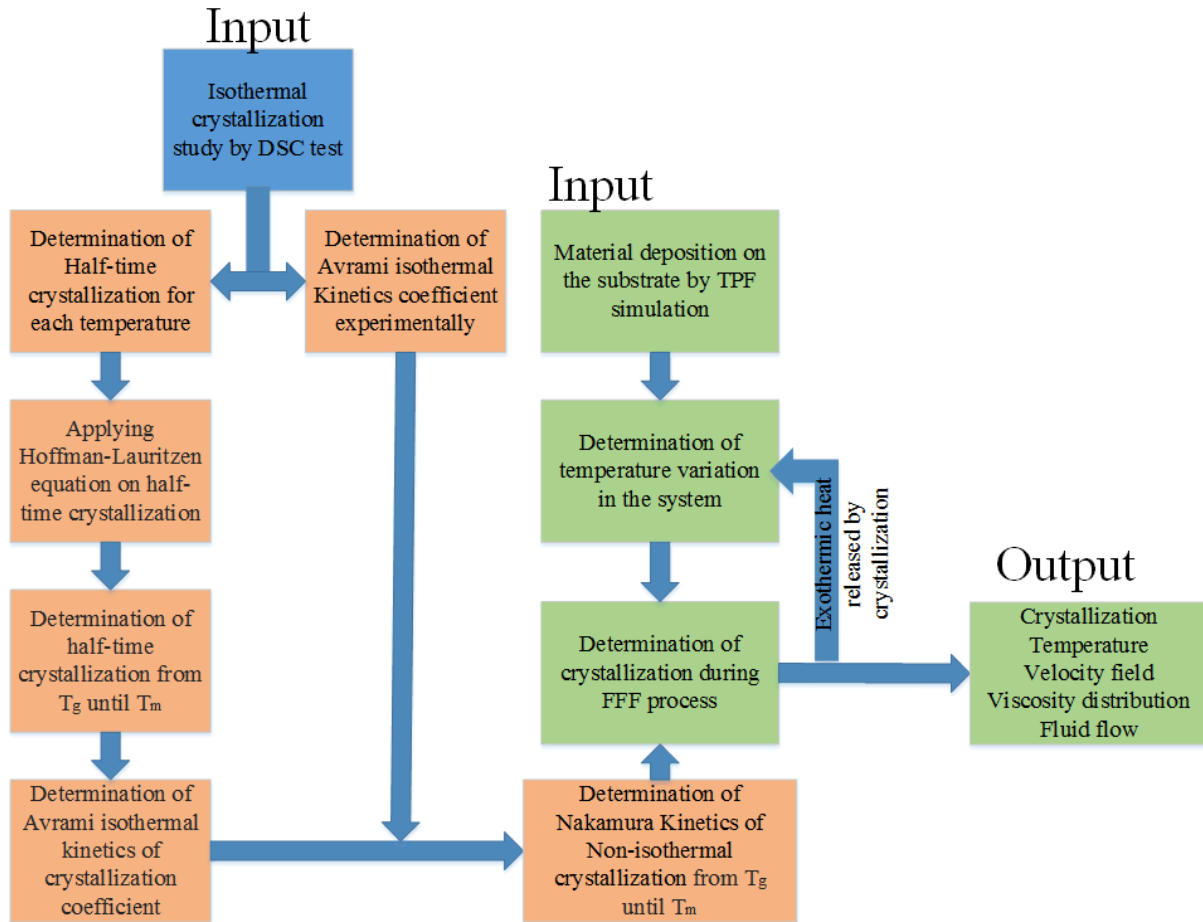


Figure 77: Sequence of the works done in this study in order to determine the crystallization kinetics in the FFF process

3.5.1 Isothermal crystallization

As it is represented in eq. 95, crystallinity ratio of a semi-crystalline polymer is the ratio of endothermic crystallization enthalpy to the enthalpy of the same polymer at its fully crystalline state. The enthalpy of fully crystalline PEEK is 130 J.g^{-1} [125]. The enthalpy of crystallization is the area under the peak of crystallization determined by DSC test. Figure 78 shows the schematic presentation of the peak in the crystallization curve.

$$\alpha(t) = \frac{\int_{t_1}^{t_i} \delta h}{\Delta H_{100}} \quad \text{eq. 95}$$

Where $\alpha(t)$ is the crystallinity ratio at different times during isothermal crystallization, δh is the crystallization enthalpy and $\Delta H_{100\%}$ is the enthalpy of crystallization for the fully crystallized polymer.

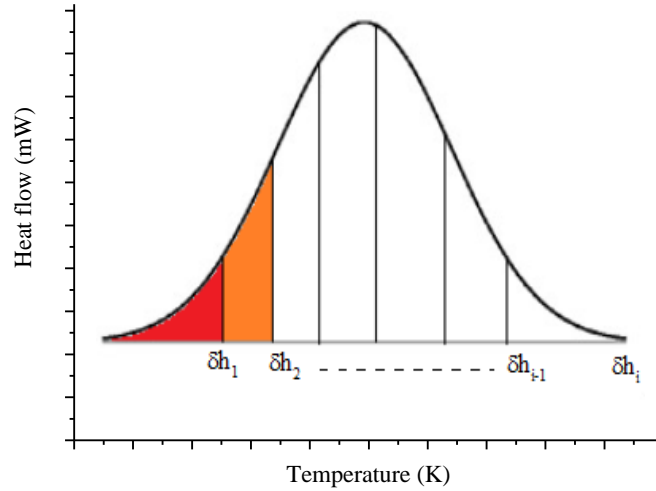


Figure 78: Schematic presentation of the crystallization curve and its enthalpy at different temperatures

For the polymers, the Avrami equation describes the kinetics of the transformation of the amorphous phase to the crystalline phase under isothermal condition [168][169]. As it is represented in eq. 96, using Avrami equation, we could determine the crystallization fraction at the isothermal temperature according to time. For each isothermal value, we have to determine the parameters of the Avrami equation separately. eq. 97 shows the logarithmic form of eq. 96.

$$\alpha = 1 - \exp(-kt^n) \quad \text{eq. 96}$$

$$\ln(-\ln[1 - \alpha(t)]) = \ln k_{av} + n \ln t \quad \text{eq. 97}$$

Where $\alpha(t)$ is the fraction of the transformed phase from the amorphous state to the crystalline state, k_{av} is the Avrami kinetics of crystallization coefficient and n is the Avrami exponent. By plotting $\ln(-\ln[1 - \alpha(t)])$ versus $\ln t$ for each isothermal temperature exclusively, n is the slope and k_{av} the intercept with the ordinate axis. The Avrami equation shows that increasing k_{av} with constant value of the n and α leads to increase of the kinetics of crystallization and consequently crystallization ratio. It could also have concluded that by increasing t and n , crystallization ratio will increase.

As the matter of fact, Avrami study is a post-treatment on the results of the DSC tests. These terms could be obtained for the temperature range from glass transition to melting temperature. However, for a few polymers and specifically PEEK, the crystallization kinetics is too fast. Accordingly, determining the isothermal crystallization for some temperature is beyond the limits of a current DSC apparatus and applying the Avrami equation on these temperatures is impossible. This lately means, even at the very fast cooling rates, from the equilibrium melting state to the targeted isothermal temperature, the polymer undergoes crystallization during the cooling ramp. Consequently, the determination of the Avrami terms by DSC for these polymers, is only possible when its crystallization kinetics is relatively slow. Experimentally, it is observed that the crystallization kinetics close to glass transition and melting temperature is very slow. Slow crystallization kinetics makes the determination of the Avrami terms possible with conventional DSC machines. Figure 79 shows the peak of non-isothermal crystallization (cooling ramp) of PEEK by DSC under cooling rate of 30 K.min⁻¹. According to Figure 79, although the cooling rate of the polymer is relatively high, the polymer undergoes crystallization starting at 583 K and finishing at 524 K. According to Figure 79, considering that there is no crystallization above 583 K, it is concluded that in the case of PEEK, we could isothermally study the crystallization for the temperature above 583 K by DSC. However, for determining the non-isothermal crystallization in the

FFF process, we have to obtain the Avrami terms for all the temperature range from the glass transition until the melting temperature.

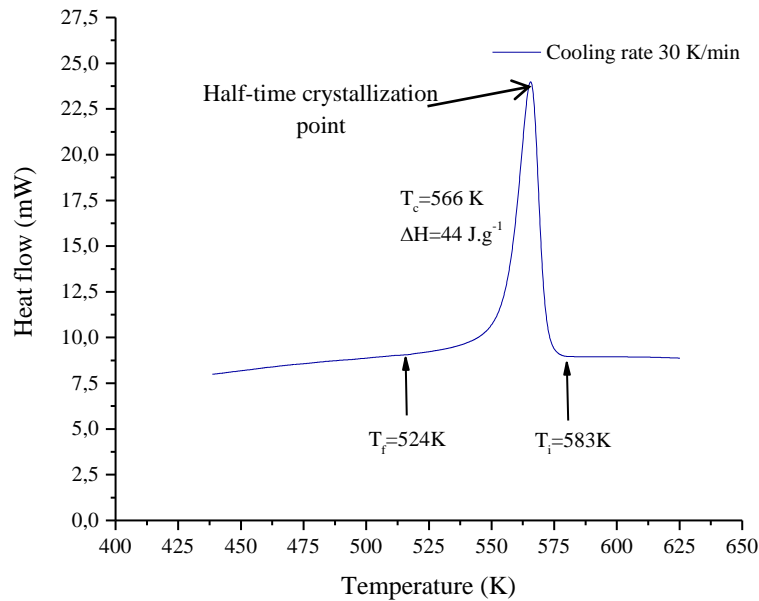


Figure 79: Crystallization of PEEK 450G with 30 K.min⁻¹ cooling rates. Crystallization starts at T = 583 K

Hoffman-Lauritzen equation has been used in order to determine the Avrami terms below 583 K. Extrapolating the Hoffman-Lauritzen equation on the results determined by experimental study and DSC test could help to predict the crystallization of PEEK in the whole crystallization range from melting temperature until glass transition. eq. 98 shows the Hoffman-Lauritzen equation which is used to predict the isothermal crystallization of PEEK below 583 K.

Hoffman-Lauritzen equation is used to predict the Avrami kinetics of crystallization ($k_{av.}$) or half-time isothermal crystallization. In this approach, it is considered that the crystallization of polymer is symmetrical from both sides of the half-time crystallization.

$$\left(\frac{1}{t_{1/2}}\right) = K_0 \exp\left(\frac{-U}{R(T - T_\infty)}\right) \exp\left(\frac{-K_G(T + T_0)}{2T^2 \Delta T}\right) \quad \text{eq. 98}$$

Where $t_{1/2}$ is the half-time crystallization. The first exponential term refers to the driving force of crystallization and the second exponential term refers to the mobility of the molecular chains. U is the diffusional activation energy for the transport of crystallizable segments at the liquid-solid interface [170][171], R is the gas constant, K_G is nucleation characteristics which influence on the position of the axial peak of the $k_{av.}$ T_∞ is the temperature where motion associated with viscous flow ceases which is normally 30 K below the glass transition ($T_g - 30 \text{ K}$) [172]. T_0 is the equilibrium melting temperature which is obtained by the linear Hoffman-Week method for PEEK [173]. Table 14 shows the values of the constants used in the Hoffman-Lauritzen equation. K_G and K_0 will be determined by interpolating the Hoffman-Lauritzen equation on the experimental data obtained by DSC.

Table 14: The value of the constants in the Hoffman-Lauritzen equation

U	6300 J.mol⁻¹
R	8.314 J.mol⁻¹.K⁻¹
T_∞	400 K
T₀	663 K

3.5.2 Non-isothermal crystallization

According to Nakamura et al. [146], the ratio of the transformed phase from an amorphous state to the crystalline phase in a semi-crystalline polymer at non-isothermal condition could be obtained using eq. 99:

$$\alpha(t) = 1 - \exp\left(-\left(\int_0^t K(T) d\tau\right)^n\right) \quad \text{eq. 99}$$

Where $\alpha(t)$ is the transformed fraction of the polymer into the crystalline state, t is the time, n is the Avrami exponent, the same as Avrami exponent in the isothermal study and $K(T)$ is Nakamura kinetics of crystallization coefficient. eq. 99 could be explained as a differential form in eq. 100.

$$\frac{d\alpha}{dt} = nK(T)(1 - \alpha) \left[\ln\left(\frac{1}{1 - \alpha}\right) \right]^{\frac{n-1}{n}} \quad \text{eq. 100}$$

Nakamura kinetics of crystallization coefficient ($K(T)$) could be obtained from the Avrami isothermal kinetics coefficient or half-time crystallization.

eq. 101 links the Nakamura kinetics of crystallization coefficient, half-time crystallization and Avrami kinetics of crystallization coefficient :

$$K(T) = k_{av.}(T)^{\frac{1}{n}} = \ln(2)^{\frac{1}{n}} * \frac{1}{t(T)^{\frac{1}{2}}} \quad \text{eq. 101}$$

Crystallization is an exothermic transition which leads to the increase of the temperature in the system. We have integrated the released heat due to the crystallization by using the specific heat capacity of PEEK.

$$C_p = \frac{\Delta H}{\Delta T} * \frac{d\alpha}{dt} \quad \text{eq. 102}$$

Where $C_p = 1800 \text{ J.kg}^{-1}.\text{K}^{-1}$ [123] and ΔH is the crystallization enthalpy. In order to consider, the fluid flow in the system, the convection term has been added to the Nakamura crystallization. By adding the convective term to the Nakamura equation, we could take into account the fluid and transferred crystalline phase during the fluid flows. Finally, non-isothermal crystallization for a polymer fluid flow is determined as eq. 103.

$$\frac{\partial \alpha}{\partial t} + \vec{u} \frac{\partial \alpha}{\partial x} + \vec{v} \frac{\partial \alpha}{\partial y} = \dot{\alpha} \quad \text{eq. 103}$$

Where α is the crystallinity and \vec{u}, \vec{v} are the velocity of the fluid in x and y directions respectively.

3.5.3 Numerical simulation

For the material deposition on the substrate, Two-Phase Flow (TPF) module of COMSOL Multiphysics has been used. For determination of the heat transfer, advection-diffusion equation was implemented in the model as a Partial Differential Equation (PDE). TPF module has been combined with the PDE to determine the heat transfer of the deposited bead. After the temperature determination of the deposited bead, Nakamura non-isothermal crystallization equation has implemented the model as a PDE equation.

The thermal conductivity of PEEK at room temperature is $0.32 \text{ W} \cdot (\text{m} \cdot \text{K})^{-1}$. The thermal diffusivity of PEEK at room temperature is about $0.24 \text{ mm}^2 \cdot \text{s}^{-1}$. Contrary to the thermal conductivity, the thermal diffusivity decreases while the temperature increases. According to our measurements, the influence of the temperature on the thermal conductivity is negligible. However, the temperature highly influences on the thermal diffusivity. The decrease of the thermal diffusivity stems mainly from variations of density when the temperature increases.

The density of PEEK is assumed at $1320 \text{ kg} \cdot \text{m}^{-3}$ [174] and the density of air is $1.225 \text{ kg} \cdot \text{m}^{-3}$. The properties of air and PEEK used in the TPF numerical simulation and eq. 57 are gathered in Table 15.

Table 15: Thermal properties of air and PEEK for determining the thermal diffusivity (from [123] [115])

Phase	Unit	Air	PEEK
Thermal conductivity	$\text{W} \cdot \text{m}^{-1} \cdot \text{K}^{-1}$	0.024	-
Density	$\text{kg} \cdot \text{m}^{-3}$	1.225	1320
Heat capacity	$\text{kJ} \cdot \text{kg}^{-1} \cdot \text{K}^{-1}$	1.005	1.7
Thermal diffusivity	$\text{m}^2 \cdot \text{s}^{-1}$	$1.95 \cdot 10^{-5}$	Figure 24 in chapter 2
Activation energy	$\text{kJ} \cdot \text{mol}^{-1}$	-	82.8
Viscosity	$\text{Pa} \cdot \text{s}$	$1.8 \cdot 10^{-6}$	-

Figure 80 shows the geometry of the model used for the numerical simulation of the material deposition on the substrate. Table 16 shows the boundary conditions used for the numerical simulation.

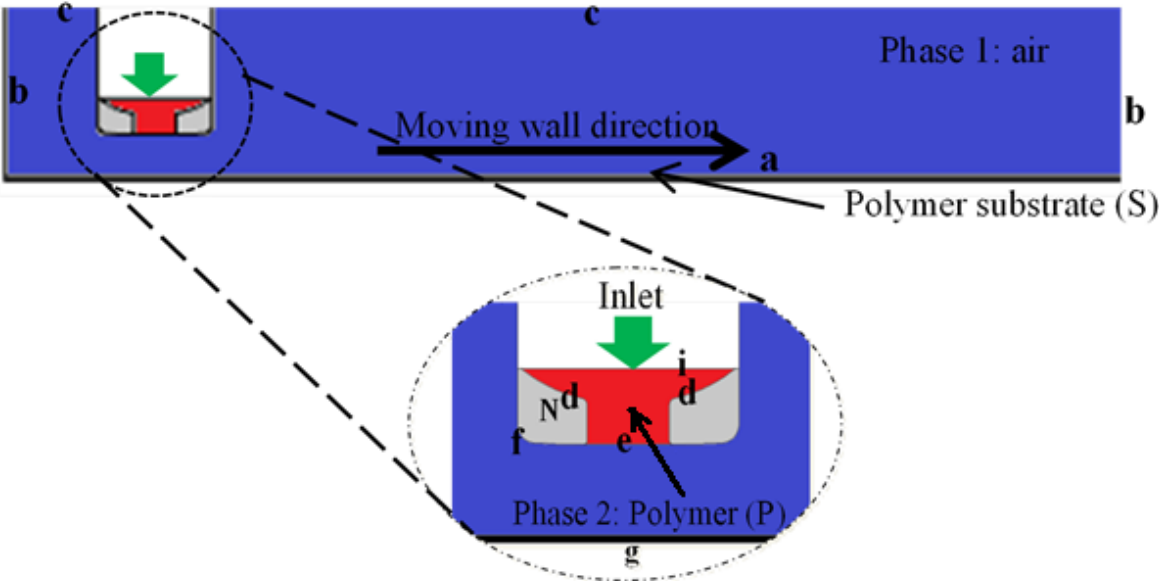


Figure 80: Illustration of the model and the geometry model used for the numerical simulation

Table 16: Boundary conditions used for TPF simulation and PDE heat transfer simulation

Boundary nomination	TPF Simulation	PDE Heat transfer simulation	Value
A	Mobile wall	-	$l = 122 \text{ mm}, v = 25 \text{ mm.s}^{-1}$
B	Outlet-Pressure	Dirichlet boundary condition	$l=, T = 30 \text{ K}, P = 0 \text{ Pa}$
C	Symmetry	Dirichlet boundary condition	$T = 303 \text{ K}$
D	No slip	Dirichlet boundary condition	$T_m = 656 \text{ K}$
E	Initial interface	-	$l = 3 \text{ mm}$
F	No slip – Zero Flux		
G	No slip	Dirichlet boundary condition	T
I	Inlet velocity	-	$L = 7.75 \text{ mm}, v = 5 \text{ mm.s}^{-1}$
A	Initial air phase : Phase1	Initial temperature	$T_{env} = 303 \text{ K}$
N	Nozzle (Iron)	Initial temperature	$T_m = 656 \text{ K}$
P	Initial polymer phase: Phase 2	Initial temperature	$T_m = 656 \text{ K}$
S	Polymer substrate (PEEK)	Initial temperature	T

3.5.4 Results of crystallization

For the study of isothermal crystallization, the selection of the temperature range is very important. The crystallization of PEEK during isothermal study must be complete under isothermal condition. Therefore, finding the temperature at which the crystallization starts is necessary. In Chapter 2, we have presented the results for non-isothermal tests by DSC at different cooling rates.

For the highest cooling rates, the crystallization temperature is shifted towards lower temperatures (towards glass transition) and at lowest cooling rates, towards melting temperature. Consequently, the cooling rate of 2 K.min^{-1} has been selected to determine the starting temperature of crystallization. We will study the isothermal crystallization of PEEK above the starting of crystallization at a cooling rate of 2 K.min^{-1} . In the figure 17 in Chapter 2, during the cooling step with cooling rate of 2 K.min^{-1} , the crystallization starts at about $583 \pm 3 \text{ K}$ ($310 \pm 3 \text{ }^\circ\text{C}$). Accordingly, the isothermal test must be done at the temperature higher than 583 K . On the other hand, at the temperature higher than 596 K ($323 \text{ }^\circ\text{C}$) the crystallization of PEEK lasts a long time which makes the test longer. As a result, the isothermal tests have been carried out between 583 K and 596 K .

According to Figure 16 in Chapter 2, during the second heating rate (2 K.min^{-1}) two endothermic peaks are observed. This lately, indicates the coexistence of two different crystalline structures in the polymer. The first endothermic peak starts at 565 K ($292 \pm 5 \text{ }^\circ\text{C}$) and the second one is around 588 K ($315 \pm 5 \text{ }^\circ\text{C}$).

The isothermal crystallization of PEEK 450G has been carried out from 595 K to 581 K . Figure 81 shows the obtained results of the isothermal test at $T = 588 \text{ K}$. As it is pointed out in Figure 81 and Figure 82, this analysis is composed of four steps, the sample is heated to 648 K at a heating rate of 50 K.min^{-1} then it remains at this temperature for 240 s (4 minutes) in order to remove all the crystalline history of the polymer. Afterwards, the polymer is cooled at the rate of 30 K.min^{-1} until the targeted isothermal temperature. The polymer is kept at its isothermal temperature until the crystallization is completed.

As it is represented in Figure 81, the glass transition of PEEK has been measured around 433 K ($160 \text{ }^\circ\text{C}$) and its melting peak occurs at 623 K ($350 \text{ }^\circ\text{C}$).

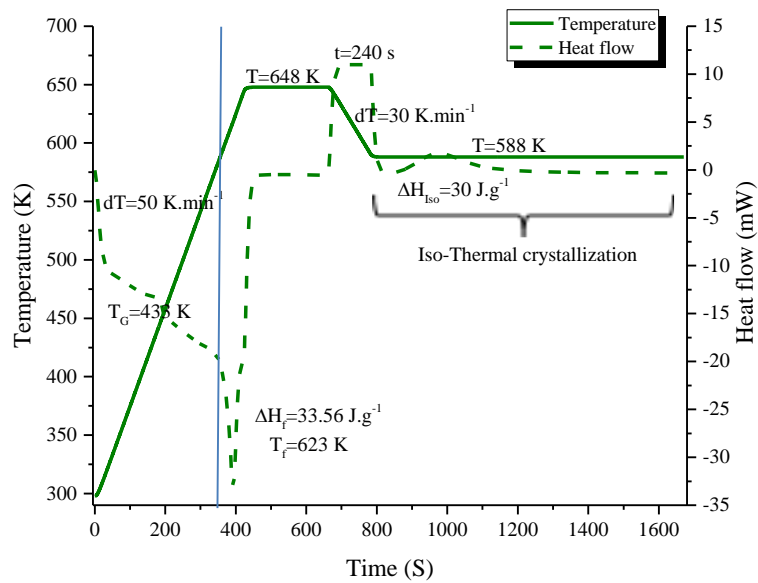


Figure 81: Isothermal study of PEEK 450G at T=588K

Figure 82 shows the results obtained for the different isothermal studies of PEEK. The isothermal crystallization has been carried out at nine different isothermal temperatures.

However, our observations for T = 581 K (308 °C), T = 583 K (310 °C), and T = 585 K (312 °C) show that before starting the isothermal crystallization, a small fraction of amorphous phase undergoes non-isothermal crystallization. As a consequence, in our study, we do not consider these isothermal temperatures.

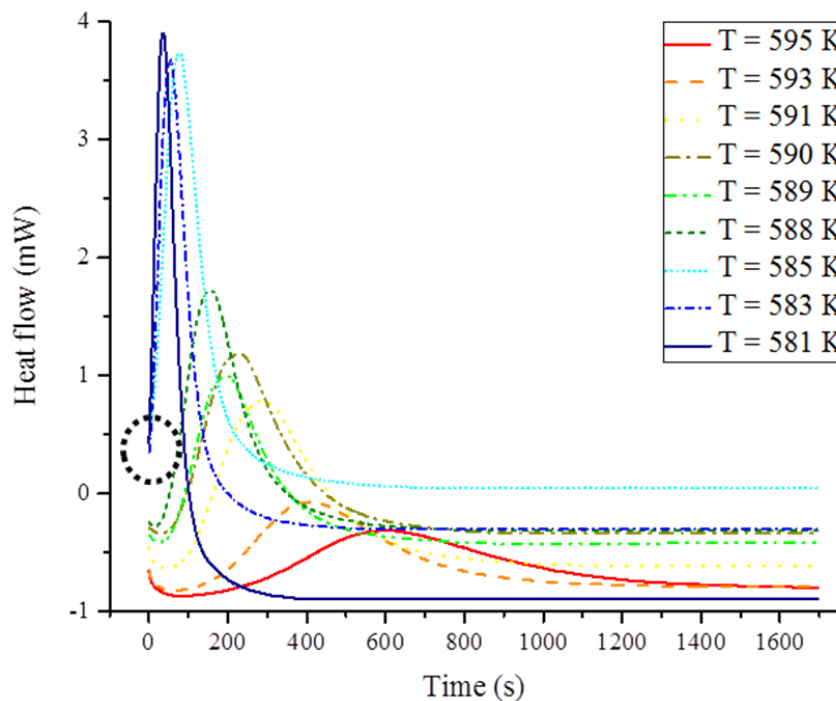


Figure 82: Isothermal study of PEEK 450G at the different temperature from 595K to 581K

Table 17 presents the obtained results from the isothermal studies such as enthalpy, crystallinity ratio, and half-time crystallization. The variation of the crystallization enthalpy is between 25 J.g⁻¹ and 30 J.g⁻¹

¹. The enthalpy is equivalent to 20 % to 23 % of crystallinity ratio. Respectively, the half-time crystallization increases while the temperature decreases which means at higher temperature, the time should be longer in order to crystallize the polymer.

Table 17: Influence of different isothermal study on the enthalpy and half-time crystallization of PEEK 450G

Isothermal temperature (K)	Sample mass (mg)	Enthalpy $\pm 0,2 \text{ J.g}^{-1}$	Crystallinity $\pm 0,2 \%$	Half-time crystallization (s)
588	10.4	30.1	23.1	98
589	8.9	30.9	23.8	199
590	10.9	28.8	22.2	230
591	12.6	31.1	24.0	290
593	9.2	30.2	23.0	404
595	9.6	25.3	19.5	586

For all the temperatures below 585 K, the crystallization point of Hoffman-Lauritzen equation has been fitted on the half-time determined experimentally, with Origin software[®]. As shown in Figure 83, the half-time crystallization obtained by DSC test and the analytically fitted Hoffman-Lauritzen curve agree well.

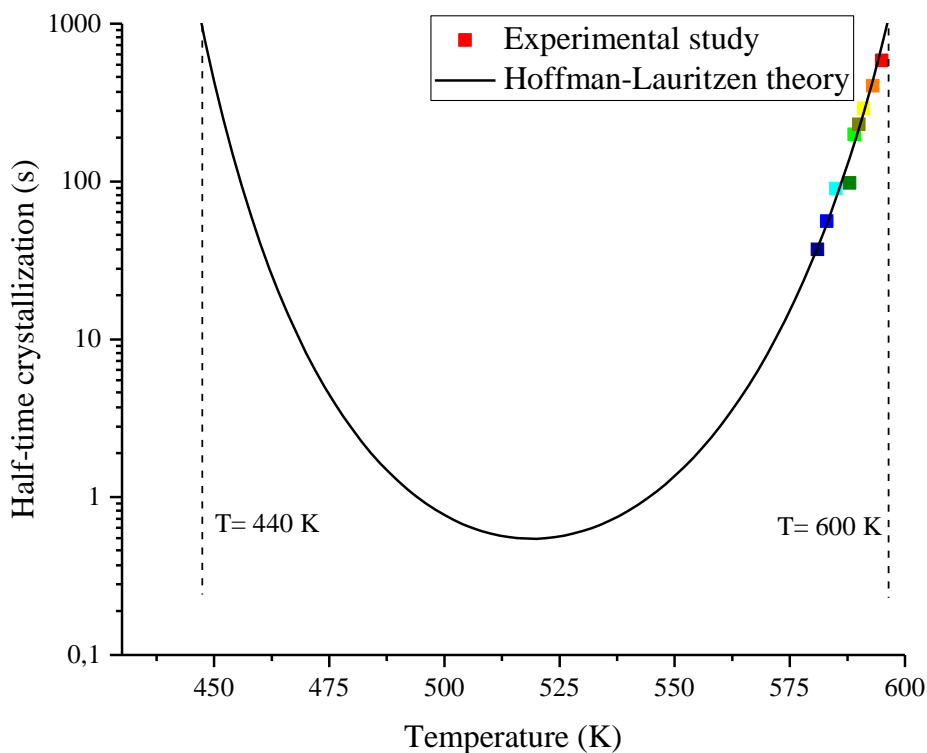


Figure 83: Half-time crystallization determination and fitted Hoffman-Lauritzen on the experimental points

Table 18 shows the values of the parameters of Hoffman-Lauritzen equation and its standard deviation for PEEK by fitting the curve on the experimental points.

Table 18: Values of the parameters of Hoffman-Lauritzen equation determined for PEEK

Parameter	Value	Standard error
K_0	$7.68 \cdot 10^8$	$1.09 \cdot 10^7$
K_G	$-8.87 \cdot 10^6$	$5.9 \cdot 10^5$

Alongside with determining the Avrami kinetics by half-time crystallization in eq. 101, Avrami kinetics of crystallization coefficient and Avrami exponent have also been determined for PEEK by applying the Avrami approach.

For each isothermal temperature from T = 595 K to 588 K, a curve of $\ln(-\ln[1 - \alpha(t)])$ versus $\ln t$ was plotted. The curve is a straight line with the slope n and intercept of k_{av} . Figure 84 shows the Avrami curves and also the fitted straight lines for each isothermal temperature. Avrami kinetics and exponents for the isothermal temperatures are represented in Table 19.

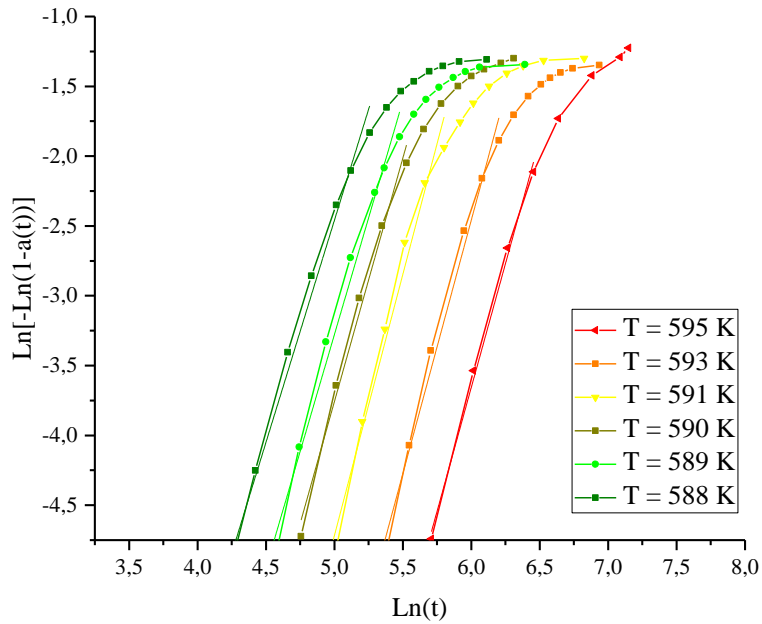


Figure 84: Plotting $\ln(-\ln[1 - \alpha(t)])$ versus $\ln t$ to determine Avrami kinetics and exponent

As it is depicted in Table 19, the Avrami exponent varies from maximum 3.74 to minimum 3.18, while its tendency at the lower temperature is around 3 and at temperature higher than 595 K is around 4. The Avrami exponent explains the shape of the growing crystal formation during crystallization [175]. When the value of n is close to 3, it is concluded that the shape of the crystallization formation is 2D spherulites [125], while $n = 4$ is 3D spherulitic formation. The Avrami kinetics represents the crystallization kinetics of the polymer. Closer is the temperature to the melting temperature or glass transition, more the crystallization kinetics decrease. It is shown in Table 19 that at 588 K the kinetics of crystallization is faster than at 595 K when we are closet to the melting temperature.

Table 19: The values of Avrami isothermal kinetics and exponent for different isothermal temperature

Temperature (K)	595	593	591	590	589	588
Avrami exponent (n)	3.55	3.63	3.74	3.49	3.35	3.18
Avrami kinetics (s^{-n})	1,46E-11	2,97E-11	6,75E-11	6,2E-10	2,06E-9	1,06E-8

Figure 85 shows the Avrami kinetics coefficient determined by Avrami approach and the predictive model of eq. 101. The predictive model agrees with the experimental results. At the temperature close to the melting temperature, the tendency of the Avrami exponent is towards 4 while for the lower temperatures, the tendency is 3. In the predictive model, for the range of 595 K until 588 K, the Avrami

exponent from the experimental study has been used, while for the temperature higher than 595 K, the assumed Avrami exponent is 4 and for the temperature below 588 K, the assumed Avrami exponent is 3. This assumption is consistent with our observations about the existence of two crystalline structures during melting of PEEK represented in Figure 16. According to DSC results in Figure 16, the transition temperature from the first crystalline structure to the second crystalline structure, takes place at about 588 K.

Figure 85 shows that the kinetics of crystallization for PEEK 450G is at its maximum value around 515 K. However, closer to melting temperature (360 °C) and glass transition (160 °C) the kinetics of crystallization is very slow.

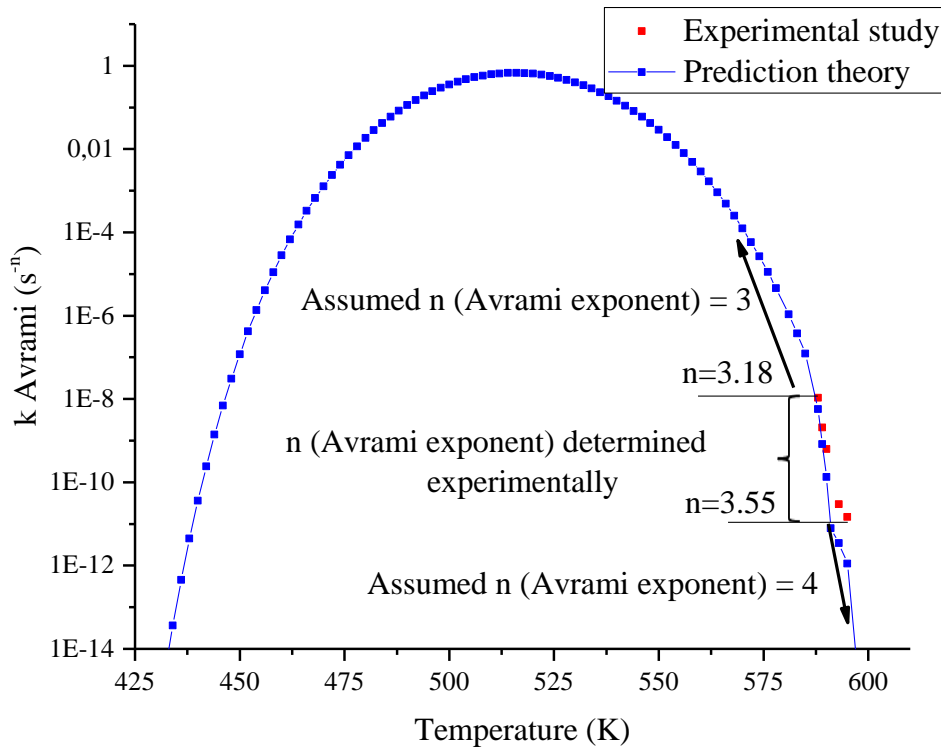


Figure 85: Determination of the Avrami kinetics along processing range near glass transition up to melting temperature

Using Avrami kinetics of crystallization and Avrami exponent and applying eq. 101 enables us to determine the Nakamura kinetics of crystallization. Figure 86 shows Nakamura crystallization kinetics coefficient for PEEK 450G and PEEK 150G [103].

Comparing two different grades of PEEK demonstrates that the kinetics of crystallization for 150G is faster than 450G. For PEEK 450G, the value of the Nakamura crystallization kinetics at its maximum state is 0.87 while this value is 2.47 for PEEK 150G. For 450G, the maximum value occurs around $T = 515$ K while for 150G the peak is at $T = 512$ K. The result is consistent with the expectations: the ability to crystallize is higher for shorter macromolecules, and it is known that PEEK 150G is made of shorter macromolecular chains compared to PEEK 450G.

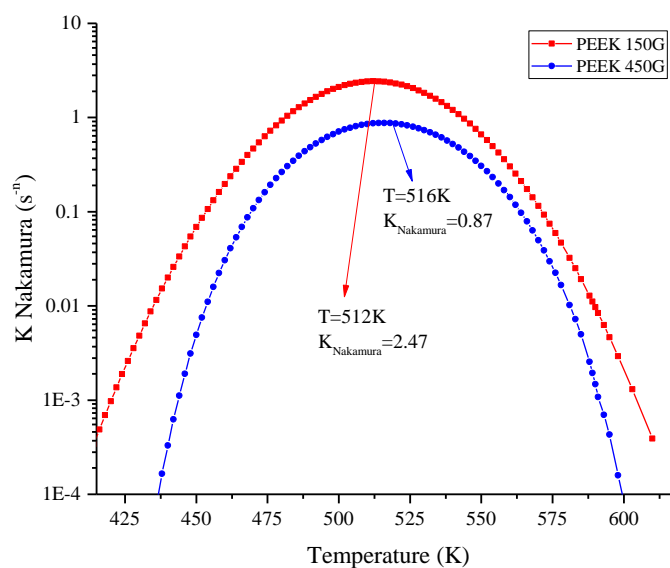


Figure 86: Nakamura Kinetics of crystallization for PEEK 450G in blue and PEEK 150G in red. PEEK 150G data are from [103]

3.5.5 Numerical study of polymer deposition in FFF process

The numerical simulation of the polymer deposition on the substrate has been carried out by COMSOL Multiphysics. By numerical simulation, the material flow, temperature distribution and relative crystallinity in the FFF process have been determined. As it is represented in Table 20, five different case studies have been selected. For three cases, the impact of the environment and substrate temperatures on the temperature field and crystallization field have been investigated. Furthermore, for the two other cases, we aim to optimize the process by finding the minimum crystallization temperature.

In case 4, we will determine the environment temperature for which the crystallization starts at 4.7 s. 4.7 s is the time of deposition of a single bead in our study. The non-existence of the crystalline phase during deposition of the second layer on the first deposited layer is a favorable condition in order to increase the interdiffusion of two layers or two beads.

In case 5, we will determine the environment temperature for which the crystallization starts after 12 s. In this case, we have considered that, it takes more than 12 s to deposit the second layer on the first layer.

All the temperatures for the case studies are synthesized in Table 20. The numerical simulation has been carried out for 12 s. The material deposition takes place from 0 s to 4.7 s, while from 0 s to 12 s, there is heat transfer and crystallization in the model. Figure 87 shows the fluid flow of the first layer deposition on the substrate.

Table 20: Case studies for the numerical simulation of temperature distribution and Crystallization rate

Case studies:	T_m	$T_{\text{substrate}}$	$T_{\text{Env.}}$
Case 1	656 K (383 °C)	303 K (30°C)	303 K (30°C)
Case 2	656 K (383 °C)	433 K (160 °C) (T_g)	303 K (160 °C)
Case 3	656 K (383 °C)	433 K (160 °C)	433 K (160 °C)
Case 4	Finding the minimum temperature for which the crystallization starts after the end of bead deposition (about 4 s)		
Case 5	Finding the minimum temperature for which the crystallization starts after 12 s.		

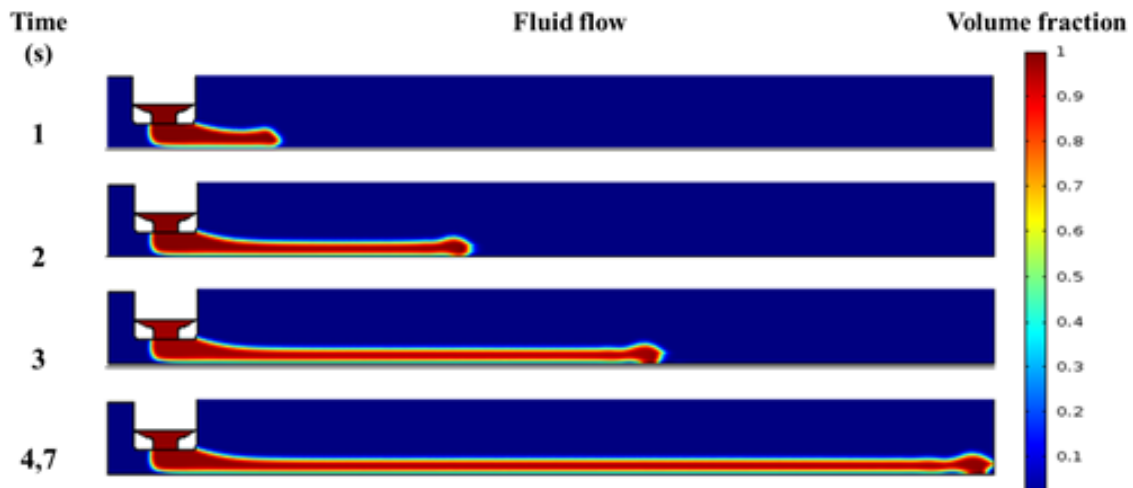


Figure 87: Numerical simulation of first layer deposition on the moving substrate at the different moments

In Figure 87, the legend represents the volume fraction of the fluid in the system: blue (which is equivalent to 0 in color legend) represents the air in the system and red (and 1 in the color legend) represents the polymer.

The temperature distribution of the deposited bead on the substrate has been determined during the material deposition. Figure 88 shows the temperature distribution of the material deposition for case 3 at different times. The results show that during the material deposition, while the cooling rate of the extrudate front is high, in the center of the extrudate the temperature is still at the melting temperature.

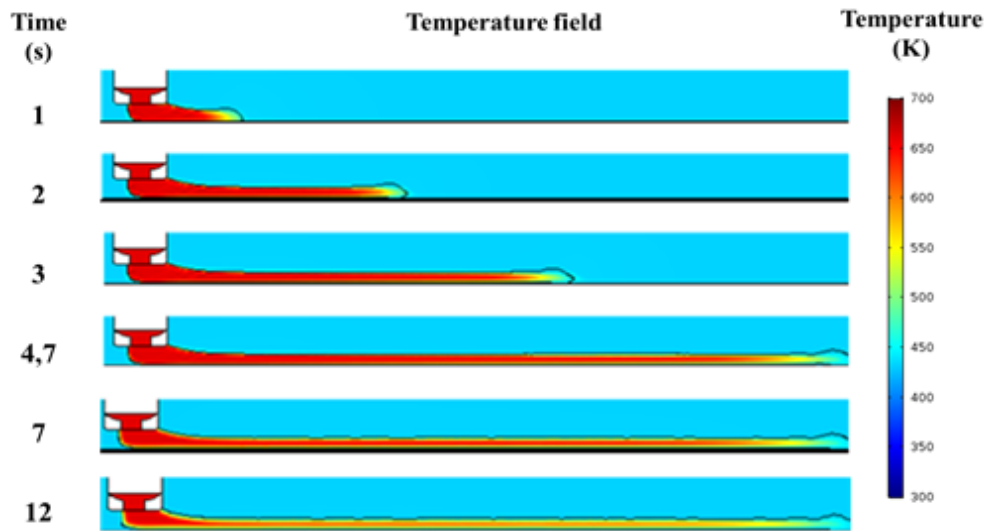


Figure 88: Temperature distribution for the Case 3 ($T_{\text{substrate}} = 433\text{K}$ and $T_{\text{env.}} = 433\text{K}$)

Figure 89 shows the temperature of the center line at different times for the case 3. Increasing the time leads to decreasing the temperature. However, the cooling rate of the extrudate center is relatively slow. At $t = 4.70$ s, the deposition of the polymer on the substrate is completed and from $t = 4.70$ s up to $t = 12$ s, heat transfer and crystallization is modeled.

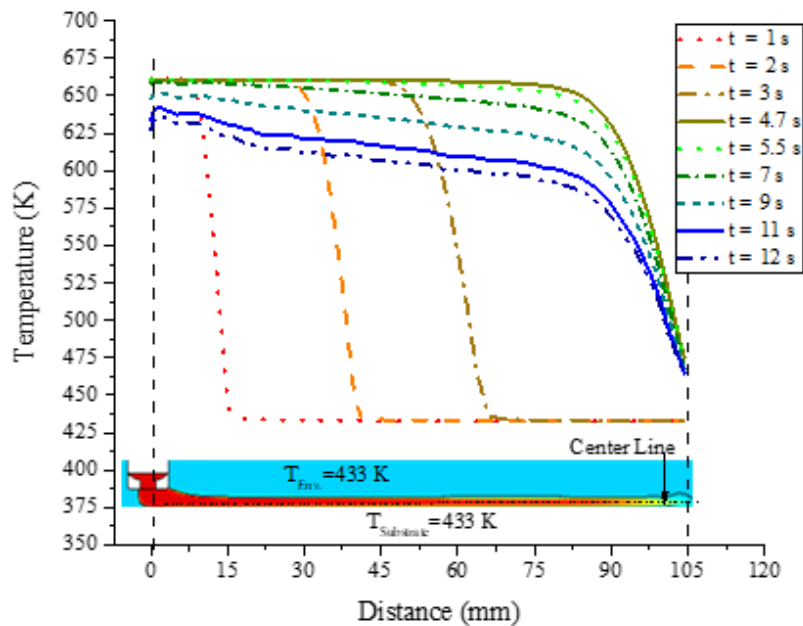


Figure 89 : Temperature distribution at different moments for the case 3 for the center line of the extrudate

The deposition of the first bead starts at $t = 0$ s and is completed at 4.7 s. The total length of the substrate is 105 mm. The mean moving velocity of the substrate is $25 \text{ mm}\cdot\text{s}^{-1}$ that is attributed to the substrate for the first 4.7 s of the simulation, after it stops.

The crystalline distribution at different times for case 3 is depicted in Figure 90. The crystalline ratio in the center of the bead when the temperature is still high is very low, while in the extrudate front where the cooling rate is high, the crystallinity reaches 23 %. On the other hand, near to the surface when the surface of the extrudate is subjected to heat transfer with air, the kinetics of crystallization is slower than

in the center of the bead. Consequently, near the surface, the crystallization could not reach its maximum value. The crystallinity ratio for the three cases at $t = 12$ s is illustrated in Figure 91.

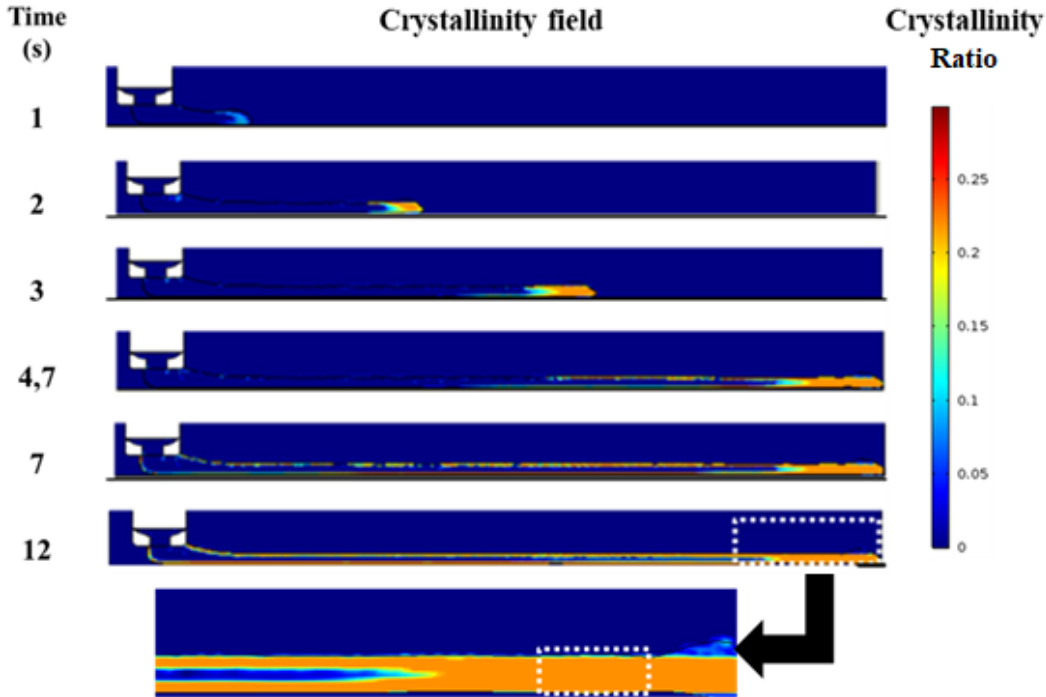


Figure 90: Distribution of the crystallinity for Case 3 ($T_{\text{substrate}} = 433 \text{ K}$ and $T_{\text{env.}} = 433 \text{ K}$)

The color legend in Figure 90 represents the crystallinity ratio of the deposited bead. Blue or zero demonstrates no crystallization or amorphous state of the polymer, while orange and red represents the crystallinity ratio. The air is also represented in blue.

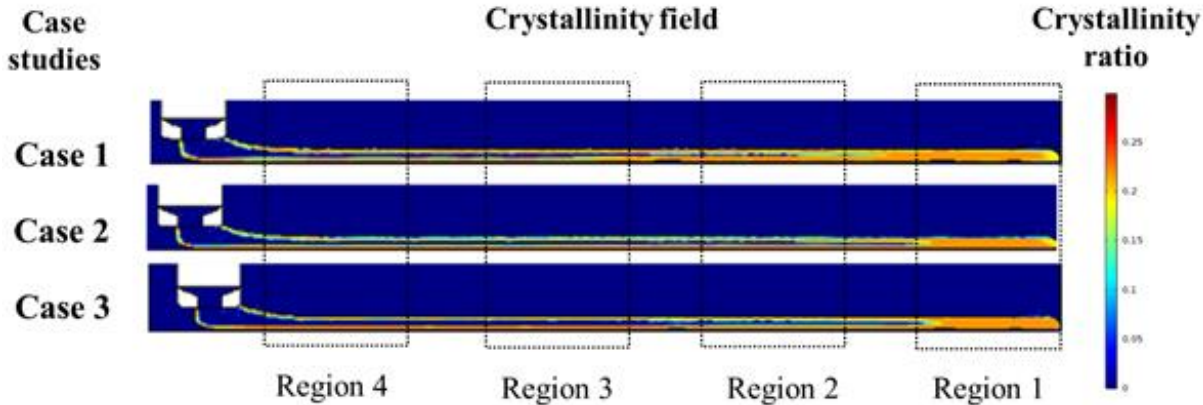


Figure 91: Non-isothermal crystallization of PEEK $t=12\text{s}$ for different case studies

Figure 91 shows the influence of the environment and the substrate temperature on the crystallinity ratio of the deposited bead for the three cases studied. As it is represented in Figure 91, at $t=12\text{s}$, the crystallization of the bead is divided into 4 different regions.

1. Region 1 is the front part of the extrudate. This region is cooled rapidly after exiting from the nozzle. The cooling rate in this part of the extrudate is relatively fast. This region reaches its maximum value of crystallization during 12 s. Because of relatively fast cooling rate and crystallization of this region, during FFF process and layer deposition, the condition of this part of the deposited bead is not favorable for coalescence and interdiffusion.

2. Region 2 of the deposited bead is the region which undergoes crystallization. Kinetics of crystallization for the three cases studied show that the crystallization rate for case 1 is much faster than other cases. The maximum kinetics of crystallization for all the three cases in this region has been determined at 0.107, 0.215 and 0.325 $\% \cdot s^{-1}$ respectively. However, close to the deposition substrate and close to the air where the cooling rate is high, the crystallization is relatively fast and reaches its maximum value.
3. In region 3 and region 4 in all the 3 cases, the center of the extrudate is still at its melting temperature and there is no crystallization observed. This part of the bead is the part of the extrudate just after exiting from the nozzle. It does not have enough time for cooling and crystallization. Consequently, after 12 s, this part of the extrudate does not undergo crystallization. However, close to the substrate and close to the boundary, where the cooling rate is high, the crystallization of the polymer is observed. For the case 1, the kinetics of crystallization has been determined between 10^{-3} and $10^{-2} \% \cdot s^{-1}$. However, for the case 2 and case 3, the kinetics of crystallization is less than $10^{-5} \% \cdot s^{-1}$.

For the case 1 and case 2, the thickness of non-crystalline phase from the surface is about 0.4 mm, while for the case 3, the crystalline phase starts close to the surface. The substrate temperature highly influences the crystallinity of the polymer in the contact region. For the Case 2 and Case 3, close to the substrate, the polymer reaches its maximum value of the crystallinity, while for the case 1 there is a layer about 0.1 mm non-crystallized zone. However, this zone is the interface of the two phases. At the interface, the determination of the thermal diffusivity is not accurate because we have used density, specific heat and viscosity as mixing laws. However, we could compare the cases qualitatively.

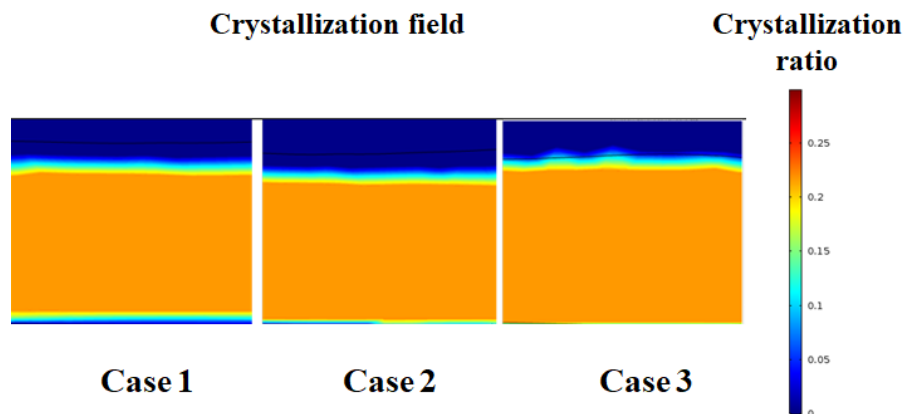


Figure 92: Influence of the Substrate and environment temperature on the crystallinity percentage of the deposited bead

Figure 93 shows the temperature distribution and crystallinity ratio for all of the three case studied at $t=12$ s at the center of the deposited bead when the deposition of the bead is completed.

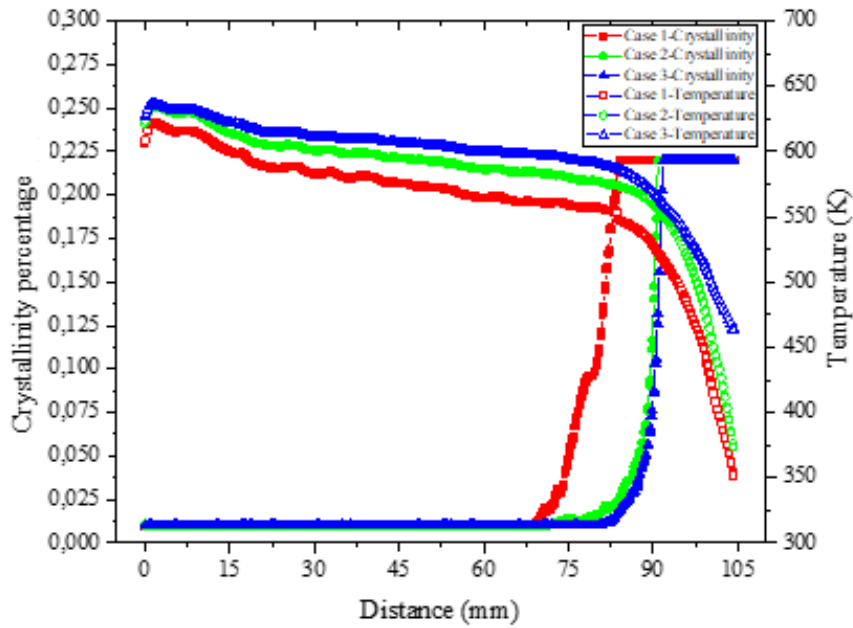


Figure 93: Temperature distribution and crystallinity ratio in the center of the deposited extrudate for the three cases

3.5.6 Determination of the optimal environment temperature in order to promote the interdiffusion of the beads and layers

The interdiffusion between deposited layers and beads takes place when two deposited consecutive layers are still in the amorphous state. Consequently, determining the optimal environment temperature to promote the interdiffusion is necessary to improve the mechanical properties of the printed parts. At the optimal environment temperature, the deposition of the bead on the substrate is completed, however, the deposited beads are still in the amorphous state. Figure 94 shows two cases for which the crystallization starts at 4.7 s and 12 s.



Figure 94: Crystallization of PEEK at 563K and 573K

As it is represented in Figure 94, at 563 K, the crystallization starts at 4.75 s. Furthermore, at 573 K, the crystallization of the deposited bead starts at 12 s. The temperature ranges to keep the deposited bead in the amorphous state is relatively narrow. At the temperature below 558 K (285 °C), the kinetics of crystallization is relatively fast, which leads to the crystallization before the deposition of a second bead. Furthermore, at temperature higher than 573 K (300 °C), the kinetics of crystallization is relatively slow. Consequently, the proposed environment temperature to promote the interdiffusion is from 558 K to 573 K. Worth to mention, the selection of the temperatures also depends on the printing velocity. At higher printing velocity, when the deposition of the second bead on the first beads is relatively fast, we could use even a lower temperature. Contrary to fast printing, when the printing velocity is slow, the temperature should be increased.

Our results on crystallization by numerical simulation are in line with experimental studies carried out with Tseng et al. [99] and Rinaldi et al. [96]. Indeed, Tseng et al. [99] have printed two series of PEEK parts: one of the batch was submitted to annealing (heat treatment). The second batch is the printed parts without heat treatment. When performing the mechanical tests, they measured identical mechanical

properties. However, in their article they did not explain the reason of that issue. Their observation confirms our numerical results concerning the crystallization of PEEK. We have shown that because of fast crystallization of PEEK, the final crystallinity ratio of the final part is at its maximum level. It could be considered that the final crystallization ratio is almost independent on the cooling rate of the printed part. Even though the printed parts are subjected to heat treatment, there is no improvement in mechanical properties.

Furthermore, their advice is to set the temperatures for the liquefier at 370–390 °C and for the platform up to 280 °C in order to optimize the mechanical properties. Their temperature proposition is also in line with our numerical measurement [99]. At this platform temperature, the polymer stays longer in the amorphous state, which increases the interdiffusion of the molecular chains. And consequently, the bonding of the deposited beads and layers is stronger.

Rinaldi et al. [96] have printed PEEK samples according to different cooling rates. They have studied the mechanical properties of printed parts according different conditions with tensile tests. They have also studied the thermal transition by DSC and the microstructure by X-Ray diffraction (XRD) and optical microscopy. No difference was found in terms of thermal transition such as glass transition, melting temperature, and crystalline ratio. Their experimental results also confirm that the crystallinity ratio of the printed parts is independent from the cooling rate for PEEK.

3.6 Conclusion

The numerical simulation of the polymer deposition on the substrate has been carried out using TPF with Level Set (LS) method. The simulation is divided in several steps in order to model the deposition of the material on a substrate, the deposition on a moving substrate and the determination of heat transfer and the variation of the viscosity in the system. Finally, the deposition of a polymer layer upon a previously deposited layer was accomplished.

In order to determine the heat transfer during the deposition of the material, we have integrated the heat transfer equation as a PDE in COMSOL software to conjugate TPF-LS with heat transfer.

In the first approach of our numerical simulation, freeform extruder simulation has been done. During free-form extrusion, the volume fraction, temperature distribution and variation of the viscosity have been determined. The influence of the viscosity on polymer flow and effects on the behavior of the extrudate have been determined. Our initial model shows that the interface of the two phases (air and polymer) is wide (about 2 mm). In this band, the viscosity changes from the viscosity of the polymer to the viscosity of the air as function of phase fraction (mixing law). In order to improve the precision of our numerical model we had to reduce the width of this transition zone. We had proceeded in two steps, we have reduced the size of the meshes and also we have reduced the numerical value of the re-initialization parameter (γ) in the LS equation (eq. 47).

The influence of the polymer viscosity on the behavior of the extrudate has been studied by numerical simulation. Our investigations show that for high viscosities, the shape of the extrudate does not change so much while at low viscosities the shape is totally different. The same variation is observed when the influence of the temperature is considered.

In order to validate our model to the first step, the FFF process applied to PLA was investigated via experiments, analytical equations and numerical simulation. The effects of the printing parameters (i.e.

nozzle diameter, feed rate and layer height) and the physical properties of the polymer (i.e. thermal transitions and rheological behavior) on the inlet velocity, shear rate and viscosity in the liquefier were determined.

Firstly, the maximum inlet velocity of the filament in the liquefier was determined according to the printing parameters, such as the nozzle diameter, feed rate and dimensions of the deposited segment. Then, the rheological behavior of PLA, such as the velocity field, shear rate and viscosity distribution in the nozzle, was studied via analytical model and numerical simulation. The shear rate reached its maximum value near the internal wall of nozzle at a high inlet velocity and small nozzle diameters. Increasing the inlet velocity or decreasing the nozzle diameter increases the shear rate and decreases the viscosity of PLA. Meanwhile, reducing the viscosity enhanced the adhesion between the deposited beads and layers, and an excessively low viscosity results in low accuracy. Moreover, at the shear rates higher than 4000 s^{-1} , PLA extrudates underwent severe deformation caused by the 'sharkskin' effect. The deformation of the extrudate influences the shape of the deposited beads and consequently reduces the control over the roughness and reliability of the manufactured part.

In parallel, a Multiphysics TPF model was developed to determine the viscosity of the polymer and shear rate according to various inlet velocities. Moreover, the numerical simulation was used to model the shape of the extrudate when it exits from the nozzle. The results obtained via numerical simulation were validated through experimental study. The numerical simulation focused on the shape of the deposited filament before deposition on the substrate for different flow regimes. The validation of this part gives access to the next steps.

The die swelling taking place in the FFF process has been predicted. The die swelling ratio highly depends on the liquefier geometry and the printing parameters. The die swelling ratio for PEEK in the FFF process depends on the printing parameters: it changes from 1 (no swelling) to 2.5. In order to reduce the die swelling, we advise to increase the temperature, decrease the inlet velocity or adapting the geometry of the nozzle (capillary diameter, capillary length, convergence angle and reservoir diameter).

The rheological properties such as viscosity and shear rate have been determined by rheometry in parallel-plate configuration for the shear rates less than 100 s^{-1} and by extensional die for the shear rates higher than 100 s^{-1} up to 10000 s^{-1} at $383 \text{ }^\circ\text{C}$. The results obtained by both methods show that the viscosity of PEEK at different temperatures at its Newtonian plateau is between $7000 \text{ Pa}\cdot\text{s}$ and $11000 \text{ Pa}\cdot\text{s}$, while at very high shear rates, the viscosity at $383 \text{ }^\circ\text{C}$ reduces up to $40 \text{ Pa}\cdot\text{s}$.

Then, we have determined the relaxation times for PEEK from the rheological measurements from $350 \text{ }^\circ\text{C}$ to $400 \text{ }^\circ\text{C}$. The relaxation times of PEEK are relatively high: At $350 \text{ }^\circ\text{C}$, it is 3.1 s and at $400 \text{ }^\circ\text{C}$ it is reduced to 1.6 s .

Isothermal and non-isothermal crystallization of PEEK has been determined by DSC experiments on cooling for a large temperature range from melting temperature up to the glass transition. Furthermore, the material deposition during the FFF process applied to PEEK has been modeled by numerical simulation. From the numerical simulation, we have determined the flow properties of the melted polymer, heat transfer, as well as the variations of viscosity and crystallinity during the deposition step. These informations are essential to optimize the mechanical resistance of printed parts and they cannot be determined by experimental measurements. It is the first time that numerical simulation is applied to the FFF process to predict the crystalline rate of parts manufactured by the FFF process.

Half-time crystallization of PEEK has been determined experimentally by DSC for the temperatures between 310 °C and 322 °C. The experimental results have been interpolated by Hoffman-Lauritzen equation in order to determine the half-time crystallization at different temperatures from melting temperature to glass transition. The Avrami kinetics coefficient has been determined from half-time crystallization. Moreover, the Avrami kinetics coefficient and Avrami exponent have been determined for the temperatures between 315 °C and 322°C separately. The comparison of the results for the Avrami kinetics coefficient by the predictive Hoffman-Lauritzen equation and Avrami equation shows a very good agreement. Our results on the crystallization of PEEK shows that the crystallization rate is at its maximum value at 512 K (240 °C). By comparing the results obtained for PEEK 450G and existing results on PEEK 150G, the crystallization kinetics for 150G is much faster than for 450G. However, both grades reach their maximum crystallization kinetics around 240 °C. Finally, the Avrami kinetics has been applied to Nakamura equation in order to determine the non-isothermal crystallization for PEEK 450G. By adding, convection term to the Nakamura non-isothermal crystallization, we are able to determine the evolution of the crystallization field during the cooling of semi-crystalline polymers with considering the fluid flow. The modified Nakamura crystallization equation with convection term has been implemented to the software in order to determine the crystallization. To our knowledge, this is the first time that the Nakamura equation has been applied to PEEK 450G in such way.

In this study, in order to model the material deposition and fluid flow, TPF numerical simulation has been carried out. Navier-Stokes, continuity and Level Set equations were used to model the material deposition. Heat transfer has been determined by implementing a partial differential equation in the model. By using TPF simulation approach, we have determined the material flow, heat transfer, and crystallization in the FFF process. The results show the gradient of crystallization rate along the filament during the deposition. The crystallization for the PEEK 450G reaches its maximum value (about 22%) of crystallization during the deposition. Furthermore, the crystallization releases heat of about 28.6 J.g⁻¹ in the system that increases the temperature of the deposited bead gradually up to 20 K. While the substrate temperature highly influences the kinetics of crystallization of the center of the beads, the environment temperature influences only the crystallization of the surface.

Although many numerical simulations of additive manufacturing approaches are based on mesh activation approach as a step by step deposition, hereby, we have proposed a new approach model of real material deposition in a two-phase system to simulate the FFF process. Our approach for determining the non-isothermal crystallization while taking into account the fluid flow could be applied to other polymer processes. To date, this approach seems to have never been used.

General conclusion

Additive manufacturing (AM) refers to a wide variety of manufacturing processes for rapid prototyping and production of final and semi-final products. Despite a growing interest from industries and a large audience in the last five years, these manufacturing processes are still not well mastered, especially for not mass-produced polymers. Indeed, when the polymeric materials display specific properties, controlling their processing is trickier. More efforts are needed to enlarge the knowledge about the physical phenomenon involved during these processes.

The industry requires high-performance polymers, that is to say, resistant materials when exposed to the harsh environment: thermo-oxidative atmosphere, oxidative chemicals combined to mechanical loads such as friction or compression. The emergence of highly stable thermoplastics since the 1980s such as the PAEK (polyaryletherketone) open the way to widespread their uses. So, high-performance thermoplastics are potential candidates to manufacture structural parts for aerospace, automotive and medical industries. However, in opposite to conventional polymers, processing high-performance thermoplastics is still a challenge because of their specific properties. The FFF (Fused Filament Fabrication) process is based on the melting of a polymeric wire or filament in an extruder; the latter is then deposited layer by layer to manufacture the final parts. These challenges are harder to be reached in case of layer by layer deposition where the bonding of the deposited layers drive the mechanical properties of the printed parts.

Indeed, 3D parts suffer from low mechanical properties and low surface quality, compared to parts manufactured by conventional processing techniques. The mechanical properties and the surface roughness of 3D parts manufactured by FFF are controlled by the adhesion of filaments and the porosity rate. The both mainly stem from the flowing ability and the surface tension of the polymer. Moreover, the adhesion of filaments depends on the interdiffusion of polymeric chains. The polymer properties such as rheological behavior, thermal properties, surface tension and crystallization play a crucial role in the understanding of the effect of the printing conditions on the quality of the final parts. To our knowledge, no study of the FFF process applied to high-performance semi-crystalline polymer was available when this work began in 2015. Since, some similar research works have started worldwide.

Our studies aim to optimize the quality of the printed parts by understanding the link between the printing parameters, the polymer properties and the mechanical properties of the 3D final parts. Our study focuses mainly on PEEK (polyetheretherketone). The relations between the printing parameters and the properties of the material (elongational viscosity, viscoelasticity, coefficient of thermal expansion, thermal capacity, thermal conductivity, kinetics of crystallization ...) on the polymer flow and the adhesion of filaments have been clarified. At the same time, the objective was to set up a numerical simulation of the phenomena involved in this process. The viscous flow of the polymer during its deposition in the molten state was modeled and simulated while considering heat transfer and crystallization. In our procedure, we combine experimental, analytical and numerical approaches.

Based on the literature review, the most influential printing parameters have been identified: the filament temperature, the environment temperature, the deposition rate and the raster orientation. The existing studies point out the lack of knowledge about the link between the printing parameters and the polymer properties in the FFF process. In the most of the studies on FFF process, the authors vary the printing parameters to print specimens, the latter are characterized by mechanical tests. However, the material's properties are among the most important properties which have not considered. Among these properties, the viscoelastic behavior, the surface tension, crystallization rate (for the semi-crystalline polymers) and, the thermal properties are the crucial properties influencing the quality such as deformation and warpage

of the manufactured parts. Furthermore, the physical phenomenon such as coalescence, material flowing, heat transfer and crystallization are the most important issues to optimize the FFF process.

After identifying the polymer properties involved in this process, the PEEK polymer has been characterized in Chapter 2. PLA is used as a comparative polymer to understand the physical phenomenon, with a lower melting point. For the both, their thermal transitions, kinetics of crystallization and sensitivity to degradation have been clarified. Contrary to the PEEK, the kinetics of crystallization of PLA is slow. In the case of PLA, the crystallization could be controlled in the FFF process by applying the high cooling rate while, in the case of PEEK, the polymer crystallizes whatever the cooling rate studied. Practically, the cooling rate depends on the temperature of the melt polymer exiting from the nozzle, the temperature of the platform (substrate) and also the environment temperature.

The thermal properties such as thermal conductivity, diffusivity and expansion coefficient have been determined. Contrary to the thermal conductivity, the thermal diffusivity decreases while the temperature increases. The rheological properties have been determined for the shear rates less than 100 s^{-1} in oscillatory mode. The comparison of PEEK with PLA shows that the viscosity of PEEK is much higher than those of PLA. Moreover, both polymers are sensitive to thermal degradation. As a consequence, the processing temperature range is limited to prevent their degradation. PLA and PEEK undergo different degradation mechanism, resulting in decreased viscosity for PLA due to chain scission mechanism. On the contrary, the degradation mechanism of PEEK occurs by molecular recombination, leading to viscosity increase. Degradation of the PEEK at low frequency and high temperature, shows the importance of the determination of shear rate in the FFF process. Considering that shear rate is depending on the printing parameters (i.e. nozzle diameter, feed rate and layer height), shear rate in the FFF process been determined in the liquefier according to printing parameters.

The 2D coalescence numerical simulation of the fluid in the air has been carried out by using CFD and TPF-LS equations. Our numerical results on the coalescence of glycerol show great accordance with the experimental ones. The experimental study of the coalescence phenomenon applied to PEEK confirms that the viscosity highly influences the bonding of polymers.

Although from one point of view, the increase of shear rate decreases the viscosity and consequently, increases the coalescence kinetics. However, from other point of view high shear rate highly impacts the quality of the printed part. Our observation has been shown that at the high shear rates, polymer flow from the nozzle undergoes the shark-skin phenomenon. Furthermore, the die swelling of the extrudate at high shear rate is more important than low shear rate.

The die swelling ratio for PEEK in the FFF process depends on the printing parameters: it changes from 1 (no swelling) to 2.5. In order to reduce the die swelling, we advise to increase the temperature, decrease the inlet velocity or adapt the geometry of the nozzle (capillary diameter, capillary length, convergence angle and reservoir diameter). Then, we have determined the relaxation times for PEEK from the rheological measurements between 350 and 400 °C. The relaxation times of PEEK are relatively high: At 350 °C, it takes 3.1 s and at 400°C it is reduced to 1.6 s.

This bonding would impact the mechanical properties of the printed parts: if the interdiffusion and bonding is not completed, the interlayer adherence would be weak, resulting in low fracture resistance of the parts. The bonding length between two adjacent PEEK filaments has been registered according to temperature. The comparison of experimental study with numerical simulation of the coalescence shows that the coalescence starts when the polymer is fully melted. Then the importance of determination of the cooling rate and crystallization kinetics is highlighted. Consequently, in order to

study the kinetics of coalescence in the FFF process we have to determine the temperature variation and crystallization kinetics. For that reason, in the third chapter we have concentrated on the determination of crystallization kinetics and temperature variation in the FFF process.

Half-time crystallization of PEEK has been determined experimentally between 310°C and 322°C. The experimental results have been interpolated by Hoffman-Lauritzen equation in order to determine the half-time crystallization at the different temperatures from the melting temperature up to the glass transition. The crystallization rate is at its maximum value at 512 K (240°C) for PEEK. By adding a convection term to the Nakamura non-isothermal crystallization, we are able to determine the evolution of the crystallization field during the cooling of semi-crystalline polymers with considering the fluid flow. TPF numerical simulation has been carried out to model the material deposition and fluid flow, with Navier-Stokes, continuity and Level Set equations. Heat transfer has been determined by implementing a partial differential equation in the model. By using TPF simulation approach, we have determined the material flow, heat transfer, and crystallization in the FFF process. The results show the gradient of crystallization rate along the filament during the deposition. The crystallinity ratio for PEEK reaches its maximum value (about 22%) during the deposition. Furthermore, the crystallization releases heat in the system that increases the temperature of the deposited bead gradually up to 20 K. While the substrate temperature highly influences the kinetics of crystallization of the center of the beads, the environment temperature influences only the crystallization of the surface. In order to promote the interdiffusion of the molecular chain of the deposited layers and beads (and increase the mechanical properties) the temperature of the environment and deposition platform must be between 285°C and 300°C. Our melting temperature and also build platform temperature proposition is in line with the proposition of the platform temperature and liquefier determined experimentally by other authors. Although many numerical simulations of additive manufacturing processes are based on mesh activation approach as a step by step deposition. Hereby, we have proposed a new approach model of real material deposition in a two-phase system to simulate the FFF process. Our approach for determining the non-isothermal crystallization while considering the fluid flow could be applied to other polymer processes. To date, this approach seems to have never been used.

We have also determined the temperature evolution of a single bead on the substrate. In this first step, the influence of the increase of temperature because of deposition of the consecutive layer deposition on the first deposited layer is not taken into account. Indeed, the deposition of a second layer on the first layer leads to the temperature increase at the interface of the two layers. The magnitude of this increase highly depends on the printing parameters such as printing speed and deposition strategy. Consequently, fine numerical simulation of the several layers' deposition according to raster orientation and printing parameters is necessary.

Raster deposition strategy of the second layer on the first deposited layer highly influence on the interdiffusion of two layers. When the passage of the second layer on the first layer takes place immediately after deposition of the first layer and before cooling and crystallization of the first layer, the interdiffusion two layers is more favorable than the cases with the deposition of the second layer after cooling and crystallization of the first layer. By modeling the second layer on the first layer we are able to determine the temperature at each point of the deposited filament.

During selection of the printing parameters, raster strategy deposition and environment temperature, we have to take relaxation time into consideration. This lately means, the interface of two layers must remain above melting temperature more than its relaxation time. As an example, the interface of two layers in PEEK must remain at 400 °C for about 1.6 s.

However, some further studies are needed in the following axis:

Previously we have explained the importance of measuring the surface tension of the polymers according to the temperature and specially at the melting state. The determination of the surface tension at high temperature and specially for the polymers with high viscosity and with sensitivity to thermal degradation needs more studies and innovations. A new method would worth to be developed.

In this work, we have studied in detail the deposition of a single bead on the printing platform. The deposition of more than two layers makes the numerical simulation much heavier and it will take longer. Consequently, for modeling the deposition of several layers, much powerful calculating servers are necessary. However, modeling several deposition layers will answer other obscure points to understand the properties of the printed parts. Furthermore, the applied pressure during deposition of the layer upon the deposited layer promotes the interdiffusion of the two layers. Understanding the applied pressure will lead to quantify the depth of the interdiffusion of the molecular chains at the interface of two layers. Moreover, by adding the mechanical behavior to the deposition model, we could model the residual stress and the influence of different printing parameters on the deformation on cooling.

The next step is to print PEEK samples under controlled environment at different temperatures and printing parameters to be mechanically tested. Furthermore, the determination of the temperature and the heat field by using infrared thermography would be necessary to validate the heat transfer predicted by our numerical model.

Hereby, we have studied the mechanism of interdiffusion of the macromolecular chains and the relaxation at temperature above the melting temperature. However, the interdiffusion starts below the melting temperature at slow rate, so, determining the relaxation times at lower temperature could help to optimize the printing speed. Also, the influence of the printing conditions on the welding (bonding) strength of a few filaments is a step towards the improvement of the bonding strength. For that, a specific mechanical test would be developed to quantify the inter-filament adhesion.

Lastly, when the use of the FFF process will be mastered for high-performance thermoplastics, polymeric based composites could be used as well. Bio-sourced composites, long carbon and glass fiber composites, and metal/polymer blends materials could be used as raw materials to reach new properties. For all these materials, the FFF process requires a fine control of the material properties during the deposition to insure the best quality of the 3D printed parts.

References

- [1] <https://www.volum-e.com/fabrication-additive-plastique/>, (n.d.).
- [2] <https://www.lesechos.fr/pme-regions/actualite-pme/0600848751374-lindustrie-prend-le-virage-de-la-fabrication-additive-2251275.php>, (n.d.).
- [3] <https://www.usinenouvelle.com/article/volum-e-investit-11-5-millions-d-euros-dans-une-plateforme-de-fabrication-additive.N463183>, (n.d.).
- [4] J. TARRIEU, Étude Et Durabilité De Solutions De Packaging Polymère D’Un Composant Diamant Pour L’Électronique De Puissance Haute Température., University of Toulouse, 2012.
- [5] M. angel Villar, Procédé de soudage laser de polymères haute performance : établissement des relations entre les paramètres du procédé, la structure et la morphologie du polymère et les propriétés mécaniques de l’assemblage, University of Toulouse, 2018.
- [6] N.W.A. Brown, Development of a Thermally-Assisted Piercing (TAP) Process for Introducing Holes into Thermoplastic Composites, University of Surrey, 2016.
<https://core.ac.uk/download/pdf/42552910.pdf>.
- [7] L. Martineau, Mise en forme de composites carbone/PEEK dans le domaine caoutchoutique, University of Toulouse, 2018.
- [8] P.-G. De Gennes, Reptation of a polymer chain in the presence of fixed obstacles, *J. Chem. Phys.* 55 (1971) 572–579. doi:10.1063/1.1675789.
- [9] T. Gornet, T. Wohlers, History of additive manufacturing, 2014. doi:10.1617/s11527-011-9818-6.
- [10] D.L. (The U. of T. at A.) Bourell, M.C. (Missouri U. of S. and T.) Leu, D.W. (Georgia I. of T.) Rosen, Identifying the Future of Freeform Processing 2009, *Rapid Prototyp. J.* (2009) 92. doi:10.1108/13552549910295514.
- [11] B.S. Shahi, Advanced Manufacturing Techniques (3D Printing), *Int. J. Mech. Prod. Eng.* 4 (2016) 16–23.
- [12] S. Crump, FDM STRATYS PATENT, 1992.
- [13] ASTM- F2792, Standard Terminology for Additive Manufacturing Technologies, (2013) 2–4. doi:10.1520/F2792-12A.2.
- [14] K. V. Wong, A. Hernandez, A Review of Additive Manufacturing, *ISRN Mech. Eng.* 2012 (2012) 1–10. doi:10.5402/2012/208760.
- [15] I. Jasiuk, D.W. Abueidda, C. Kozuch, S. Pang, F.Y. Su, J. McKittrick, An Overview on Additive Manufacturing of Polymers, *Jom.* 70 (2018) 275–283. doi:10.1007/s11837-017-2730-y.
- [16] I. Gibson, D. Rosen, B. Stucker, Additive manufacturing technologies, 3D printing, Rapid prototyping and direct digital manufacturing, Springer, 2015.
- [17] L. Novakova-Marcincinova, I. Kuric, Basic and Advanced Materials for Fused Deposition Modeling Rapid Prototyping Technology, *Manuf. Ind. Eng.* 11 (2012) 24–27.
- [18] <https://3dprint.com/76728/indmatec-peek-3d-printer/>, (2015).
- [19] https://www.aniwaa.com/best-peek-3d-printer-pe-ultem/#What_are_the_best_PEEK_3D_printers_and_ULTEM_3D_printers, (n.d.).

- [20] R. Jones, P. Haufe, E. Sells, P. Iravani, V. Olliver, C. Palmer, A. Bowyer, RepRap – the replicating rapid prototyper, *Robotica*. 29 (2018) 177–191. doi:10.1017/S026357471000069X.
- [21] C. Schelly, G. Anzalone, B. Wijnen, J.M. Pearce, Open-source 3-D printing technologies for education: Bringing additive manufacturing to the classroom, *J. Vis. Lang. Comput.* 28 (2015) 226–237. doi:10.1016/j.jvlc.2015.01.004.
- [22] “RepRap - RepRapWiki”, Reprap.org, 2016. [Online]. Available: <http://reprap.org>. [Accessed: 14- Nov- 2016]., (2016).
- [23] <https://www.3dhubs.com/3d-printers/mendel-prusa>, (n.d.).
- [24] J. Wang, H. Xie, Z. Weng, T. Senthil, L. Wu, A novel approach to improve mechanical properties of parts fabricated by fused deposition modeling, *Mater. Des.* 105 (2016) 152–159. doi:10.1016/j.matdes.2016.05.078.
- [25] M.A. Yardimci, Process analysis and planning for fused deposition modeling, University of Illinois at Chicago, 1999.
- [26] M.A. Yardimci, D.I. Guceri, S.C. Danforth, Thermal analyse of Fused deposition modeling, in: 8th, *Solid Free. Fabr. Symp.*, University of Texas, 1996: pp. 689–698.
- [27] A.W. Fatimatuzahraa, B. Farahaina, W.A.. Yusoff, The effect of employing different raster orientations on the mechanical properties and microstructure of Fused Deposition Modeling parts, in: 2011 IEEE Symp. Business, Eng. Ind. Appl., Ieee, 2011: pp. 22–27. doi:10.1109/ISBEIA.2011.6088811.
- [28] J. De Ciurana, L. Serenó, È. Vallès, Selecting process parameters in RepRap additive manufacturing system for PLA scaffolds manufacture, *Procedia CIRP*. 5 (2013) 152–157. doi:10.1016/j.procir.2013.01.031.
- [29] B.M. Tymrak, M. Kreiger, J.M. Pearce, Mechanical properties of components fabricated with open-source 3-D printers under realistic environmental conditions, *Mater. Des.* 58 (2014) 242–246. doi:10.1016/j.matdes.2014.02.038.
- [30] J.C. Riddick, M.A. Haile, R. Von Wahlde, D.P. Cole, O. Bamiduro, T.E. Johnson, Fractographic analysis of tensile failure of acrylonitrile-butadiene-styrene fabricated by fused deposition modeling, *Addit. Manuf.* 11 (2016) 49–59. doi:10.1016/j.addma.2016.03.007.
- [31] A.K. Sood, R.K. Ohdar, S.S. Mahapatra, Experimental investigation and empirical modelling of FDM process for compressive strength improvement, *J. Adv. Res.* 3 (2012) 81–90. doi:10.1016/j.jare.2011.05.001.
- [32] B.H. Lee, J. Abdullah, Z. a. Khan, Optimization of rapid prototyping parameters for production of flexible ABS object, *J. Mater. Process. Technol.* 169 (2005) 54–61. doi:10.1016/j.jmatprotec.2005.02.259.
- [33] K. Thrimurthulu, P.M. Pandey, N. Venkata Reddy, Optimum part deposition orientation in fused deposition modeling, *Int. J. Mach. Tools Manuf.* 44 (2004) 585–594. doi:10.1016/j.ijmachtools.2003.12.004.
- [34] G. Gomez-Gras, R. Jerez-Mesa, J.A. Travieso-Rodriguez, J. Lluma-Fuentes, Fatigue performance of fused filament fabrication PLA specimens, *Mater. Des.* 140 (2018) 278–285. doi:10.1016/j.matdes.2017.11.072.
- [35] B. Wittbrodt, J.M. Pearce, The effects of PLA color on material properties of 3-D printed components, *Addit. Manuf.* 8 (2015) 110–116. doi:10.1016/j.addma.2015.09.006.

- [36] D. Bell, T. Siegmund, 3D-printed polymers exhibit a strength size effect, 21 (2018) 658–665. doi:10.1016/j.addma.2018.04.013.
- [37] K.M. Rahman, T. Letcher, R. Reese, Mechanical Properties of Additively Manufactured PEEK Components Using Fused Filament Fabrication, in: Proc. ASME 2015 Int. Mech. Eng. Congr. Expo., 2015: p. V02AT02A009. doi:10.1115/IMECE2015-52209.
- [38] M.F. Arif, S. Kumar, K.M. Varadarajan, W.J. Cantwell, Performance of biocompatible PEEK processed by fused deposition additive manufacturing, Mater. Des. 146 (2018) 249–259. doi:10.1016/j.matdes.2018.03.015.
- [39] S. Xiaoyong, C. Liangcheng, M. Honglin, G. Peng, B. Zhanwei, L. Cheng, Experimental analysis of high temperature PEEK materials on 3D printing test, Proc. - 9th Int. Conf. Meas. Technol. Mechatronics Autom. ICMTMA 2017. (2017) 13–16. doi:10.1109/ICMTMA.2017.0012.
- [40] D. Ahn, J.-H. Kweon, S. Kwon, J. Song, S. Lee, Representation of surface roughness in fused deposition modeling, J. Mater. Process. Technol. 209 (2009) 5593–5600. doi:10.1016/j.jmatprotec.2009.05.016.
- [41] R. Anitha, S. Arunachalam, P. Radhakrishnan, Critical parameters in influencing the quality of prototypes in fused deposition modelling, 118 (2001) 2–5.
- [42] P. Vijay, P. Danaiah, K. V. D. Rajesh, Critical Parameters Effecting the Rapid Prototyping Surface Finish, J. Mech. Eng. Autom. 1 (2012) 17–20. doi:10.5923/j.jmea.20110101.03.
- [43] R.G. Randall, Sintering Theory and Practice, 1996.
- [44] K. Taki, K. Tabata, S.-I. Kihara, M. Ohshima, Bubble coalescence in polymeric foaming process, Foam. 2004 4th Int. Conf. Thermoplast. Foam Process. Technol. - Tech. Pap. (2004) 1–39.
- [45] J. Muller, Etude des changements de phase de polymère dans le procédé de rotomoulage : coalescence et cristallisation couplées à la thermique du procédé, (2008) 1–205.
- [46] S.A. Reffas, M. Elmeguenni, M. Benguediab, Analysis of Void Growth and Coalescence in Porous Polymer Materials. Coalescence in Polymer Materials, Eng. Technol. Appl. Sci. Res. 3 (2013) 452–460.
- [47] O. Pokluda, C.T. Bellehumeur, J. Vlachopoulos, Modification of Frenkel's Model for Sintering, AIChE J. 43 (1997) 3253–3256. doi:10.1002/aic.690431213.
- [48] A.C. Abbott, G.P. Tandon, R.L. Bradford, H. Koerner, J.W. Baur, Process-structure-property effects on ABS bond strength in fused filament fabrication, Addit. Manuf. 19 (2018) 29–38. doi:10.1016/j.addma.2017.11.002.
- [49] S. Bakrani Balani, F. Chabert, V. Nassiet, A. Cantarel, C. Garnier, Toward improvement of the properties of parts manufactured by FFF (Fused Filament Fabrication) through understanding the influence of temperature and rheological behaviour on the coalescence phenomenon, in: AIP Conf. Proc. 1896, American Institute of Physics, 2017. doi:10.1063/1.5008034.
- [50] A.C. Abbott, G.P. Tandon, R.L. Bradford, H. Koerner, J.W. Baur, Process-structure-property effects on ABS bond strength in fused filament fabrication, 19 (2018) 29–38.
- [51] J. Frankel, Viscous flow of crystalline bodies under the action of surface tension, J. Physics, USSR. (1945).
- [52] J.D. Eshelby, Discussion in paper by Shaler AJ, Seminar on kinetics of sintering, Met. Trans.

- 185 (1949) 806–807.
- [53] R.W. Hopper, Coalescence of Two Equal Cylinders: Exact Results for Creeping Viscous Plane Flow Driven by Capillarity, *J. Am. Ceram. Soc.* 67 (1984) C-262-C-264. doi:10.1111/j.1151-2916.1984.tb19692.x.
- [54] C. Bellehumeur, P.E. E-mail, Modeling of Bond Formation Between Polymer Filaments in the Fused Deposition Modeling Process, (2004).
- [55] E. Scribber, A.P.R. Eberle, D.G. Baird, Viscoelastic coalescence of thermotropic liquid crystalline polymers: The role of transient rheology, *J. Rheol. (N. Y. N. Y.)*. 49 (2005) 1159. doi:10.1122/1.2039827.
- [56] C.T. Bellehumeur, M. Kontopoulou, J. Vlachopoulos, The role of viscoelasticity in polymer sintering, 1998. doi:10.1007/s003970050114.
- [57] M.M. Ristić, S.D. Milosević, Frenkel's Theory of Sintering, *Sci. Sinter.* 38 (2006) 7–11. doi:10.2298/SOS0601007R.
- [58] P. Chen, J. Sanyal, M.P. Duduković, Numerical simulation of bubble columns flows: Effect of different breakup and coalescence closures, *Chem. Eng. Sci.* 60 (2005) 1085–1101. doi:10.1016/j.ces.2004.09.070.
- [59] C. Verdier, Coalescence of polymer droplets: experiments on collision, *Comptes Rendus l'Académie Des Sci. - Ser. IV - Phys.* 1 (2000) 119–126. doi:10.1016/S1296-2147(00)70015-1.
- [60] S. Aid, A. Eddhahak, Z. Ortega, D. Froelich, A. Tcharkhtchi, Predictive coalescence modeling of particles from different polymers: application to PVDF and PMMA pair, *J. Mater. Sci.* 52 (2017) 11725–11736. doi:10.1007/s10853-017-1302-4.
- [61] J.R. Castrejón-Pita, E.S. Betton, K.J. Kubiak, M.C.T. Wilson, I.M. Hutchings, The dynamics of the impact and coalescence of droplets on a solid surface, *Biomicrofluidics.* 5 (2011). doi:10.1063/1.3567099.
- [62] P.E. Murray, Numerical simulation of coalescence of inviscid drops at a solid surface, *Commun. Numer. Methods Eng.* 12 (1996) 447–454.
- [63] R.O. Fox, F. Laurent, M. Massot, Numerical simulation of spray coalescence in an Eulerian framework: Direct quadrature method of moments and multi-fluid method, *J. Comput. Phys.* 227 (2008) 3058–3088. doi:10.1016/j.jcp.2007.10.028.
- [64] M.M. Mohammadi, S. Shahhosseini, M. Bayat, Direct numerical simulation of water droplet coalescence in the oil, *Int. J. Heat Fluid Flow.* 36 (2012) 58–71. doi:10.1016/j.ijheatfluidflow.2012.04.001.
- [65] B.S. Sikarwar, S. Khandekar, K. Muralidhar, Coalescence of pendant droplets on an inclined super-hydrophobic substrate, in: *AIP Conf. Proc.*, 2013: pp. 505–512. doi:10.1063/1.4816902.
- [66] J. Zheng, H. Shi, G. Chen, Y. Huang, H. Wei, S. Wang, W. Wen, J. Zheng, H. Shi, G. Chen, Y. Huang, H. Wei, Relaxation of liquid bridge after droplets coalescence, 115115 (2016). doi:10.1063/1.4967883.
- [67] M. Sellier, E. Treluyer, Modeling the coalescence of sessile droplets, (2009) 1–14. doi:10.1063/1.3154552.
- [68] Q. Li, M. Liang, J. Chen, K. Wang, Q. Li, M. Liang, J. Chen, K. Wang, Investigation of Micro-Perspective Coalescence Behavior of Dispersed Phase Droplets in Uniform Electric Field, *LDIS.* 36 (2015) 1595–1600. doi:10.1080/01932691.2014.962038.

- [69] W. Du, L. Douadji, M. Delmotte, P. Mazabraud, A. Tcharkhtchi, Modélisation du mécanisme de coalescence des grains de polymère ., in: Congr. Fr. Therm. SFT 2007, 2007.
- [70] M. Asgarpour, Sintering and densification of polymer particles during rotational molding, 2016.
- [71] C. Pujos, Estimation de la rheologie d'un polymère dans une filière d'extrusion Simulation d'écoulement avec transferts thermiques et Inversion de mesures, L'universite Bordeaux 1, 2006.
- [72] J.E. Seppala, K.D. Migler, Infrared thermography of welding zones produced by polymer extrusion additive manufacturing, *Addit. Manuf.* 12 (2016) 71–76. doi:10.1016/j.addma.2016.06.007.
- [73] V.W. Wang, C.A. Hieber, K.K. Wang, Dynamic simulation and graphics for the injection molding of three-dimensional thin parts, *J. Polym. Eng.* 7 (1986).
- [74] F. Liravi, R. Darleux, E. Toyserkani, Additive manufacturing of 3D structures with non-Newtonian highly viscous fluids: Finite Element modeling and experimental validation, *Addit. Manuf.* 13 (2016) 113–123. doi:10.1016/j.addma.2016.10.008.
- [75] T. Köpplmayr, E. Mayrhofer, Numerical Simulation of Viscoelastic Layer Rearrangement in Polymer Melts using OpenFOAM, in: 2015. doi:10.1063/1.4918407.
- [76] R. Comminal, J. Spangenberg, J.H. Hattel, Numerical simulations of viscoelastic flows with free surfaces, *Congrès Français de Mécanique.* (2013) 1–6.
- [77] C. LE BOT, Impact et solidification de gouttes métalliques sur un substrat solide, L'universite de Bordeaux 1, 2003.
- [78] A.D. Amico, A.M. Peterson, An adaptable FEA simulation of material extrusion additive manufacturing heat transfer in 3D, *Addit. Manuf.* 21 (2018) 422–430. doi:10.1016/j.addma.2018.02.021.
- [79] R. Jerez-Mesa, J.A. Travieso-Rodriguez, G. Gomez-Gras, X. Corbella, R. Busqué, Finite element analysis of the thermal behavior of a RepRap 3D printer liquefier, *Mechatronics.* 36 (2016) 119–126. doi:10.1016/j.mechatronics.2016.04.007.
- [80] R. Comminal, Numerical simulation of viscoelastic free surface flows using a streamfunction / log conformation formulation and the volume of fluid method, Technical University of Denmark, 2015.
- [81] R. Comminal, M.P. Serdeczny, D.B. Pedersen, J. Spangenberg, Numerical modeling of the strand deposition flow in extrusion-based additive manufacturing, *Addit. Manuf.* 20 (2018) 68–76.
- [82] F. Peng, B.D. Vogt, M. Cakmak, Complex flow and temperature history during melt extrusion in material extrusion additive manufacturing, *Addit. Manuf.* 22 (2018) 197–206. doi:10.1016/j.addma.2018.05.015.
- [83] T.A. Osswald, J. Puentes, J. Kattinger, Fused filament fabrication melting model, *Addit. Manuf.* 22 (2018) 51–59. doi:10.1016/j.addma.2018.04.030.
- [84] G. Percoco, F. Lavecchia, L.M. Galantucci, Compressive properties of FDM rapid prototypes treated with a low cost chemical finishing, *Res. J. Appl. Sci. Eng. Technol.* 4 (2012) 3838–3842.
- [85] L.M. Galantucci, F. Lavecchia, G. Percoco, Quantitative analysis of a chemical treatment to

- reduce roughness of parts fabricated using fused deposition modeling, *CIRP Ann. - Manuf. Technol.* 59 (2010) 247–250. doi:10.1016/j.cirp.2010.03.074.
- [86] L.M. Galantucci, F. Lavecchia, G. Percoco, Experimental study aiming to enhance the surface finish of fused deposition modeled parts, *CIRP Ann. - Manuf. Technol.* 58 (2009) 189–192. doi:10.1016/j.cirp.2009.03.071.
- [87] S. Singamneni, A. Roychoudhury, O. Diegel, B. Huang, Modeling and evaluation of curved layer fused deposition, *J. Mater. Process. Technol.* 212 (2012) 27–35. doi:10.1016/j.jmatprotec.2011.08.001.
- [88] R.J.A. Allen, R.S. Trask, An experimental demonstration of effective Curved Layer Fused Filament Fabrication utilising a parallel deposition robot, *Addit. Manuf.* 8 (2015) 78–87. doi:10.1016/j.addma.2015.09.001.
- [89] P.M. Pandey, N.V. Reddy, S.G. Dhande, Improvement of surface finish by staircase machining in fused deposition modeling, *J. Mater. Process. Technol.* 132 (2003) 323–331.
- [90] D. Chakraborty, B. Aneesh Reddy, A. Roy Choudhury, Extruder path generation for Curved Layer Fused Deposition Modeling, *Comput. Aided Des.* 40 (2008) 235–243. doi:10.1016/j.cad.2007.10.014.
- [91] A. Robisson, T. Brommer, *Amorphous Polymers : Polymer Conformation*, 2008.
- [92] J. Jensen, *Plastics-It's all about molecular structure*, *Plast. Eng.* (2016). http://read.nxtbook.com/wiley/plasticsengineering/september2016/consultantscorner_plastics.html.
- [93] F. Zhao, D. Li, Z. Jin, Preliminary investigation of poly-ether-ether-ketone based on fused deposition modeling for medical applications, *Materials (Basel)*. 11 (2018). doi:10.3390/ma11020288.
- [94] J.J. Otero, A. Vijverman, M.Y. Mommaerts, Use of fused deposit modeling for additive manufacturing in hospital facilities: European certification directives, *J. Cranio-Maxillofacial Surg.* 45 (2017) 1542–1546. doi:10.1016/j.jcms.2017.06.018.
- [95] X. Deng, Z. Zeng, B. Peng, S. Yan, W. Ke, Mechanical properties optimization of poly-ether-ether-ketone via fused deposition modeling, *Materials (Basel)*. 11 (2018). doi:10.3390/ma11020216.
- [96] M. Rinaldi, T. Ghidini, F. Cecchini, A. Brandao, F. Nanni, Additive layer manufacturing of poly (ether ether ketone) via FDM, *Compos. Part B Eng.* 145 (2018) 162–172. doi:10.1016/j.compositesb.2018.03.029.
- [97] C. Yang, X. Tian, D. Li, Y. Cao, F. Zhao, C. Shi, Influence of thermal processing conditions in 3D printing on the crystallinity and mechanical properties of PEEK material, *J. Mater. Process. Technol.* 248 (2017) 1–7. doi:10.1016/j.jmatprotec.2017.04.027.
- [98] L. Martineau, F. Chabert, G. Bernhart, T. Djilali, L. Martineau, F. Chabert, G. Bernhart, T. Djilali, Mechanical behavior of amorphous PEEK in the rubbery state, in: *ECCM17 - 17th Eur. Conf. Compos. Mater., Munich*, 2017.
- [99] J.W. Tseng, Y. Liu, K. Yen, J. Belkner, B. Tobias, H. Liu, B. Wang, Screw extrusion-based additive manufacturing of PEEK, *Mater. Des.* 140 (2018) 209–221. doi:10.1016/j.matdes.2017.11.032.
- [100] R. Ebewele, *Polymer Science and Technology*, CRC, New york, 1985. doi:10.1016/0025-5416(85)90434-3.

- [101] M.F. Talbott, G.S. Springer, L.A. Berglund, The Effects of Crystallinity on the Mechanical Properties of PEEK Polymer and Graphite Fiber Reinforced PEEK, *J. Compos. Mater.* 21 (1987) 1056–1081. doi:10.1177/002199838702101104.
- [102] J.R. Atkinson, J.N. Hay, M.J. Jenkins, Enthalpic relaxation in semi-crystalline PEEK, *Polymer (Guildf)*. 43 (2002) 731–735.
- [103] X. Tardif, B. Pignon, N. Boyard, J.W.P. Schmelzer, V. Sobotka, D. Delaunay, C. Schick, Experimental study of crystallization of PolyEtherEtherKetone (PEEK) over a large temperature range using a nano-calorimeter, *Polym. Test.* 36 (2014) 10–19. doi:10.1016/j.polymertesting.2014.03.013.
- [104] C. Wei, M. Chen, F. Yu, Temperature modulated DSC and DSC studies on the origin of double melting peaks in poly (ether ether ketone), *Polymer (Guildf)*. 44 (2003) 8185–8193. doi:10.1016/j.polymer.2003.10.009.
- [105] S. Kumar, D.P. Anderson, Crystallization and morphology of poly (aryl-ether-ether- ketone), *Polymer (Guildf)*. 27 (1986) 329–336.
- [106] D.C. Bassett, R.H. Olley, I.A.M. al Raheil, On crystallization phenomena in PEEK, *Polymer (Guildf)*. 29 (1988) 9–11.
- [107] H. Chen, R.S. Porter, Observation of two-stage crystallization of poly (ether ether ketone) by thermal mechanical analysis, *Polymer (Guildf)*. 34 (1993) 4576–4578.
- [108] B.B. Sauer, W.G. Kampert, E.N. Blanchard, S.A. Threefoot, B.S. Hsiao, Temperature modulated DSC studies of melting and recrystallization in polymers exhibiting multiple endotherms, *Polymer (Guildf)*. 41 (2000) 1099–1108.
- [109] L. Jin, J. Ball, T. Bremner, H. Sue, Crystallization behavior and morphological characterization of poly (ether ether ketone), *Polymer (Guildf)*. 55 (2014) 5255–5265. doi:10.1016/j.polymer.2014.08.045.
- [110] C. Fournies, M. Dosie, M.H.J. Koch, J. Roovers, Cold Crystallization of Narrow Molecular Weight Fractions of PEEK, *Macromolecules*. (1999) 8133–8138. doi:10.1021/ma9909206.
- [111] A. Kumar, W. Virginia, *Fundamentals of polymer engineering*, second, Marcel Dekker, New York, 2003.
- [112] J.M. Dealy, J. Wang, *Melt Rheology and its Applications in the Plastics Industry*, second, Springer Science, 2013. doi:10.1007/978-94-007-6395-1.
- [113] G. Schramm, *A Practical Approach to Rheology and Rheometry*, 1994.
- [114] M. Kaseem, Y. Gun, Melt Flow Behavior and Processability of Polylactic Acid / Polystyrene (PLA / PS) Polymer Blends, *J. Polym. Environ.* (2016). doi:10.1007/s10924-016-0873-5.
- [115] N. Shibuya, R.S. Porter, A kinetic study of PEEK sulfonation in concentrated sulfuric acid by ultraviolet- visible spectroscopy, *Polymer (Guildf)*. 35 (1994) 3237–3242.
- [116] I. Morrison, *Kirk-Othmer Encyclopedia of Chemical Technology*. Kirk-Othmer encyclopedia of Chemical Technology, 8 (n.d.) 697–739. doi:10.1002/0471238961.
- [117] Z. Grzesik, Surface Modification of Polyetheretherketone by Helium / nitrogen and Nitrous Oxide Plasma Enhanced Chemical Vapour Deposition, 33 (2014) 147–153. doi:10.1515/htmp-2013-0022.
- [118] N. Bhatnagar, S. Jha, S. Bhowmik, Energy dispersive spectroscopy study of surface modified

- PEEK, 2 (2011) 52–57. doi:10.5185/amlett.2010.12188.
- [119] C. Dreiser, L.J. Krätz, H. Bart, KINETICS AND QUANTITY OF CRYSTALLIZATION FOULING ON POLYMER SURFACES : IMPACT OF SURFACE CHARACTERISTICS AND PROCESS CONDITIONS, 2013 (2013) 291–295.
- [120] D. Rymuszka, K. Terpiłowski, L. Hołysz, D. Mańko, Influence of plasma treatment on polyetheretherketone (PEEK) surface properties, (2015) 10–11.
- [121] K. Grundke, P. Uhlmann, T. Gietzelt, B. Redlich, H.J. Jacobasch, Studies on the wetting behaviour of polymer melts on solid surfaces using the Wilhelmy balance method, Colloids Surfaces A Physicochem. Eng. Asp. 116 (1996) 93–104. doi:10.1016/0927-7757(96)03624-2.
- [122] D. Wyart, Polyetherether cétones (PEEK) : élaboration et propriétés Polyethers cétones (PEEK) : élaboration et propriétés, Tech. l'ingenieur. (2014).
- [123] VICTREX, Victrex ® PEEK 450g, 2014.
- [124] A. Södergård, M. Stolt, Industrial Production of High Molecular Weight Poly(Lactic Acid), John Wiley & Sons, Inc., 2010. doi:10.1002/9780470649848.ch3.
- [125] C. Bas, A.C. Grillet, F. Thimon, N.D. Albérola, Crystallization kinetics of poly(aryl ether ether ketone): Time-temperature-transformation and continuous-cooling-transformation diagrams, Eur. Polym. J. 31 (1995) 911–921. doi:10.1016/0014-3057(95)00060-7.
- [126] D.E. Henton, P. Gruber, J. Lunt, J. Randall, Polylactic Acid Technology, in: Nat. Fibers, Biopolym. Biocomposites, 2005: pp. 527–578. doi:10.1201/9780203508206.ch16.
- [127] D. Garlotta, A Literature Review of Poly Lactic Acid, J. Polym. Environ. 9 (2001) 63–84. doi:10.1023/A:1020200822435.
- [128] J.F. Turner, A. Riga, A. O'Connor, J. Zhang, J. Collis, Characterization of drawn and undrawn poly-L-lactide films by differential scanning calorimetry, J. Therm. Anal. Calorim. 75 (2004) 257–268. doi:10.1023/B:JTAN.0000017347.08469.b1.
- [129] J. Zhang, D.X. Yan, J.Z. Xu, H.D. Huang, J. Lei, Z.M. Li, Highly crystallized poly (lactic acid) under high pressure, AIP Adv. 2 (2012). doi:10.1063/1.4769351.
- [130] D. Battagazzore, S. Bocchini, A. Frache, Crystallization kinetics of poly(lactic acid)-talc composites, Express Polym. Lett. 5 (2011) 849–858. doi:10.3144/expresspolymlett.2011.84.
- [131] J. Lamethe, Etude de l'adhésion de composites thermoplastiques semi-cristallins; application à la mise en oeuvre par soudure, Université Paris VI- Pierre et Marie Curie, 2005.
- [132] K.B. Larson, K. Koyama, Measurement by the flash method of thermal diffusivity, heat capacity, and thermal conductivity in two-layer composite samples, J. Appl. Phys. 39 (1968) 4408–4416. doi:10.1063/1.1656985.
- [133] J. Escobedo, G.A. Mansoori, Surface tension prediction for pure fluids, AIChE J. 42 (1996) 1425–1433.
- [134] A. Williams, Free Energy Relationships in Organic and Bio-Organic Chemistry, The Royal Society of Chemistry, 2003. doi:10.1360/zd-2013-43-6-1064.
- [135] M. Day, D. Sally, D.M. Wiles, D. Chemistry, Thermal Degradation of Poly (aryl-Ether- Ether-Ketone) : Experimental Evaluation of Crosslinking Reactions, J. Appl. Polym. Sci. 40 (1990) 1615–1625.
- [136] S. Bakrani, F. Chabert, V. Nassiet, A. Cantarel, Influence of printing parameters on the

- stability of deposited beads in fused filament fabrication of poly (lactic) acid, *Addit. Manuf.* 25 (2019) 112–121. doi:10.1016/j.addma.2018.10.012.
- [137] R. Al-Itry, K. Lamnawar, A. Maazouz, Improvement of thermal stability, rheological and mechanical properties of PLA, PBAT and their blends by reactive extrusion with functionalized epoxy, *Polym. Degrad. Stab.* 97 (2012) 1898–1914. doi:10.1016/j.polymdegradstab.2012.06.028.
- [138] M. Day, D. Sally, D.M. Wiles, Thermal Degradation of Poly(aryl-Ether-Ether-Ketone): Experimental Evaluation of Crosslinking Reaction, *J. Appl. Polym. Sci.* 40 (1990) 1615–1625.
- [139] F. J., Viscous Flow of Crystalline Bodies under the Action of Surface Tension,”, *J. Phys.* 9 (1945) 385.
- [140] J. Vlachopoulos, O. Pokluda, C.T. Bellehumeur, J. Machopoulos, Modification of Frenkel ’ s Model for Sintering, *Aiche J.* 43 (1997). doi:10.1002/aic.690431213.
- [141] C. Bellehumeur, L. Li, Q. Sun, P. Gu, Modeling of Bond Formation Between Polymer Filaments in the Fused Deposition Modeling Process, *J. Manuf. Process.* 6 (2004) 170–178.
- [142] M. Van Sint Annaland, N.G. Deen, J.A.M. Kuipers, Numerical simulation of gas bubbles behaviour using a three-dimensional volume of fluid method, *Chem. Eng. Sci.* 60 (2005) 2999–3011. doi:10.1016/j.ces.2005.01.031.
- [143] COMSOL Multiphysics, CFD Module User’s Guide, 2017.
- [144] M. Aashammer, Modeling of Heat Transfer in Two-Phase Flow Using the Level-Set Method, 2013.
- [145] L.D. Landau, E.M. Lifshitz, Fluid Mechanics, Second, PERGAMON PRESS, 1987.
- [146] K. Nakamura, K. Katayama, T. Watanabe, Some Aspects of Nonisothermal Crystallization of Polymers. I. Relationship Between Crystallization Temperature, Crystallinity, and Cooling Conditions, *J. Appl. Polym. Sci.* 16 (1972) 1077–1091.
- [147] A. Levy, A Novel Physics Node for Nakamura Crystallization Kinetics, in: Proc. 2016 COMSOL Conf. Munich, 2016.
- [148] J.F. Agassant, P. Avenas, B. Sergent, Jean , Philippe Vergnes, M. Vincent, *Mise en forme des polymères*, LAVOISIER, Paris, 2014.
- [149] J.P. Tordella, An Instability in the Flow of Molten Polymers, *Rheol. Acta.* 3 (1958) 216–221.
- [150] J.M. Piau, J.F. Agassant, *Rheology for polymer melt processing*, Elsevier, 1996.
- [151] W.J. Schrenk, N.L. Bradley, T. Alfrey, Interfacial Flow Instability in Multilayer Coextrusion, *Polym. Eng. Sci.* 18 (1978) 1–4.
- [152] R.I. Tanner, A theory of die-swell, *Polym. Sci. Part A-2 Polym. Phys.* 8 (1970) 2067–2078.
- [153] P. G. Lafleur, *Extrusion des polymères*, Lavoisier, Paris, 2014.
- [154] R. Poole, The Deborah and Weissenberg numbers. The British Society of Rheology, *Rheol. Bull.* 53 (2012) 32–39.
- [155] K. Wang, *Viscoelasticity From Theory to Biological Applications*, 2012. doi:10.5772/50137.
- [156] N. Cogswell, Converging Flow of Polymer Melts in extrusion dies, *J. Rheol. (N. Y. N. Y.)* 25

- (1981) 605–617. doi:10.1122/1.549651.
- [157] C.J.S. Petrie, Extensional viscosity: A critical discussion, *J. Nonnewton. Fluid Mech.* 137 (2006) 15–23. doi:10.1016/j.jnnfm.2006.01.011.
- [158] W.P. Cox, E.H. Merz, Correlation of dynamic and steady flow viscosities, *J. Polym. Sci.* 28 (1958) 619–622.
- [159] J. Liang, Influence of Die Angles on Pressure Drop during Extrusion, (2001) 1150–1154.
- [160] Y. Nakayama, *Introduction to Fluid Mechanics*, Butterworth-Heinemann, 1973. doi:10.1093/biomet/60.1.125.
- [161] S. Voyutskii, *Autohesion and Adhesion of High Polymers*, WILEY, New York, 1963.
- [162] R. Vasenin, Adhesion pressure in the diffusion theory of the adhesion of polymers, *Polym. Sci. U.S.S.R.* 3 (1962) 608–615.
- [163] P.-G. De Gennes, *Comptes Rendus de l'Académie des Sciences, Comptes Rendus l'Académie Des Sci.* B291 (1980) 219–221.
- [164] L. Lieng-Huang, Kinetics of Polymer-Polymer Interdiffusion, in: *Fundam. Adhes.*, Springer Science+Business Media, LLC, New York, 1991: pp. 181–202. doi:10.1007/978-1-4899-2073-7.
- [165] N. Boyard, ed., *Heat Transfer in Polymer Composite Materials*, WILEY, 2016.
- [166] W. Alexiewicz, K. Grygiel, Cole-cole plots for linear and nonlinear dielectric relaxation in solutions of rigid, highly dipolar, symmetric-top molecules in spherical solvents, *Acta Phys. Pol. A.* 114 (2008) 687–698. doi:10.12693/APhysPolA.114.687.
- [167] J.G. Powles, Cole-Cole Plots as they should be, *J. Mol. Liq.* 56 (1993) 35–47.
- [168] P. Cebe, S. Hongt, Crystallization behaviour of poly(ether- ether-ketone), *Polymer (Guildf)*. 27 (1986) 1183–1192.
- [169] S. Tan, A. Su, J. Luo, E. Zhou, Crystallization kinetics of poly (ether ether ketone) (PEEK) from its metastable melt, *Polymer (Guildf)*. 40 (1999) 1223–1231.
- [170] J. Huang, Dispersion , Crystallization Kinetics , and Parameters of Hoffman – Lauritzen Theory of Polypropylene and Nanoscale Calcium Carbonate Composite, *Polym. Eng. Sci.* (2009) 1855–1864. doi:10.1002/pen.
- [171] T. Choupin, B. Fayolle, G. Regnier, C. Paris, J. Cinquin, B. Brule, Isothermal crystallization kinetic modeling of poly (etherketoneketone) (PEKK) copolymer, *Polymer (Guildf)*. 111 (2017). doi:10.1016/j.polymer.2017.01.033.
- [172] S. Vyazovkin, J. Stone, N. Sbirrazzuoli, Hoffman – Lauritzen parameters for non-isothermal crystallization of poly (ethylene terephthalate) and poly (ethylene oxide) melts, *J. Therm. Anal. Calorim.* 80 (2005) 177–180.
- [173] C. Nicodeau, *Continuous welding modeling of thermoplastic matrix composites*, Ecole Nationale Supérieure d'Art et Métiers, 2005.
- [174] S. Holmes, J.W. Gillespie, Thermal Analysis for Resistance Welding of Large-Scale Thermoplastic Composite Joints, *J. Reinf. Plast. Compos.* 12 (1993) 723–736.
- [175] M.C. Kuo, J.C. Huang, M. Chen, Non-isothermal crystallization kinetic behavior of alumina nanoparticle filled poly (ether ether ketone), *Mater. Chem. Phys.* 99 (2006) 258–268.

doi:10.1016/j.matchemphys.2005.10.021.

Annexes

Annex Contents

A1 Annex I: Advantages and drawbacks of the polymeric based processes.....	ii
A2 Annex II: Methods for the characterization of polymers.....	iii
A2.1 DSC (Differential scanning calorimeter).....	iii
A2.2 TMA (Thermo-mechanical analyzer).....	iii
A2.3 Hot-disk thermal conductivity measurement.....	iv
A2.4 Surface tension measurement.....	iv
A2.5 Extensional die for viscosity measurement.....	v
A3 Annex III: VICTREX 450G datasheet.....	vii
A4 Annex IV: Heating furnace and 3D stage design.....	ix
A4.1. Motorized 3D stage.....	ix
A4.2. High-temperature furnace.....	xv
A5 Annex V: Encountered numerical errors during simulation.....	xx
A6 Annex VI: Temperature sweep tests by oscillatory test.....	xxii

A1 Annex I: Advantages and drawbacks of the polymeric based processes

Process	Description	Advantages	Disadvantages
Powder bed fusion (PBF)	<ol style="list-style-type: none"> 1. A roller or blade is used to deposit a thin layer of powder on a build plate. 2. Laser fuses certain areas in the powder. 3. Build plate is lowered by the height of the powder layer. 4. Repeat steps 1–3 for height of part. 5. Excess powder is removed 	<p>Excess powder serves as support, so no support structures required.</p> <p>Superior mechanical properties.</p>	<p>Expensive, high material Waste.</p> <p>Few compatible materials.</p> <p>Rough or grainy surface</p>
Typical materials	Polystyrene, Polyester, Polyamide 11 and 12, Polypropylene, Polyurethane, Polyetheretherketone (PEEK)		
Material jetting	<ol style="list-style-type: none"> 1. Liquid polymer is jetted onto a build plate in droplets. 2. Ultraviolet (UV) source cures the polymer. 3. Build plate is lowered or print head is raised by the height of the droplet layer. 4. Repeat steps 1–3 for height of part. 5. Support material is removed 	<p>Manufacture multi-material parts</p> <p>Low residual stresses</p> <p>High dimensional accuracy</p>	<p>Weak mechanical properties.</p> <p>Adverse environmental effects.</p>
Typical materials	Acrylates, acrylics, Polylactic (PLA), Epoxies, Starch		
Vat photopolymerization	<ol style="list-style-type: none"> 1. Build plate is positioned on top of a vat of photopolymer. 2. UV source below vat cures certain areas in thin layer contacting the build plate. 3. Build plate is raised by thickness of cured layer. 4. Repeat steps 1–3 for height of part. 5. Support material is removed 	<p>High resolution to build time ratio.</p> <p>Good durability.</p> <p>Can produce multi-material parts, but it is difficult.</p>	<p>Relatively expensive due to requirement for vat Change Requires support material.</p> <p>Cannot create parts with enclosed volumes due to liquid environment.</p>
Typical materials	Acrylates, acrylics, epoxies		
Material extrusion	<ol style="list-style-type: none"> 1. Thermoplastic filament is passed through a heated print head as the print head moves over certain areas of a build plate. 2. Once the layer is complete, either the print head or build plate moves by height of layer. 3. Repeat steps 1 and 2 for height of part. 4. Support material is removed. 	<p>Can be optimized for strong material properties.</p> <p>Low costs of machines.</p>	<p>Low resolution and poor surface finish require significant.</p> <p>Post-processing.</p> <p>High residual stresses.</p>
Typical materials	Acrylonitrile butadiene styrene (ABS), PLA, Acrylics, Polycarbonate (PC), Polyetherimide (PEI), high impact Polystyrene, PEEK		

A2 Annex II: Methods for the characterization of polymers

A2.1 DSC (Differential scanning calorimeter)

Differential scanning calorimeter, or DSC, is a thermo-analytical technique to study the thermal transitions including glass transition, melting temperature and, crystallization of polymers. Polymer samples release or absorb heat during its transition temperatures and crystallization. The principle of this technique is based on the difference between the amounts of absorbed heat or released heat during transitions by the polymeric sample and the reference pan. As it is represented in Figure 1 the analyses are based on the comparison of the absorbed heat between the sample in an aluminum pan and an empty pan as the reference. The sample is placed in a pan in order to keep the analyses safe from contamination.

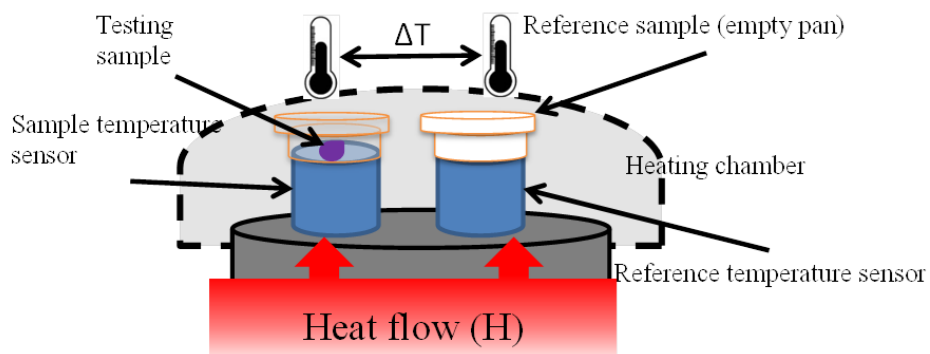


Figure 1: The Principle of the Differential Scanning Calorimeter (DSC)

A2.2 TMA (Thermo-mechanical analyzer)

This technique is used to measure the expansion of a material over a temperature range. The sample is kept in a thermal furnace. This thermal furnace regulates the temperature of the sample during the test. A sensitive probe placed on the sample, measures the variation of the dimension of the sample according to the temperature to measure the thermal expansion coefficient. The principle is represented in Figure 2.

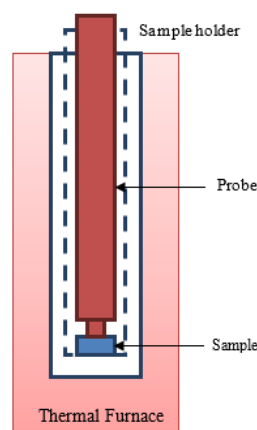


Figure 2: Schematic presentation of the TMA analyzer

A2.3 Hot-disk thermal conductivity measurement

As it is represented in Figure 3 the probe is embedding between two samples. Probe is made of a two coils of nickel. The system is considered semi-infinite and isotropic. All of the system is placed in a fixture in order to get better contact between the samples and probe.

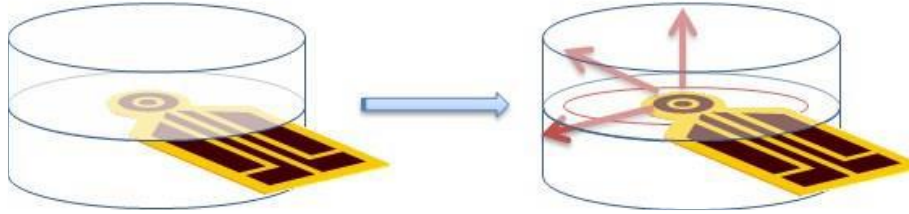


Figure 3 : schematic representation of the probe embedded between two samples

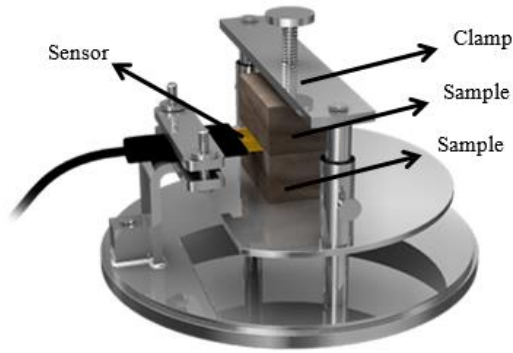


Figure 4: schematic representation of the sample holder used for testing the conductivity of the polymer by Hot Disk

During the test, the electric power (P_0) is delivered to the sample during a certain time (t). By Joule's law, the probe emits some amount of heat. Heat emitted from the probe diffuse in the sample homogenously.

By increasing the temperature, the electric resistance of the probe ($R(t)$) changes according to the time. Increase of the temperature and consequently, the variation of the electric resistance of the probe are dependent. The electric resistance of the probe according to time is determine by eq. 1.

$$R(t) = R_0 [1 + \alpha \overline{\Delta T(\tau)}] \quad \text{eq. 1}$$

Where R_0 is the electric resistance of the probe at the start of the test in ohm, α is the resistance coefficient of the probe and $\overline{\Delta T(\tau)}$ is the mean value of the temperature increase according to time. τ is the temporal data which could determine from the eq. 2.

$$\tau = \sqrt{\frac{at}{r^2}} \quad \text{eq. 2}$$

Where a is the thermal diffusivity of the sample and, r is the diameter of the sample.

A2.4 Surface tension measurement

Contact angle meter uses the sessile drop technique for determining the contact angle of a liquid on a solid substrate. As it is represented in Figure 5, this method is based on the determination of the contact angle between the solid substrate and several liquids with known surface tension. A droplet of 6 μl of

water, diiodomethane, glycerol and, ethylene glycol has been deposited on a solid substrate of PLA and PEEK by using a special syringe. The surface tension of the liquids used for the tests are represented in the Table 1. The value of surface tension is measured using contact angle and Owens-Wendt-Rabel-Kaelble (OWRK) method. The total value of the surface tension is the sum of polar and dispersive components Table 1.

Table 1: Surface tension of the liquids used for the test

Liquid	γ_l^d	γ_l^p
Water	21.75	51.0
Glycerol	37.0	26.4
Diiodomethane	50.8	0
Ethylene Glycol	29.3	19

$$\gamma = \gamma_s^d + \gamma_s^p \quad \text{eq. 3}$$

Where γ_s^d is the dispersive component and γ_s^p is the polar component of the surface tension. Interactions caused by temporary fluctuations of the charge distribution in the atoms-molecules are called dispersive interactions (van der Waals interactions). Polar interactions comprise Coulomb interactions between permanent dipoles and between permanent and induced dipoles (e.g. hydrogen bonds).

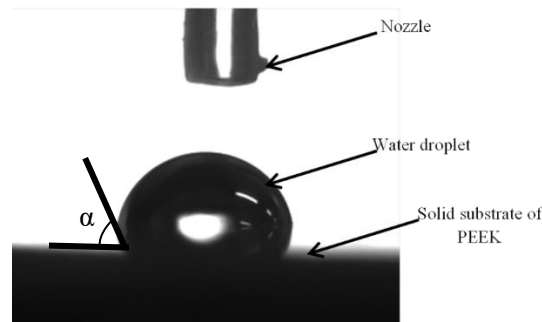


Figure 5: The deposited drop of water on the solid PEEK in the room temperature

The used tensiometer is a Krüss DSA100 with DSA3 software and a heating furnace TC21, a high-temperature DO3241 dosage system and a metallic syringe with the diameter of 1.8mm.

For the surface tension measurement in the melted state, a pellet is melted in the syringe and deposited on the different substrates with thermally stable surface tension.

A2.5 Extensional die for viscosity measurement

The parallel-plate configuration of the rheometer is the suitable way to determine the viscosity of the fluids at relatively low frequencies (shear rates) from 0.01 Hz to 100 Hz. However, at higher frequencies (shear rates) the rheometers could not be used. Additionally, with this configuration of rheometer, determining the extensional viscosity of the polymers is not possible. For these reasons, we have used an extruder with the extensional die in order to determine the viscosity at high shear rates. In order to determine the viscosity by extensional die, the fluid is under extensional stress. In our studies, we have determined the viscosity of the polymer by parallel-plate configuration for low shear rates from 0.01 Hz to 100 Hz, and then, by an extruder equipped with a die for high shear rates up to 10 000 s⁻¹.

As it is illustrated in Figure 6, in this method, the viscosity is determined by an extruder implemented by a die and several heat and pressure sensors.

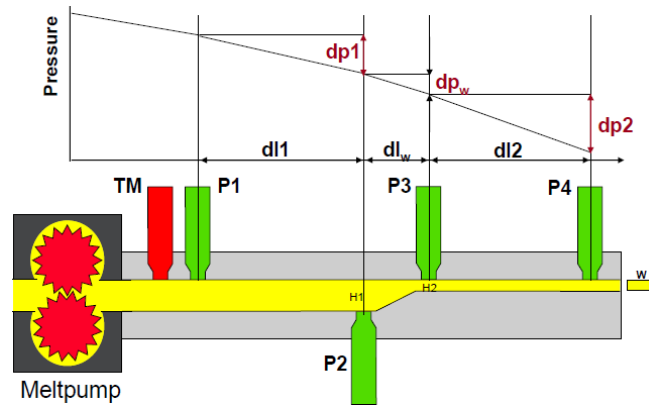


Figure 6: Schematic representation of the die used to determine the viscosity at the high shear rate and extensional viscosity

The die has three different regions to determine the viscosity. The first region which is between P1 and P2 sensors is used to determine the viscosity at low shear rate. The second region is between P2 and P3 which is suitable to determine the extensional or elongation viscosity. The third part of the die is used to determine the viscosity at high shear rates between P3 and P4.

A3 Annex III: VICTREX 450G datasheet

VICTREX[®] PEEK 450G

► Product Description:

High performance thermoplastic material, unreinforced PolyEtherEtherKetone (PEEK), semi crystalline, granules for injection moulding and extrusion, standard flow, FDA food contact compliant, colour natural/beige.

► Typical Application Areas:

Applications for higher strength and stiffness as well as high ductility. Chemically resistant to aggressive environments, suitable for sterilisation for medical and food contact applications.

► Material Properties

	CONDITIONS	TEST METHOD	UNITS	TYPICAL VALUE
Mechanical Data				
Tensile Strength	Yield, 23°C	ISO 527	MPa	98
Tensile Elongation	Break, 23°C	ISO 527	%	45
Tensile Modulus	23°C	ISO 527	GPa	4.0
Flexural Strength	At 3.5% strain, 23°C	ISO 178	MPa	125
	At yield, 23°C			165
	125°C			85
	175°C			19
	275°C			12.5
Flexural Modulus	23°C	ISO 178	GPa	3.8
Compressive Strength	23°C	ISO 604	MPa	125
	120°C			70
Charpy Impact Strength	Notched, 23°C	ISO 179/1eA	kJ m ⁻²	7.0
	Unnotched, 23°C	ISO 179/U		n/b
Izod Impact Strength	Notched, 23°C	ISO 180/A	kJ m ⁻²	8.0
	Unnotched, 23°C	ISO 180/U		n/b
Thermal Data				
Melting Point		ISO 11357	°C	343
Glass Transition (Tg)	Onset	ISO 11357	°C	143
	Midpoint			150
Coefficient of Thermal Expansion	Along flow below Tg	ISO 11359	ppm K ⁻¹	45
	Average below Tg			55
	Along flow above Tg			120
	Average above Tg			140
Heat Deflection Temperature	As moulded, 1.8 MPa	ISO 75-f	°C	152
	Annealed 200°C / 4h, 1.8MPa			160
Thermal Conductivity	Along flow, 23°C	ISO 22007-4	W m ⁻¹ K ⁻¹	0.32
	Average, 23°C			0.29
Relative Thermal Index	Electrical	UL 746B	°C	260
	Mechanical w/o impact			240
	Mechanical w/impact			180
Flow				
Melt Viscosity	400°C	ISO 11443	Pa.s	350
Miscellaneous				
Density	Crystalline	ISO 1183	g cm ⁻³	1.30
Shore D hardness	23°C	ISO 868		84.5
Water Absorption by immersion	Saturation, 23°C	ISO 62-1	%	0.45
	Saturation, 100°C			0.55

Electrical Properties				
Dielectric Strength	2mm thickness	IEC 60243-1	kV mm ⁻¹	23
	50µm thickness			200
Comparative Tracking Index		IEC 60112	V	150
Loss Tangent	23°C, 1MHz	IEC 60250	n/a	0.004
Dielectric Constant	23°C, 1kHz	IEC 60250	n/a	3.1
	23°C, 50Hz			3.0
	200°C, 50Hz			4.5
Volume Resistivity	23°C	IEC 60093	Ω cm	10 ¹⁶
	125°C			10 ¹⁵
	275°C			10 ⁹

Fire Smoke Toxicity				
Glow Wire Test	2mm thickness	IEC 60695-2-12	°C	960
Limiting Oxygen Index	0.4mm thickness	ISO 4589	% O ₂	24
	3.2mm thickness			35
Toxicity Index	CO content	NES 713	n/a	0.074
	CO ₂ content			0.15
	Total gases			0.22

Typical Processing Conditions	
Drying Temperature / Time	150°C / 3h or 120°C / 5h (residual moisture <0.02%)
Temperature settings	355 / 360 / 365 / 370 / 375°C (Nozzle)
Hopper Temperature	Not greater than 100°C
Mould Temperature	170°C - 200°C
Runner	Die / nozzle >3mm, manifold >3.5mm
Gate	>1mm or 0.5 x part thickness

Mould Shrinkage and Spiral Flow					
Spiral Flow	375°C nozzle, 180°C tool	1mm thick section	Victrex	mm	110
Mould Shrinkage	375°C nozzle, 180°C tool	Along flow	ISO 294-4	%	1.0
		Across flow			1.3

A4 Annex IV: Heating furnace and 3D stage design

In chapter 2 and chapter 3, we have explained in detail the importance of controlling the environment's temperature. Controlling the environment's temperature is necessary to enhance the crystallization kinetics and the bonding of the deposited beads and layers.

In our studies, we used an extruder from Thermo Fisher Company (Figure 7). This extruder is suitable for melting high temperature and high viscosity polymers. It is equipped with different heat and pressure sensors to make the control of the polymer flow and polymer properties possible.

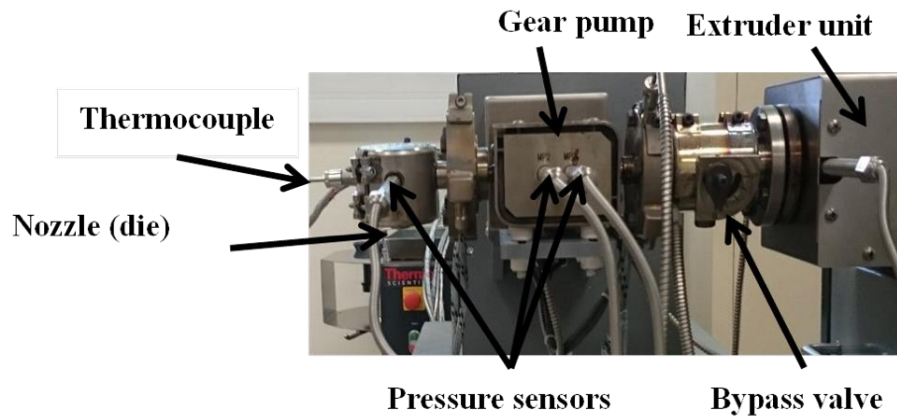


Figure 7: Extruder system

At the beginning of the thesis, we planned to print PEEK samples to characterize their mechanical resistance. As no suitable printer existed at this time, we decided to extrude PEEK filaments with an extruder and to deposit them directly on a stage. For that, we had to design a 3D stage and a furnace compatible with the extruder. To vary the cooling rate of the polymer after exiting from the nozzle and so, to control the crystallization kinetics, the printing process must be done in a heating chamber. As a consequence, we have to design a printer and a 3D stage which could maintain the temperature at high temperature (up to 250°C) and also compatible with the extruder. In the following parts, we will present our design for the motorized 3D stage and heating furnace.

A4.1. Motorized 3D stage

In this section, we present our design for the motorized 3D stage. Considering that the extruder is fixed, the motorized 3D stage must be able to move in three directions the deposition plate. The 3D stage must be designed according to the criteria mentioned in the Figure 8 and Table 2.

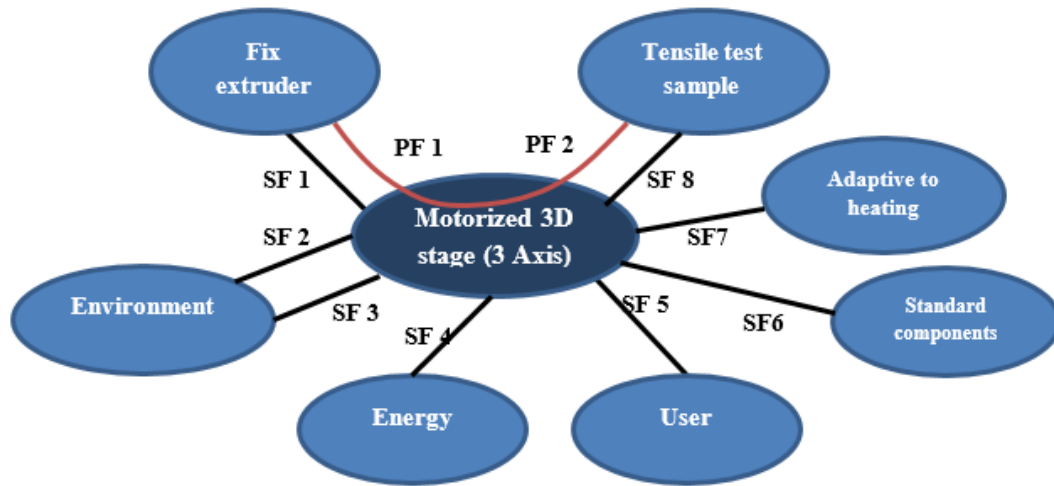


Figure 8: Pieuvre diagram of the 3D stage

PF 1: Movement of the support according to the nozzle of the extruder (the extruder nozzle is fixed).

PF 2: Observation with IR camera.

SF 1: Compatible to the extruder.

SF 2: Compatible to the environment.

SF 3: Resistance at the environment (high temperature).

SF 4: Compatible to the source of energy.

SF 5: Removing the samples must be easy for the user.

SF 6: Must use maximum standard parts and less machining for fabrication of the 3D stage

SF 7: Compatible to the heating furnace (platform enters in the heating furnace).

SF 8: Adaptable to manufacture the tensile test samples.

PF is the principal function and SF is the service function.

Table 2: Designing criteria of the 3D stage

Function	Function name	Criteria	Level	Flexibility
PF 1	Permit the printing of the tensile test sample of PEEK via extruder	Minimum range in the x-direction	200 mm	F1
		Minimum range in the y-direction	55 mm	F1
		Minimum range in the z-direction	15 mm	F1
		The precision of 3 axis	0.1 mm	F0
		Articulation angles	To determine	F1
		Minimum velocity	30 mm.s ⁻¹	F0
PF 1	Observation with IR camera	Placing An IR transparent window for temperature measurement		F0
SF 1	Compatible to the extruder	The distance between the extruder and the ground	1 m	F0
		The position of the 3D stage	Outside of heating furnace	F0
		Easy assembly and disassembly of the 3D stage	Easy	F0
SF 2	Compatible to the environment	Wires and cablings	No interference from different parts and wires of the extruder	F0

SF 3	Resistance at the environment	Resistance at the high temperature	250°C -280°C	F0
SF 4	Compatible to the source of energy	Compatible to the EDF (Electricity of France)	230 V	F1
SF 5	Easy to remove the printed sample	Easy assembly and disassembly of a cohesive film on the printing platform	Easy	F0
SF 6	Using standard components	Reducing the machining and using maximum possible standard component for 3D stage		F1
SF 7	Adaptive to heating chamber	The printing platform of the 3D stage must be inside of a heating chamber.		F0
SF 8	Compatible to the tensile test sample	The maximum length of the sample	70 mm	F1
		Maximum width of the sample	15 mm	F1
		The maximum height of the sample	6 mm	F1
		The extra margin for y and x directions	5 mm - 10 mm	F0

There are two different configurations for the structure of the printers.

- Cartesian movement structure: In these printers, the movement is based on three axes. Normally the head of the extruder is z-axis and the platform move in x and y directions.
- Delta movement structure: In these movement structure, the platform of the deposition is fixed while the nozzle is mobile. The nozzle is linked to three arms, in order to satisfy the movement in three axes. Contrary to the Cartesian structure, the bars could only move vertically.

Cartesian and Delta structures are represented in Figure 9.

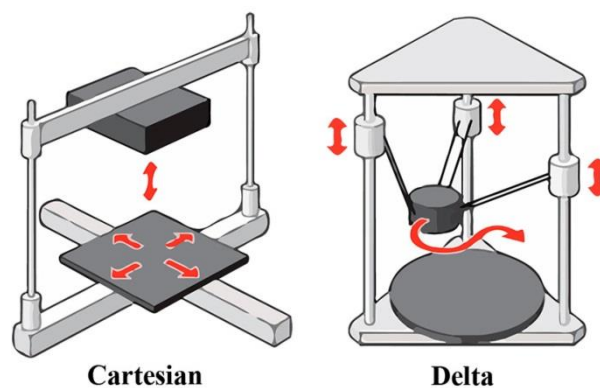


Figure 9: Illustration of the Cartesian and Delta movement structure of the printers

Each of these structures has their advantages and disadvantages. Comparing these structures, we have decided to use a delta structure for the 3D stage. The main reason that we prefer the Delta structure than Cartesian structure is the complexity of the Cartesian structure in our case. The advantages and disadvantages of Delta structure and Cartesian structure are represented in Table 3 and Table 4.

According to our configuration and the fact that the 3D stage must be adapted to the extruder, and lack of free space under the extruder, we have selected the inverse Delta configuration.

Table 3: Advantages and disadvantages of the Cartesian structure

Cartesian structure	
Advantages	Disadvantages
<ul style="list-style-type: none"> - The majority of the parts used for Cartesian structure are the standard components which are founded in the market - Distribution of the mass on the linkages components. The mass of the platform is properly spread on the shafts. 	<ul style="list-style-type: none"> - Complex parts for machining. - The transition in z direction necessities replacement of all the structure. Which may cause the problems. - Cartesian system takes much space compared to the size of the sample. Considering the system must be adapted to the extruder and the small size of the sample the Cartesian system will be very big.

Table 4: Advantages and disadvantages of the Delta structure

Delta structure	
Advantages	Disadvantages
<ul style="list-style-type: none"> - Already existed design easy to implement. - Inversing the delta system will reduce the stress applied on the linkage. - The standard components for the Delta structure is more than Cartesian structure And we have less components to manufacture by machining. - Known precision for x and y axis, the verification is necessary for Delta structure. 	<ul style="list-style-type: none"> - The value of the applied force is unknown in the Delta structure. - Delta structure is more adapted for fast printing (not our case). - The angle of the ball joints become so small for the small moving distances. - Keeping the deposition surface flat is a major issue considering we are using the inverse Delta configuration

In order to get the best design which confirming the desire criteria, several Delta configurations for the 3D stage has been designed. During the design, we have tried to use as much as possible the standard parts in order to reduce the cost of machining and manufacturing the non-standard parts. Final assembly for the Delta 3D stage compatible with the extruder is represented in Figure 10.

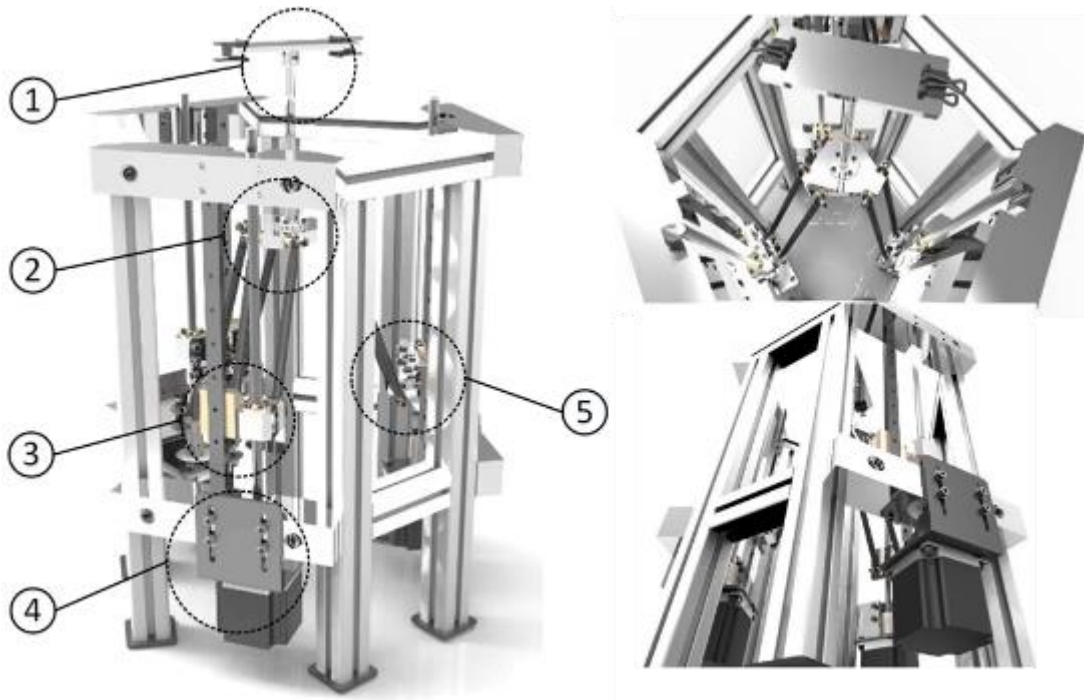


Figure 10: 3D stage assembly designed for the printing of the PEEK compatible with the extruder

In the Figure 11(a) and Figure 11(b), we will represent the sub-assembly of each part of the printer.



Figure 11: Deposition platform marks as n. 1 in the 3D stage assembly



(a)



(b)

Figure 12: Primary platform marks as n. 2 in the 3D stage assembly



Figure 13: Linear guide rail marks as n. 3 in the 3D stage assembly

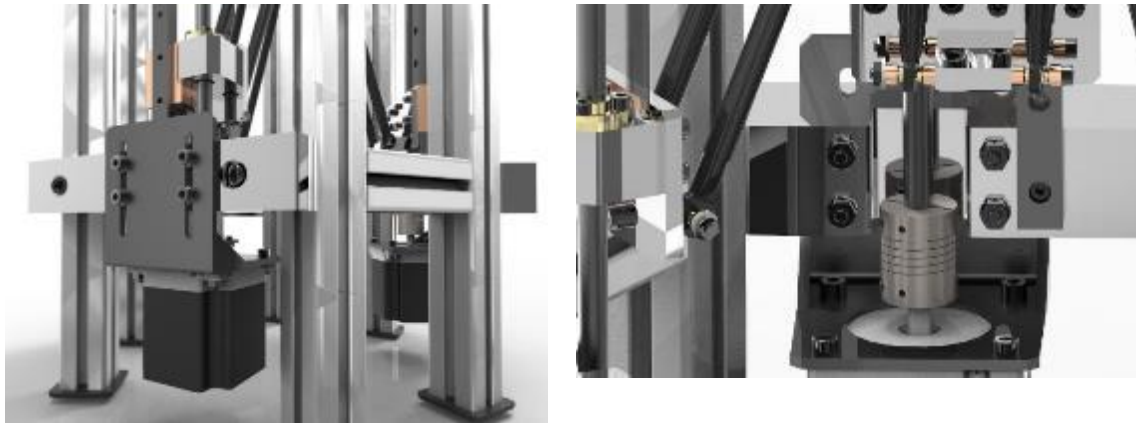


Figure 14: The assembly of the motors marks as n. 4 in the 3D stage assembly

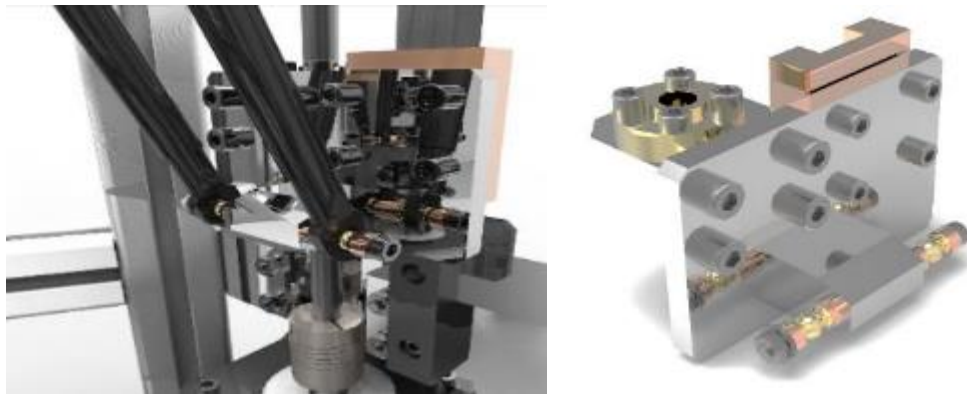


Figure 15: Guiding intermediate sub-assembly marks as n. 5 in the 3D stage assembly

The standard parts used in the 3D stage are presented in Table 5.

Table 5: The standard parts necessary for the 3D stage assembly

Number	The part's name	Quantity
1	Linear rail MGN 12	3
2	Linkage for Delta printers	6
3	Plated linear shaft $8\phi * 400\text{mm}$	4
4	Stepper motor NEMA 23	3
5	Flexible coupler $6.35 * 8 \text{ mm}$	3
6	Trapezoidal 8mm lead screw and nut kit	2
7	Electronic kit RUMBA	1
8	Stepper driver PAP TB6600	3

9	NEMA 23 motor support	3
10	Electric power 24V – 400 W	1
11	Cooling fan	3
12	Aluminum profile of the structure	1 (3m)
13	Nut for groove	1

Although we have decided to use standard parts as much as possible, however, there are still some parts which must be manufactured separately. Table 6 shows the non-standard parts which must be manufactured separately.

Table 6: The parts which must be manufactured

Number	The part's name	Manufacturing process	Quantity
1	Structure part	Milling	6
2	Printing platform	Milling	1
3	Primary printing platform	Milling	1
4	Lower centering bushing	Lathe machining	1
5	Guiding the intermediate part	Cutting	3
6	Supporting nut	Milling	3
7	Linkage fixation clevis	Milling	3

Furthermore, during the design phase of the 3D stage, we have decided to reduce as much as possible the price of manufacturing by using the standard parts and also designing the parts which do not need special machining process.

A1.2. High-temperature furnace

As we have explained previously, in order to control the kinetics of coalescence and cooling rate of the deposited beads, the printing environment must be controlled. To control the environment temperature of the beads, we have designed a heating furnace. The designed furnace must be adaptable to the extruder and designed 3D stage. Design criteria for the heating furnace are represented in Figure 16.

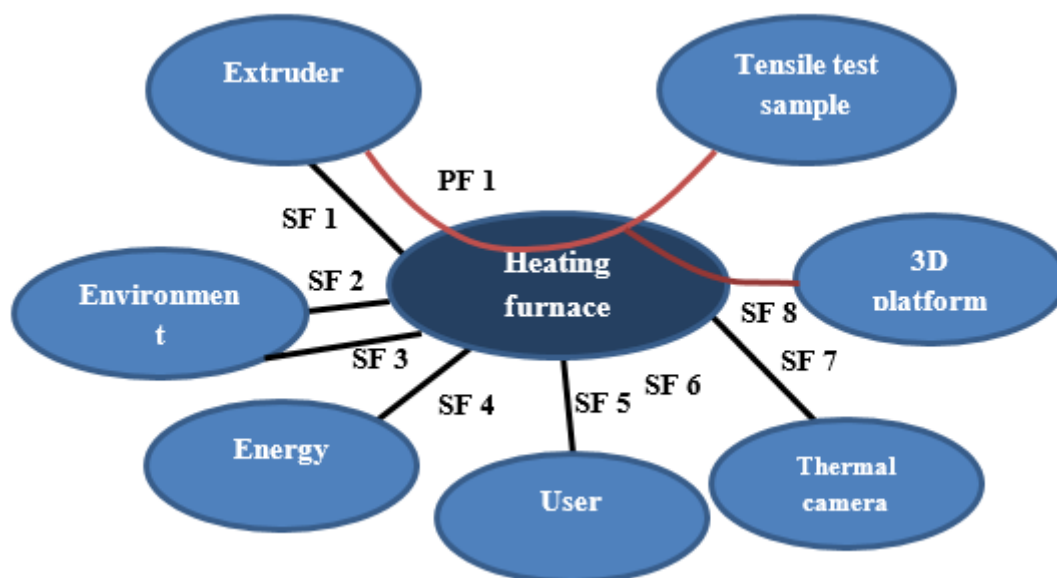


Figure 16 : The Pieuvre diagram for heating furnace

PF 1: Permit the printing of the tensile test sample of PEEK via extruder and 3D stage

SF 1: Compatible to the extruder

SF 2: Compatible to the environment

SF 3: Keeping maintaining the desired temperature inside the furnace while outside is cold

SF 4: Compatible to the source of energy

SF 5: Facility of use for the user (Easy to remove the printed sample)

SF 6: IR transparent window for the thermography measurement

SF 7: Temperature resistance IR window for the thermography measurement

SF 8: Compatible to the 3D stage

The detail of the design criteria for the heating furnace is represented in Table 7.

Table 7: Designing criteria of the heating furnace

Function	Function name	Criteria	Level	Flexibility
PF 1	Permit the printing of the tensile test sample of PEEK via extruder and 3D stage	Minimum internal length of the furnace	400 mm	F1
		The minimum internal width of the furnace	150 mm	F1
		The minimum internal height of the furnace	160 mm	F1
		Maintaining the internal temperature	250°C -280°C	F0
SF 1	Compatible to the extruder	The position of the heating furnace	Under the nozzle	F0
		Easy assembly and disassembly of the 3D stage	Easy	F0
SF 2	Compatible to the environment	Wires and cablings	No interference from different parts and wires of the extruder	F0
SF 3	Resistance at the environment	Keeping maintaining the desired temperature inside the furnace while outside is cold	Bellow 50°C	F0
SF 4	Compatible to the source of energy	Compatible to the EDF (Electricity of France)	230 V	F1
SF 5	Facility of use for the user	Easy assemblage and disassembling of printed part. Taking the part of the printing platform	Easy	F1
SF 6	Thermography measurement	IR transparent window for the thermography measurement	Transparent for the spectrum from 0.76 μm until 4 μm	F0
SF 7	Thermography measurement	Temperature resistance IR window for the thermography measurement	Resistance at high temperature up to 260°C	F0
SF 8	Compatible to the 3D stage	The heating furnace must be compatible with the 3D stage and has enough space for the movement in 3 axis		F0

According to detailed criteria explained in Table 7, we have done our heating furnace. Heating furnace compatible with the extruder is represented in Figure 17.

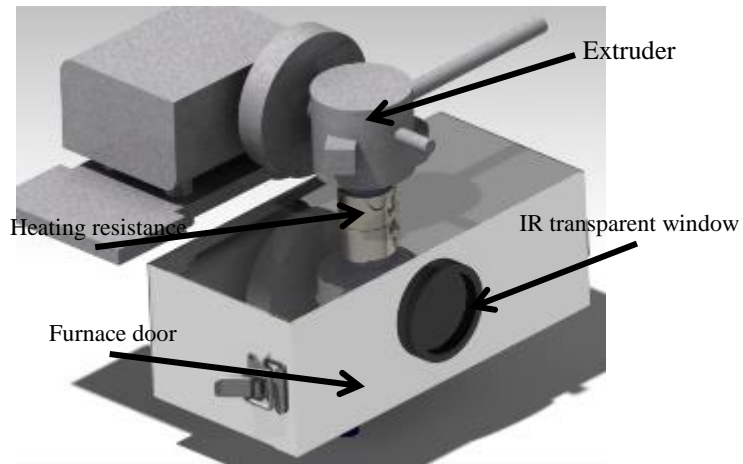


Figure 17: Heating furnace designed according to the design criteria

Figure 18 shows the exploded view of the heating furnace. As it is represented in Figure 18 and Figure 19, the heating furnace is composed of three regions: Internal wall, external wall and the insulation between the internal and external walls. The temperature of the internal space of the heating furnace is until 250 °C. The heating of the furnace is done by heating resistance.

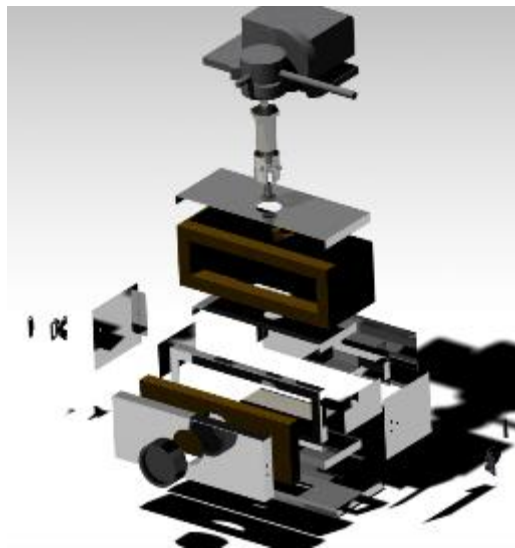


Figure 18: Exploded view of the heating furnace

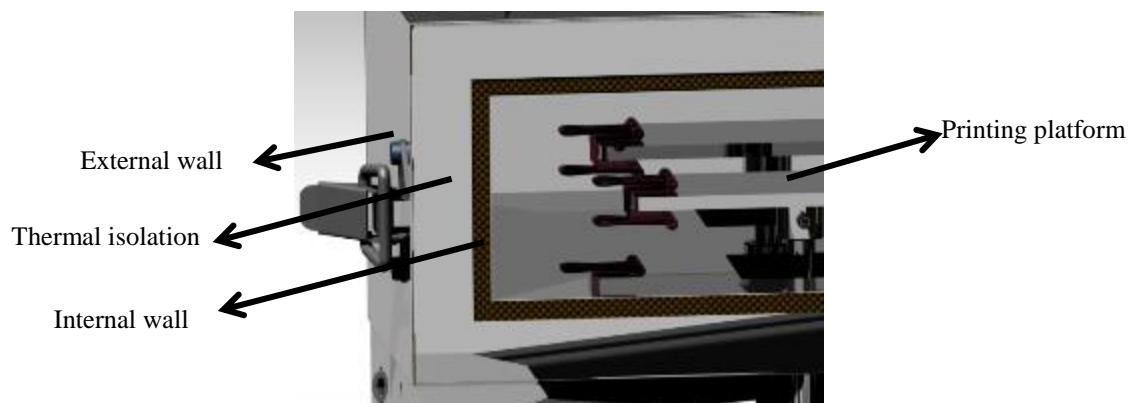


Figure 19: Detail view of the heating furnace

In order to measure the thermal field of the polymer during deposition by infrared (IR) thermal camera, an IR transparent window must be integrated into the design. Figure 20 shows the selected IR window for our heating furnace (<https://www.flir.com/products/ir-windows/>). This window is IR transparent, and temperature resistant up to 270°C.



Figure 20: IR transparent window for the measurement of the temperature in the heating furnace

Finally, by assembling the 3D stage, heating furnace, and the extruder we design the high temperature set up for printing PEEK. Figure 21 shows the 3D printer compatible with the extruder for printing PEEK.

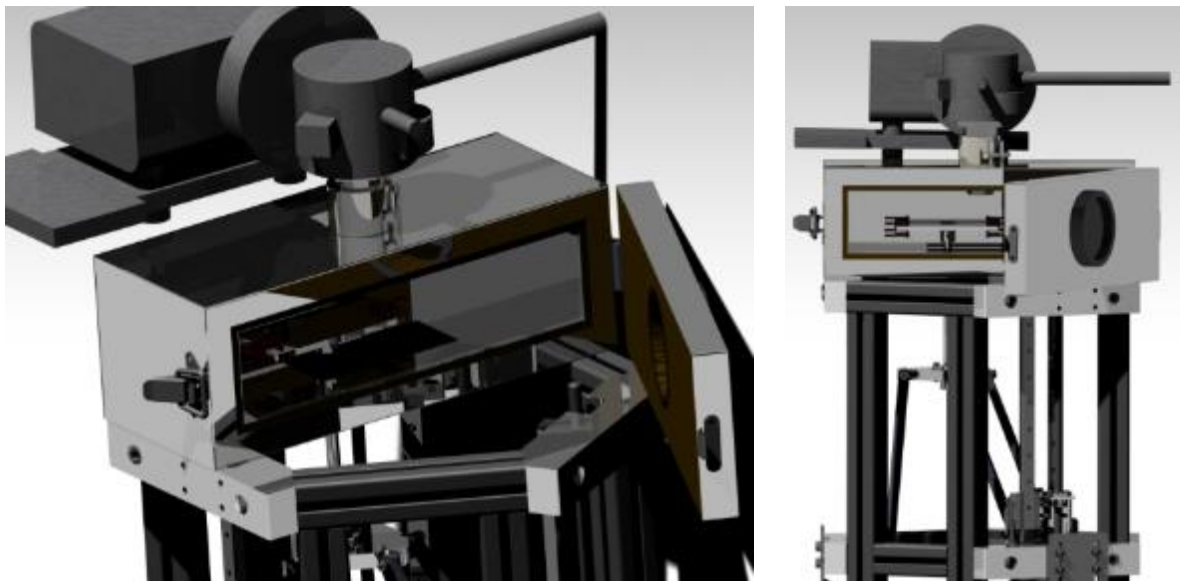


Figure 21: Final assembly of the 3D stage and heating furnace compatible to the extruder in order to print PEEK

Heating and insulation of the heating chamber

For the external walls, we have used stainless steel sheets of 0.3 mm diameter. In order to insulate inside of the heating furnace from the outside environment and control the temperature inside the furnace, we will use ceramic fiber as insulation. The ceramic fiber is heat resistant to up to 1400 °C.

In order to control the temperature inside the heating furnace, we use the heating resistance in the chamber. The heating chamber will be accompanied by the thermocouple and the controllers in order to control precisely the temperature inside the heating chamber. No fan has been used in the configuration in order to reduce the air turbulence. The heating in the furnace is by conduction.

A5 Annex V: Encountered numerical errors during simulation

During numerical simulation of the material deposition on the platform, we have encountered several numerical errors and problems. These errors are mostly because of non-homogenous meshes.

During numerical simulation, there is a fluid flow from the outlet to the system. Figure 22 shows two numerical error occurring in our model. Although for these boundaries we have selected no backward flow, however, the external fluid flow enters in the model. One of the options in order to reduce this upward flow of material is to reduce the size of the meshes. However, using too fine meshes increases the time of the calculation.

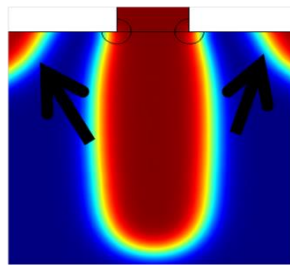


Figure 22: Entering unlikely flow in the system

By using axisymmetric model and the appropriate size of the meshes, we could reduce this numerical error properly.

Figure 23 shows the polymer deposition on a substrate. Close to the surface, the volume fraction must be 1, while as it represented in Figure 23 close to the surface, there is a fine layer where the volume fraction is not 1.

For solving this problem, we have changed the meshes near the substrate to the boundary layer. Using boundary layer meshes could reduce this problematic; however, it is not solving the problem totally.

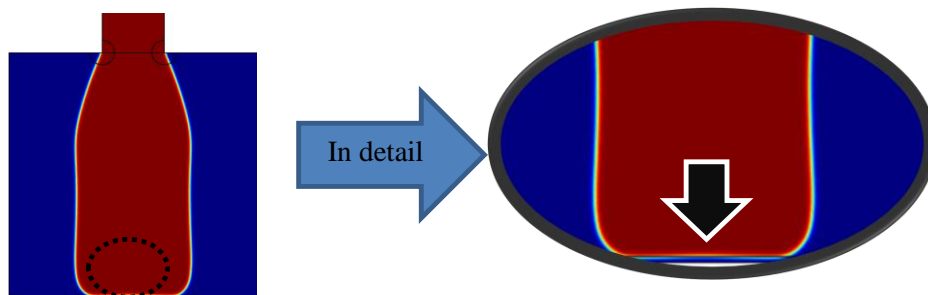


Figure 23: Volume fraction close to the surface of the deposition

During the simulation of material deposition, selecting the velocity of substrate and inlet velocity is very important. In the case, if the inlet velocity (velocity of material which exits from the nozzle) is high; there is material leakage on opposite side of the substrate velocity. Figure 24 shows material leakage during deposition.

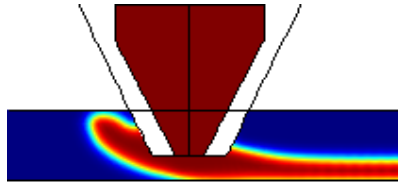


Figure 24: Material leakage during deposition of the polymer

During the polymer extrusion, when the polymer exits from the nozzle, it swells. This means the diameter of the filament increases. Here, reducing the size of the meshes reduces the swelling of the filament. However, after a certain size of the meshes, it remains stable. Figure 25 shows the swelling of the filament when it exits from the nozzle.

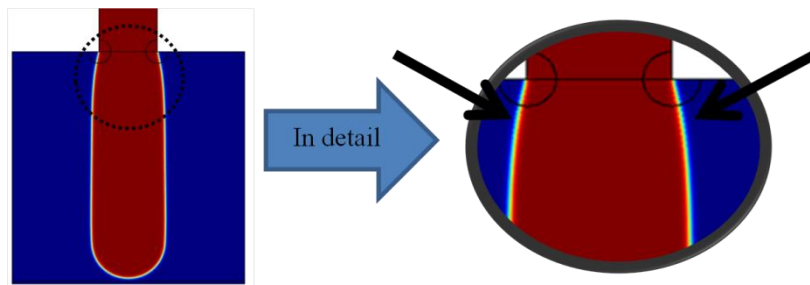


Figure 25: Swelling of the polymer filament when it exits from the nozzle

We have to mention, the swelling represented here is due to numerical errors which is not related to the die swelling represented in the section 3.5.4 which is because by molecular chain relaxation.

Figure 26 shows the cross-section of a deposited filament in the y - z plan on the substrate. In the case of depositing material, the shape of the deposited filament is the elliptical shape (Figure 26 (a)). However, if the selected outlet debit of the polymer from the nozzle (or inlet velocity of the material in our numerical simulation) is very big, the height of the deposited bead exceeds the selected height (distance between the nozzle and deposition platform). In this case the elliptical shape of bead changes to the shape represented in Figure 26 (b). However, by 2D numerical simulation, the axes are x - z , which means it is not possible to model the cross section of the deposited material. Here, in the case of over deposition of the material, there will be leakage (Figure 24) which we could not see in experimental studies.

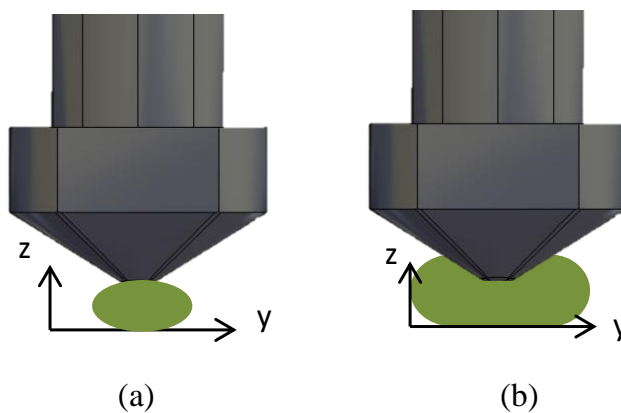


Figure 26: The cross-section of the deposited material, (a) when the material is not over deposited, (b) in the case of over deposition of the material

A6 Annex VI: Temperature sweep tests by oscillatory test

Rectangular torsion and parallel plate configurations of the rheometer have been used to determine the imaginary G'' and real G' modulus of PEEK from room temperature up to 400 °C.

Prior to temperature sweep test, the strain sweep test has been carried out in order to determine the linear viscoelastic domain of the PEEK. At 1 rad.s⁻¹ the response of PEEK is still in the linear viscoelastic domain.

In the solid state, oscillatory tests were performed at 1 rad.s⁻¹, from 25°C to the melting temperature of PEEK (about 330°C) at 3°C.min⁻¹ by means of rectangular torsion configuration. In the melting state, oscillatory test has been carried out by parallel-plate configuration. The test were performed at 1 rad.s⁻¹, from 340°C to 400°C at 3°C.min⁻¹.

For rectangular torsion, the sample is a parallelepipedic specimen where the dimensions are 45x9.85x1.87 mm. A 25 mm diameter disk is used for the parallel-plate configuration test. The gap between two plates is 2 mm. The obtained results for the temperature sweep test of PEEK are represented in Figure 28.

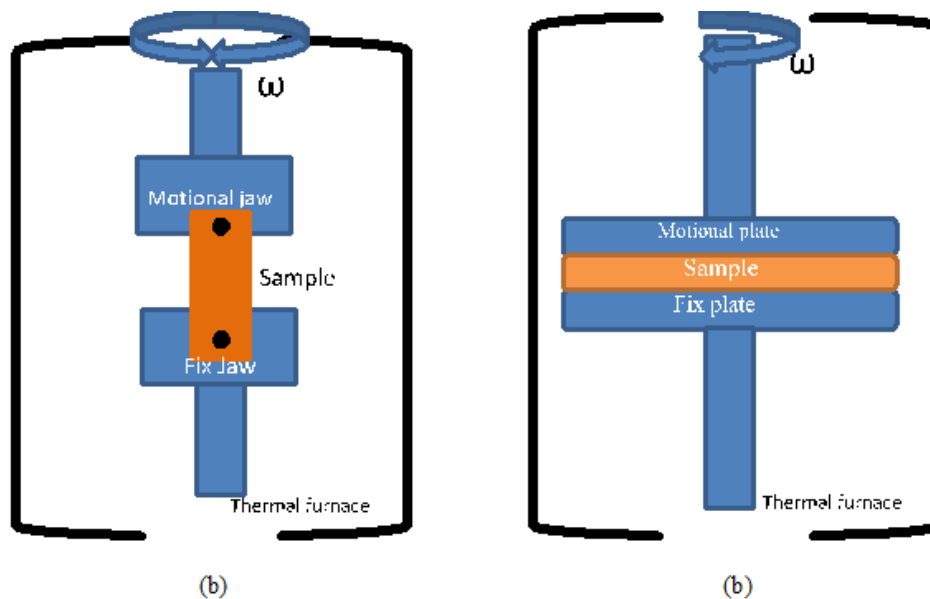


Figure 27: Schematic presentation of the (a) Rectangular torsion configuration (b) Parallel plate configuration, for Rheometer

Figure 28 shows the complex modulus of PEEK composed of imaginary G'' and real G' part. Indeed, viscoelastic materials exhibit a behavior between totally elastic and totally viscous. G'' which represents the loss modulus of the viscoelastic material is the dissipated energy during loading. G' or the storage modulus is the real part of the complex modulus. The storage modulus characterizes stiffness of viscoelastic materials; it reaches the maximum value when the material is purely elastic.

The results obtained from rectangular torsion rheometer show that PEEK has good mechanical resistance at the high temperature (until 300°C). In fact, PEEK keeps its storage modulus even at 300°C.

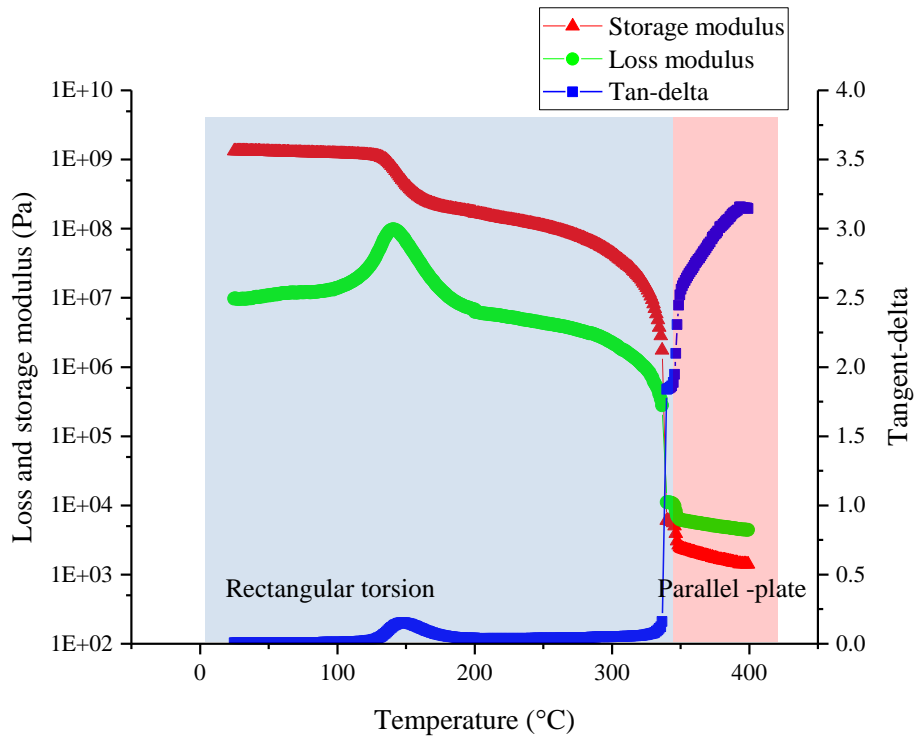


Figure 28: Loss (G'') and Storage (G') modulus of PEEK determined by frequency sweep test by rectangular torsion and parallel -plate configuration

Résumé :

La fabrication additive (FA) fait référence à une grande variété de procédés de fabrication pour le prototypage rapide et la production de produits finis et semi-finis. Contrairement aux procédés classiques ou soustractifs, en fabrication additive, le matériau est ajouté progressivement couche par couche pour former les pièces. La fabrication additive permet la fabrication de pièces complexes impossibles ou peu rentables à fabriquer avec les procédés traditionnels. Le procédé FFF (Fused Filament Fabrication) est basé sur la fusion d'un filament polymère ; le filament est ensuite déposé couche par couche pour fabriquer les pièces finales. Malgré l'intérêt croissant des industries et du grand public ces dernières années, ces procédés de fabrication ne sont toujours pas bien maîtrisés, en particulier pour les polymères qui ne sont pas de grande consommation. Dans cette thèse, nous allons nous intéresser à l'imprimabilité du PEEK (Polyétheréthercétone).

Dans un premier temps, nous avons déterminé les propriétés du polymère influençant la qualité des pièces imprimées par FFF. Les propriétés rhéologiques, la tension superficielle, la conductivité thermique et la dilatation thermique ont été déterminées expérimentalement. Ensuite, le phénomène de coalescence des filaments polymères a été étudié par des mesures expérimentales, un modèle analytique et par simulation numérique. De plus, la stabilité du filament et ses propriétés d'écoulement lorsqu'il sort de l'extrudeuse dans le procédé FFF ont été déterminées expérimentalement puis par analytique et simulation numérique. Ensuite, nous nous sommes concentrés sur la détermination du gonflement des filaments de PEEK. Enfin, la cinétique de la cristallisation isotherme et non isotherme du PEEK a été étudiée expérimentalement. La cinétique de cristallisation a été appliquée au procédé FFF par simulation numérique afin de déterminer la température d'environnement optimale pour contrôler la cristallisation des pièces imprimées. La cristallisation du PEEK atteint sa valeur maximale (environ 22%) de cristallisation pendant le dépôt. En outre, la cristallisation libère de la chaleur dans le système, ce qui augmente progressivement la température du filament déposé jusqu'à 20 °C.

Mots clefs : Thermoplastiques hautes performances, Impression 3D, Fused Filament Fabrication (FFF), Cristallisation, Propriétés Rhéologiques, Simulation numérique

Abstract:

Additive manufacturing (AM) refers to a wide variety of manufacturing processes for rapid prototyping and production of final and semi-final products. In opposite to conventional or subtractive processes, in additive manufacturing, the material is gradually added layer by layer to form the parts. AM enables the fabrication of complex parts which were impossible or not cost-effective to manufacture with the traditional processes. Fused Filament Fabrication (FFF) is based on the melting of a polymeric filament in an extruder; the filament is then deposited layer by layer to manufacture the final parts. Despite growing interest from industries and a large audience in recent years, these manufacturing processes are still not well mastered, especially for not mass-produced polymers. In this thesis, we will take an insight into the printability of PEEK (Polyetheretherketone). The aim is to find the printing conditions to obtain the best quality of the printed parts by FFF process. In the first step, we have determined the polymer properties influencing the quality of the printed parts by FFF. The rheological properties, the surface tension, the thermal conductivity and thermal expansion have been determined experimentally. Then, the coalescence phenomenon of the polymeric filaments has been studied by experimental, analytical and numerical simulation. Furthermore, the stability of the filament and its flow properties when it exits from the extruder in the FFF process has been determined by experimental, analytical and numerical simulation. Then, we have focused on the determination of the die swelling of PEEK extrudate. Lastly, the kinetics of isothermal and non-isothermal crystallization of PEEK has been studied by experimental study. The kinetics of crystallization has been applied to FFF process by numerical simulation in order to determine the optimum environment temperature to control the crystallization of printed parts. The crystallization of PEEK reaches its maximum value (about 22%) of crystallization during the deposition. Furthermore, the crystallization releases heat in the system that increases the temperature of the deposited bead gradually up to 20 °C.

Key-words: High-performance thermoplastic, 3D printing, Fused Filament Fabrication (FFF), Crystallization, Rheological properties, Numerical simulation.